Organic matter stored in ice-rich permafrost

Future permafrost thaw and greenhouse gas release

Loeka Laura Jongejans

Dissertation
zur Erlangung des akademischen Grades
"doctor rerum naturalium"
(Dr. rer. nat.)
in der Wissenschaftsdisziplin "Geochemie"

eingereicht in Form einer kumulativen Arbeit an der
Mathematisch-Naturwissenschaftlichen Fakultät
der Universität Potsdam
und
Alfred-Wegener-Institut
Helmholtz Zentrum für Polar- und Meeresforschung

Eingereicht: 13. Dezember 2021
Disputation: 24. August 2022

Hauptbetreuer: Prof. Dr. Guido Grosse
Betreuer: Dr. Jens Strauss

Gutachter*innen: Prof. Dr. Guido Grosse
Prof. Dr. Susanne Liebner
Prof. Dr. Carsten Müller

https://doi.org/10.25932/publishup-56491
https://nbn-resolving.org/urn:nbn:de:kobv:517-opus4-564911

Abstract

The Arctic is changing rapidly and permafrost is thawing. Especially ice-rich permafrost, such as the late Pleistocene Yedoma, is vulnerable to rapid and deep thaw processes such as surface subsidence after the melting of ground ice. Due to permafrost thaw, the permafrost carbon pool is becoming increasingly accessible to microbes, leading to increased greenhouse gas emissions, which enhances the climate warming.

The assessment of the molecular structure and biodegradability of permafrost organic matter (OM) is highly needed. My research revolves around the question “how does permafrost thaw affect its OM storage?” More specifically, I assessed (1) how molecular biomarkers can be applied to characterize permafrost OM, (2) greenhouse gas production rates from thawing permafrost, and (3) the quality of OM of frozen and (previously) thawed sediments.

I studied deep (max. 55 m) Yedoma and thawed Yedoma permafrost sediments from Yakutia (Sakha Republic). I analyzed sediment cores taken below thermokarst lakes on the Bykovsky Peninsula (southeast of the Lena Delta) and in the Yukechi Alas (Central Yakutia), and headwall samples from the permafrost cliff Sobo-Sise (Lena Delta) and the retrogressive thaw slump Batagay (Yana Uplands). I measured biomarker concentrations of all sediment samples. Furthermore, I carried out incubation experiments to quantify greenhouse gas production in thawing permafrost.

I showed that the biomarker proxies are useful to assess the source of the OM and to distinguish between OM derived from terrestrial higher plants, aquatic plants and microbial activity. In addition, I showed that some proxies help to assess the degree of degradation of permafrost OM, especially when combined with sedimentological data in a multi-proxy approach. The OM of Yedoma is generally better preserved than that of thawed Yedoma sediments. The greenhouse gas production was highest in the permafrost sediments that thawed for the first time, meaning that the frozen Yedoma sediments contained most labile OM. Furthermore, I showed that the methanogenic communities had established in the recently thawed sediments, but not yet in the still-frozen sediments.

My research provided the first molecular biomarker distributions and organic carbon turnover data as well as insights in the state and processes in deep frozen and thawed Yedoma sediments. These findings show the relevance of studying OM in deep permafrost sediments.

Zusammenfassung

Die Arktis ist eine der sich am schnellsten verändernden Regionen der Erde, was zum tauen des dortigen Permafrosts führt. Eisreicher Permafrost, wie der spätpleistozäne Yedoma, ist besonders anfällig für schnelle und tiefe Auftauprozesse infolge von Absenkungen der Oberfläche nach dem Schmelzen des Grundeises. Durch das Auftauen des Permafrosts wird der im Permafrost gespeicherte Kohlenstoff für Mikroben zunehmend zugänglich, was zu erhöhten Treibhausgasemissionen führt und die Klimaerwärmung verstärkt.

Die Untersuchung der molekularen Struktur und der biologischen Abbaubarkeit von organischem Material (OM) im Permafrost ist dringend erforderlich. In meiner Forschung geht es um die zentrale Frage inwieweit das Auftauen des Permafrost die Speicherfähigkeit von OM beeinflusst. Insbesondere untersuchte ich (1) wie molekulare Biomarker bei der Charakterisierung von Permafrost-OM verwendet werden können, (2) Treibhausgasproduktionsraten in auftauendem Permafrost und (3) die Qualität von OM in gefrorenen und (vorher) aufgetauten Sedimenten.

Dazu habe ich tiefe (bis zu 55 m) Yedoma und aufgetaute Yedoma Permafrostsedimente aus Jakutien (Republik Sacha) untersucht. Es wurden Sedimentkerne unter Thermokarstseen auf der Bykovsky-Halbinsel (südöstlich des Lenadeltas) und im Yukechi-Alas (Zentraljakutien) entnommen, und deren Biomarkerkonzentrationen gemessen. Desweiteren wurden Bodenproben von der Permafrostklippe Sobo-Sise (Lenadelta) und der Taurutschung Batagai (Jana-Hochland) genommen und untersucht. Darüber hinaus habe ich Inkubationsexperimente durchgeführt, um die Treibhausgasproduktion in auftauenden Permafrost zu quantifizieren.

Ich habe gezeigt, dass Biomarker-Proxies nützlich sind, um die Quelle des OM zu ermitteln und zwischen OM aus Landpflanzen, Wasserpflanzen und mikrobieller Aktivität zu unterscheiden. Außerdem sind einige Proxies hilfreich, den Abbaugrad von Permafrost-OM zu beurteilen. Dies trifft insbesondere in Kombination mit sedimentologischen Daten in einem Multi-Proxy-Ansatz. Ich zeigte dass der OM von Yedoma im Allgemeinen besser erhalten ist als der von aufgetauten Yedoma-Sedimenten. Die Treibhausgasproduktion in den erstmalig auftauenden Permafrostsedimenten war am höchsten. Dies bedeutet, dass die gefrorenen Yedoma-Sedimente das meiste labile OM enthielten. Außerdem zeigte ich, dass sich die methanproduzierenden Gemeinschaften in den frisch aufgetauten Sedimenten etabliert hatten, jedoch nicht in den noch gefrorenen Sedimenten.

Meiner Forschung hat die ersten molekularen Biomarkerverteilungen und Kohlenstoffumsatzdaten geliefert und Einsichten in den Zustand und Prozesse von gefrorenen und aufgetauten Yedoma-Sedimenten geschaffen. Diese Ergebnisse demonstrieren die Relevanz der Untersuchung von OM in tiefen Permafrostsedimenten.

Samenvatting

Het Noordpoolgebied verandert snel en permafrost ontdooit. Met name ijsrijke permafrost, zoals Yedoma uit het laat Pleistoceen, is gevoelig voor snelle en diepe dooiprocessen als gevolg van bodemdaling na het smelten van bodemijs. Door het ontdooien van permafrost wordt het permafrostkoolstofreservoir beter toegankelijk voor microben, wat tot verhoogde broeikasgasemissies leidt en de klimaatopwarming versterkt.

Het is van groot belang om de moleculaire structuur en de biologische afbreekbaarheid van organisch materiaal (OM) in permafrost vast te leggen. Mijn onderzoek draait om de vraag "hoe beinvloedt permafrostdooi de OM-opslag?" Specifiek heb ik onderzocht (1) hoe moleculaire biomarkers kunnen worden gebruikt om permafrost-OM te karakteriseren, (2) wat broeikasgasproductiesnelheden in ontdooiende permafrost zijn en (3) wat de kwaliteit is van het OM in bevroren en (eerder) ontdooide sedimenten.

Ik heb diepe (max. 55 m) Yedoma en ontdooide Yedoma permafrostsedimenten uit Jakoetië (republiek Sacha) onderzocht. Sedimentkernen zijn genomen onder thermokarstmeren op het Bykovsky schiereiland (ten zuidoosten van de Lenadelta) en in de Yukechi Alas (centraal Jakoetië). Ook zijn bodemmonsters genomen van de permafrostklif Sobo-Sise (Lenadelta) en de zogenaamde *thaw slump* Batagai (Jana-hoogvlakte). In alle monsters heb ik de biomarkerconcentraties gemeten. Ook heb ik incubatie-experimenten uitgevoerd om de broeikasgasproductie in ontdooiende permafrost te kwantificeren.

Mijn onderzoek wijst uit dat de biomarkerproxies nuttig zijn bij het vaststellen van de bron van het OM en om onderscheid te kunnen maken tussen OM van landplanten, waterplanten en OM afkomstig van microbiële activiteit. Daarnaast heb ik aangetoond dat sommige proxies nuttig zijn om de mate van degradatie van het OM vast te stellen, vooral in combinatie met sedimentologische data in een multi-proxy-benadering. Het blijkt dat het OM in Yedoma over het algemeen beter bewaard gebleven is dan het OM in ontdooide Yedoma-sedimenten. De broeikasgasproductie bleek het hoogst in de voor het eerst ontdooide permafrostsedimenten, wat betekent dat de bevroren Yedoma-sedimenten het meeste labiele OM bevatten. Bovendien heb ik aangetoond dat de methaan-producerende gemeenschappen zich wel in de recentelijk ontdooide sedimenten hebben gevestigd, maar nog niet in de nog bevroren sedimenten.

Mijn onderzoek heeft de eerste moleculaire biomarker- en koolstofomzetdata en inzichten opgeleverd in de toestand en processen van diepe, bevroren en ontdooide Yedoma-sedimenten. Deze resultaten tonen de relevantie van het bestuderen van OM in diepe permafrostsedimenten.

Voor mijn ouders, de geografen

Acknowledgements

I could not have not done this work without the support of many people and organizations.

I first would like to thank Jens, for being my day-to-day supervisor. You are a great supervisor as teaching and supporting your students in one of your top priorities. You are warm and welcoming and make me feel good at my job. Josi, thank you for guiding me, for listening and trusting me. Kai, thank you for your scientific support and answering all my questions. Jorien, thank you for your interest in my project and serving in my thesis advisory committee. Guido, thank you for your support and making my time at AWI possible.

A big thanks to Anke, Conny, Dyke, Flavio and Justin for your support in the lab. You helped me with many samples, preparation steps and measurements. Thank you Misha and Gosha, for welcoming me during my visits to Yakutsk and for showing me around.

I thank the DBU for the PhD grant I received and for making me part of their big network. I thank Claudia and Claudia from POLMAR for running the graduate school so well and always being there for me. I thank the PoGS for the many workshops and programs, as well as the funding for a few conferences.

Josi and Maren, it was great to work with you on the "Permafrost im Wandel" outreach project. We developed very cool products and it was great to share our knowledge, enthusiasm and ideas with the school kids. Especially the Explore Science Festival in Bremen was fun.

I thank my office buddies, Lydia, Maren and Torben, for the pleasant atmosphere you created in the office and for many chats, cakes and tea. Especially Maren, we spent quite some time together, thanks for being there for me. Paul, thanks for your realism and inspiring conversations. I thank Anna, Bennet and Sonya for being lovely colleagues and friends. Thanks to Jens, Bennet, Michael, Seth, Boris and my parents for proofreading.

Michael, thank you for giving me inspiration, for all the videos, many (scientific) discussions and for making me laugh. Alex, thank you so much for showing me the way. Thanks for our talks, walks, cooking and yoga; thanks for being a great friend. Ebuka, thank you for checking in with me, for remembering all details and being your honest and critical you. Thank you for making us part of your family and you being part of mine.

I thank my friends in Potsdam, Amsterdam, in between and all around, for your friendship. While being away, I missed many things over the years. Especially, I lost lovely people in my family while I was living abroad and I tear up when I think how long I have been so far away from you. Thank you, my dearest family, for loving so much.

Boris, thank you for standing by my side. For lifting me up. Thank you for proofreading so many texts, all your thoughts and most of all believing in me. You are absolutely the best thing that happened to me in Potsdam. Pappa and mamma, thank you for motivating and supporting me to do what I like. Thank you for your visits, for bringing the grandparents, for being brave and coming back after the accident, for bringing home closer and for always laughing with me. Mamma, thank you for mental sparring and your ideas. Thank you both for making nature and geography a part of my life.

Table of Contents

List of Figures

List of Tables

List of Abbreviations

Notation	**Meaning**	**SI-Unit**
%	percent	
$\sim$	approximately	
$\pm$	plus minus	
°	degree	
°C	degree Celsius	0 °C = 273.15 °K
μg	microgram	10^{-6} g
μL	microliter	10^{-6} L
μm	micrometer	10^{-6} m
‰	per mille	
^{14}C	radiocarbon	
a.s.l.	above sea level	m
ACL	average chain length	
arl	above river level	m
ASE	accelerated mass extractions	
AWI	Alfred Wegener Institute	
BP	before present (referring to 1950)	
brGDGT	branched GDGTs	
bs	below surface	
bss	below sediment surface	
C	carbon	
C/N	organic carbon to nitrogen ratio	
C_{23}	chain with 23 carbon atoms	
cal	calibrated	
CH_4	methane	
CH_4-C	methane carbon equivalent	
cm	centimeter	10^{-2} m
CO_2	carbon dioxide	
CO_2-C	carbon dioxide carbon equivalent	
CPI	carbon preference index	
d	day	86400 s
Da	dalton	1 Da = 1 g mol^{-1}
DCM	dichloromethane	
DNA	deoxyribonucleic acid	
DOC	dissolved organic carbon content	mg L^{-1}
EC	electrical conductivity	mS cm^{-1}
eV	electron volt	1 eV = 1.602 $\cdot 10^{-19}$ J
FA	fatty acid	

Notation	Meaning	SI-Unit
g	gram	
GC-MS	gas chromatography mass spectrometry	
GDGT	glycerol dialkyl glycerol tetraether	
gdw	gram dry weight	
GFZ	German Research Centre for Geosciences	
GHG	greenhouse gas	
Gt	gigatonne	10^{15} g
h	hour	3600 s
ha	hectare	10^4 m^2
HPA	higher-plant alcohol index	
HPFA	higher-plant fatty acid index	
HPLC	high-performance liquid chromatography	
IA	*iso*- and *anteiso*-index	
isoGDGT	isoprenoidal GDGTs	
ka	Latin: kiloannum	10^3 years
km	kilometer	10^3 m
KOH	potassium hydroxide	
kV	kilovolt	10^3 V
ky	kyr, kiloyear	10^3 years
L	liter	10^{-3} m^3
m	meter	
m/z	mass-to-charge ratio	
mA	milliampere	10^{-3} A
MeOH	methanol	
mg	milligram	10^{-3} g
min	minute	60 s
mL	millimeter	10^{-3} L
MIS	Marine Isotope Stage	
mm	millimeter	10^{-3} m
MPa	mega Pascal	10^6 Pa
mS	millisiemens	10^{-3} S
n	"normal", in e.g., *n*-alkane	
n	number of samples	
ng	nanogram	10^{-6} g
NNE	north northeast	
NSO	nitrogen-, sulfur- and oxygen-containing compounds	
OC	organic carbon	
OEP	odd-over-even predominance	
OM	organic matter	
p	estimated probability of rejecting the null hypothesis	
P_{aq}	proxy for input of aquatic plants	
pH	potential of hydrogen, measure of acidity	
POC	particulate organic matter	
psi	pound-force per square inch	$6.895 \cdot 10^3$ Pa
P_{wax}	proxy for input of terrestrial plants	

Notation	**Meaning**	**SI-Unit**
R	correlation coefficient	
RCP	representative concentration pathway, scenario used by IPCC	
s	second	
SSW	south southwest	
TC	total carbon content	wt%
TIC	total inorganic carbon content	wt%
TN	total nitrogen content	wt%
TOC	total organic carbon content	wt%
UAV	unmanned aerial vehicle	
v/v	volume ratio	
VPDB	Vienna Pee Dee Belemnite	‰
vol%	volume percent	
wt%	weight percentage	
y	year	
$\delta^{13}C$	isotopic ratio between stable carbon isotopes ^{13}C and ^{12}C	‰ vs. VPDB

1

Introduction

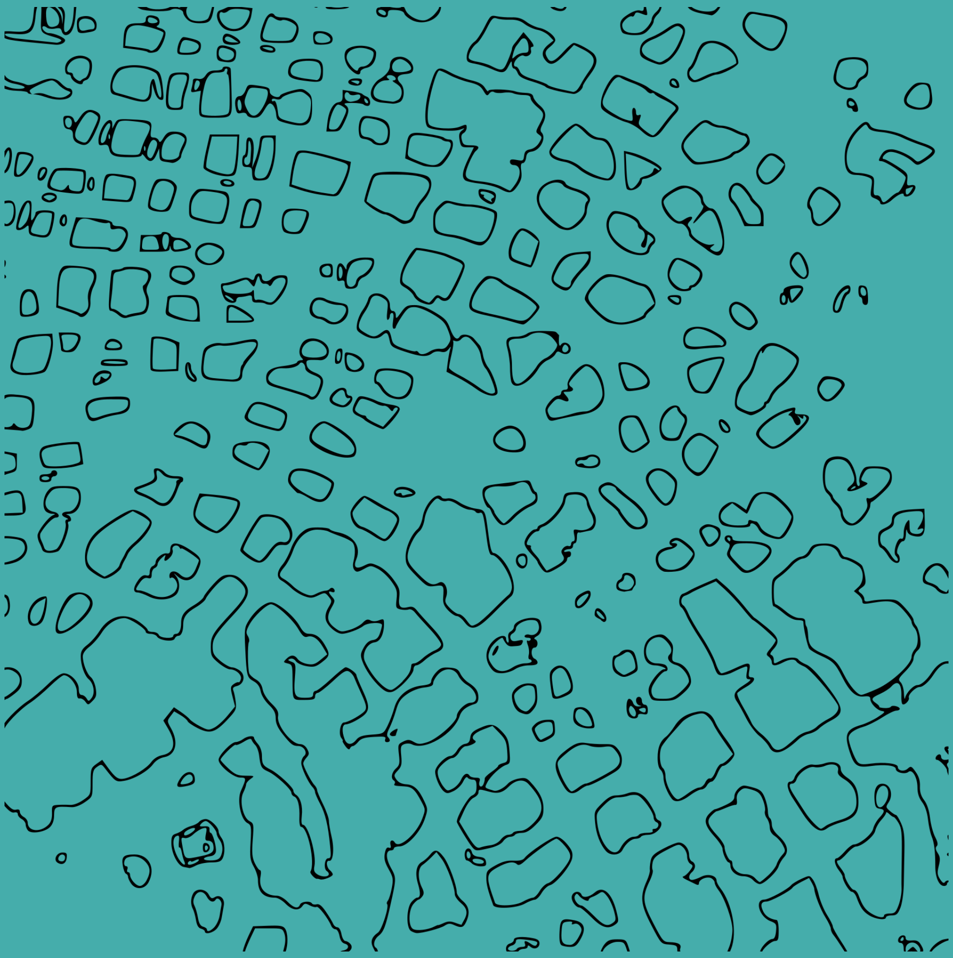

The mountains look down
The waves gently touch the rocks
A tern flies above

1 Introduction

1.1 Motivation

Rapid climate change in the Arctic has severe consequences for both ecosystems and livelihoods on a local and global scale.

A large part of the Arctic is underlain by permafrost – ground that remains below 0 °C for at least two years. The changes in the ground thermal regime in the Arctic lead to ground subsidence, which can damage infrastructure (Shiklomanov et al., 2017a; Shiklomanov et al., 2017b; Vincent et al., 2017). In a circumpolar study, Hjort et al. (2018) found that $\sim$70% of the infrastructure in the permafrost region is located in areas with high potential of near-surface thaw by 2050. In the Russian Arctic, it was shown that the bearing capacity of pile foundations has reduced in the past decades, leading to damage of buildings, pipelines and railroads (Grebenets et al., 2012; Rajendran et al., 2021; Streletskiy et al., 2012). The oil spill in Norilsk in the summer of 2020 was likely caused by permafrost thaw (Rajendran et al., 2021), and had disastrous consequences for the Arctic wilderness.

Arctic coasts are among the fastest eroding on Earth (Jorgenson & Brown, 2005). The shoreline retreat rates are enhanced by a warming ocean, decreased sea ice extent and a higher storm frequency (Manson & Solomon, 2007; Stroeve & Notz, 2018; Timmermans & Labe, 2020). The erosion of permafrost coasts leads to a large influx of sediments, organic matter and nutrients into the nearshore zone, which can reduce photosynthetic uptake of CO_2 in the ocean which results in ocean acidification and increase greenhouse gas release from the ocean (Andersson et al., 2011; Tank et al., 2012). In addition, a large fraction of the organic matter transported into the ocean is mineralized by microbes and hence contributes to greenhouse gas emission (Battin et al., 2009).

Ocean warming and acidification lead to changes in the species composition, spatial distribution and abundance of many marine species (Meredith et al., 2019). These environmental changes impact the livelihood of indigenous communities in the Arctic. The reduced mobility following changed ice and snow conditions and landscape instability leads to reduced access to fishing or hunting grounds, and reduced fresh water availability (Daley et al., 2015; Goldhar et al., 2013, 2014; Inuit Circumpolar Council-Alaska, 2015).

The processes mentioned above mainly have local or regional impacts. However, a main question regarding the warming Arctic concerns the permafrost climate feedback, which is of global importance. Biomass produced over tens of thousands of years was sequestered in frozen sediments and soils, producing a large carbon store. Microbial decomposition of this organic matter enabled through ground warming and thaw, will lead to increased greenhouse gas release to the atmosphere, thereby enhancing the climate warming (Schuur et al., 2015).

1.2 Aims and research questions

The permafrost climate feedback plays a major role in the Earth system: a warming Arctic leads to the mobilization of the permafrost carbon store, which in turn enhances the warming (Meredith et al., 2019). Deep permafrost deposits (>10 m) likely hold a significant organic matter (OM) pool that will be affected by abrupt permafrost thaw processes. Large uncertainties remain in the amount of OM that will be mobilized with permafrost thaw, and how this will affect carbon release. My main question was "how does permafrost thaw affect its OM storage?" In order to answer this question, I addressed three research questions in my project:

1. How can lipid biomarkers be used in the characterization of permafrost OM?
2. What are greenhouse gas production rates from thawing permafrost?
3. What is the OM quality of frozen and (previously) thawed sediments?

1.3 Scientific background

1.3.1 The Arctic in a changing climate

Global surface air temperatures have increased at 0.086 to 0.095 °C per decade from 1880-2012 (Hansen et al., 2010; Jones et al., 2012b; Lawrimore et al., 2011; Rohde et al., 2013). In the Arctic, the temperature trend and variability is larger than in lower latitudes (Figure 1.1) and the Arctic surface air temperature has increased more than twice as much as the global average over the last two decades (Richter-Menge et al., 2017). This is called Arctic amplification and is the result of the interplay of many different factors such as changes in the surface-albedo, the surface radiation flux, and the atmospheric and oceanic heat transport (Serreze & Barry, 2011; Stuecker et al., 2018).

Rising air temperatures are accompanied by increasing ground temperatures. Using the dataset from the Global Terrestrial Network for Permafrost, Biskaborn et al. (2019) showed that permafrost ground is warming at a global scale. They found that the mean annual ground temperature at the depth of zero annual amplitude (the depth where the ground temperature is not affected by seasonal changes) in the continuous and the discontinuous permafrost zone increased between 2007 and 2016 by 0.39 ± 0.15 °C and 0.20 ± 0.10 °C, respectively. Modeling studies indicated that precipitation in the Arctic will generally increase, due to increased evapotranspiration and enhanced moisture flow from lower latitudes (Bintanja, 2018; Vihma et al., 2016). However, increased river runoff and a decrease in snow and permafrost extent can result in local soil drying (Meredith et al., 2019).

All these changes lead to a change in Arctic vegetation. The growing season starts earlier and lasts longer, leading to increased productivity. Several studies pointed out a greening trend in the tundra, resulting from higher summer, spring and winter temperatures, a longer growing season, changing moisture and nutrient availability following active layer thickening, and changed herbivore grazing patterns (**e.g.**; Ju & Masek, 2016; Vickers et al., 2016; Xu et al., 2013). Although it is still unclear what the main drivers are, there have also been indications of tundra browning (Bhatt et al., 2017; Phoenix & Bjerke, 2016). Phoenix and Bjerke (2016)

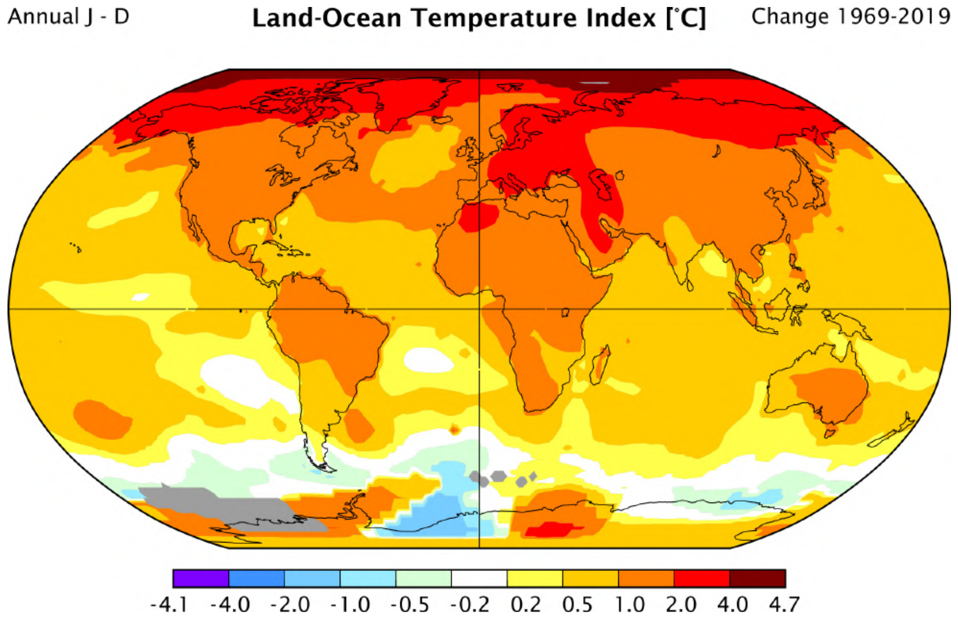

Figure 1.1: Surface temperature change between from 1969 to 2019. Mean period: annual January (J) – December (D). Land-Ocean Temperature Index shows surface air temperature anomalies over land and sea ice, and sea surface temperature anomalies over (ice-free) water. Source: GISTEMP Team (2020) and Lenssen et al. (2019).

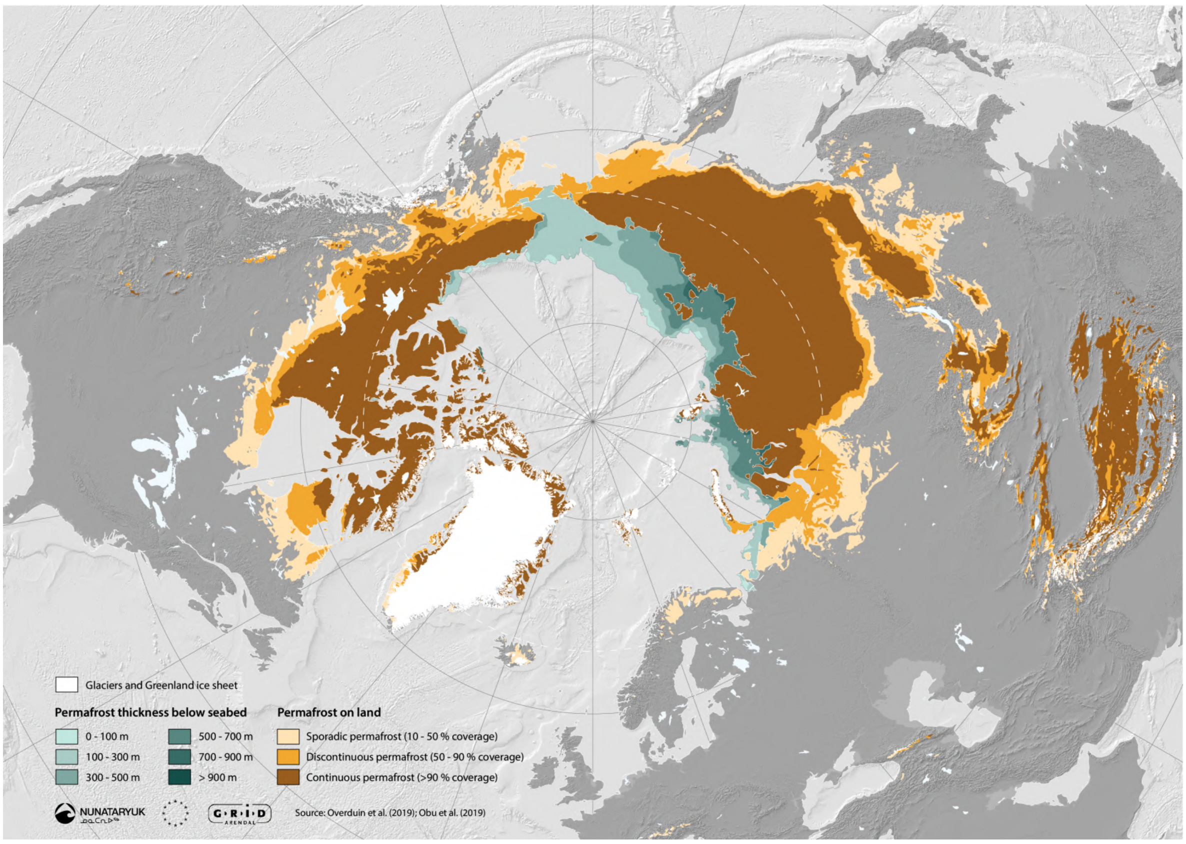

Source: Overduin et al. (2019); Obu et al. (2019)

Figure 1.2: Extent of permafrost on the Northern Hemisphere. This map was adapted by G. Fylakis from GRID-Arendal based on data from Overduin et al. (2019) and Obu et al. (2019), and a product of the NUNATARYUK project in collaboration with GRID-Arendal

proposed tundra browning might be caused by winter warming events – where a reduced snow cover might have led to freezing and desiccation of vegetation – or permafrost degradation.

Shrubification and tree-line advances, as well as the removal of vegetation by fire disturbance, or permafrost degradation, could decrease surface albedo, thereby enhancing local warming (Miller & Smith, 2012; Yoshikawa et al., 2002; Zhang et al., 2013).

1.3.2 Northern Hemisphere permafrost region

Permafrost is ground that is below 0 °C for at least two consecutive years. Permafrost covers vast areas of North America and Russia (Figure 1.2). The permafrost region spans ~20.8 x 10^6 km^2, but not this whole region is underlain by permafrost. The continuous (> 90% coverage) and discontinuous permafrost zones (> 50% coverage) together cover 13.8 x 10^6 km^2 (Figure 1.2) (Obu et al., 2019).

During the late Pleistocene, large areas of Beringia remained unglaciated. The climate was extremely cold and dry, which favored eolian (i.e. wind deposited) sedimentation and syngenetic permafrost formation, meaning the permafrost formed at the same time as the sediment accumulation took place (Kanevskiy et al., 2011). Yedoma permafrost is late Pleistocene ice-rich syngenetic permafrost that can be up to 50 m thick (Kanevskiy et al., 2011; Schirrmeister et al., 2013). While it is thought that Yedoma formation in Alaska and Yukon can mainly be explained by eolian sedimentation, Schirrmeister et al. (2013) showed that Siberian Yedoma often has a polygenetic origin including eolian sedimentation, nival, alluvial and slope processes, as well as cryogenic weathering. In both regions, however, Yedoma deposits are very ice-rich due to the presence of large syngenetic ice wedges up to tens of meters high that formed in large polygonal ice wedge systems. Presently, about 18% of the permafrost region is covered by the Yedoma domain, of which in turn 18% is underlain by Yedoma deposits (Strauss et al., 2021b). The comparison of the current Yedoma domain (2.4 x 10^6 km^2) and the maximum extent during the Last Glacial Maximum (3.3 x 10^6 km^2) (Strauss et al., 2017; Walter et al., 2007; Zimov et al., 2006) shows that a large share of the Yedoma domain and Yedoma deposits have been degraded.

1.3.3 Permafrost degradation

The degradation of permafrost includes the decrease of both the areal extent and the thickness of permafrost (Van Everdingen, 1998), a consequence of permafrost warming and thawing. Whereas gradual top-down thawing, such as active layer thickening, affects centimeters over decades, abrupt thaw processes affect sediments at a depth of more than 10 meters deep in days to several years (Turetsky et al., 2020).

1.3.3.1 Thermokarst development

Thermokarst is the most common process of abrupt and deep (> 10 m) permafrost degradation and involves ground surface subsidence following the melting of ground ice. Thawing of ice-rich permafrost deposits can lead to surface displacement of tens of meters, which can have a large impact on the landscape above and infrastructure such as houses, roads or pipelines.

Thermokarst has different stages and, in particular, includes the development of thermokarst lakes (Figure 1.3) (**e.g.**; Grosse et al., 2013; Morgenstern et al., 2011; Walter Anthony et al., 2014). First, an initial lake is formed by the coalescence of ponds above the melting of massive

Figure 1.3: Photo of a thermokarst landscape in the Yukechi Alas, Central Yakutia. Photo: M. Ulrich, 2014.

ice-wedges (Figure 1.4a and b). Then, the lake can expand and grow deeper, thereby thawing the sediments directly underneath the lake, which is called a talik (Figure 1.4c). During the phase of lake initiation and expansion, methane (CH_4) emissions from the talik sediments are high due to microbial decomposition of the now thawed OM. In addition, nutrients can be released to the lake water such as nitrogen and phosphor (Walter Anthony et al., 2014), which can increase primary production in the lake, leading to the uptake of carbon dioxide (CO_2) from the atmosphere. Afterwards, the lake drains partially, for example due to horizontal outflow through thermal- or coastal erosion, or vertical outflow through open taliks (Figure 1.4d). Regrowth of vegetation, as well as peat formation, can result in soil C uptake. After complete drainage, sediments and remaining OM will freeze once more, eventually establishing permafrost conditions (Figure 1.4e). Finally, a new thermokarst lake can form in the existing drained basin. The formation of new thermokarst lakes and talik expansion will release CH_4 from previously frozen late Pleistocene sediments. However, several studies showed a net decrease of thermokarst lake coverage over the past few decades, especially in the discontinuous permafrost zone (Nitze et al., 2017; Smith, 2005).

1.3.3.2 Retrogressive thaw slumps

Thawing of ice-rich sediments on a slope can result in mass wasting processes such as the formation of retrogressive thaw slumps (Figure 1.5). They form by a slope failure after which the thawed sediments and meltwater slide downslope exposing underlying ice-rich sediments, which thaw and leave a U-shaped slump behind (Figure 1.6). They often occur along coastlines, riverbanks and lakeshores. A typical retrogressive thaw slump morphology consists of a vertical headwall, the slump floor and a slump lobe (Lewkowicz, 1987) (Figure 1.6). Hereby, retrogressive thaw slumps can displace large volumes of sediments, OM and nutrients to the nearshore (Lantuit & Pollard, 2005; Tanski et al., 2017).

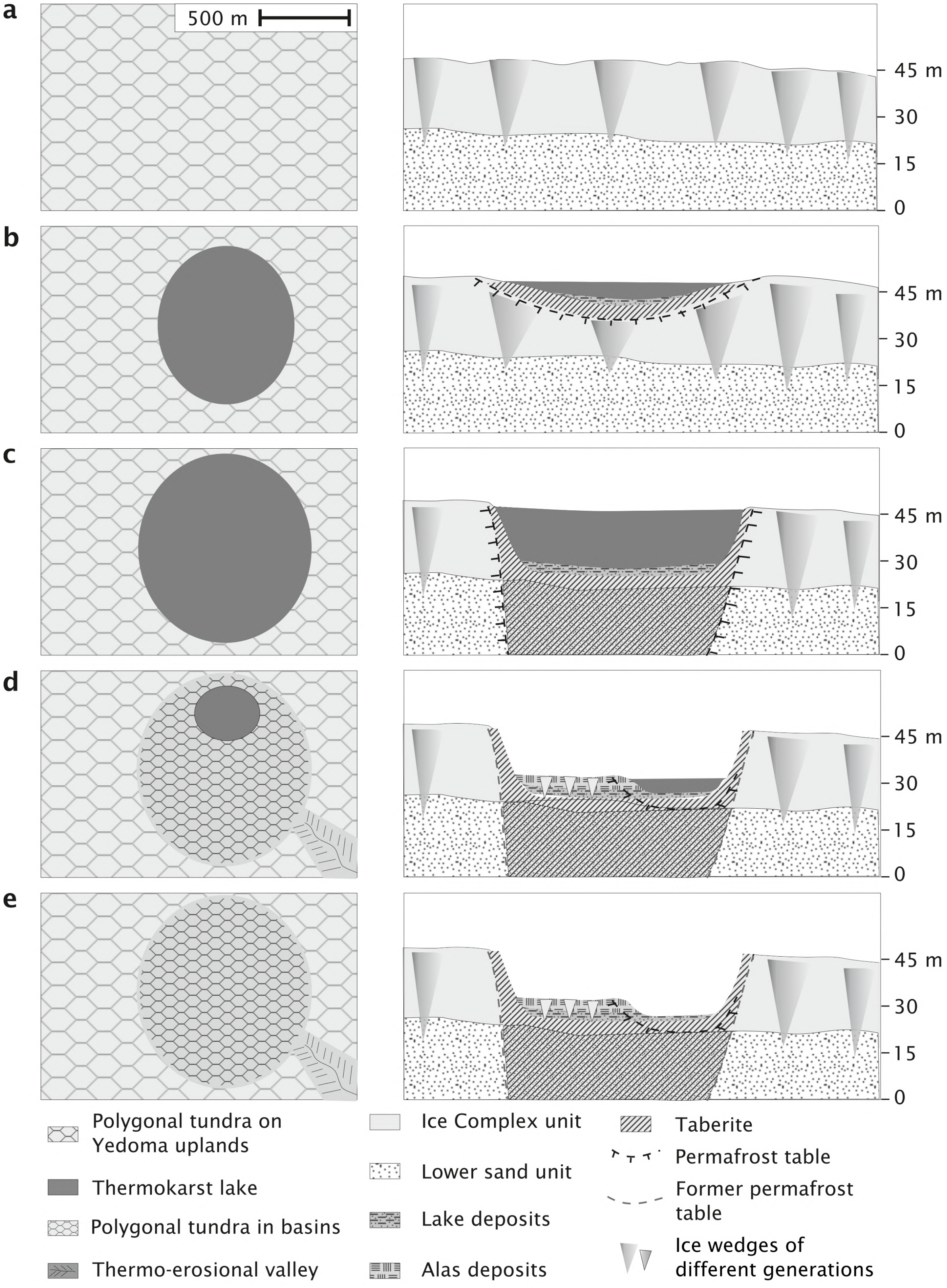

Figure 1.4: Thermokarst lake development schematic from above (left) and in profile (right). (a) Permafrost landscape with massive ice wedges, (b) formation of thermokarst lake, (c) expanding and deepening thermokarst lake and talik, (d) partial drainage of thermokarst lake and vegetation regrowth, (e) regrowth of permafrost and freezing of sediments and organic matter. Modified after Morgenstern et al. (2011).

Figure 1.5: Photo of the Batagay thaw slump in the Verkhoyansky District in Sakha Republic, Russia. Photo: A. Kizyakov, 2019.

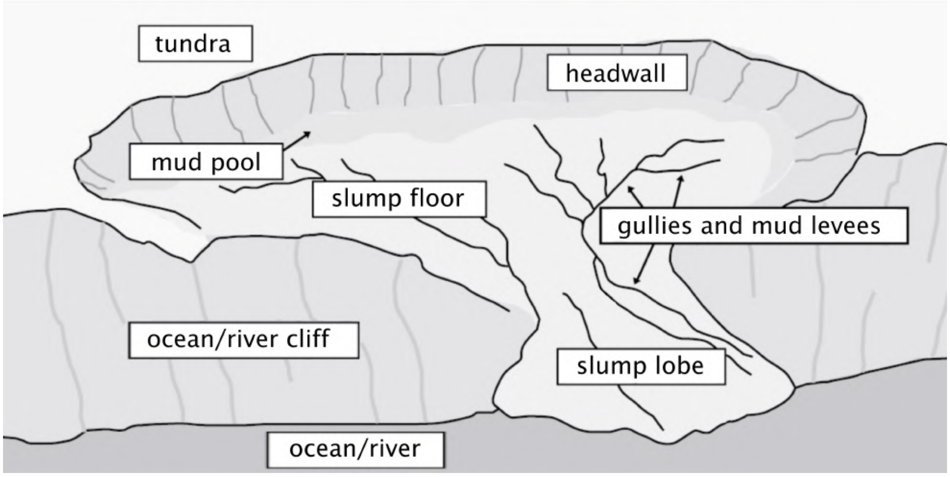

Figure 1.6: Conceptual diagram of retrogressive thaw slump. Modified after Lantuit and Pollard (2005).

1.3.4 Organic matter in permafrost deposits

The permafrost zone contains a large amount of OM. Permafrost warming and thereby thaw leads to the mobilization of previously freeze-locked OM. Following microbial decomposition, greenhouse gases, such as CO_2 and CH_4, are released to the atmosphere. These additional greenhouse gas emissions accelerate global warming, representing a positive feedback loop, called the permafrost carbon feedback (Schuur et al., 2015). Currently, abrupt permafrost thaw processes (e.g., formation of thermokarst lakes and thaw slumps) are not considered by climate models (Meredith et al., 2019). Recently, it was estimated that greenhouse gas release following abrupt thaw processes might be on the order of 80 ± 19 Gt (1 Gt = 10^{15} g) by 2300, which is equivalent to about 40% of the estimated release resulting from gradual thaw (McGuire et al., 2018; Turetsky et al., 2020).

The global permafrost region C pool was recently estimated at 1568 Gt (Strauss et al., 2021a), which is roughly twice the amount that is currently stored in the atmosphere (~880 Gt; Figure 1.7). Furthermore, Strauss et al. (2021a) showed that from the global permafrost region C pool, ~1000 Gt C is frozen perennially in the permafrost. As frozen conditions cease or slow down decomposition, this C pool is not included in the active carbon cycle (Strauss et al., 2017). This large pool of OM accumulated in the permafrost over tens of thousands of years. This was possible due to the syngenetic deposition and fast freezing of the sediments upon deposition, as well as the low decomposition rates in a cold and often anaerobic environment (Schirrmeister et al., 2011a; Strauss et al., 2017).

Previous studies used biochemical proxies to determine the degree of decomposition of OM. For example, higher stable carbon isotopes ratios and lower carbon/nitrogen ratios in the soil indicate stronger decomposed OM (Andersson et al., 2012; Schirrmeister et al., 2011a; Strauss et al., 2015). However, these proxies are also influenced by OM source (Meyers, 1994). Hence, more advanced proxies need to be studied to better identify the decomposition signal. Biomarkers are molecular fossils derived from once-living organisms (Peters et al., 2005). The analysis of lipid biomarkers is useful in determining the OM source and quality. For example, a dominance of long hydrocarbon chains compared to short chains in the sediments (average chain length) indicates that the OM is likely produced by higher land plants (Andersson & Meyers, 2012; Strauss et al., 2015). Another example is the ratio between odd- and even chained hydrocarbons (carbon preference index), which decreases with OM decomposition. Strauss et al. (2015) found that the OM stored in Yedoma was of higher quality for future decomposition than the thermokarst deposits. Otherwise, few studies have analyzed biomarkers in ice-rich permafrost sediments or sub-aquatic sediments.

Microbes in the Arctic are adapted to low temperatures, low availability of nutrients, and low oxygen and water content (Mackelprang et al., 2017). Anaerobic decomposition is limited to a very small group of methanogenic archaea (methane producing single-celled prokaryotic organisms), which are very vulnerable to disturbance such as oxygenation (Holm et al., 2020). When considering a timespan of months to years, aerobic decomposition of OM contributes more C to the atmosphere than anaerobic decomposition (Knoblauch et al., 2013; Lee et al., 2012; Schädel et al., 2016). In long-term incubation experiments, however, it was shown that, when taking into account the 28 times stronger global warming potential of CH_4 compared to CO_2 over a 100-year timescale (Myhre et al., 2013), C loss was higher from anaerobic decomposition than from aerobic decomposition (Knoblauch et al., 2018).

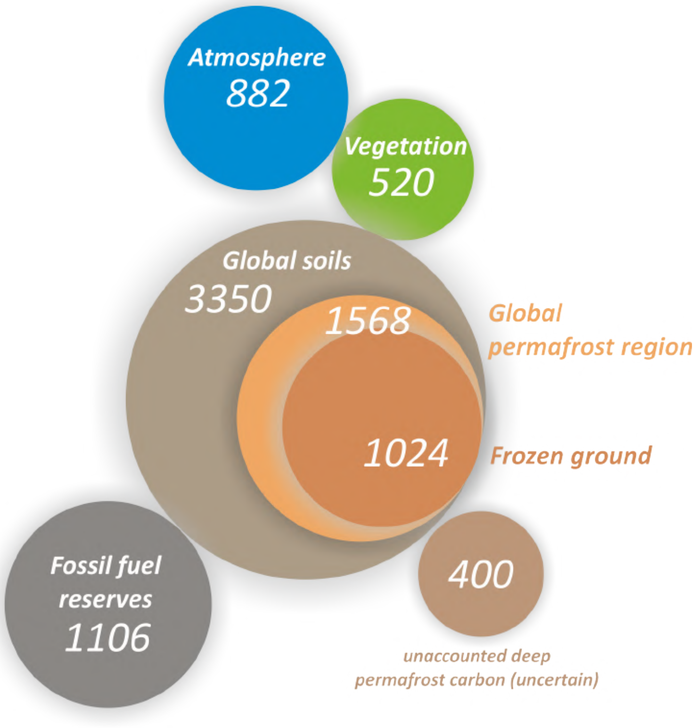

Figure 1.7: Terrestrial and atmospheric carbon stocks in gigatonnes. From Strauss et al. (2021a)

1.4 Material and methods

1.4.1 Study sites

In my thesis, I present data from sediment samples taken in the Russian Arctic. The sample material is unique as deep permafrost sediments are rarely studied. The sediment samples were taken in four separate field expeditions to Siberia.

The four study sites are situated in Yakutia, Sakha Republic (Figure 1.8). Yakutia, spanning ∼2,500 km from north to south and ∼2,000 km from east to west, with several mountain ranges and large rivers such as the Lena and its tributaries, as well as the Olenyok and Kolyma, and with more than 800,000 lakes, offers a large variety of landscapes and ecosystems. This region is characterized by a cold to extremely cold subarctic climate. Furthermore, a large share of Yakutia is underlain by permafrost; the study sites lie in the continuous permafrost zone (Figure 1.1) with permafrost reaching hundreds of meters in depth (Grigoriev, 1960). During the late Pleistocene, large parts of Siberia remained unglaciated and thick ice-rich Yedoma sediment deposits accumulated.

The Bykovsky Peninsula (Figure 1.8, Site 1) is situated on the Laptev Sea coast, southeast of the Lena Delta. In this coastal setting, thermokarst lakes and older basins are affected by storms, flooding, salt diffusion and the transition to thermokarst lagoons (Angelopoulos et al., 2020). A sediment core (31 m long) was retrieved from below a thermokarst lake using a drilling rig placed on a truck that was standing on the lake ice cover (Figure 1.9a).

The Yukechi Alas (Site 2) is a region in Central Yakutia and consists of thermokarst affected landscapes containing many thermokarst lakes. Drained lake basins are often used in this region for horse- and cattle herding and hay farming (Crate et al., 2017; Windirsch

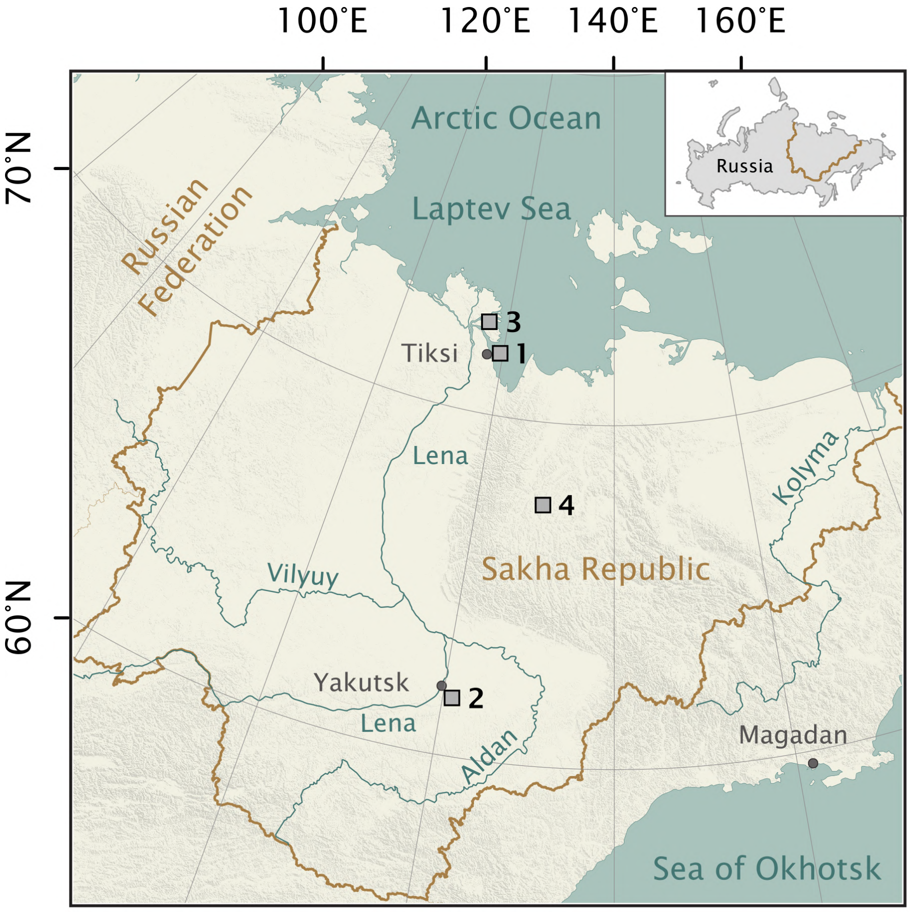

Figure 1.8: Location of study sites in Yakutia (Sakha Republic; brown line) in the Russian Federation (top right): 1. Bykovsky Peninsula, 2. Yukechi Alas, 3. Sobo-Sise Cliff and 4. Batagay thaw slump. Source: ESRI.

et al., 2020). Sediment cores (17 m long) were taken from below two thermokarst lakes using a drilling rig (Figure 1.9b).

The Sobo-Sise cliff (∼100 km north northwest of the Bykovsky Peninsula; Site 3) is a 1,660 m long permafrost exposure on the Sardashskaya Channel, one of the main channels of the Lena River. The Sobo-Sise Island is characterized by Yedoma uplands and slopes, as well as thermokarst basins and lakes. The cliff exposes Yedoma deposits and a Holocene cover layer. Sediment samples were collected on the cliff headwall using a hole saw operated by a technician lowered with a rope (Figure 1.9c).

The Batagay mega thaw slump (Site 4) is the world's largest retrogressive thaw slump and is located in the Yana Highlands, in interior Yakutia. This is among the coldest areas in the Northern Hemisphere. The thaw slump started forming in recent decades and today, headwall retreat exceeds 30 m y^{-1} (Opel et al., 2019; Savvinov et al., 2018). The main headwall was sampled by a climber on a rope, and two additional blocks were sampled in the slump bottom as well as a baidzherakh using a hole saw (Figure 1.9d).

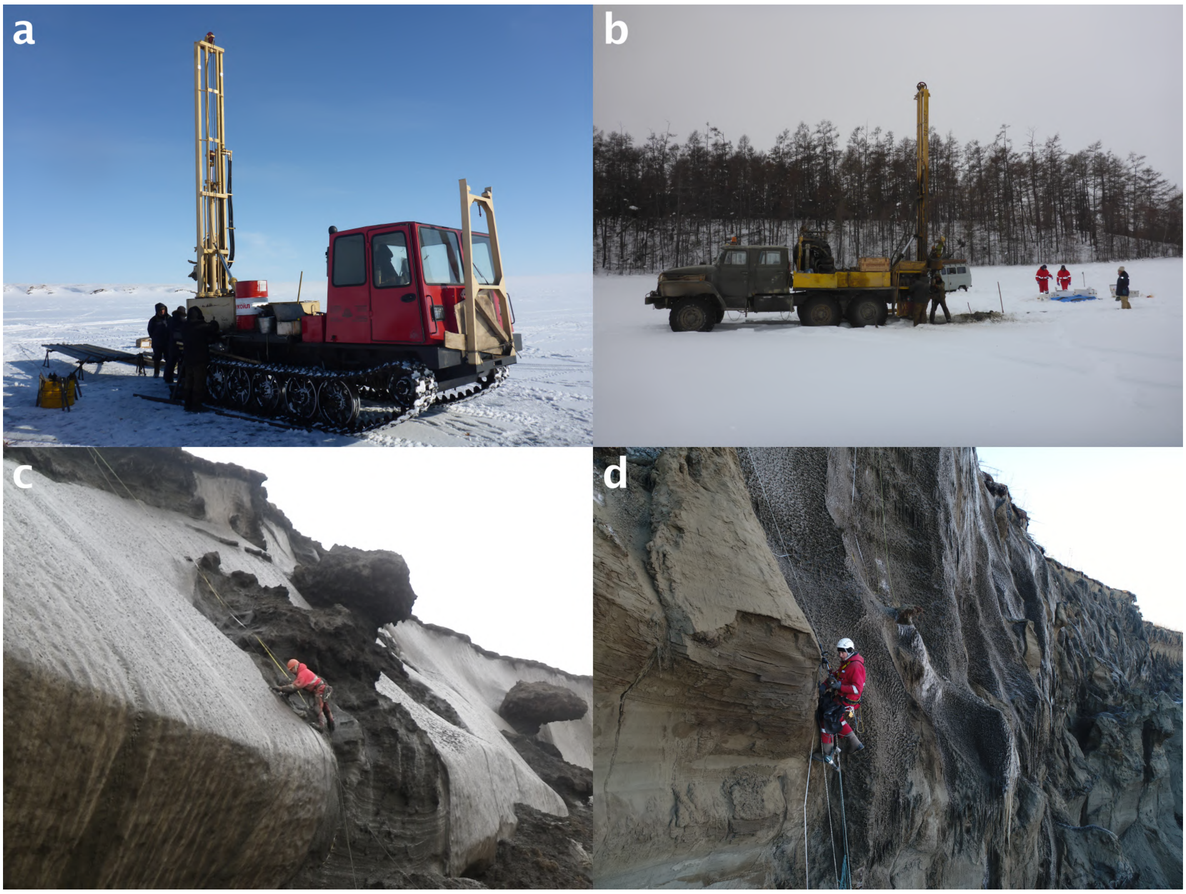

Figure 1.9: Photos of study sites taken during fieldwork. Upper row: drilling rig on the Bykovsky Peninsula (a) and in the Yukechi Alas (b). Bottom row: headwall sampling by climber on rope of the Sobo-Sise cliff (c) and the Batagay thaw slump (d). Photos: J. Strauss, G. Grosse, S. Wetterich and A. Kizyakov.

1.4.2 Main laboratory methods

Sediment samples were analyzed in the laboratories from AWI Potsdam and Bremerhaven, and the German Research Centre for Geosciences (GFZ) in Potsdam. After thawing and homogenizing the samples, I measured the total organic carbon content, dissolved organic carbon content, total nitrogen content, stable carbon isotopes and radiocarbon ages. Lipid biomarker concentrations were measured using gas-chromatography mass-spectrometry. Prior to measurements, the OM was extracted from the sediments (accelerated solvent extractions) and, following the removal of the asphaltenes, the maltene fraction was separated into different OM fractions (medium pressure liquid chromatography). From the biomarker concentrations, I calculated several proxies of which I listed the main ones in Table 1.1. The ACL and P_{aq} are proxies used in the assessment of the source of OM, where a high ACL indicates terrestrial OM, and a high P_{aq} points to aquatically derived OM (Ficken et al., 2000; Poynter & Eglinton, 1990). The CPI and OEP are used to deduce the OM quality or the state of decomposition of the OM. They express the ratio of odd to even n-alkane chains and decrease with ongoing decomposition (Marzi et al., 1993; Zech et al., 2009). A subset of the samples was selected for the anaerobic incubation experiments that I carried out for one year long at 4 °C. I measured anaerobic greenhouse gas production in the headspace of the bottles using gas-chromatography biweekly.

Acronym	Proxy	Equation
ACL	Average chain length	$ACL_{23-33} = \frac{\Sigma\, i\, C_i}{\Sigma\, C_i}$
P_{aq}	Aquatic organic matter proxy	$P_{aq} = \frac{C_{23}+C_{25}}{C_{23}+C_{25}+C_{29}+C_{31}}$
CPI	Carbon preference index	$CPI_{23-33} = \frac{\Sigma\, odd\, C_{23-31}+odd\, C_{25-33}}{2\, \Sigma\, even\, C_{24-32}}$
OEP	Odd over even predominance	$OEP_{26-33} = \frac{\Sigma\, odd\, C_{27-33}}{\Sigma\, even\, C_{26-32}}$

Table 1.1: Overview of the main biomarker proxies. Acronyms and equations of calculated indices from *n*-alkane concentrations.

1.5 Thesis structure

This thesis includes four publications that were published or are in review in international peer-reviewed journals (Chapter 2 to 5) (Table 1.2). The first and third research questions, regarding the lipid biomarkers in and OM quality of frozen and thawed permafrost sediments, are addressed in all four publications. The second research question addresses the greenhouse gas production in thawed permafrost sediments and is presented in Chapter 3. In Chapter 2, "Bykovsky Peninsula", the reconstruction of the sedimentation history of the sediments and the OM decomposition potential in thawed Yedoma sediments below a thermokarst lake on the Bykovsky Peninsula are presented. In Chapter 3, "Yukechi Alas", the comparison of greenhouse gas production under anaerobic conditions in thawed sediments below two thermokarst lakes in the Yukechi Region was presented, as well as OM characteristics. In Chapter 4, "Sobo-Sise cliff", the sources and quality of OM mobilized in the rapidly eroding permafrost cliff in the Lena Delta is described. In Chapter 5, "Batagay thaw slump", investigations of sediments exposed on the main headwall of the Batagay thaw slump and analyses of lipid biomarker concentrations in ancient permafrost sediments are presented. Chapter 6 synthesizes the four papers, describes the implication of these studies, and provides an outlook for future research.

1.6 Overview of publications

Here, I listed the author contributions to the four publications within the thesis, as well as the complementary research (Table 1.2).

1.6.1 Publication "*n*-Alkane Characteristics of Thawed Permafrost Deposits Below a Thermokarst Lake on Bykovsky Peninsula, Northeastern Siberia"

J. Strauss, G. Grosse, and M.N. Grigoriev developed the overall coring plans for the Bykovsky Peninsula field campaign. J. Strauss, M.N. Grigoriev, G.M. Maksimov, L. Schirrmeister, B.K. Biskaborn, and G. Grosse conducted the fieldwork. L.L. Jongejans and J. Strauss developed the study design for biomarker analysis of the core. L.L. Jongejans and B.K. Biskaborn performed the laboratory analyses and led the data interpretation for the long (PG2412) and short (PG2420) sediment cores, respectively. All co-authors contributed with their specific expertise to data interpretation and provided feedback to the manuscript. L.L. Jongejans led the writing of the manuscript.

1.6.2 Publication "Greenhouse gas production and lipid biomarker distribution in Yedoma and Alas thermokarst lake sediments in Eastern Siberia"

L.L. Jongejans wrote the initial draft of the manuscript. L.L. Jongejans and J. Strauss designed the lab studies. G. Grosse, M. Ulrich, J. Strauss, A.N. Fedorov, and P.Ya. Konstantinov selected the field sites and conducted the drilling expedition. L.L. Jongejans, S. Liebner, and C. Knoblauch conducted the incubation experiments. L.L. Jongejans and K. Mangelsdorf carried out the lipid biomarker analysis. All authors contributed to the manuscript drafts and to manuscript finalization.

1.6.3 Publication "Organic matter characteristics of a rapidly eroding permafrost cliff in NE Siberia (Lena Delta, Laptev Sea region)"

L.L. Jongejans helped with the data analysis and interpretation of the biomarkers. Furthermore, L.L. Jongejans contributed significantly to the writing and revising of the manuscript.

1.6.4 Publication "Molecular biomarkers in Batagay megaslump permafrost deposits reveal clear differences in organic matter preservation between glacial and interglacial periods"

L.L. Jongejans and J. Strauss were responsible for the conceptualization of the research. Field work was carried out by L.L. Jongejans, T. Opel, J. Courtin, H. Meyer, S. Wetterich, A. Kizyakov, A.G. Shepelev and I.I. Syromyatnikov. Data acquisition and analysis was done by L.L. Jongejans, K. Mangelsdorf, C. Karger and J. Strauss. L.L. Jongejans wrote the original draft; all authors contributed to the review and editing of the manuscript.

1.6.5 Contributions to complementary research

In all complementary studies, L.L. Jongejans provided feedback to and helped to revise the manuscript. In Jongejans et al. (2018), L.L. Jongejans co-designed the study, carried out the laboratory analyses and led the writing of the manuscript. In Windirsch et al. (2020), L.L. Jongejans developed the bootstrapping routine and provided expertise on carbon stock upscaling. In Jenrich et al. (2021), L.L. Jongejans contributed to data interpretation with her expertise on estimating carbon stocks, as well as on the study area. In Ulrich et al. (2021), L.L. Jongejans supervised part of the laboratory analyses and data interpretation, and helped to shape the study. In Strauss et al. (2021b), L.L. Jongejans contributed a dataset.

Table 1.2: Overview of publications

	Publication
Chapter 2	Jongejans, L. L., Mangelsdorf, K., Schirrmeister, L., Grigoriev, M. N., Maksimov, G. M., Biskaborn, B. K., Grosse, G., & Strauss, J. (2020a). *n*-Alkane Characteristics of Thawed Permafrost Deposits Below a Thermokarst Lake on Bykovsky Peninsula, Northeastern Siberia. *Frontiers in Environmental Science*, *8*, 118. https://doi.org/10.3389/fenvs.2020.00118
Chapter 3	Jongejans, L. L., Liebner, S., Knoblauch, C., Mangelsdorf, K., Ulrich, M., Grosse, G., Tanski, G., Fedorov, A. N., Konstantinov, P. Y., Windirsch, T., et al. (2021f). Greenhouse gas production and lipid biomarker distribution in Yedoma and Alas thermokarst lake sediments in Eastern Siberia. *Global Change Biology*. https://doi.org/10.1111/gcb.15566
Chapter 4	Haugk, C., Jongejans, L. L., Mangelsdorf, K., Fuchs, M., Ogneva, O., Palmtag, J., Mollenhauer, G., Mann, P. J., Overduin, P. P., Grosse, G., Sanders, T., Tuerena, R., Schirrmeister, L., Wetterich, S., Kizyakov, A., & Strauss, J. (2022). Organic matter characteristics of a rapidly eroding permafrost cliff in NE Siberia (Lena Delta, Laptev Sea region). *Biogeosciences*, *19*, 2079–2094. https://doi.org/10.5194/bg-19-2079-2022
Chapter 5	Jongejans, L. L., Mangelsdorf, K., Karger, C., Opel, T., Courtin, J., Meyer, H., Wetterich, S., Kizyakov, A., Grosse, G., Shepelev, A., Syromyatnikov, I. I., Fedorov, A., & Strauss, J. (2022). Molecular biomarkers in Batagay megaslump permafrost deposits reveal clear differences in organic matter preservation between glacial and interglacial periods. *The Cryosphere*, *16*, 3601–3617. https://doi.org/10.5194/tc-16-3601-2022
	Complementary research
Jongejans et al. (2018)	Jongejans, L. L., Strauss, J., Lenz, J., Peterse, F., Mangelsdorf, K., Fuchs, M., & Grosse, G. (2018). Organic matter characteristics in yedoma and thermokarst deposits on Baldwin Peninsula, west Alaska. *Biogeosciences*, *15*(20), 6033–6048. https://doi.org/10.5194/bg-15-6033-2018
Windirsch et al. (2020)	Windirsch, T., Grosse, G., Ulrich, M., Schirrmeister, L., Fedorov, A. N., Konstantinov, P. Y., Fuchs, M., Jongejans, L. L., Wolter, J., Opel, T., & Strauss, J. (2020). Organic carbon characteristics in ice-rich permafrost in alas and Yedoma deposits, central Yakutia, Siberia. *Biogeosciences*, *17*(14), 3797–3814. https://doi.org/10.5194/bg-17-3797-2020
Jenrich et al. (2021)	Jenrich, M., Angelopoulos, M., Grosse, G., Overduin, P. P., Schirrmeister, L., Nitze, I., Biskaborn, B. K., Liebner, S., Grigoriev, M., Murray, A., Jongejans, L. L., & Strauss, J. (2021). Thermokarst Lagoons: A Core-Based Assessment of Depositional Characteristics and an Estimate of Carbon Pools on the Bykovsky Peninsula. *Frontiers in Earth Science*, *9*, 518. https://doi.org/10.3389/feart.2021.637899
Ulrich et al. (2021)	Ulrich, M., Jongejans, L. L., Grosse, G., Schneider, B., Opel, T., Wetterich, S., Fedorov, A. N., Schirrmeister, L., Windirsch, T., Wiedmann, J., & Strauss, J. (2021). Geochemistry and Weathering Indices of Yedoma and Alas Deposits beneath Thermokarst Lakes in Central Yakutia. *Frontiers in Earth Science*, *9*, 701. https://doi.org/10.3389/feart.2021.704141
Strauss et al. (2021)	Strauss, J., Laboor, S., Schirrmeister, L., Fedorov, A. N., Fortier, D., Froese, D., Fuchs, M., Günther, F., Grigoriev, M., Harden, J., Hugelius, G., Jongejans, L. L., Kanevskiy, M., Kholodov, A., Kunitsky, V., Kraev, G., Lozhkin, A., Rivkina, E., Shur, Y., . . . Grosse, G. (2021b). Circum-Arctic Map of the Yedoma Permafrost Domain. *Frontiers in Earth Science*, *9*, 1001. https://doi.org/10.3389/feart.2021.758360

2

Bykovsky Peninsula

Waves in the distance
Swallowing new sediments
Here fresh water still

2 *n*-Alkane Characteristics of Thawed Permafrost Deposits Below a Thermokarst Lake on Bykovsky Peninsula, Northeastern Siberia

2.1 Abstract

Rapid permafrost thaw by thermokarst mobilizes previously frozen organic matter (OM) down to tens of meters deep within decades to centuries, leading to microbial degradation and greenhouse gas release. Late Pleistocene ice-rich Yedoma deposits that thaw underneath thermokarst lakes and refreeze after lake drainage are called taberal sediments. Although widespread, these have not been the subject of many studies. To study OM characteristics and degradability in thawed Yedoma, we obtained a 31.5 m long core from beneath a thermokarst lake on the Bykovsky Peninsula, northeastern Siberia. We reported radiocarbon ages, biogeochemical parameters [organic carbon (OC) content and bulk carbon isotopes] and *n*-alkane distributions. We found the most degraded OM in frozen, fluvial sediments at the bottom of the core, as indicated by the lowest *n*-alkane odd-over-even predominance (OEP; 2.2). Above this, the thawed Yedoma sediments had an *n*-alkane distribution typical of emergent vegetation, suggesting a landscape dominated by low-centered polygons. These sediments were OC poor (OC content: 0.8 wt%, 60% of samples < 0.1 wt%), but the OM (OEP: 5.0) was better preserved than in the fluvial sediments. The upper part of the Yedoma reflected a transition to a drier, grass dominated environment. Furthermore, this unit's OM was least degraded (OEP: 9.4). The thermokarst lake that formed about 8 cal ka BP thawed the Yedoma in the talik and deposited Holocene lake sediments containing well-preserved OM (OEP: 8.4) with the highest *n*-alkane concentrations (20.8 mg g^{-1} sediment). Old, allochthonous OM was found in the thawed Yedoma and frozen fluvial deposits. Using an *n*-alkane endmember model, we identified a mixed OM input in all units. In our study, the thawed Yedoma sediments contained less OC than reported in other studies for still frozen Yedoma. The Yedoma OM was more degraded compared to previous biomarker research on frozen Yedoma. However, this signal is overprinted by the input signal. The fluvial deposits below the Yedoma contained more OM, but this OM was more degraded, which can be explained by the OM input signal. Continued talik deepening and expansion of this thermokarst lake and others similar to it will expose OM with heterogeneous properties to microbial degradation.

2.2 Introduction

Current climate change is causing rapid changes in the Arctic. Accordingly, permafrost deposits are warming and thawing in many regions including Siberia (Biskaborn et al., 2019). Thawing leads to increased microbial decomposition of the previously freeze-locked organic matter (OM) (Mackelprang et al., 2011; Schuur & Abbott, 2011). The amount of organic carbon (OC) that may be mobilized from thawed permafrost sediments is constrained by the OM quantity and quality. Top-down thaw by deepening of the seasonally thawed layer (active layer) largely affects OM in the active layer and near surface permafrost, some of which has already been influenced by early Holocene deeper active layer thaw (French, 1999; Lacelle et al., 2019). Deep permafrost thaw processes, however, such as thermokarst development, may expose OM from Late Pleistocene permafrost deposits to microbial degradation down to tens of meters deep for the first time (Heslop et al., 2019; Turetsky et al., 2020).

Ice-rich, syngenetic Yedoma deposits are late Pleistocene permafrost deposits that are widespread in northern Siberia and Alaska (Schirrmeister et al., 2013) and contain a significant OC pool (Hugelius et al., 2014; Strauss et al., 2013). Yedoma deposits that thaw in situ in taliks underneath thermokarst lakes become diagenetically altered due to ice-loss and compaction. Following lake drainage, these talik sediments can refreeze again, after which they are called taberal sediments: in situ thawed, diagenetically altered and refrozen sediments (Romanovskii, 1993). Strauss et al. (2013) estimated that about 10% of the Yedoma region is covered by lakes and rivers and 56% by drained lake basins with likely refrozen taberal deposits. After thawing of the Yedoma deposits, anaerobic conditions in the water-logged compacted talik sediments promote methane production (Walter et al., 2006; Zimov et al., 1997). Although spatially widespread, taberal sediments have not been subject of many studies yet and are rarely included in OC storage estimates or studies of OM degradability.

A first estimate of the taberal deposit OC pools suggests 114 Gt OC, which is about 25% of the Yedoma domain OC storage (398 Gt) (Strauss et al., 2017; Walter Anthony et al., 2014). In several studies, it is also shown that the OM degradability in Yedoma deposits is higher compared to that in Holocene deposits (Jongejans et al., 2018; Knoblauch et al., 2013; Stapel et al., 2018; Strauss et al., 2015). However, the fate of OM in Yedoma deposits affected by thawing and subsequent qualitative and quantitative changes is poorly understood. Various studies indicate that OM from thawed Yedoma becomes partially degraded. For example, Wetterich et al. (2009) found that plant material was further degraded in taberal deposits than in Yedoma deposits in the Dmitry Laptev Strait.

The study of the biomolecules and other OM characteristics can give important insights into OM degradability and could hence greatly improve estimates of permafrost OM mobilization (Andersson & Meyers, 2012; Sánchez-García et al., 2014). A few studies have previously focused on molecular biomarkers in northeastern Siberian permafrost deposits (Höfle et al., 2013; Stapel et al., 2018; Strauss et al., 2015; Zech et al., 2010). In general, the abundance and distribution of *n*-alkanes, which are long-chained, single bonded hydrocarbons, are used as indicator for OM characterization. The length of *n*-alkanes is an indicator for OM source. Long chained *n*-alkanes (>22 carbon atoms) mainly originate from vascular plants, for example in leaf waxes, whereas short chains (12–20 carbon atoms) are produced by bacteria and algae (Killops & Killops, 2013). The ratio of odd to even chains – expressed as carbon preference index (CPI) (Bray & Evans, 1961; Marzi et al., 1993) or odd-over-even predominance (OEP) (Struck et al., 2019; Zech et al., 2009) – is an indicator for OM degradability and decreases with ongoing alteration of the OM. Furthermore, several studies in temperate latitudes showed that relative *n*-alkane proportions can be used to distinguish between vegetation types. n-C_{23} and n-C_{25} are predominant in aquatic macrophytes and Sphagnum mosses (Bingham et al., 2010; Bush & McInerney, 2013; Ficken et al., 1998), n-C_{27} and n-C_{29} are mainly produced by trees and shrubs, and n-C_{31} and n-C_{33} mostly derive from grasses and herbs (Schäfer et al., 2016; Zech et al., 2009). Very few comparable studies were carried out for talik or taberal sediments (Romankevich et al., 2017; Ulyantsev et al., 2017).

Thus, for the first time we present molecular biomarker characteristics from Yedoma deposits thawed in situ in the talik underneath a thermokarst lake. This study aims to answer the following research questions: (1) what is the sedimentation history of the Yedoma deposits at the study site and (2) what is the OM degradation potential of Yedoma deposits already thawed in a talik?

2.3 Study area

To answer these research questions, we analyzed a 31.5 m long sediment core from sediments underneath Goltsovoye Lake, a thermokarst lake on Bykovsky Peninsula in northeastern Siberia. The Bykovsky Peninsula is a remnant of a former late Pleistocene Yedoma accumulation plane, situated in the foreland of the Kharaulakh Ridge at the Laptev Sea coast (Figure 2.1a). The area is characterized by continuous permafrost, which reaches depths down to 600 m (Grigoriev, 1960). The modern surface morphology is characterized mainly by Yedoma uplands (up to 45 m a.s.l.) and thermokarst depressions and lakes, as well as thermal erosional valleys (Grosse et al., 2007; Siegert et al., 2002). Nival and slope processes in the nearby Kharaulakh Ridge and in situ frost weathering after deposition led to the formation of the Yedoma uplands in the mountain foreland during the late Pleistocene (Schirrmeister et al., 2002a; Strauss et al., 2012a). Strong permafrost degradation since the late Pleistocene to early Holocene transition resulted in thermokarst development and thermal erosion of the Yedoma uplands, which characterize the modern relief of the Bykovsky Peninsula (Grosse et al., 2005). The Bykovsky Peninsula is covered by about 14.4% by thermokarst lakes and lagoons while 46.1% are covered by drained thermokarst lake basins (Grosse et al., 2005).

Goltsovoye Lake (71.74515°N, 129.30217°E) is a medium-sized thermokarst lake (dimensions: 630 by 480 m, surface: $\sim$23 ha) located close to the southern coast of the peninsula (Figure 2.1b). The lake reaches a water depth of about 5 m and has a talik reaching about 30 m deep (Strauss et al., 2018). It is mainly surrounded by Yedoma deposits that are eroded along the lake shore, and drained thermokarst lake basins which are characterized by ice wedge polygons. Several other thermokarst lakes in the vicinity transitioned to thermokarst lagoons already due to coastal erosion and inundation with sea water, allowing salt water to interact with the former freshwater taliks (Jenrich et al., 2021).

Previous permafrost research on the Bykovsky Peninsula included cryostratigraphical and cryolithological research on Yedoma and thermokarst-affected deposits (Grosse et al., 2007; Kunitsky, 1989; Romankevich et al., 2017; Schirrmeister et al., 2018; Schirrmeister et al., 2002a; Schirrmeister et al., 2002b; Slagoda, 1993, 2004, 2005; Ulyantsev et al., 2017). The total organic carbon (TOC) content of Yedoma deposits on the east coast of the Bykovsky Peninsula (Mamontovy Khayata) ranges from 2 to 14 wt%, whereas Holocene cover deposits on top of the Yedoma have a TOC between 2 and 27 wt% (Schirrmeister et al., 2002a). In a transect study in the central part of Bykovsky Peninsula, Fuchs et al. (2018) found mean TOC values of 5.1 ± 4.3 wt% for the upper 3 m on Yedoma uplands consisting of Holocene cover deposits and 7.9 ± 9.0 wt% for drained thermokarst lake basin deposits.

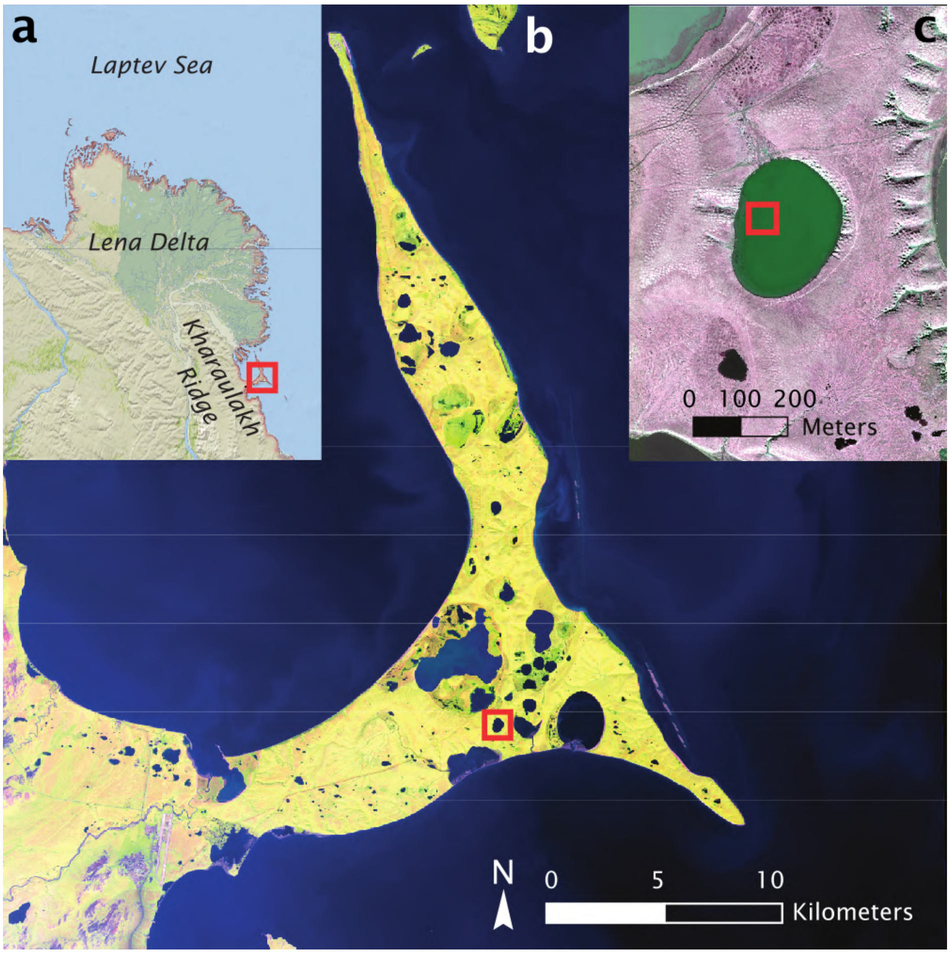

Figure 2.1: Bykovsky Peninsula in northeastern Siberia. (a) Bykovsky Peninsula (red square) at the Laptev Sea coast, southeast of the Lena Delta and east of the Kharaulahk Ridge, (b) Goltsovoye Lake (red square) close to southern coast of Bykovsky Peninsula, (c) coring location PG2412 and PG2420 (red square; ∼ 20 m apart) in Goltsovoye Lake. Source imagery: (a) ESRI Basemap: National Geographic World Map, (b) ESA Sentinel-2 False Color Composite (11-8-2) acquired 2019-08-03, (c) World View 3 Image acquired 2016-09-02 (©DigitalGlobe).

Despite the coastal setting, the modern climate of the Bykovsky Peninsula is rather continental with long, severe winters (September-May) and short, cold summers. The mean air temperature (2000–2016) is -29 °C in January and +8 °C in July (Tiksi Hydrometeorological Observatory) and the mean annual precipitation is less than 350 mm. Mean ground temperatures reach -9 to -11 °C. This region is dominated by moss-grass low shrub tundra and is therefore classified as northern tundra (Treshnikov, 1985).

2.4 Material and methods

2.4.1 Field work

Field work on the Bykovsky Peninsula was carried out in April 2017 (Strauss et al., 2018). Over the course of 4 days, a 31.5 m long sediment core (PG2412; 71.74515°N, 129.30217°E) was retrieved from the deepest point in Goltsovoye Lake (Figure 2.1c), using a URB2-4T drilling rig placed on a truck. The ice cover of the thermokarst lake was 195 cm thick and sediments started at 510 cm from the ice surface. For the depth assignment of the sample material, the water column with the ice cover was included (e.g., see Figure 2.2). Thus, depth measurements started at the ice surface. The core consisted of unfrozen talik sediments (until 3425 cm) and frozen sediments below the talik. The upper few meters of sediment consist of gray silty, fine sand and include plant remains and biogenic shells. Deeper in the core, coarser sandy intervals containing 2-cm-big pebbles alternate with fine sand intervals with large wooden remains. In general, abundant wooden remains and organic-enriched layers were observed between 3665 and 1900 cm. The core material was documented and protected and transported frozen to Potsdam for subsampling. During drilling, core loss happened in the intervals: 3550–3510 cm, 2135–2050 cm and 910–755 cm.

We compare the data from the PG2412 sediment core with the data from a 5 m long sediment core (PG2420; 71.74530°N, 129.30243°E) that was drilled ~20 m away from PG2412, using a UWITEC piston coring system (Biskaborn & Sens, 2020; Strauss et al., 2018). From here on, we will refer to core PG2412 as the long core and PG2420 as the short core.

2.4.2 Laboratory analyses

The long core was described in detail and subsampled for laboratory analyses. Pore water was extracted from thawed samples using rhizon soil moisture samples (membrane pore size: 0.12–0.18 mm). The pH and electrical conductivity (mS cm^{-1}) were measured from the pore water. The sediment samples were freeze-dried and the water content was determined based on the weight difference before and after drying.

Eighteen samples were selected for radiocarbon dating from the long core. Macrofossils such as plant (sedges and twigs) and wooden remains were dated using Accelerator Mass Spectrometry in the AWI MICADAS Laboratory in Bremerhaven. For two of the samples, bulk sediment was dated due to the lack of visible macrofossils. Radiocarbon dates were calibrated using the CALIB 7.1 software and the IntCal13 calibration curve, and expressed as calibrated kilo years before present (cal ka BP) (Stuiver et al., 2017).

The grain size distribution of 71 samples from the long core was measured with a laser particle size analyzer (Malvern Mastersizer 3000, <1 mm fraction) after removal of organic material by treating the samples with hydrogen peroxide (30%). The samples were washed, freeze-dried, manually homogenized and sieved (<1 mm fraction measured) before measuring. Here, we show the grain size distribution of the fraction from 0.1 mm to 1 mm.

Homogenized bulk samples (n = 92, sample interval: ~35 cm) from the long core were analyzed for total nitrogen (TN) and total carbon (TC; Elementar Vario El III), and total organic carbon (TOC; Elementar Vario Max C), which are expressed in weight percentage (wt%). The stable carbon isotopic composition was determined for all samples with TOC values above the detection limit (0.1 wt%). The measured δ^{13}C (ThermoFisher Scientific Delta-V-Advantage gas mass spectrometer equipped with a FLASH elemental analyzer EA 2000 and a CONFLO IV gas mixing system) is compared to the standardized Vienna Pee Dee Belemnite (VPDB) and expressed in per mille (‰ vs. VPDB). TOC values below the detection limit were not considered in further calculations.

For the short core, the same methods were used for radiocarbon dating, TOC content and stable carbon isotopes.

2.4.2.1 Biomarker analysis

Twenty three samples from the long core were analyzed for lipid biomarkers at the German Research Centre for Geosciences (GFZ) after Schulte et al. (2000). Extraction of OM was done with a Dionex 200 ASE extractor using dichloromethane/methanol (DCM/MeOH, 99:1 v/v, heating phase 5 min, static phase 20 min at 75 °C and 5 MPa). The extracts were passed over a sodium sulfate column with *n*-hexane and four internal standards were added for compound quantification: 5α-androstane, ethylpyrene, 5α-androstan-17-one and erucic acid. Using medium-pressure liquid chromatography (MPLC) after Radke et al. (1980), the extracts were separated into an aliphatic, aromatic and NSO (nitrogen-, sulfur- and oxygen-containing compounds) fraction.

n-Alkanes were measured in the aliphatic fraction using gas chromatography/mass spectrometry (GC-MS; GC Trace GC Ultra and MS DSQ, Thermo Electron Corporation) as described by Jongejans et al. (2018) (capillary column from BPX5, 22 mm x 50 m, 0.25 mm). Compounds were identified and quantified with respect to the internal standards from full scan mass spectra (m/z 50–600 Da, 2.5 scans s^{-1}) using the software XCalibur.

2.4.2.2 Biomarker indices

The total lipid concentration of *n*-alkanes is expressed in microgram per gram of sediment (μg g^-1 sed.) and per gram of TOC (μg g^{-1} TOC).

The average chain length (ACL) of *n*-alkanes provides a measure for the main focus of the *n*-alkane chain length distribution and is used to identify OM source. Long-chain *n*-alkanes are produced by terrestrial higher plants for instance in mosses (*n*-C_{23} and *n*-C_{25}), in leaf waxes (*n*-C_{27} and *n*-C_{29}) and in grasses (*n*-C_{31} and *n*-C_{33}) (**e.g.**; Ficken et al., 1998; Zech et al., 2009), whereas short-chain *n*-alkanes are mainly produced by bacteria and algae (Killops & Killops, 2013). The ACL was calculated for *n*-alkanes with carbon number 23 to 33 according to Equation 2.1 where i is the carbon number (Poynter & Eglinton, 1990).

$$ACL_{23-33} = \frac{\Sigma\, i\, C_i}{\Sigma\, C_i} \tag{2.1}$$

The carbon preference index (CPI) and odd-over-even predominance (OEP) indicate the maturity of the OM. High values typically correspond to fresh, undegraded OM, and the ratios decrease with degradation (Bray & Evans, 1961; Marzi et al., 1993). The starting values depend on the composition of the source material. These indices were calculated following Equation 2.2 (Marzi et al., 1993) and 2.3 (Struck et al., 2019; Zech et al., 2009), respectively. As both indices are used in other studies, both parameters are presented here.

$$CPI_{23-33} = \frac{\Sigma\, odd\, C_{23-31} + odd\, C_{25-33}}{2\, \Sigma\, even\, C_{24-32}} \tag{2.2}$$

$$OEP_{26-33} = \frac{\Sigma\, odd\, C_{27-33}}{\Sigma\, even\, C_{26-32}} \tag{2.3}$$

Schäfer et al. (2016) developed an n-alkane endmember model to distinguish between trees and shrubs, and grasses and herbs. It is based on the n-alkane ratio (after Equation 2.4) and the OEP.

$$n - Alkane\, ratio = \frac{C_{31} + C_{33}}{C_{27} + C_{31} + C_{33}} \tag{2.4}$$

In their pilot study, Ficken et al. (2000) proposed the proxy P_{aq} for submerged or floating macrophytes (P_{aq}>0.4) versus emergent (0.1<P_{aq}<0.4) and terrestrial plant input (P_{aq}<0.1; Equation 2.5).

$$P_{aq} = \frac{C_{23} + C_{25}}{C_{23} + C_{25} + C_{29} + C_{31}} \tag{2.5}$$

As this proxy has only been used in tropical and temporal regions, we focus on the trend of the P_{aq} and do not put weight on the proposed ranges. Zheng et al. (2007) developed the proxy P_{wax} to express the share of OM derived from terrestrial plants (Equation 2.6).

$$P_{wax} = \frac{C_{27} + C_{29} + C_{31}}{\Sigma \quad odd\, C_{23-31}} \tag{2.6}$$

2.5 Results

Based on clustering of the n-alkane parameters (see "n-Alkane Distributions"), we divided the long core into four units. Unit I ranged from 3665 to 3300 cm, Unit II from 3300 to 1800 cm, Unit III from 1800 to 1000 cm and Unit IV from 1000 to 510 cm. We decided to separate the results and discussion following the statistical clustering of the n-alkane parameters. The short core was divided into 3 units from the bottom to the top: Unit A from 1010 to 855 cm, Unit B1 from 855 to 820 cm and Unit B2 from 820 to 510 cm (Figure 2.3). For both the long and the short core, we describe the radiocarbon ages and biogeochemical parameters (see section "Bulk Sediment"; Figure 2.2 and 2.3). For the long core, the hydrochemical parameters are characterized (see section "Hydrochemistry"; Figure 2.4), as well as the n-alkane parameters (see section "n-Alkane Distributions"; Figure 2.5). We further calculated general statistics for all parameters (Appendix A: Table A.1). All reported datasets were published in the open access PANGAEA archive (Biskaborn & Sens, 2020; Jongejans et al., 2020b).

2.5.1 Bulk sediment

2.5.1.1 Long core PG2412

The calibrated radiocarbon ages of the macrofossils and bulk sediment of the long core (Figure 2.2a) showed a general trend over depth ranging from 47.5 cal ka BP at 3300 cm to 3.6 cal ka BP at 558 cm (surface sediments). In Unit I, II and III, seven samples had an infinite age (i.e., below the radiocarbon detection limit; >42.4 to >56.1 ka BP) that could not be calibrated.

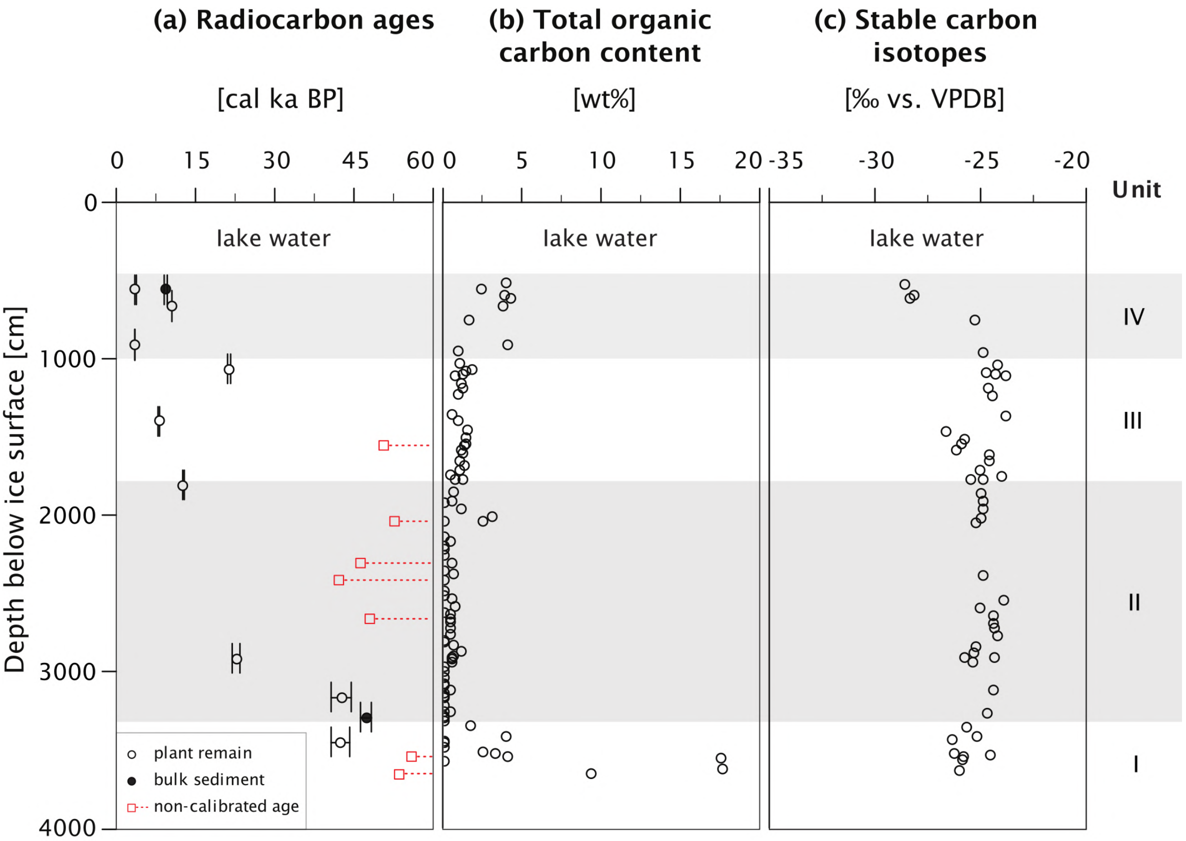

Figure 2.2: Radiocarbon ages and biogeochemical parameters of sediment core PG2412, Goltsovoye Lake. (a) Calibrated radiocarbon ages (open circles: plant remains dated, closed circles: bulk sediment dated, red squares: non-calibrated infinite ages), (b) total organic carbon content and (c) stable carbon isotopes. Units indicated on the right.

Unit IV is of Holocene age. The bulk sediment at 558 cm was 5.7 ka older (9.3 cal ka BP) than the macro remains dated from the same sample (3.6 cal ka BP).

In the bottom of the core, the sediments were coarser (Figure A.1). Unit I contained coarse sand and rounded pebbles (up to 2 cm diameter), as well as finer sandy horizons that were mostly layered. The grain size distribution of Unit I and II (up to ~25 m) was predominantly unimodal indicating fine sand (Figure A.1). Units III and IV had a polymodal grain size distribution and the sediments were mostly very coarse silt to very fine sand.

During the drilling, the talik boundary was located at 3425 cm. Initial temperature data of the borehole (date: 2017-04-23), however, indicated the talik to be ~32 m deep (Strauss et al., 2018). Unit II, III, and IV were completely unfrozen. The cryostructure below 3425 cm was dominantly pore ice (ice between the organic remains) and partly structureless. Segregated ice was rare (ice lens at 3550 cm, 4 x 0.2 cm; ice band at 3592 cm, 1 cm thick).

Unit I was especially enriched in OM. Layers up to 30 cm thick containing twigs, stems, organic layers and lenses, and wooden remains up to 4 cm long in a frozen sandy matrix were found in the interval from 3665 to 3395 cm depth (Figure A.2a). Signs of cryoturbation were present at 3558 to 3555 cm (Figure A.2b). In the lowermost layer (3665-3650 cm), vertically oriented twigs up to 2 cm in length were discovered. Furthermore, organic remains were found from 2173–2311 cm, 1989–2050 cm, 1430–1590 cm, 950–1100, and 510–755 cm. The TOC was highest in the bottom of the core (maximum of 17.8 wt% at 3635 cm) (Figure 2.2b). Unit II and III were very OC poor, but TOC increased again in Unit IV (median: 1.1 wt%). The

δ^{13}C ranged from -28.6 ‰ vs. VPDB in Unit IV (523 cm) to -23.8 ‰ vs. VPDB in Unit III (1370 cm) (median: -24.9 ‰ vs. VPDB) (Figure 2.2c).

2.5.1.2 Short core PG2420

The short core was dated from 23.8 to 0 cal ka BP (Figure 2.3a) (Biskaborn & Sens, 2020). Unit A was deposited during the late Pleistocene, whereas Unit B1 and B2 were of Holocene age. The radiocarbon ages of Unit A ranged from 23.77 ± 0.06 cal ka BP (bulk sediment at 937 cm) to 11.41 ± 1 cal ka BP (bulk sediment at 860 cm). In Unit B, the samples had radiocarbon ages between 10.10 ± 0.05 cal ka BP (at 815 cm) and recent (at 514 cm, surface sediment). Almost all radiocarbon ages from bulk sediments were older than the respective picked plant remains (except for the sample at 767 cm), with a maximum difference of 8.9 cal ka at 885 cm. However, both profiles show a general depth-related trend to older ages with increasing depth.

The sediments ranged from silty sand in Unit A to clayey silt in Unit B2. Unit B1 was composed of a peat layer. The sediments in Unit A were coarser than in Unit B1 and B2 (Strauss et al., 2018). The TOC was lowest in Unit A (1.1 wt% at 875 cm), had its maximum in Unit B1 (9.8 wt% at 900 cm), and decreased to ~4 wt% in Unit B2 (median: 3.6 wt%; Figure 2.3b).

The bulk carbon isotope ratio was highest in Unit A (-24.4 ‰ vs. VPDB at 920 cm) and lowest at the bottom of in Unit B1 (-31.2 ‰ vs. VPDB at 842 cm). Above, in Unit B2, the bulk δ^{13}C signal ranged between -30.3 and -27.0 ‰ vs. VPDB (median: -28.2 ‰ vs. VPDB; Figure 2.3c).

2.5.2 Hydrochemistry

The water content of the long core ranged from 10.5 to 65.4 wt% and was highest in Unit I (frozen part) and the upper three samples of Unit IV (sediment surface samples) (median: 17.1 wt%; Figure 2.4a). There was not much variation in Unit II and III. The pH slightly increased from 7.2 in Unit I to 8.7 in Unit II, was relatively constant in Units II and III, but was much lower in the topmost three samples with the minimum of 6.3 at 596 cm (median: 8.2; Figure 2.4b). The electrical conductivity increased from Unit I to Unit II and decreased to the top from Unit III and IV (median: 778 mS cm^{-1}; Figure 2.4c). In all hydrochemical parameters, the lowermost and uppermost samples of the core were substantially different from the middle part.

2.5.3 *n*-Alkane distributions

The *n*-alkane concentration varied from 0.6 to 20.8 mg g^{-1} sed. (median: 1.8 mg g^{-1} sed.; Figure 2.5a). In contrast to the other samples of Unit I (median: 2.1 mg g^{-1} sed.), the lowermost sample showed a relatively high value (14.3 mg g^{-1} sed.). In Unit II and III, the *n*-alkane concentrations were generally low (median: 0.9 and 5.3 mg g^{-1} sed., respectively). In contrast, Unit IV was characterized by higher concentrations (median: 19.3 mg g^{-1} sed.). The *n*-alkane concentration per gram of TOC primarily increased from the bottom to the top of the core from 50.1 to 581.4 mg g^{-1} TOC with some stagnation in Unit II and III (median:

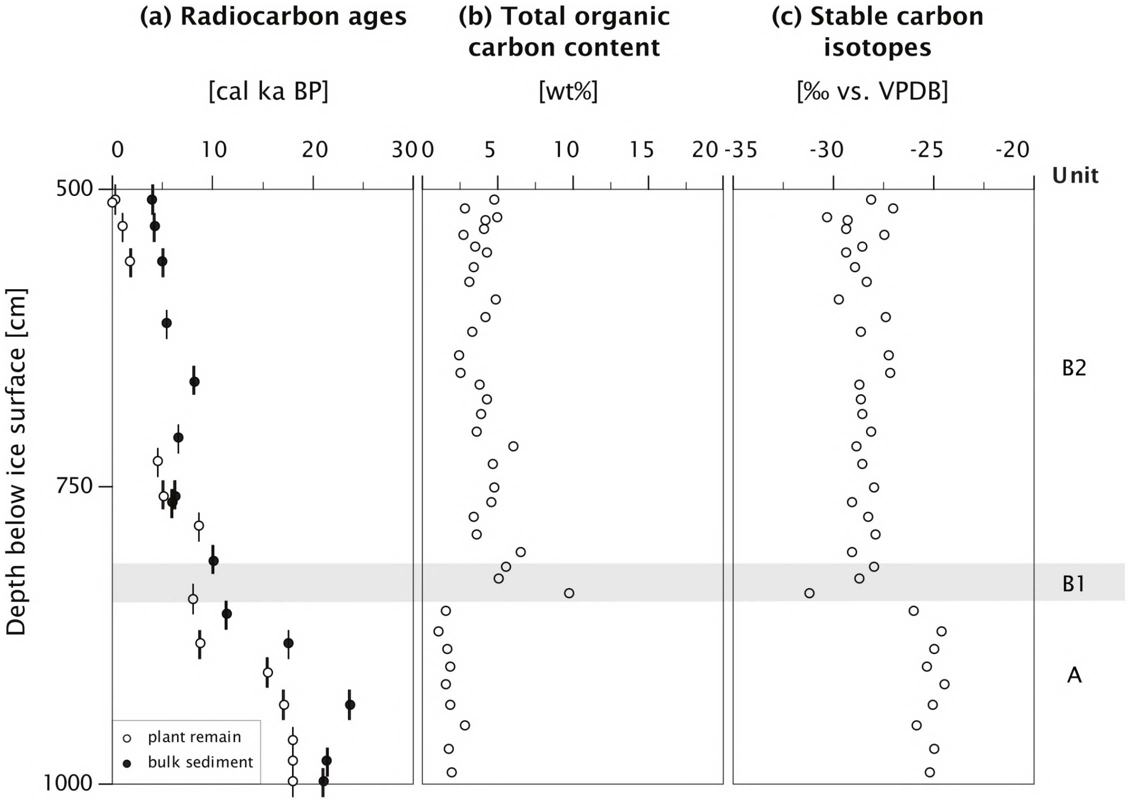

Figure 2.3: Radiocarbon ages and biogeochemical parameters of sediment core PG2420, Goltsovoye Lake sediment core PG2420. (a) Calibrated radiocarbon dates (open circles: plant remains dated, closed circles: bulk sediment dated), (b) total organic carbon, and (c) stable carbon isotopes. Units indicated on the right.

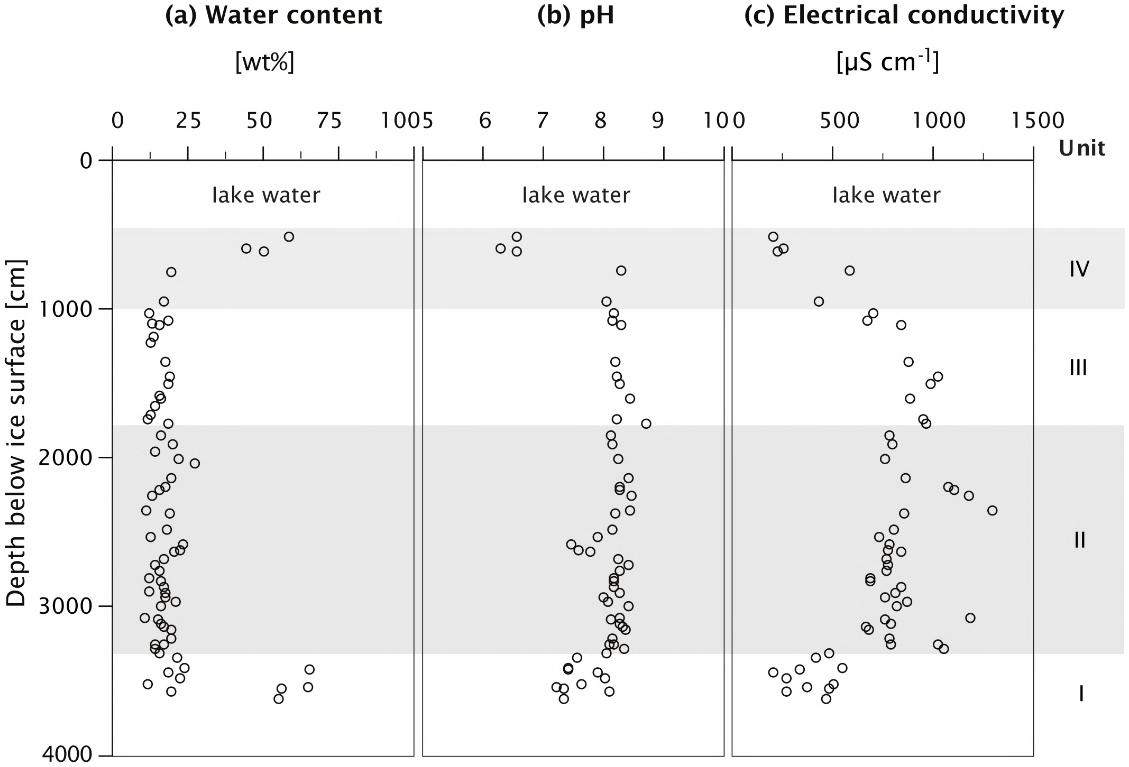

Figure 2.4: Hydrochemical parameters of sediment core PG2412, Goltsovoye Lake. (a) Water content, (b) pH, and (c) electrical conductivity. Units indicated on the right.

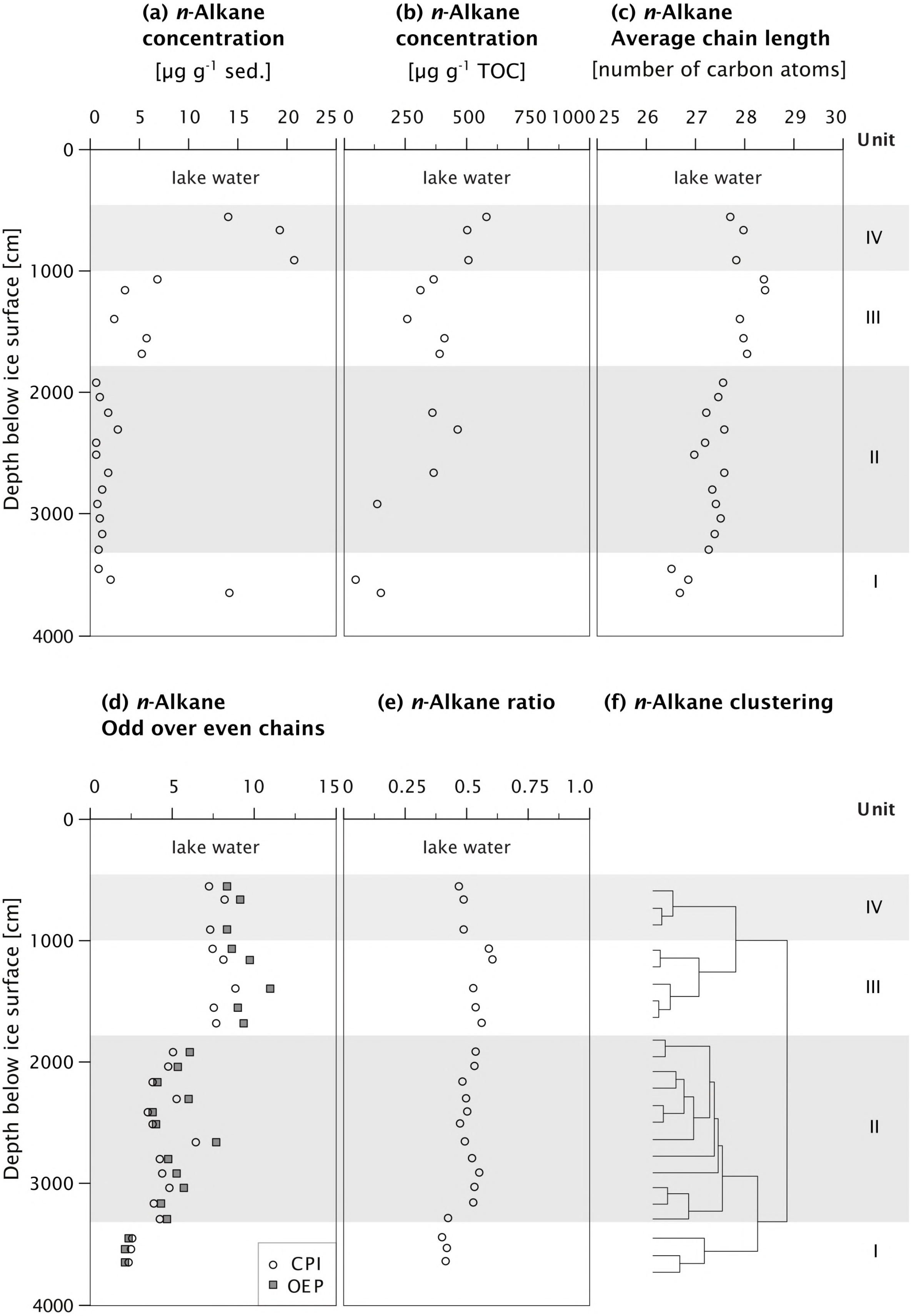

Figure 2.5: *n*-Alkane parameters of sediment core PG2412, Goltsovoye Lake. (a) *n*-Alkane concentration per gram sediment, (b) *n*-alkane concentration per gram organic carbon (note: samples with TOC < 0.1 wt% not shown), (c) *n*-alkane average chain length, (d) *n*-alkane carbon preference index (CPI) and odd-over-even predominance (OEP; gray squares), (e) *n*-alkane ratio (after Schäfer et al., 2016), and (f) *n*-alkane clustering. Units indicated on the right.

367.5 mg g^{-1} TOC; Figure 2.5b). The sediments were dominated by long-chain n-alkanes as indicated by a median ACL_{23-33} of 27.5 (Figure 2.5c), representing the main focus of the n-alkane chain length distribution. The ACL increased from the bottom to the top and ranged from 26.5 in Unit I to 28.4 in Unit III. In Unit IV, the values were a bit lower again around 27.8. The CPI and OEP both increased stepwise from Unit I to II and III before they slightly decreased between Units III and IV. Overall, CPI and OEP were between 2.3 and 8.9 (median CPI: 4.8), and 2.2 and 11.0 (median OEP: 5.7), respectively (Figure 2.5d). The n-alkane ratio ranged from 0.4 to 0.6 and was slightly higher in Units II and III (Figure 2.5e).

Clustering of the n-alkane data revealed four different units, which were also visible in the stepwise changes in the n-alkane proxies (Figure 2.5). These units seem to represent environmental changes reflected by different n-alkane distributions and were therefore used as subunits of the investigated sediment core (Figure 2.5f). All described n-alkane parameters were used as input for the clustering. Clustering was carried out in R v. 3.6.1 using the "chclust" function in package "rioja" with method "coniss."

Odd-carbon number chains dominated the n-alkane distributions of all samples. The dominating chain varied between mid- and long-chain n-alkanes (Figure A.3). Unit I was dominated by n-C_{23} and n-C_{25}. Unit II and III were dominated by either n-C_{27} or n-C_{29}. The upper samples from Unit III (1158 and 1070 cm) were dominated by n-C_{31} and Unit IV again by n-C_{27}. In order to see how the odd chains varied over depth with respect to each other, we calculated the relative n-alkane concentration per gram TOC for the odd chains C_{23-33} (Figure 2.6). The n-C_{33} was least abundant and showed a relatively constant depth profile. The n-C_{27} and n-C_{29} n-alkanes were most abundant. The relative concentration of n-C_{31} and n-C_{25} decreased upwards in the core, whereas n-C_{31} generally increased upwards.

The P_{aq} and P_{wax} were strongly negatively correlated (Pearson correlation index R = -0.995, $p<0.01$; Figure 2.7). The P_{aq} decreased with depth with a maximum of 0.68 in Unit I and a minimum of 0.26 in Unit III (median: 0.41).

2.6 Discussion

In the following, we discuss the sedimentation and post-depositional history of permafrost and lacustrine deposits on Bykovsky Peninsula based on sediment and biomarker parameters observed in our cores.

Generally, it should be noted that age reversals in the sediment core suggest that old organic material has been remobilized in the thermokarst lake environment, i.e., due to thaw and erosion of surrounding permafrost outcrops along the lake shore, which is typical for such dynamic environments (Lenz et al., 2016a). Accordingly, the radiocarbon concentrations of bulk samples represent a mixture of reworked particulate organic matter and fresh organic material from the ecosystem at the time of deposition, causing bulk radiocarbon dates to be offset toward older ages compared to dated plant samples (Gaglioti et al., 2014).

The sedimentary record in our core starts with fluvial sediments that were deposited during the early Weichselian (see section "Unit I – Early Weichselian fluvial sedimentation"), after which Yedoma sedimentation took place (see sections "Unit II – Yedoma Deposition in Wetland Landscapes Dominated by Low-Centered Polygons" and "Unit III/Unit A – Yedoma

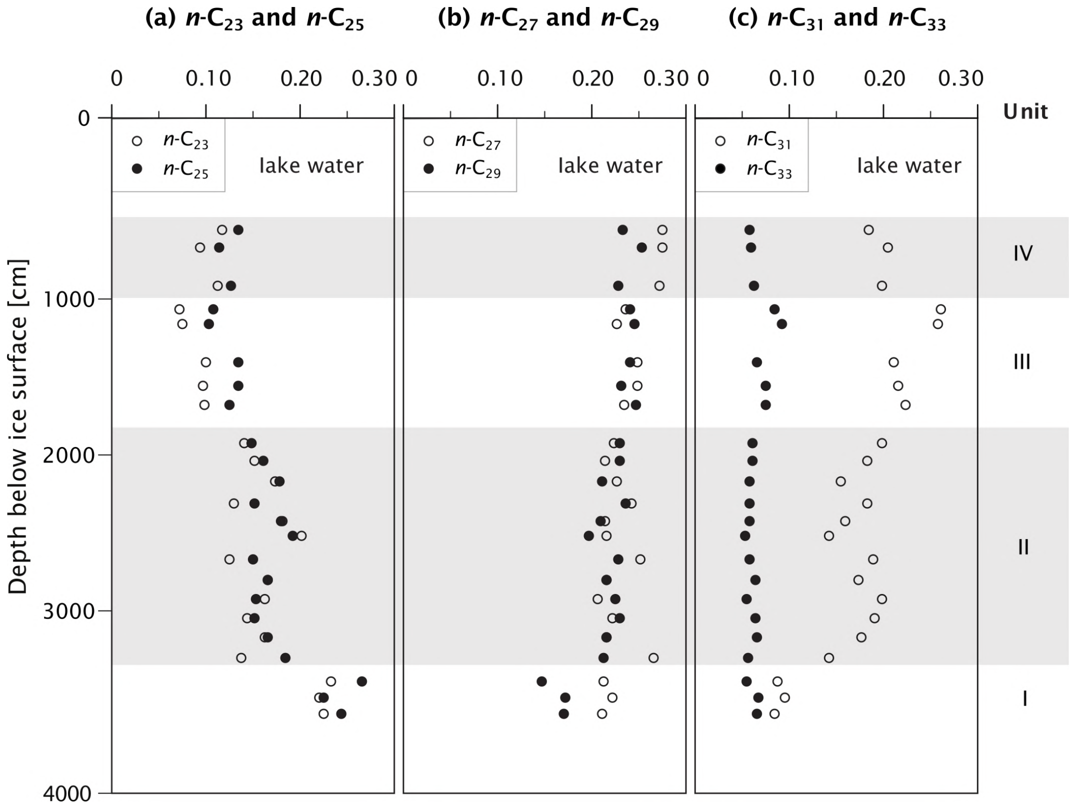

Figure 2.6: Relative concentration of odd chain n-alkanes of sediment core PG2412, Goltsovoye Lake.(a) n-C$_{23}$ (open circles) and n-C$_{25}$ (closed circles), (b) n-C$_{27}$ (open circles) and n-C$_{29}$ (closed circles) and (d) n-C$_{31}$ (open circles) and n-C$_{33}$ (closed circles). Example of formula for n-C$_{23}$: n-C$_{23}$/(n-C$_{23}$ + n-C$_{25}$ + n-C$_{27}$ + n-C$_{29}$ + n-C$_{31}$ + n-C$_{33}$). Units indicated on the right.

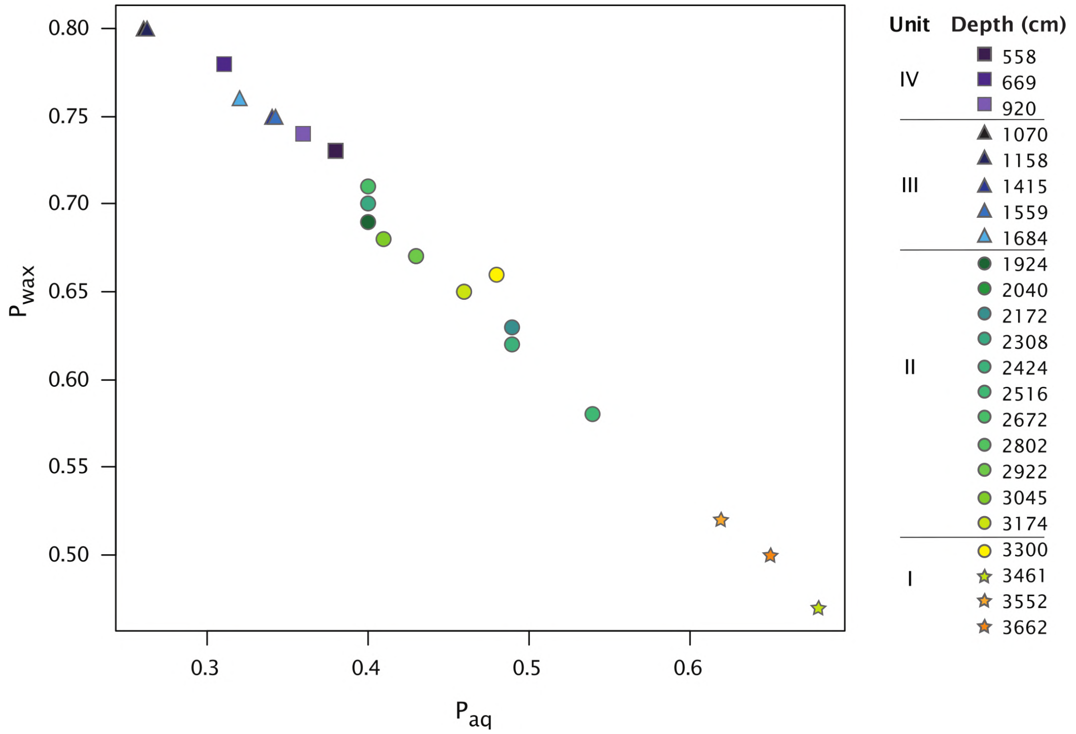

Figure 2.7: n-Alkane proxies aquatic (P$_{aq}$) vs. terrestrial (P$_{wax}$) plant input of sediment core PG2412, Goltsovoye Lake. Unit I: orange stars, Unit II: green circles, Unit III: blue triangles, Unit IV: purple squares.

Deposition Under Cold-Dry Conditions During the Late Weichselian”). During the Holocene, a thermokarst lake formed, which thawed the Yedoma sediments and allowed the deposition of lacustrine sediments (see section “Unit IV/Unit B – Holocene Thermokarst Lake Formation and Lacustrine Sedimentation”). The estimated talik depth based on the core field description following the drilling (3425 cm) was about 2 m deeper than the talik defined by the 0 °C boundary based on the borehole temperature measurements ($\sim$32 m). This inconsistency is caused by drilling heat that has slightly warmed the sediments in the core, making it challenging to visually identify the frozen-unfrozen boundary in the core during the field description. Temperature data from the lake from 1984 indicated that the talik was about 30 m deep (Grigoriev, 1993), which is similar to our findings.

The homogeneous water contents across all units of the long sediment core, with the exception of the uppermost and lowermost samples, suggest that variations are due to potential changes in pore space. The higher OM content in some samples of the fluvial unit may have led to a higher water content, although Strauss et al. (2012a) found that the TOC content was too low to affect the total absolute water content of frozen Yedoma substantially. Nevertheless, higher TOC values can be a reason for the increasing water contents toward the top of the core.

The electrical conductivity is low (Figure 2.4), reflecting a meteoric source for pore waters in interaction with sediment. The electrical conductivity variations over depth might be explained by variation in solid phase surface area: low in Unit I and high in Unit II, leading to lower concentrations in the thawed Unit I and dissolution of mineral material in Unit II. The upwardly decreasing conductivity in Units III and IV suggests a combination of interactions with the solid phase and diffusive exchange with lake water, which has a conductivity of around 200 mS cm^{-1} (Strauss et al., 2018). The EC values in the pore water of the Yedoma sediments (669–1301 mS cm^{-1}, median: 812 mS cm^{-1}) are comparable to thawed Yedoma sediments studied in the Ivashkina Lagoon (Schirrmeister et al., 2018). They found that the EC of water extracts from undisturbed Yedoma sediments at the Mamontovy Khayata were an order of magnitude lower.

2.6.1 Depositional history at the study site

2.6.1.1 Unit I - Early Weichselian fluvial sedimentation

The coarser sediments and the presence of rounded pebbles in Unit I and the lower part of Unit II, point to a strong fluvial influence. Significant differences in the biogeochemistry (Figure 2.8) and hydrochemistry between Unit I and II (TOC: $p<0.05$, δ^{13}C: $p<0.01$, water content: $p<0.01$, pH: $p<0.01$ and EC: $p<0.01$) corroborates a different source material. Previous studies found fluvial sediments underneath the Yedoma deposits on the Bykovsky Peninsula (Grosse et al., 2007; Schirrmeister et al., 2008b; Siegert et al., 2002; Slagoda, 1993), similar to sites in the Lena Delta (Schirrmeister et al., 2003; Wetterich et al., 2008) and on Cape Mamontov Klyk at the western Laptev Sea coast (Schirrmeister et al., 2008a). On the Bykovsky Peninsula, the meandering paleo-Lena River deposited fluvial sediments during the early Weichselian period (100–50 ka BP) (Kunitsky, 1989; Slagoda, 1993, 2004, 2005; Wetterich et al., 2008). The two infinite ages we found in Unit I at 3662 and 3552 cm and the coarse fluvial material suggest that Unit I underneath Goltsovoye Lake has likely formed as part of a regional fluvial depositional environment of the early Weichselian.

The transport and input of allochthonous organic material (large organic remains and driftwood; Figure A.2) by the paleo-river also explains the high variability and the high values of TOC and n-alkane concentrations (g^{-1} sed.) in Unit I compared to Unit II (Figure 2.8a and 2.8c). The CPI and OEP are lowest in Unit I (median: 2.5 and 2.2) and significantly lower than in Unit II ($p<0.01$ and $p<0.05$, respectively; Figure 2.8e and 2.8f), which reflects the strong OM degradation before and during the transport. The organic-rich woody layers in Unit I most likely did not originate from in situ growing trees, but are considered an accumulation of fluvial transported driftwood material from further south.

The n-alkane composition is substantially different in Unit I compared to the units above, as can be seen in the proportion of n-C_{23}, n-C_{27} and n-C_{29} and n-C_{31} (Figure A.3). Unit I is enriched in n-C_{23} and has the lowest concentration of n-C_{27} C n-C_{29} and n-C_{31}. The relative abundance of the shorter chains n-C_{23} and n-C_{25} are highest in Unit I (Figure 2.6). Furthermore, the P_{aq}, representing aquatic OM contents, is highest (>0.6) and the P_{wax}, representing terrestrial OM, lowest (~0.5) (Figure 2.7) in Unit I compared to the other units. Also, the ACL_{23-33}, indicating the main focus of the n-alkane distribution, is lowest (~26.7) in this unit (Figure 2.5C). The tendency of long chain n-alkanes with lower carbon numbers point to the presence of OM from submerged or floating macrophytes (Ficken et al., 2000), which fits to an aquatic environment in a fluvial regime.

2.6.1.2 Unit II – Yedoma deposition in wetland landscapes dominated by low-centered polygons

In the finer, thawed sediments of Unit II (Figure A.1), four of the radiocarbon ages were infinite (Figure 2.2a). Age reversals could point to either reworked sediments or the incorporation of older organic matter. However, in Yedoma sediments, reworking of sediments is not usual due to the syngenetic freezing upon sedimentation. Soil movement as a result of cryoturbation is often restricted to tens of centimeter (Kaiser et al., 2007), while larger cryoturbation patterns sometimes are observed in particular settings. Reworking after in situ thawing of the sediments in the talik can happen due to volume loss after melting of ice. Such partial reworking of Yedoma upon thaw underneath lakes was previously described by Farquharson et al. (2016). However, there are no substantial differences in biogeochemical, hydrochemical and n-alkane parameters between samples with finite and infinite ages. Also, the incorporation of allochthonous ancient OM in Yedoma deposits is common (Jongejans et al., 2018; Vasilchuk et al., 2017) and hence the most likely explanation of the age reversals in this unit.

The sediments in Unit II are generally OC poor (median TOC: 0.6 wt% and 18 samples with TOC < 0.1 wt%; Figure 2.2b). The low TOC content of the sediments likely results from a combination of OM poor deposition as well as partial OM decomposition after thawing of the sediments. The relatively low CPI and OEP (median: 4.3 and 5.0) reveal partly degraded OM.

The changes in n-alkane distribution (Figure A.3) and relative n-alkane concentration (Figure 2.6) over depth indicates different OM sources. A lower P_{aq} (0.4–0.5) and higher P_{wax} (0.6–0.7) compared to Unit I (Figure 2.7) and slightly increased ACL_{23-33} values (Figure 2.5c)

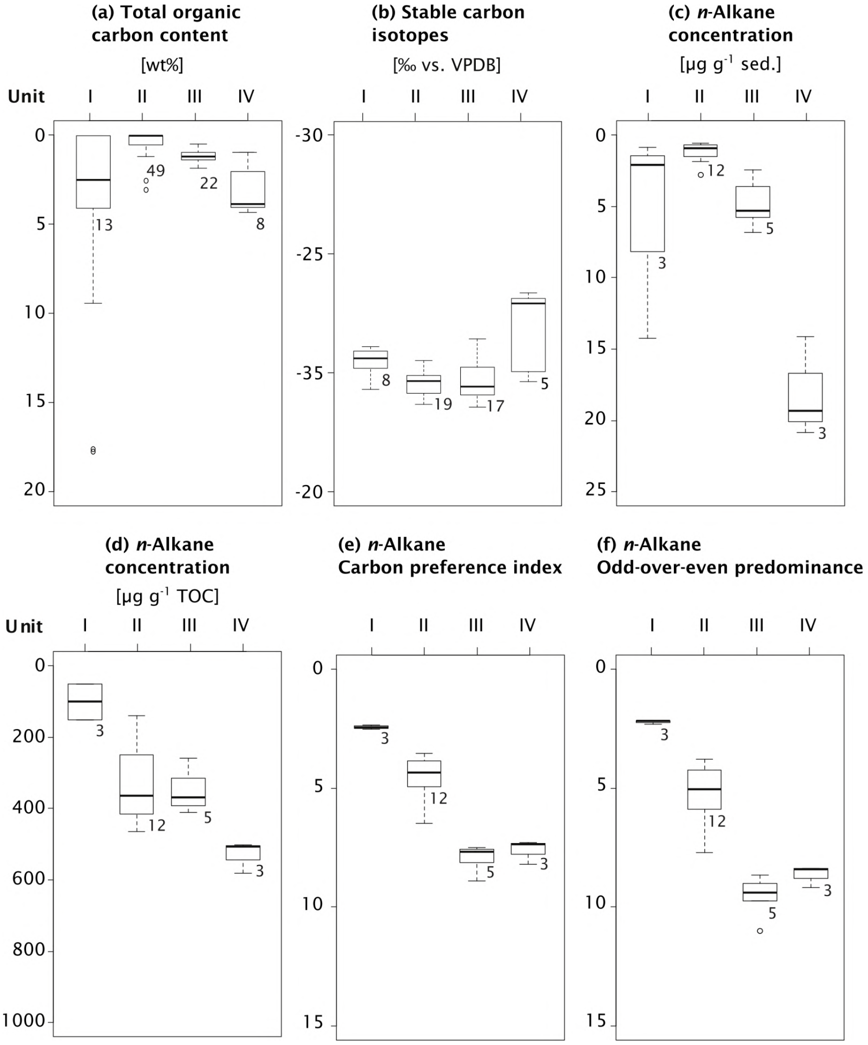

Figure 2.8: Box-whisker plots of biogeochemical and biomarker parameters of sediment core PG2412, Goltsovoye Lake. (a) Total organic carbon content, (b) stable carbon isotopes, (c) n-alkane concentration per g sed., (d) n-alkane concentration per g TOC, (e) n-alkane carbon preference index, and (f) n-alkane odd-over-even predominance. Samples sorted according to n-alkane clustering. Box-whisker plots according to Tukey with outliers outside of 1.5 interquartile range (IQR). IQR = Q3-Q1, range between upper and lower quartiles. Numbers denote sample count.

indicate the presence of emergent macrophytes. The relative large proportion of n-C_{23} and n-C_{25} in Unit I and II (Figure 2.6) is often found in Sphagnum mosses (Bingham et al., 2010; Bush & McInerney, 2013; Ficken et al., 1998). The presence of moss points to wet conditions and thus, these findings indicate a wet environment with shallow-water plant species. Therefore, we interpret this unit as a low-centered polygon environment, whereby water accumulates in the centers of the polygons (Liljedahl et al., 2016). The Yedoma deposition in Unit II could correspond to the relatively wetter conditions of the Kargin Interstadial (Schirrmeister et al., 2002b).

In their study of methane emissions from low-center polygons in the Lena Delta, Kutzbach et al. (2004) found that the amount of methane released relied heavily on the microrelief of the polygons. Small changes in microrelief led to different hydrologic conditions, thereby influencing the aeration status, OM content and vegetation cover. Also, the water table relative to the roots influences the aeration status. Especially vascular plants can form major pathway for methane transport into the atmosphere. The wetland conditions of the low-centered polygon environment of Unit II probably has led to substantial methane emission in the past.

2.6.1.3 Unit III/Unit A – Yedoma deposition under cold-dry conditions during the Late Weichselian

Unit III of the long sediment core corresponds to Unit A of the short core. Unit III contains one infinite age (at 1559 cm; Figure 2.3) and the dated sample at 1070 cm, which gained a late Pleistocene (MIS 2) age (21.39 ± 0.27 cal ka BP) is older than the general radiocarbon age trend, indicating the presence of reworked or eroded material in this sample. Unit A was deposited during the same period. The age difference between the bulk sediment and the picked plant remains in the short core points to a considerable amount of reworked particulate carbon from the surrounding environment.

The biogeochemical parameters are similar for Units III (median TOC: 1.15 wt%, median δ^{13}C: -24.6 ‰ vs. VPDB; Figure 2.2) and Unit A (median TOC: 1.7 wt%, median δ^{13}C: -25.0 ‰ vs. VPDB; Figure 2.3). The multimodal grain size distribution of Unit III (Figure A.1) suggests that multiple transport, accumulation and re-sedimentation processes were involved in the formation, which is in agreement with previous studies of Yedoma deposits (Schirrmeister et al., 2008b; Strauss et al., 2012a).

The lower part of Unit III is dominated by n-C$_{27}$ and n-C$_{29}$ and the upper part (at 1158 and 1070 cm) by n-C$_{31}$ suggesting a transition to a grass/herb dominated environment (Figure 2.6 and A.3) (Schäfer et al., 2016; Zech et al., 2009). In this interval, also the ACL$_{23-33}$ is shifted to the highest values (Figure 2.5c). The P$_{aq}$ proxy shows the lowest value (below 0.34) and the P$_{wax}$ the highest (above 0.75) (Figure 2.7). These findings point to a less aquatic and drier environment, which could correspond to the cold and dry steppe-like tundra that characterized the late Weichselian and the Last Glacial Maximum. This is in agreement with paleo-ecological data from the Mamontovy Khayata Yedoma cliff at the east coast of Bykovsky Peninsula from this period (Schirrmeister et al., 2002b). The TOC and n-alkane concentration (g^{-1} sed.) are significantly higher than in the unit below (p<0.01) (Figure 2.8a and 2.8c). The CPI and OEP show maxima at the top of Unit III (median: 7.7 and 9.4; Figure 2.8e and 2.8f), indicating that this material shows a low level of degradation.

Few other studies focus on n-alkane concentrations in Siberian Yedoma sediments. The Yedoma sediments from this study (Unit II and III; 138–2455 mg g^{-1} TOC) have n-alkane concentrations comparable to the data from other studied Yedoma deposits in the Ivashkina Lagoon (267–1199 mg g^{-1} TOC) (Ulyantsev et al., 2017), on the Buor Khaya Peninsula (387–1715 mg g^{-1} TOC) (Strauss et al., 2015) and at the cliff of Sobo-Sise in the Lena Delta (176–639 mg g^{-1} TOC) (Neubauer, 2016) (Figure 2.9a).

2.6.1.4 Unit IV/Unit B – Holocene thermokarst lake formation and lacustrine sedimentation

Unit IV of the long sediment core corresponds to Unit B of the short core. Unit B1 consists of a peat layer (Figure 2.3). Likely, this basal peaty layer formed during a wetland phase prior to the lake phase and therefore represents the transition to a thermokarst lake. The thickness

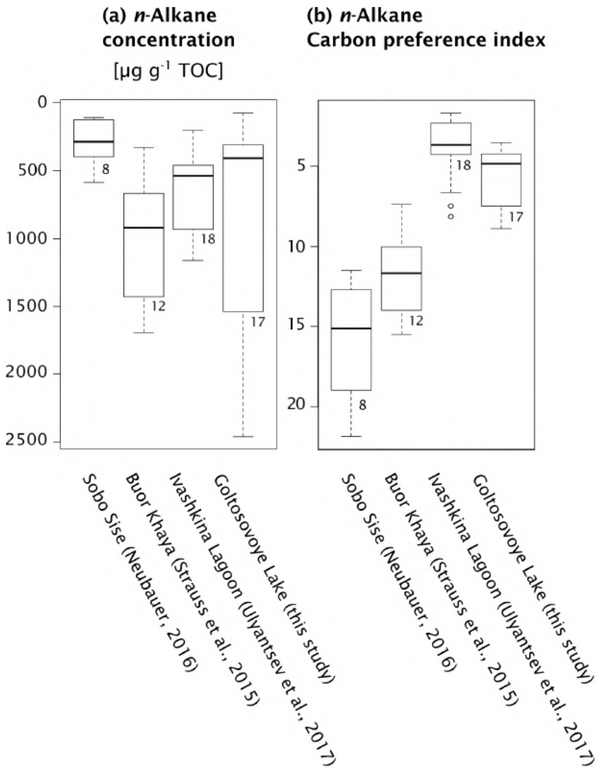

Figure 2.9: Box-whisker plots of biomarker parameters from Siberian Yedoma studies. (a) *n*-Alkane concentration and (b) *n*-alkane carbon preference index. Box-whisker plots according to Tukey with outliers outside of 1.5 IQR. Numbers denote sample count.

of the peaty layer of Unit B1 (35 cm) suggests an extended wetland phase. Similar to other young thermokarst lakes (Kessler et al., 2012; Walter Anthony et al., 2018), talik growth and expansion into the previously deposited late Pleistocene Yedoma deposits certainly thawed the Yedoma OM, resulting in high methane production also underneath Goltsovoye Lake. With subsequent lake basin deepening due to subsidence of the thawing ice-rich permafrost, contemporary lake mud containing in situ produced OM and reworked old OC from the surrounding slopes accumulated, similarly to other thermokarst lakes in northern Siberia (Biskaborn et al., 2013b; Schleusner et al., 2015).

The radiocarbon age of the peat layer (848 cm depth) is 8 ± 0.05 cal ka BP (Figure 2.3) and probably indicates that thermokarst lake formation started around 8000 years BP. The total thaw depth (talik depth ~32 m, altitude difference between lake and Yedoma uplands ~20 m) of ~52 m is relatively shallow for 8000 years of thermokarst development (M. Angelopoulos, personal communication, 2020). Previous talik modeling studies of Alaskan thermokarst lakes showed faster talik growth rates for lakes in North America (**e.g.**; Creighton et al., 2018; Kessler et al., 2012; Ling & Zhang, 2003; West & Plug, 2008). However, talik growth could be slowed by characteristics of Siberian Yedoma, such as its higher ice volume in these sediments or the presence of bedfast ice during an extended shallow lake phase (<2 m).

In the long core, the transition from a dry and cold, grass-dominated landscape to a thermokarst lake lies between Unit III and Unit IV. The biogeochemical parameters of Unit IV (median TOC: 3.9 wt%, δ^{13}C: -28.2‰ vs. VPDB; Figure 2.2) are very similar to Unit B (median TOC: 4.2 wt%, median δ^{13}C: -28.6 ‰ vs. VPDB; Figure 2.3). We found substantial differences between Unit III and IV for the TOC ($p<0.01$), δ^{13}C ($p<0.05$) and the *n*-alkane concentration (p<0.05) (Figure 2.8). Also, the TOC and stable carbon isotope ratio are significantly different between Unit A and B in the short core (p<0.01). The sediments of Unit IV have a higher TOC compared to the thawed Yedoma sediments, which is characteristic for lake sediments with input of lake primary production (Jongejans et al., 2018; Walter Anthony et al., 2014). This is also suggested by the relatively high CPI and OEP in Unit IV (median: 7.3 and 8.4) compared to the lower units.

The dominating n-alkane chain in Unit IV is n-C_{27} (Figure A.3). The ACL, n-alkane ratio, P_{wax}, CPI and OEP are lower in Unit IV compared to Unit III (Figure 2.8) and P_{aq} is partly a bit higher. The OM in this unit is likely a mixture derived from primary production in the thermokarst lake and from thawing permafrost surrounding the lake. As found in other thermokarst lake systems, the lake primary productivity is largely influenced by local thermal erosion, surrounding depositional characteristics and drainage processes strongly affecting hydrochemistry and water level (**e.g.**; Biskaborn et al., 2013a; Lenz et al., 2016a).

2.6.2 Organic matter degradation

The state of OM degradability of Yedoma and other deposits underneath Goltsovoye Lake can be assessed with the n-alkane proxies. In thermokarst-affected Yedoma uplands, the previously undisturbed sediments thaw from the top downwards and therefore, the sediments closer to the surface are expected to have been exposed to thawed conditions for the longest time. Intuitively, one would expect the most degraded OM in the top sediments and the least degraded OM in the bottom sediments of the core. However, based on the CPI and OEP parameters, we found an opposite trend with the furthest degraded OM in the deepest part of the core (Figure 2.5d, 2.8e and 2.8f). As described above, the OM incorporated into the sediments underneath Goltsovoye Lake accumulated under different environmental conditions. Both the OM origin and the depositional conditions have an effect on the CPI and OEP values. Different OM origin and composition lead to different starting values of the parameters for the deposited OM (see for comparison Figure 2.9b) and different environmental conditions can lead to different degradation levels during deposition. Since the OEP and CPI, as well as the n-alkane concentrations and the ACL, show stepwise changes from unit to unit, we interpret the CPI and OEP profiles to be still dominated by the OM input and the degradation level of the time of deposition was largely preserved, rather than being overprinted by the thaw process underneath the thermokarst lake. Thus, the higher terrestrial character (highest P_{wax}) of the OM in Unit III might have caused the highest CPI and OEP values in this core interval, while high degradation of presumably reworked material in the fluvial deposits of Unit I might have led to the lowest values in this core sequence. Overall, the CPI and OEP values still indicate relatively less degraded OM material at least for the Units IV and III and partly also for Unit II.

Romankevich et al. (2017) and Ulyantsev et al. (2017) studied n-alkane parameters of a 38 m long sediment core from the Ivashkina Lagoon (Figure 2.9a and 2.9b), about 3 km east of the Goltsovoye Lake. They found alluvial sands in the bottom (38–22 m), containing highly altered OM (median CPI: 2.7) (Romankevich et al., 2017), which is in line with our findings. In the Yedoma sediments overlying these sands (22–3 m), they distinguished changes in sediment and OM source, as well as burial conditions. In the middle part of the core (~21–13 m), the OM was enriched in n-C_{29} and n-C_{31}, and intermediate bulk CPI values (median: 3.8) could point to microbial degradation. Less degraded material was found in the upper 5 m of the sediment core. Generally, their interpretation corresponds to our findings. Our n-alkane concentration does not differ significantly in the Ivashkina Yedoma deposits compared to the Goltsovoye Yedoma deposits. However, the OM in the Ivashkina deposits is further degraded (CPI: $p<0.01$; Figure 2.9b).

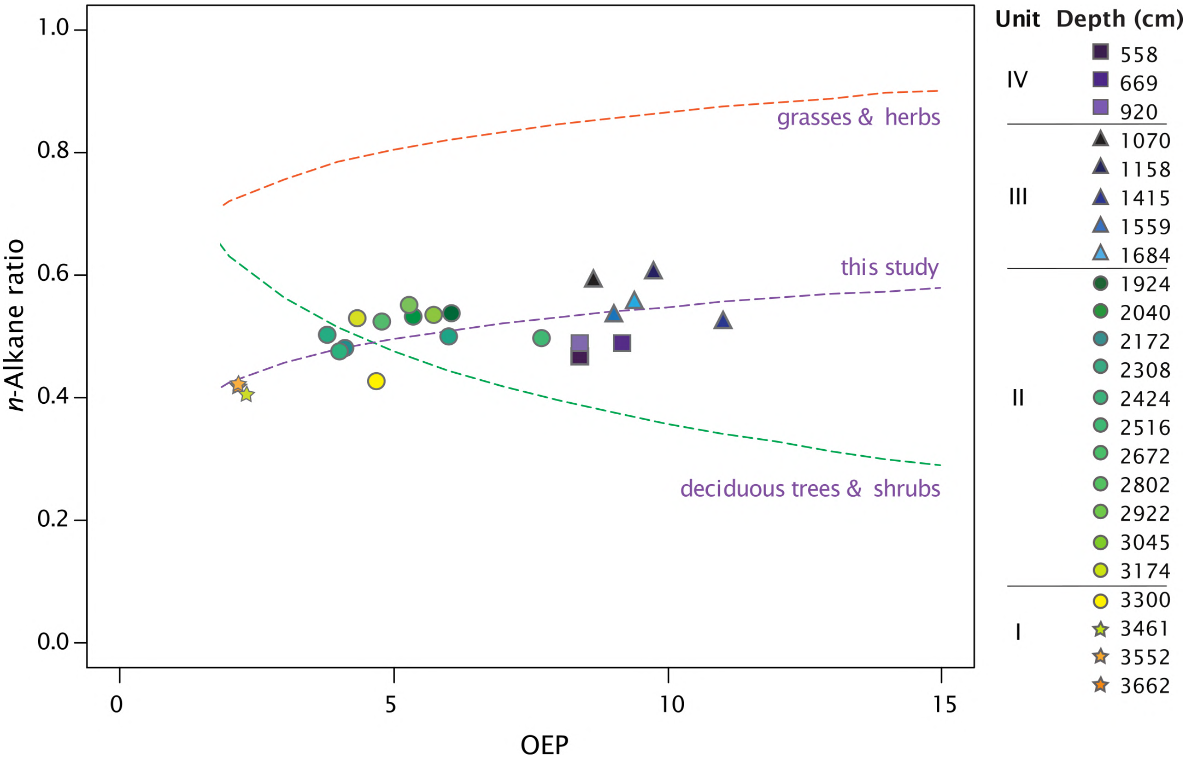

Figure 2.10: n-Alkane endmember model of sediment core PG2412, Goltsovoye Lake. Degradation line for grasses and herbs [dashed orange; y = 0.09*ln(OEP) + 0.66] and deciduous trees and shrubs [dashed green; y = 0.17*ln(OEP) + 0.75] after Zech et al. (2013) and Schäfer et al. (2016). Fitted line for this study [dashed purple; y = 0.08*ln(OEP) + 0.37]. n-Alkane ratio: (n-C_{31} + n-C_{33})/(n-C_{27} + n-C_{31} + n-C_{32}). Unit I: orange stars, Unit II: green circles, Unit III: blue triangles, Unit IV: purple squares.

We plotted the n-alkane ratio of our samples against the OEP (Figure 2.10). The samples clearly plot according to the n-alkane cluster units with lowest OEP and n-alkane ratio in Unit I and maxima in Unit III. Schäfer et al. (2016) calculated degradation lines for grasses and herbs (orange dashed line) and for deciduous trees and shrubs (green dashed line) based on the data from their study in Central Europe and that of Zech et al. (2013) of eastern Germany. The degradation lines are based on (1) the degradation of the organic material, which is indicated by the OEP, and (2) the vegetation type, which is indicated by the n-alkane ratio. We fitted a logarithmic function to the data of this study (purple dashed line). From this, we argue that the OM in our study contains a mixture of long and mid-chain n-alkanes. Due to the lack of typical deciduous trees and shrubs on the Bykovsky Peninsula, the presence of the n-C_{27} alkanes has to be explained by a different source. Using this endmember model is a first-order approximation to decipher a general pattern. First, one cannot assume a similar plant composition in Arctic regions compared to temperate regions. Second, some plant genera such as Artemisia or Sphagnum, have been found to have a dominance of the

n-C_{29} alkane, thereby ‘mimicking’ deciduous trees and shrubs (Ficken et al., 1998; Struck et al., 2019). Third, lake aquatic organisms can contribute to mid-chain alkanes (n-C_{21} to n-C_{27}), which also leads to the overestimation of the presence of trees and shrubs (Ficken et al., 2000). Finally, samples with poorly preserved OM (low OEP values) can be difficult to interpret, as the degradation signal may have altered the n-alkane patterns (Struck et al., 2018). Even though this endmember model does not seem to reflect the OM source patterns in our samples, it does show a mixed character of the OM. Furthermore, this is the first time this endmember model has been applied to Arctic sediments samples. More calibrations studies should be carried out to test this promising method for OM characterization studies in Arctic sediments.

In our study, the frozen fluvial sediments below the thawed Yedoma deposits had higher TOC values than in the thawed Yedoma, but this OM at the very bottom of the core also showed a higher level of degradation. The TOC content of the thawed Yedoma deposits is relatively low (median TOC: 0.8 wt% and 22 samples with TOC below detection limit) compared to previous research of still frozen Yedoma on the Bykovsky Peninsula that reported TOC values of 1.2 to 14 wt% (Schirrmeister et al., 2002a; Strauss et al., 2020). Furthermore, compared to Yedoma deposits on the Buor Khaya Peninsula and the Yedoma cliff of Sobo-Sise (median CPI: 11.7 and 15.2, respectively), a degradation signal of the Yedoma OM is traceable (Figure 2.9b). As we have no information about the detailed OM characteristics of undisturbed Yedoma deposits of the study area, we argue that the OM signal of these thawed Yedoma deposits is a mixture of a source signal and a degradation signal of OM thaw and partial microbial decomposition after talik formation. Still, we find that for our biomarker proxies, the OM input signal exceeds the degradation signal in this study.

Continued thermokarst lake growth of Goltsovoye Lake will lead to further talik deepening and thus thawing of more sediments as well as erosion of surrounding sediments into the lake. Walter et al. (2006) showed that methane release at the lake margins accounted for the largest portion of methane release from thermokarst lakes. As we took our sediment core from the deepest point of the lake, the sediments likely have been thawed the longest time for this lake, while sediments nearer to the shore would have been exposed to thaw only more recently. Our study highlights that thawed deposits underneath a thermokarst lake vary in the OM composition and degradability and that this is primarily a result of OM origin and depositional environment, and less of permafrost thaw history. To understand future responses of further permafrost thaw and to assess the greenhouse gas emission potential, more knowledge is needed about the OM characteristics of the permafrost deposits. A direct comparison of thawed and still frozen Yedoma OM from nearby sites would be useful to better understand the impacts of thaw and microbial decomposition. The applied study of n-alkanes proves to be very useful in identifying OM sources, level of degradation and assessment of the depositional environment. Further research using other biogeochemical assessments such as those based on amino acids (Hutchings et al., 2019), Sphagnum-derived phenols (Abbott et al., 2013) and pectin-like polysaccharides as well as C/N burial profiles (Schellekens et al., 2015) would also be valuable.

2.7 Conclusion

Our study of OM degradation in thermokarst-affected permafrost sediments in an ice-rich Yedoma permafrost landscape relied on a unique set of two drilling cores from beneath a thermokarst lake in northeastern Siberia. Using *n*-alkane indices, we were able to distinguish four depositional units for the frozen and thawed sediments underneath Goltsovoye Lake on Bykovsky Peninsula. The lowest sediments (36.6-33 m) are of fluvial origin and were deposited prior to Yedoma formation. Their OM is characterized by a high degradation level and a relatively large share of aquatic OM (e.g., macrophytes). Yedoma formation started in a relatively wet, low-centered polygon landscape (33-18 m) with low amounts of but largely less degraded OM. Subsequently, *n*-alkane indices indicate a transition to a drier environment during the peak period of the Last Glacial Maximum (18-10 m) that was partly grass dominated (12 to 10 m). Furthermore, the OM in this sediment interval shows a low level of degradation. In the middle Holocene, a thermokarst lake formed and deposited lacustrine sediments (10-5.1 m), accompanied by talik formation that subsequently thawed the previously accumulated ice-rich Yedoma deposits. These lake sediments exhibit a higher TOC and *n*-alkane concentrations compared to the Yedoma sediments below.

Both the Yedoma deposits and the fluvial deposits contain old allochthonous OM. Moreover, using the *n*-alkane endmember model, we found a mixed input of the OM in all units. In the thawed Yedoma sediments, less OC was found compared to frozen Yedoma deposits reported elsewhere, suggesting a combination of OC poor deposition and partial mobilization of OC and release as methane from the thermokarst lake talik. Higher OC contents were found in the frozen fluvial sediments below the Yedoma deposits. However, using the *n*-alkane parameters, we found a trend toward increasingly degraded OM in these sediments in the bottom of the core. Overall, the *n*-alkane proxies suggest that the input signal of the OM still exceeds the degradation signal from thaw underneath the lake and that these parameters can still provide valuable information on the origin, degradation level and deposition conditions of the deposited OM.

2.8 Acknowledgements

We thank the Hydrobase Tiksi, Arctica GeoZentr, Stanislav Ostreldin, Waldemar Schneider, and Sergey Pravkin for their logistic contribution to the field expedition Bykovsky 2017. We thank Dirk Wagner (GFZ) for supporting the expedition. We thank the MICADAS Team at AWI Bremerhaven for dating the radiocarbon samples. We thank Paul Overduin for discussing the hydrochemical results and for providing comments to the manuscript, and we thank Michael Angelopoulos for discussing the thermokarst lake talik results. We also thank Angélique Opitz, Dyke Scheidemann, Jonas Sernau, Mirjam Sens (AWI), Cornelia Karger, and Anke Sobotta (GFZ) for their support and assistance in the lab.

3

Yukechi Alas

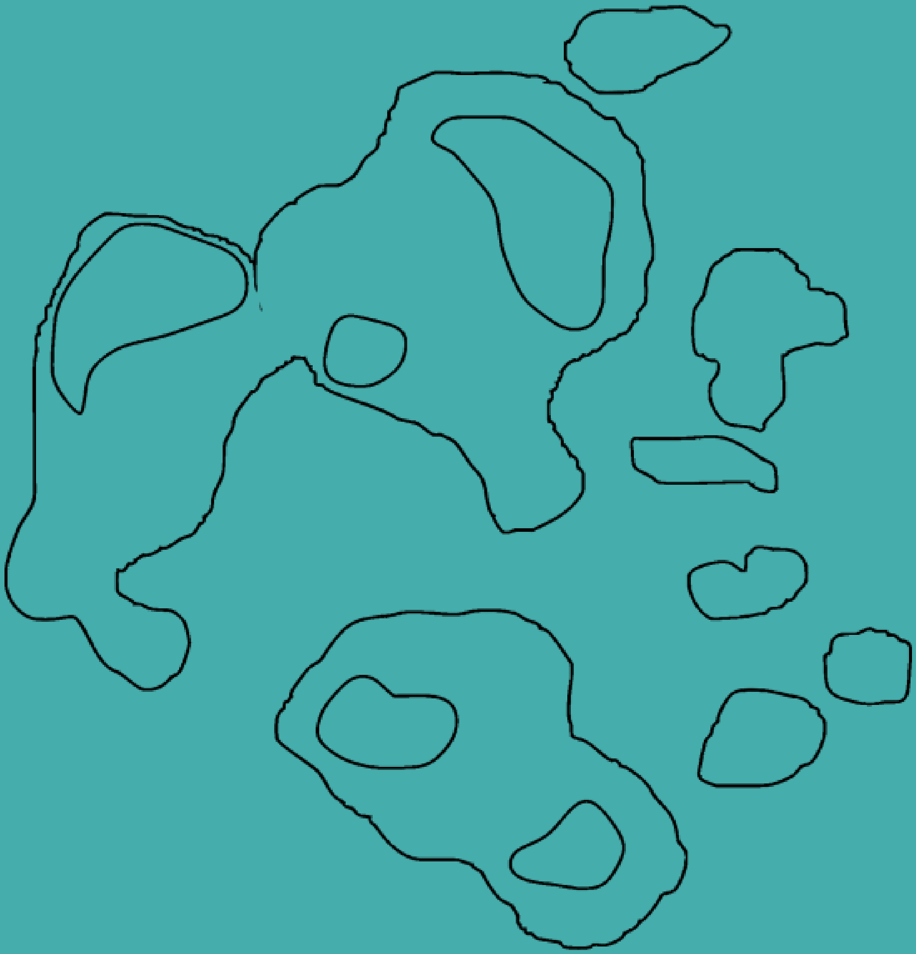

Where the sun can see
The basin through the forest
A new lake has formed

3 Greenhouse gas production and lipid biomarker distribution in Yedoma and Alas thermokarst lake sediments in Eastern Siberia

3.1 Abstract

Permafrost thaw leads to thermokarst lake formation and talik growth tens of meters deep, enabling microbial decomposition of formerly frozen organic matter (OM). We analyzed two 17-m-long thermokarst lake sediment cores taken in Central Yakutia, Russia. One core was from an Alas lake in a Holocene thermokarst basin that underwent multiple lake generations, and the second core from a young Yedoma upland lake (formed ∼70 years ago) whose sediments have thawed for the first time since deposition. This comparison provides a glance into OM fate in thawing Yedoma deposits. We analyzed total organic carbon (TOC) and dissolved organic carbon (DOC) content, *n*-alkane concentrations, and bacterial and archaeal membrane markers. Furthermore, we conducted 1-year-long incubations (4 °C, dark) and measured anaerobic carbon dioxide (CO_2) and methane (CH_4) production. The sediments from both cores contained little TOC (0.7 ± 0.4 wt%), but DOC values were relatively high, with the highest values in the frozen Yedoma lake sediments (1620 mg L^{-1}). Cumulative greenhouse gas (GHG) production after 1 year was highest in the Yedoma lake sediments (226 ± 212 μg CO_2-C gdw^{-1}, 28 ± 36 μg CH_4-C gdw^{-1}) and 3 and 1.5 times lower in the Alas lake sediments, respectively (75 ± 76 μg CO_2-C gdw^{-1}, 19 ± 29 μg CH_4-C gdw^{-1}). The highest CO_2 production in the frozen Yedoma lake sediments likely results from decomposition of readily bioavailable OM, while highest CH_4 production in the non-frozen top sediments of this core suggests that methanogenic communities established upon thaw. The lower GHG production in the non-frozen Alas lake sediments resulted from advanced OM decomposition during Holocene talik development. Furthermore, we found that drivers of CO_2 and CH_4 production differ following thaw. Our results suggest that GHG production from TOC-poor mineral deposits, which are widespread throughout the Arctic, can be substantial. Therefore, our novel data are relevant for vast ice-rich permafrost deposits vulnerable to thermokarst formation.

3.2 Introduction

Rapid warming of the Arctic results in permafrost warming (Biskaborn et al., 2019) and thaw, enabling microbial decomposition of previously frozen organic matter (OM) (Schuur et al., 2008; Walter Anthony et al., 2016). Soil organic carbon (OC) that has been stored for millennia could be released to the atmosphere as greenhouse gases (GHG). OC release from permafrost regions will continue gradually with ongoing warming, thereby accelerating warming (Schuur et al., 2015). Factors controlling GHG release from thawing permafrost are complex and therefore not fully considered by most climate models (Turetsky et al., 2020).

Thermokarst lake and talik formation is the most common expression of deep permafrost degradation (>10 m depth) (Grosse et al., 2013). Ground subsidence following thawing of ice-rich ground beneath the lake leads to lake formation. A positive downward heat flux from the water further enhances thaw and lead to the formation of a talik. After lake drainage or desiccation, a subaerial thermokarst lake basin remains, which is called an alas (Soloviev, 1973). Consequently, the talik can refreeze and OC becomes freeze-locked again. Thermokarst and talik formation, especially in ice-rich Late Pleistocene Yedoma deposits, result in deep thaw and subsequent ground subsidence. Apart from being ice-rich and susceptible to ground subsidence, deep Yedoma deposits are an important pool of permafrost OM (Schirrmeister et al., 2013; Strauss et al., 2017). In contrast, gradual top-down thawing, such as active layer deepening, affects only centimeters per decade (Grosse et al., 2011; Turetsky et al., 2020). Turetsky et al. (2020) estimated that abrupt thaw processes, such as thermokarst lake development, could lead to an additional net OC release from permafrost regions of 80 ± 19 Gt by 2300 under RCP 8.5. Thermokarst development in Yedoma regions, therefore, contributes globally relevant GHG emissions to the active carbon cycle (Turetsky et al., 2020).

The amount of OM that can be mobilized upon thaw is highly dependent on the state of OM degradation. Several studies have analyzed permafrost OM on a molecular level using lipid biomarkers to assess OM degradability (Jongejans et al., 2018; Sánchez-García et al., 2014; Stapel et al., 2018; Strauss et al., 2015). The ratio of odd to even chained *n*-alkanes, the carbon preference index (CPI), has been used as an indicator for OM degradability where high values suggest better preserved OM (Marzi et al., 1993). Other proxies can give insights into the source of OM, such as the average chain length (ACL) (Killops & Killops, 2013; Poynter & Eglinton, 1990). Branched glycerol dialkyl glycerol tetraethers (GDGTs), as well as archaeol and isoprenoid GDGTs (isoGDGT-0), are markers for past bacterial and archaeal biomass, respectively (Stapel et al., 2016; Weijers et al., 2006). In their study of Siberian Yedoma deposits, Stapel et al. (2018) found that increased concentrations of archaeal biomarkers correlated to increased OM contents, suggesting microbial activity and methane (CH_4) production during deposition.

Only a limited number of biogeochemical studies has been carried out so far on talik sediments underneath thermokarst lakes (Heslop et al., 2019; Heslop et al., 2015; Jongejans et al., 2020a; Romankevich et al., 2017; Ulyantsev et al., 2017). The study of talik sediments is however highly relevant for climate studies as it allows important insights into the pathways of previously frozen OM upon rapid thaw and thus the potential for GHG production below thermokarst lakes. While many studies suggested a higher biolability of old Yedoma OM upon thaw compared to Holocene thermokarst deposits (Dutta et al., 2006; Jongejans et al., 2018; Lee et al., 2012; Neubauer, 2016; Schuur et al., 2009; Strauss et al., 2017; Strauss et al., 2015; Zimov et al., 2006), a few studies showed opposite findings (Kuhry et al., 2020; Schädel et al., 2014). Furthermore, climatic conditions during permafrost formation were shown to play a crucial role for OM decomposition after thaw (Knoblauch et al., 2013; Walz et al., 2018). In addition, studies of biolability of dissolved OC (DOC) showed that old OC was more biolabile compared to modern OC (Mann et al., 2015; Vonk et al., 2013b).

Schädel et al. (2016), Schädel et al. (2014) and Treat et al. (2015) compiled an overview of incubation studies of permafrost regions. Many of these incubation experiments included subsurface sediments (<1 m depth) (**e.g.**; Aalstad et al., 2018; Čapek et al., 2015; Diáková et al., 2016; Elberling et al., 2013; Estop-Aragonés & Blodau, 2012; Waldrop et al., 2010) and only few studies have incubated permafrost sediments from >10 m deep (Dutta et al., 2006; Knoblauch et al., 2013; Lee et al., 2012). Even though several studies showed that aerobic decomposition released more OC than anaerobic decomposition over short time scales (months-years) (Knoblauch et al., 2013; Lee et al., 2012; Schädel et al., 2016), CH_4 emissions from permafrost regions are projected to become more important on longer time scales (decades-centuries) (Dean et al., 2018; Knoblauch et al., 2018). Furthermore, Knoblauch et al. (2018) showed that after multiple years, the production of carbon dioxide (CO_2) carbon equivalents is higher under anaerobic conditions when taking into account the much stronger global warming potential of CH_4 compared to CO_2 (28 over a 100-year timescale) (Myhre et al., 2013). Moreover, increased thermokarst lake initiation, especially in the continuous permafrost zone (Nitze et al., 2017) might lead to a landscape-scale increase of anaerobic decomposition processes.

Here, we studied greenhouse gas production, long-chained *n*-alkanes, branched GDGTs and archaeal microbial markers in talik sediments to determine the OM characteristics of Yedoma sediments thawed under subaquatic conditions underneath two different thermokarst lakes. We focused on the following research questions: 1) can we characterize the OM degradability of thawed Yedoma deposits using biomarker analyses and 2) how much GHG is produced in these deposits after thaw? For the first time, to our best knowledge, we present OC turnover data from Siberian Yedoma talik sediments. Furthermore, the combination of biomarker degradation proxies and incubation data from >10 m deep permafrost sediments that are thawed underneath a thermokarst lake is unique so far.

3.3 Methods and materials

3.3.1 Study area

The study site is located in Central Yakutia (Sakha Republic), East Siberia, about 80 km southeast from the city of Yakutsk (Figure 3.1a). The region is part of the continuous permafrost zone with permafrost reaching several hundred meters in depth. The Yukechi study site (61.76495°N, 130.46664°E) includes drained lake basins (alases) and thermokarst lakes formed in Yedoma uplands with ice-rich deposits tens of meters thick that cover about two thirds of the study area (Soloviev, 1973; Ulrich et al., 2019; Windirsch et al., 2020). Taiga vegetation, predominantly larch trees and sparse pine and birch communities, dominate the region. Underneath the forest, the active layer reaches a thickness of ~1 m (Fedorov et al., 2014). The drained lake basins are covered by a steppe-like grass vegetation and are characterized by an active layer reaching >2 m thickness (Soloviev, 1959). The region is characterized by a strong continental climate with a mean annual air temperature of -10.7 °C (mean January: -41 °C, mean July: 18.5 °C) and a mean annual precipitation of 246 mm (period: 1982 - 2012; Yakutsk Weather Station: RSM00024959) (Climate-data.org, 2020). Two different types of thermokarst lakes were selected for this study: an Alas lake and a Yedoma lake (Figure 3.1b). The Alas lake is located within the Yukechi Alas, which is a Holocene thermokarst basin of ~300-500 m in diameter and ~10-15 m lower compared to surrounding Yedoma uplands (Ulrich et al., 2019). The Alas lake has a diameter of ~57 m, a surface area of 1 ha and an average water depth of 1.9 m (measured in summer 2014). The Yedoma thermokarst lake is a younger lake and is located on the Yedoma uplands. Its lake level lies approximately 18 m higher than the Alas lake level (Figure 3.1c). With a diameter of ~43 m and surface area of 0.6 ha, the Yedoma lake is smaller than the Alas lake but deeper (average water depth of 3.7 m). Using historical aerial imagery, this lake was estimated to be about 70 years old and developed in a small forest-free grassland area (Ulrich et al., 2017).

Thermokarst lake development in the Yukechi Alas has been monitored by the Melnikov Permafrost Institute in Yakutsk since 1992 (Fedorov & Konstantinov, 2003). Previous research by Ulrich et al. (2017) included remote sensing as well as field and statistical analysis of thermokarst-lake change in the Yukechi Alas. In addition, Windirsch et al. (2020) assessed the local sediment genesis and its effect on permafrost carbon storage by analyzing sediment cores taken from Yedoma upland sediments in the close vicinity of the studied Yedoma lake YU-L15 (140 m SSW) and Alas deposits adjacent to Alas lake YU-L7 (110 m NNE) (Appendix B: Figure B.1).

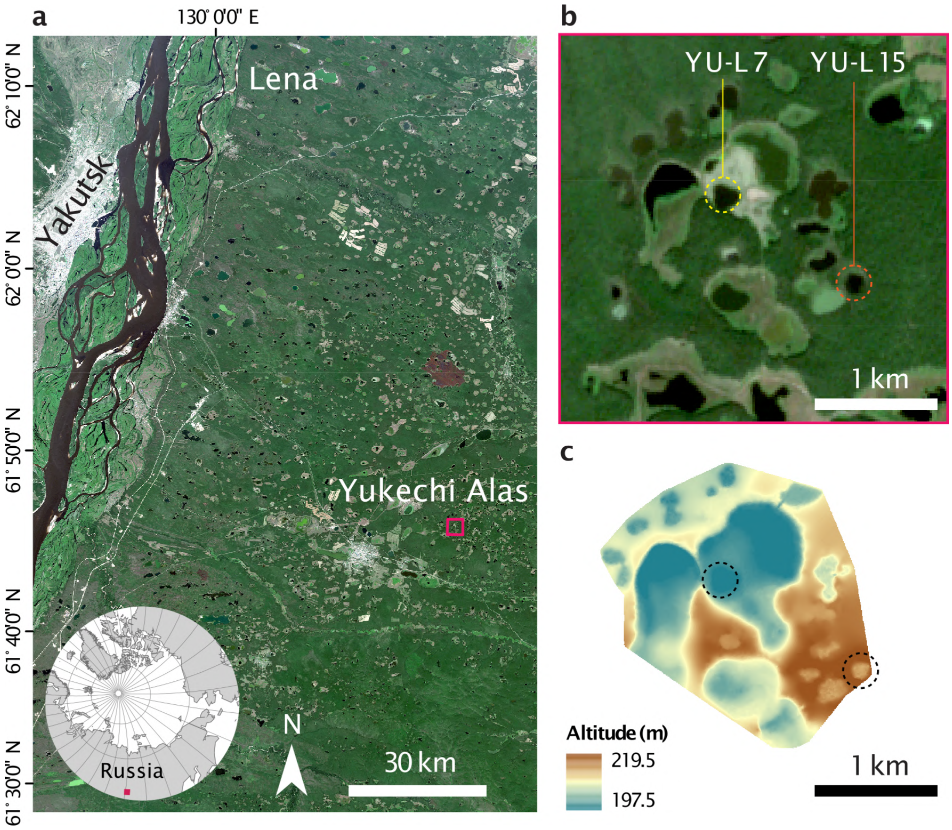

Figure 3.1: Location of study site. (a) Location of study area (pink square) in Central Yakutia close to Yakutsk in Siberia (globe in lower left corner). (b) Close-up of study area with coring location: YU-L7 below Alas lake (yellow circle) and YU-L15 below Yedoma lake (orange circle). (c) Digital elevation model of study area with core locations indicated. Source of (a) and (b): Sentinel-2 (ESA) 2018-08-03, (c): Ulrich et al. (2017).

3.3.2 Field work

During the field campaign to Yukechi in March 2015, we retrieved two sediment cores from the bottom of two thermokarst lakes (Figure 3.1b). Drilling was carried out from the lake ice using a URB2-4T drilling rig mounted on a truck. The cores were drilled with 15.7 cm diameter for the uppermost parts and 8 cm in diameter in the lower parts. The sediment cores were removed from the core barrel using compressed air. Sediment core YU-L7 was 17.7 m long and retrieved from the Alas lake (61.76397°N, 130.46442°E). At the sampling position, the Alas lake had an ice cover of 70 cm and a water depth of 2.3 m on 23 March 2015. The sediment core consisted entirely of unfrozen sediments, which are part of the talik underneath the thermokarst lake. Sediment core YU-L15 was 17.2 m long and taken from the Yedoma upland lake (61.76086°N, 130.47466°E). This lake had a 71-cm thick ice cover and a water depth of 4.3 m at the sampling position on 23 March 2015. The sediment core consisted of unfrozen talik sediments down to a depth of 8.1 m followed by frozen sediments below. The cores were described visually in the field, packed in plastic core wrapper, and kept frozen.

In both lakes, the ice was covered by ∼35 cm snow. Directly underneath the ice cover, the pH and electrical conductivity of the lake water were 8.0 and 2.45 mS cm^{-1} for the Alas lake and 8.3 and 2.29 mS cm^{-1} for the Yedoma lake.

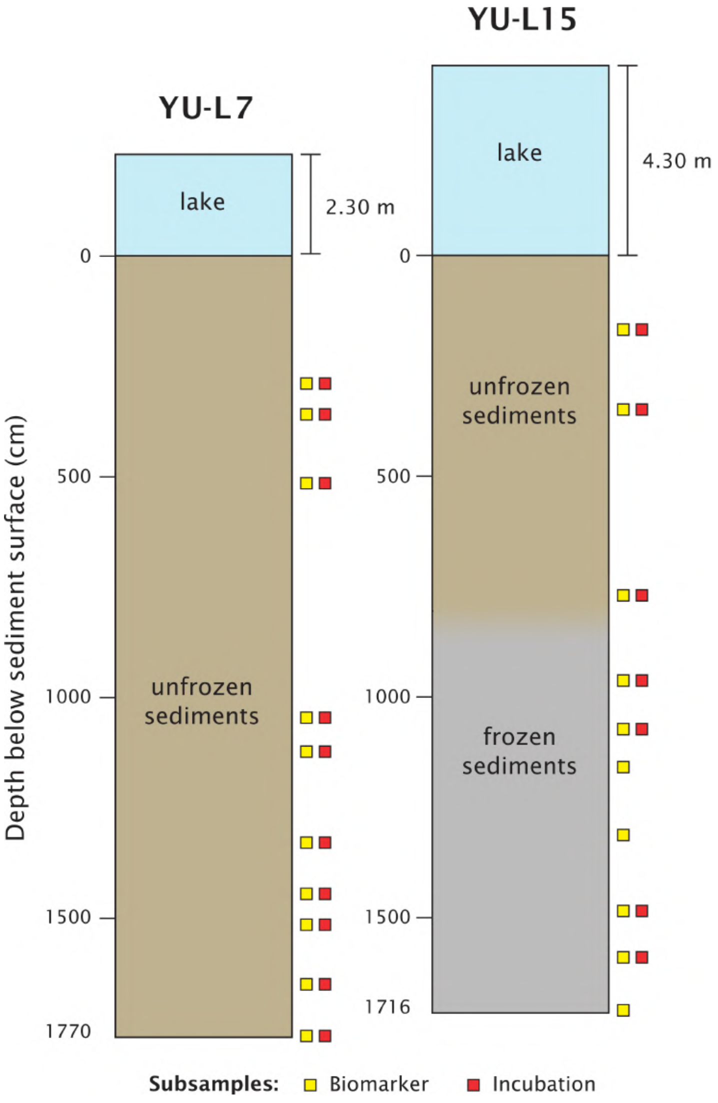

Figure 3.2: Schematic overview of sediment cores beneath Alas lake YU-L7 (left) and Yedoma lake YU-L15 (right). Subsamples were analyzed for lipid biomarkers (yellow squares) and incubation experiments (red squares).

3.3.3 Laboratory analyses

We cut the sediment cores into halves with a band saw and cleaned the cutting surfaces by removing the material that was superficially thawed during the saw process. Then, we sub-sampled the cores for different biogeochemical laboratory analyses (Figure 3.2). Ten sediment samples were taken from each core (every 1 to 2 meters according to the stratigraphy) and analyzed for total OC (TOC) content, lipid biomarkers and anaerobic GHG production. Radiocarbon ages from both sediment cores were published separately (Jongejans et al., 2019). Sedimentological and geochemical data are prepared for publication in an additional study.

3.3.3.1 Organic carbon content

Sediment samples (n=20) were analyzed for total carbon (TC) and total nitrogen (TN) content with an elemental analyzer (VarioMAX Elementar Analyser). The inorganic carbon content (TIC) was quantified from the amount of CO_2 that was released after sample treatment with phosphoric acid. The TOC content was calculated by subtracting the TIC from the TC and is expressed in weight percentage (wt%). We calculated the TOC to TN weight ratio, which will be referred to as the C/N ratio. This ratio can be used as OM degradation proxy where the C/N ratio decreases with decomposition (**e.g.**; Gundelwein et al., 2007).

In addition, we extracted 3-10 ml pore water from sediment samples from both cores (n=57) that were thawed overnight at 20 °C using rhizon samplers (membrane pore size: 0.12-0.18 μm). These samples were taken from different depths than the samples for lipid biomarkers and incubations but from same stratigraphic zones. The samples were acidified with 20 μl hydrochloric acid (35%) to pH 2 and kept cool at 4 °C. The dissolved OC (DOC) content was measured as non-purgeable OC fraction using a Total Organic Analyzer TOC-VCPH/CPN (Shimadzu) and is expressed in mg L^{-1}.

3.3.3.2 Lipid biomarkers

Extraction and measurement

Sediment samples (n=20) from the main stratigraphic units were analyzed for *n*-alkanes and lipid biomarkers (Figure 3.2). Approximately eight grams of dried, ground sediments were extracted using accelerated solvent extractions (ASE) with dichloromethane/methanol (DCM/MeOH; 99:1 v/v) using a Dionex 200 ASE Extractor. Each sample was held in a static phase (5 min heating) for 20 minutes (75 °C, 5 MPa). Afterwards, the samples were concentrated using a TurboVap500 at 42 °C. We removed asphaltenes by dissolving the extracts in DCM/MeOH (99:1 v/v) and adding a 40x excess of *n*-hexane, leading to precipitation of *n*-hexane insoluble substances. Four internal standards were added for compound quantification: 5α-androstane, ethylpyrene, 5α-androstan-17-one and erucic acid. We separated the maltene fraction (*n*-hexane soluble compounds) by medium pressure liquid chromatography (MPLC) (Radke et al., 1980) into an aliphatic, aromatic and NSO (nitrogen, sulfur and oxygen containing) fraction using *n*-hexane.

The *n*-alkanes were measured in the aliphatic fraction by gas chromatography-mass spectrometry (GC-MS) using a Trace GC Ultra coupled to a DSQ MS (Thermo Electron Corporation) with helium as carrier gas (1 ml min^{-1}). The GC was equipped with a cold injection system and a BPX5 (SGE) column (50 m x 0.22 mm x 0.25 μm). The injector temperature was programmed from 50 °C to 300 °C at a rate of 10 °C s^{-1}. The oven was heated from its initial temperature of 50 °C (1 min isothermal) to 310 °C with a heating rate of 3 °C min^{-1} (30 min isothermal). The MS was operated in the electron impact ionization mode at 50 eV. Full-scan mass spectra were obtained from m/z 50 to 600 Da with a scan rate of 2.5 scans s^{-1}. Compounds were identified and quantified using the software Xcalibur™.

The branched and isoprenoid glycerol dialkyl glycerol tetraethers (GDGTs), as well as the dialkyl glycerol diether lipid (archaeol) (Figure B.2) were measured in the NSO fraction using a Shimadzu LC-10AD high-performance liquid chromatograph (HPLC) coupled to a Finnigan TSQ 7000 mass spectrometer via an atmospheric pressure chemical ionization interface (corona current of 5 mA (5 kV), vaporizer T of 350 °C, capillary T of 200 °C, nitrogen sheath gas at 60 psi, no auxiliary gas). The sample was separated at 30 °C in a column oven using a Prevail Cyano column (2.1 x 150 mm, 3 μm; Alltech) equipped with a pre-column filter. Compounds were eluted isocratically with *n*-hexane (99%) and isopropanol (1%) for 5 min, followed by a linear gradient to 1.8% isopropanol in 40 min and in 1 min to 10% isopropanol. It was held for 5 min to clean the column, set back to initial conditions in 1 min and held for 16 min for equilibration. The flow rate was set to 200 μl min^{-1}. Mass spectra were obtained by selected ion monitoring (SIM) in the positive ion mode and at a scan rate of 0.33 scans s^{-1}. Compounds were identified using the software Xcalibur™ and quantified using a daily-measured external archaeol standard. Here, we present the concentration of branched GDGTs, isoGDGT-0 and archaeol.

From both sediment cores, we selected 5 samples for open-system pyrolysis after Horsfield et al. (1989) and Stapel et al. (2018). The bitumen-free ASE residues were pyrolyzed (temperatures: 300-600 °C) and the pyrolysates, which were trapped with liquid N2, were measured on a pyrolysis gas chromatograph (Agilent GC 6890A chromatograph) equipped with a flame ionization detector (Py-GC-FID). The compounds were identified and quantified relative to an *n*-butane external standard using the Agilent ChemStation software. We integrated short (C_1-C_5), intermediate (C_6-C_{14}) and longer ($\geq C_{15}$) *n*-alkanes and *n*-alk-1-enes. In immature OM, these aliphatic compounds represent aliphatic side chains as well as alcohols and fatty acids formerly covalently linked via ether or ester bonds to the complex organic matrix.

Lipid biomarker indices

From the *n*-alkane concentrations, we calculated two indices. The average chain length (ACL) of *n*-alkanes is a measure of the chain length distribution (Poynter & Eglinton, 1990), and indicates the OM source. It was calculated according to Equation 3.1 where i is the carbon number. We focus on long-chain *n*-alkanes, which are produced by terrestrial higher plants, for example in mosses (*n*-C_{23} and *n*-C_{25}), in leaf waxes (*n*-C_{27} and *n*-C_{29}) and in grasses (*n*-C_{31} and *n*-C_{33}) (**e.g.**; Ficken et al., 1998; Zech et al., 2009).

$$ACL_{23-33} = \frac{\Sigma\, i\, C_i}{\Sigma\, C_i} \tag{3.1}$$

The carbon preference index (CPI) is an index for OM degradability. Higher values typically indicate better preserved OM and the ratio decreases with degradation (Bray & Evans, 1961; Marzi et al., 1993). The CPI was calculated according to Equation 3.2.

$$CPI_{23-33} = \frac{\Sigma\, odd\, C_{23-31} + odd\, C_{25-33}}{2\, \Sigma\, even\, C_{24-32}} \tag{3.2}$$

3.3.4 Incubations

From the 20 sediment samples, 17 samples were used in the incubation experiments to estimate GHG production from degrading OM. From each sample, we prepared three replicates for quality control. The frozen samples were thawed at 4 °C overnight under an oxygen free atmosphere in a glovebox. After homogenization, approximately 10 g of sediment was weighed into 120 mL glass bottles and 10 mL of autoclaved tap water added to each bottle with sediment. The 51 bottles were sealed with rubber stoppers and the headspace gas was exchanged with pure nitrogen to create an anaerobic atmosphere, comparable to the ambient conditions in the talik sediments below the thermokarst lakes. Samples were incubated anaerobically at 4 °C for one year. CO_2 and CH_4 concentrations were measured biweekly in a 250 μL subsample using gas chromatography with an Agilent GC 7890A equipped with an Agilent HP-PLOT Q column. We used a thermal conductivity detector and flame ionization detector for measuring CO_2 and CH_4 concentrations, respectively, helium as a carrier gas and an oven temperature of 100 °C. From the concentrations, we calculated the average CH_4 and CO_2 production of the three replicates, which are expressed in μg CH_4-C and CO_2-C per gram dry weight (gdw) and per gram TOC (an explanation of the calculations is added in Appendix B ("Greenhouse gas production and DIC", page 144).

3.3.5 Statistical analysis

We identified the stratigraphical units of the two sediment cores by constrained hierarchical clustering of all measured parameters. We carried out this statistical clustering in R v. 3.6.1 using the "chclust" function in package "rioja" with method "coniss." (Juggins, 2020). We calculated the correlation (Pearson) between all parameters and reported the statistically significant correlations (p-values < 0.05). Also, we compared the two sediment cores and the units using Kruskal-Wallis and Mann-Whitney Wilcoxon non-parametric tests. Using a forward-selection stepwise multiple regression, we tried to identify what parameters explained the most variance in the cumulative CH_4 and CO_2 production. We carried out the regression in R using the package "MASS" with the function "stepAIC" (Venables & Ripley, 2002) and direction "forward". This method iterates the Akaike information criteria (AIC) for the regression model when taking out one parameter at the time. The AIC statistic is a method to evaluate how well the model fits. We calculated the relative importance of the significant variables with the function "calc.relimp" from the package "relaimpo" (Groemping, 2006).

3.4 Results

3.4.1 Organic matter characteristics

3.4.1.1 Alas lake sediment core YU-L7

Core YU-L7 was divided into a bottom unit including sediments from 1769 to 1331 cm below the sediment surface (bss), a middle unit from 1125 to 518 cm bss and a top unit from 362 to 290 cm bss (Figure 3.3). This division was based on constrained hierarchical clustering of all measured parameters (Figure B.3). The TOC ranged between 0.3 to 1.6 wt% (median: 0.8 wt%; Figure 3.3a) and was lowest in the middle unit. The C/N had a median of 8.3 and was highest in the bottom unit with the maximum of 10.7 at 1516 cm bss (Figure 3.3b). DOC values showed little variation and were between 97 and 242 mg L^{-1} (median: 169 mg L^{-1}) (Figure 3.3c). The *n*-alkane concentration per gram dry weight (gdw) was highest at 362 cm bss with 20.1 μg gdw^{-1} and lowest at 518 cm bss with 3.1 μg gdw^{-1} (median: 8.24 μg gdw^{-1}) (Figure 3.3d). The *n*-alkane concentration per gram TOC varied between 599 and 2048 μg and was especially high at 1048 and 362 cm bss (median: 993 μg g^{-1} TOC). The ACL showed little variation over depth between 29.0 and 29.9 (Figure 3.3e). Long chain (*n*-C_{29} and *n*-C_{31}) alkanes dominated all samples. The CPI ranged between 7.1 and 10.4 and did not show substantial variation between the units (Figure 3.3f). The brGDGT concentration ranged from 2.1 and 79.1 ng gdw^{-1} and was highest at 1516 and 1446 cm bss (median: 40.0 ng gdw^{-1}) (Figure 3.3g). The brGDGT concentration per gram TOC varied between 2674 and 5455 ng (median: 2.9 μg g^{-1} TOC). The archaeol concentration showed quite some variation between 0 and 38.7 ng gdw^{-1} with relatively high values at 1331, 1516 and 290 cm bss (Figure 3.3h). Per gram TOC, the archaeol concentration was highest at 591 cm bss (3755 ng g^{-1}). The isoGDGT-0 concentration showed a similar pattern to the brGDGT concentration and ranged from 0 to 15.8 ng gdw^{-1}, and from 0 to 1084 ng g^{-1} TOC (Figure 3.3i). The results from the open-system pyrolysis (Figure 3.5) suggested a more aliphatic character for samples with higher TOC values (at 1331 cm bss, followed by 1561 and 362 cm bss). All results were published in the PANGAEA research data repository, specifically the biogeochemical parameters, *n*-alkane and brGDGT concentrations, cumulative greenhouse gas production and dissolved organic carbon content (Jongejans et al., 2021a, 2021b, 2021c, 2021d, 2021e).

3.4.1.2 Yedoma lake sediment core YU-L15

Core YU-L15 was divided into two parts: the bottom unit included the sediments from 1713 to 778 cm bss and the top unit from 353 to 170 cm bss (Figure 3.4 and B.3). The TOC varied between 0.2 and 1.4 wt% (median: 0.5 wt%; Figure 3.4a). The TOC was slightly higher in the lowermost three samples (1713-1488 cm bss) and those at the top compared to the intermediate samples between 1315 and 778 cm bss. The C/N ratio had its maximum (13.2) as well as its minimum (8.9) in the top unit (Figure 3.4b). In the bottom unit, the C/N varied between 9.1 and 11.0 (core median: 9.7). The DOC concentration showed a lot of variation ranging from 51 to 1620 mg L^{-1} with highest concentrations at the base of the core (1694-1185 cm bss) (median: 448 mg L^{-1}; Figure 3.4c). In the top unit of YU-L15, DOC values were between 437 and 615 mg L^{-1}. The *n*-alkane concentration was lowest in the upper

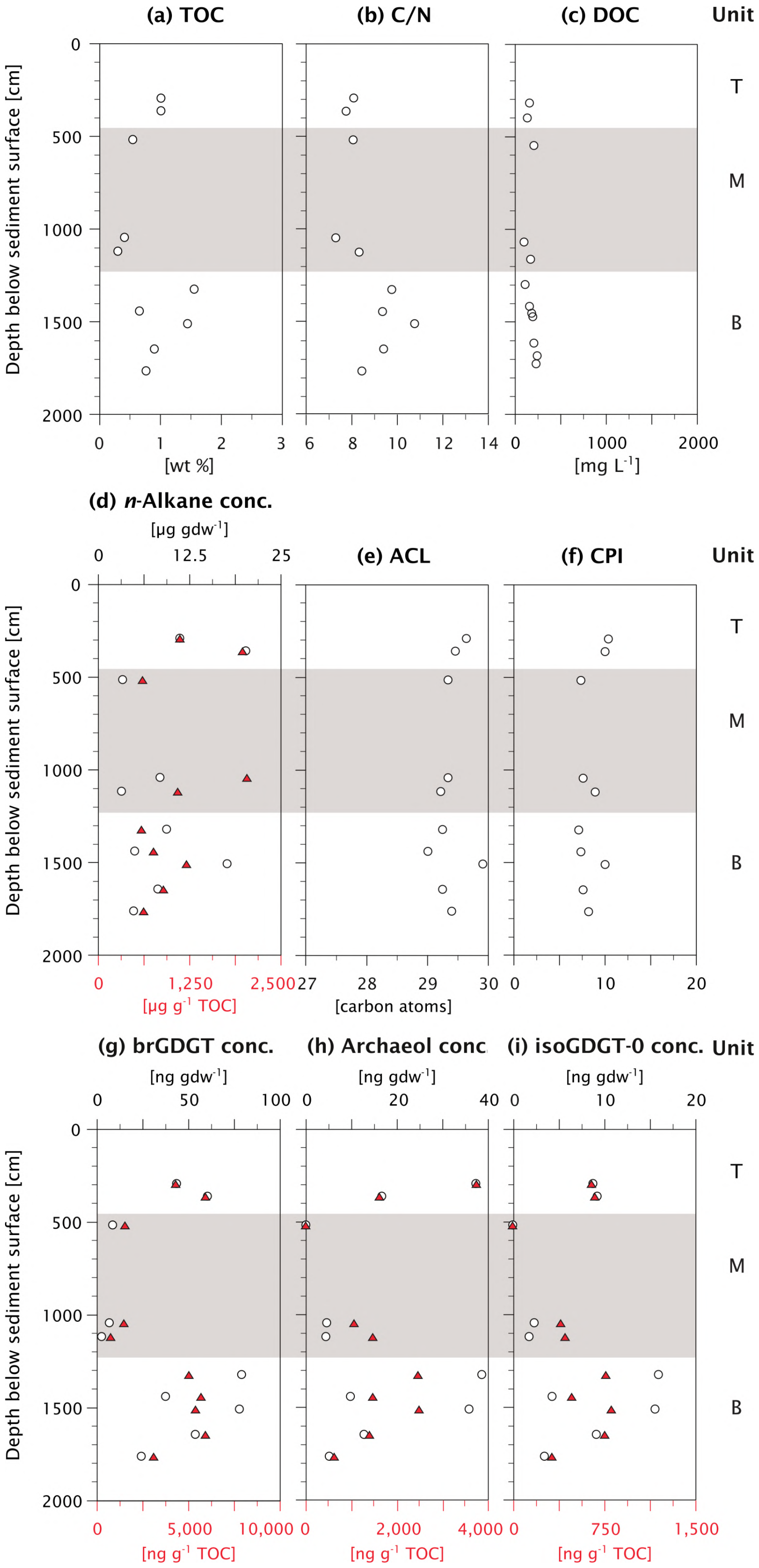

Figure 3.3: Biogeochemical parameters of Alas lake sediment core YU-L7. (a) Total organic carbon (TOC) content, (b) ratio of carbon to nitrogen content (C/N), (c) dissolved organic carbon (DOC) content of original pore water samples, (d) *n*-alkane concentration, (e) average chain length, (f) carbon preference index (CPI), (g) branched glycerol dialkyl glycerol tetraether (brGDGT) concentration, (h) archaeol concentration and (i) isoGDGT-0 concentration. Concentrations per gram dry weight (gdw) (white circles) and per gram TOC (orange triangles). Units indicated on right: top (T), middle (M; grey area) and bottom (B).

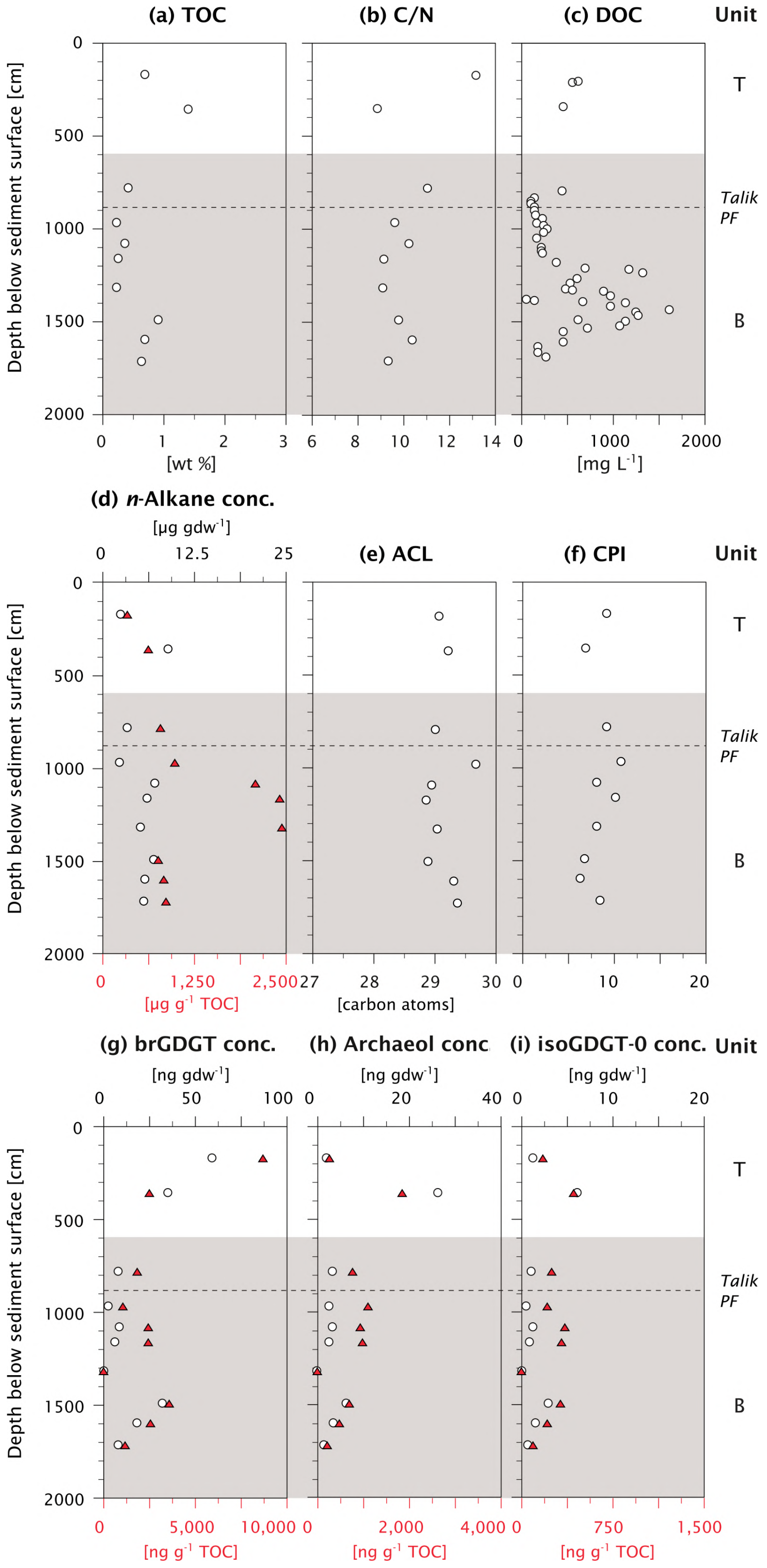

Figure 3.4: Biogeochemical parameters of Yedoma lake sediment core YU-L15. (a) Total organic carbon (TOC) content, (b) ratio of carbon to nitrogen content (C/N), (c) dissolved organic carbon (DOC) content of original pore water samples, (d) *n*-alkane concentration, (e) average chain length, (f) carbon preference index (CPI), (g) branched glycerol dialkyl glycerol tetraether (brGDGT) concentration, (h) archaeol concentration and (i) isoGDGT-0 concentration. Concentrations per gram dry weight (gdw) (white circles) and per gram TOC (orange triangles). Units indicated on right: top (T) and bottom (B; grey area), boundary talik to permafrost (PF) indicated with grey dashed line.

sample at 170 cm bss (2.2 μg gdw^{-1}) and highest at 353 cm bss (median: 8.8 μg gdw^{-1}) (Figure 3.4d). Per gram TOC, the *n*-alkane concentration was between 346 and 2456 μg and especially high between 1516 and 1076 cm bss. The ACL was higher than 28.8 in all samples (median: 29.0; Figure 3.4e). All samples were dominated by *n*-C$_{29}$ and *n*-C$_{31}$. The CPI varied between 6.3 and 10.7 (Figure 3.4f). The brGDGT concentration was highest in the upper sample (58.7 ng gdw^{-1}) and lowest at 1315 cm bss (median: 7.9 ng gdw^{-1}) (Figure 3.4g). The brGDGT concentration per gram TOC was up to 8744 ng g^{-1}. The archaeol (Figure 3.4h) and isoGDGT-0 concentration (Figure 3.4i) showed a very similar pattern with the highest concentration at 353 cm bss (26.1 and 6.1 ng gdw^{-1}, respectively) and a median of 2.8 and 1.1 ng gdw^{-1}, respectively. Per gram TOC, the maxima were 1861 and 433 ng g^{-1} for archaeol and isoGDGT-0, respectively. Following the pyrolysis, the samples with the highest TOC values (353-1488 cm bss) are also among those with the highest aliphatic character (Figure 3.5).

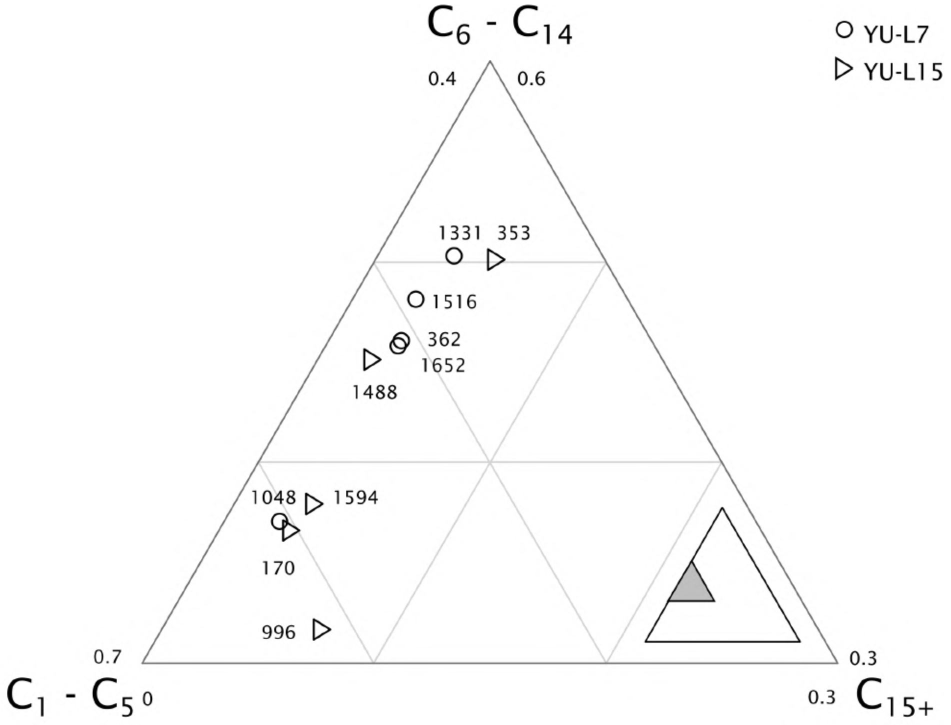

Figure 3.5: Horsfield-diagram of Alas and Yedoma lake sediment cores: chain length distribution of short (C$_1$-C$_5$), intermediate (C$_6$-C$_{14}$) and long (C$_{15}$+) *n*-alkanes and *n*-alk-1-enes after pyrolysis of the bitumen-free macromolecular organic matrix after Horsfield et al. (1989). Symbols correspond to samples from Alas lake sediment core YU-L7 (circles) and Yedoma lake sediment core YU-L15 (triangles).

3.4.2 Greenhouse gas production

3.4.2.1 Alas lake sediment core YU-L7

In total, we measured anaerobic GHG production of ten samples from the Alas lake sediment core YU-L7 (Figure 3.6). CH$_4$ production after one year was highest (81.3 ± 38.2 μg CH$_4$-C gdw^{-1}; mean ± standard deviation) in the sample closest to the sediment surface in the top part at 290 cm bss (Figure 3.6a). Furthermore, CH$_4$ production also exceeded 20 μg for the sediments at 1048 cm (54.5 ± 42.7 μg CH_4-C gdw^{-1}) and 1769 cm bss (38.7 ± 66.3 μg CH_4-C gdw^{-1}). When normalized to gram TOC, CH_4 production was highest in the middle part of the core at 1048 cm bss (13.2 ± 10.4 mg CH_4-C g^{-1} TOC). There was no trend in depth observed. For the three samples with the highest CH_4 production, the maximum production rates ranged from 0.62 to 0.91 μg CH_4-C gdw^{-1} day^{-1} (Figure 3.6b). After ~350 days, the rates of these samples decreased. In samples yielding higher CH_4 concentrations, CH_4 production started after ~200 days and increased exponentially. In 6 out of 10 samples, the CH_4 rates increased over time. Cumulative GHG production and rates for all replicates are shown in Appendix B (Figure B.6 to B.22).

CO_2 production was highest in the top part of the sediment core at 362 cm bss (227.15 ± 248.8 μg CO_2-C gdw^{-1}), closely followed by the sample at 1446 cm bss in the bottom unit (197.6 ± 225.7 μg CO_2-C gdw^{-1}) (Figure 3.6c). In the middle unit, CO_2 production was very low. The CO_2 production per gram TOC was highest at 1446 cm bss (30.5 ± 34.8 mg CO_2-C g^{-1} TOC). In contrast to CH_4, CO_2 was produced from the start of the incubation and after which the rates decreased (e.g. Figure B.6). Maximum rates of all samples varied between 1.52 and 3.17 μg CO_2 C gdw^{-1} day^{-1} (Figure 3.6d).

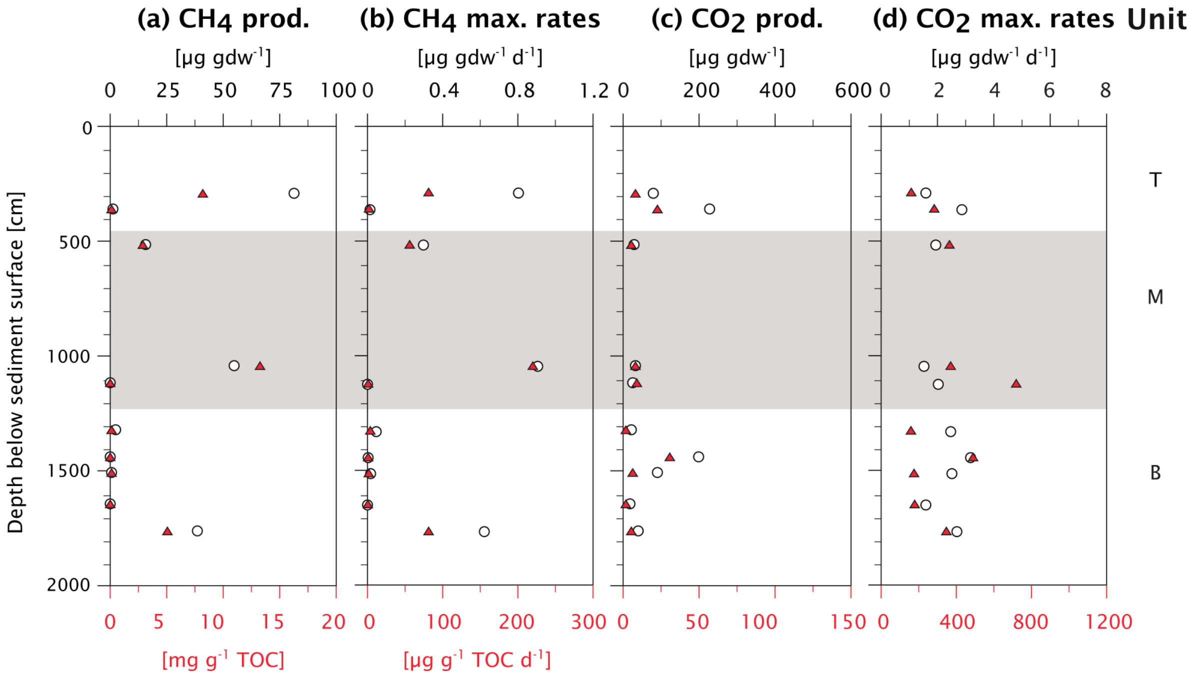

Figure 3.6: Greenhouse gas production after one year from Alas lake sediment core YU-L7. (a) Cumulative methane (CH_4) production, (b) maximum CH_4 rates, (c) cumulative carbon dioxide (CO_2) production, (d) maximum CO_2 rates. Production and production rates per gram dry weight (gdw; white circles) and per gram TOC (orange triangles). Units indicated on right: top (T), middle (M; grey area) and bottom (B).

3.4.2.2 Yedoma lake sediment core YU-L15

Anaerobic GHG production was measured on seven samples from the Yedoma lake sediment core YU-L15 (Figure 3.7). CH_4 production in the Yedoma lake sediment core YU-L15 was highest in the top of the core (Figure 3.7a). The maximum was at 353 cm bss with 87.0 ± 44.0 μg CH_4-C gdw^{-1}. The sample at 170 and 966 cm bss also showed substantial CH_4 production

(64.1 ± 57.2 and 41.6 ± 26.9 μg CH_4-C gdw^{-1}, respectively). The CH_4 production normalized to gram TOC was highest in the sample at 966 cm bss (18.8 ± 12.2 mg CH_4-C g^{-1} TOC). Like in the Alas lake core, CH_4 production started after 200 days for most samples and increased exponentially (e.g. Figure B.6). In 5 samples, the CH_4 production rates increased over time and were highest at the end of the incubations from 300 days and onwards. The three samples with the highest cumulative CH_4 production (353, 170 and 966 cm bss) also had the highest rates ranging from 0.56 to 1.15 μg CH_4-C gdw^{-1} day^{-1} (Figure 3.7b).

The CO_2 production was highest in the bottom of the core (Figure 3.7c). The maximum CO_2 production was observed in the sample at 1488 cm bss (561.5 ± 527.4 μg CO_2-C gdw^{-1}). In the sample at 1076 cm (407.7 ± 680.1 μg CO_2-C gdw^{-1}) and 170 cm bss (350.2 ± 346.9 μg CO_2-C gdw^{-1}), CO_2 production was also high. All samples produced more than 50 μg CO_2-C, except for the sample at 1594 and 966 cm bss. The production per gram TOC was highest at 1076 cm bss (120.6 ± 201.2 mg CO_2-C g^{-1} TOC). CO_2 production started at the beginning of the incubation and increased gradually over time. Maximum CO_2 production rates ranged from 1.05 to 7.67 μg CO_2 C gdw^{-1} day^{-1} (Figure 3.7d).

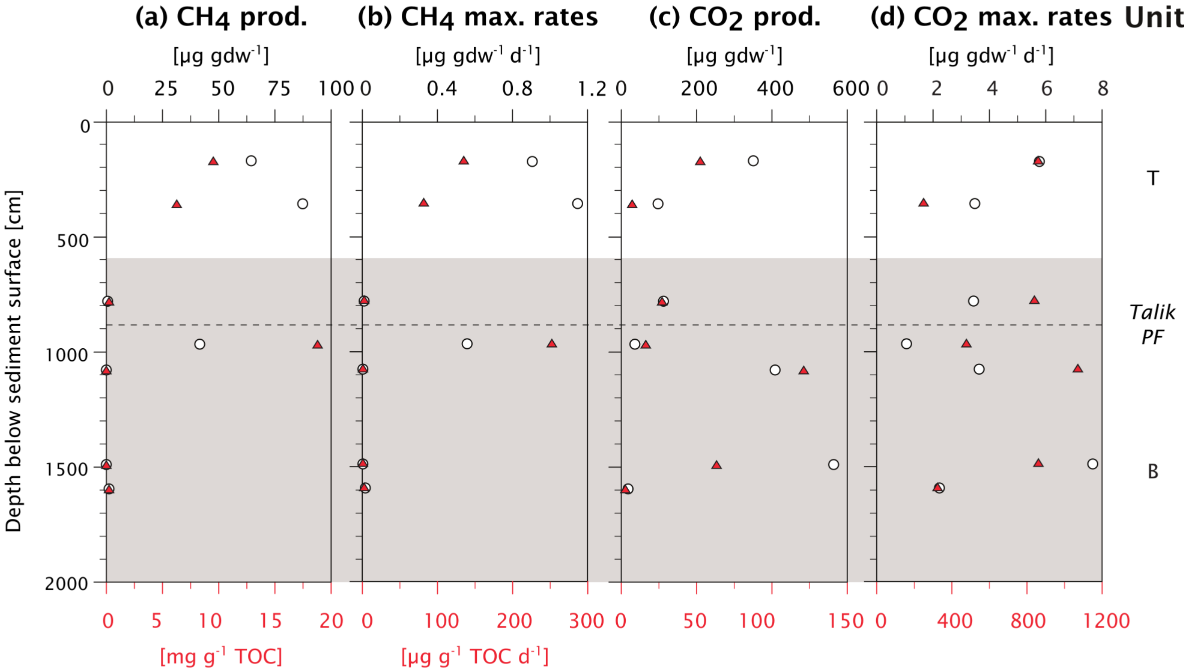

Figure 3.7: Greenhouse gas production after one year from Yedoma lake sediment core YU-L15. (a) Cumulative methane (CH_4) production, (b) maximum CH_4 rates, (c) cumulative carbon dioxide (CO_2) production, (d) maximum CO_2 rates. Production and production rates per gram dry weight (gdw; white circles) and per gram TOC (orange triangles). Units indicated on right: top (T), middle (M; grey area) and bottom (B).

3.4.2.3 Carbon mineralization

Total anaerobic C production ranged from 0.02 to 0.23 mg gdw^{-1} in YU-L7 (max: 0.08 mg C gdw^{-1} as CH_4) and from 0.02 to 0.56 mg gdw^{-1} in YU-L15 (max: 0.09 mg C gdw^{-1} as CH_4). After one year, on average 2.3 ± 3.1% of the initial carbon was mineralized to CO_2 and 0.4 ± 0.6% to CH_4 (Figure B.4). In the first 100 days, 10 ± 21% of the cumulative CH_4 was produced. Production of CH_4 commenced after 200 days and CH_4 production rates were highest after 300 days in most samples. In six samples (YU-L7: 1125, 1446 and 1652 cm bss, YU-L15: 778, 1076 and 1488 cm bss; Figure B.10, B.12, B.14, B.18, B.20, B.22), the CH_4 production was higher in the first week compared to the following weeks.

The CO_2 production rates were highest in the first 100 days in 8 out of 17 samples. In 4 samples, the rates were highest after 300 days. Within the first 100 days, 49 ± 28% of the cumulative CO_2 was produced within the first 100 days. CO_2 production was generally highest at the beginning of the incubations and gradually decreased over time.

3.4.3 Statistical correlation and regression

Considering both cores, the TOC correlated positively with the *n*-alkane, brGDGT, archaeol and isoGDGT-0 concentration ($p<0.01$) (Figure B.5). The CO_2 production was correlated with the ACL (R: -0.56, $p<0.05$) and with the DOC content in adjacent samples (R: 0.58, $p<0.05$). The CH_4 production was negatively correlated with the depth (R: -0.58, $p<0.05$).

Using the forward-selection stepwise multiple regression method, we found that the CH_4 production could not be explained by our data; no fitting model was found. The cumulative CO_2 production can be explained by a generalized linear regression model as shown in Equation 3.3. This model describes 73.5% of the variance of the cumulative CO_2 production, of which 58.5% is explained by the DOC content and the ACL alone. This clear relation of the CO_2 production with a high DOC and low ACL is also shown in Figure 3.8.

$$CO_2 = 0.27\,DOC - 498.07\,ACL + 60.92\,CPI + 13.46\,n - alkane\ conc. + 14026.43 \tag{3.3}$$

3.5 Discussion

3.5.1 Organic matter degradation potential

3.5.1.1 Organic carbon quantity

Sedimentary OC exists bound to the sediments or in the pore water. Total organic carbon contains both the particulate (POC) and dissolved fraction of OC. In both Yukechi cores, the TOC was very low (median YU-L7: 0.8 wt% and median YU-L15: 0.5 wt%) (Figure 3.4). Windirsch et al. (2020) found similar low values in sediment cores drilled on dry land within the same Alas basin (median: <0.1 wt%, max: 2.4 wt%) and on Yedoma upland nearby (median: <0.1 wt%, max: 1.7 wt%). They reported that the Yedoma sediments are rather coarse-grained (i.e. fine sand dominated) at the Yukechi study site compared to other Yedoma sites such as the Kolyma upland region, where Yedoma is dominated by fine-grained silt-sized grain fractions (Schirrmeister et al., 2020). OM in the mineral fraction is mainly bound to silt and clay (Mueller et al., 2015). Fluvial deposition of the Yukechi sands may explain the lack of OM (Windirsch et al., 2020). In contrast to our study site, Yedoma deposits in other regions of Siberia are characterized by finer-grained silty sediments with relatively high TOC values with a median of 1.9 wt% (Strauss et al., 2020; Strauss et al., 2012a).

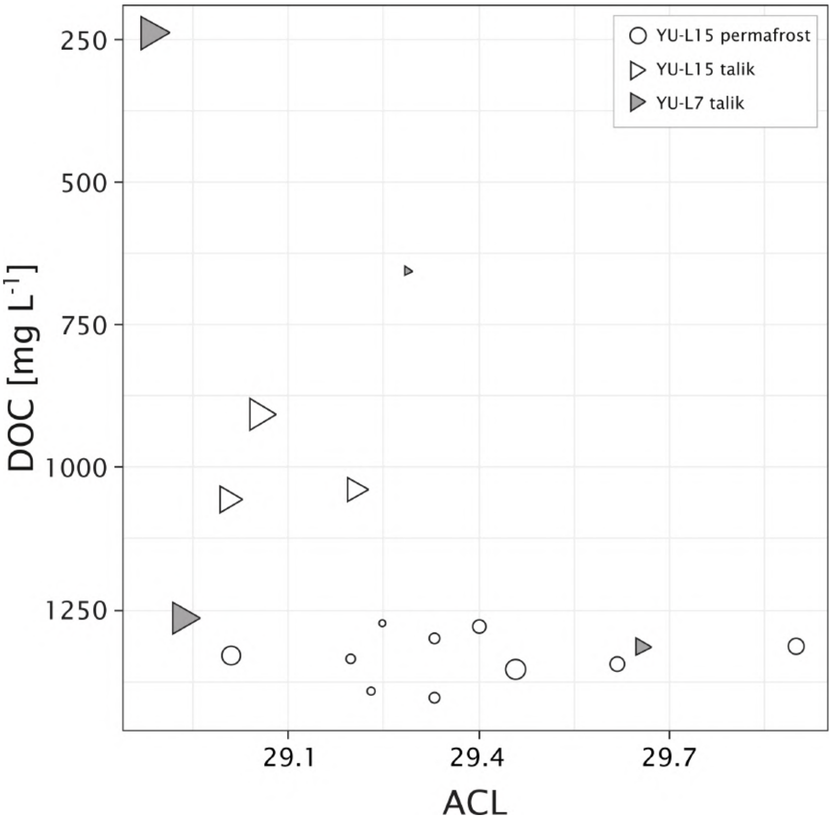

Figure 3.8: Bivariate scatterplot of the *n*-alkane average chain length (ACL) and dissolved organic carbon (DOC) content. The relation between these parameters with the cumulative carbon dioxide (CO_2) production after one year (indicated by symbol size). Samples from Alas lake sediment core (circles), talik of Yedoma lake sediment core (white triangles) and permafrost from Yedoma lake sediment core (grey triangles).

In contrast to the TOC, the DOC values from the frozen Yedoma sediments of YU-L15 are very high (median: 373 mg L^{-1}, max: 1620 mg L^{-1}; Figure 3.3), yet comparable to pore water from Yedoma deposits on Buor Khaya, northeastern Siberia (median: 317 mg L^{-1}, max: 1371 mg L^{-1}) (Schirrmeister et al., 2017). In addition, Ewing et al. (2015) reported high maximum DOC values in Alaskan Yedoma pore water (median: 618 mg L^{-1}, max: 1551 mg L^{-1}). For comparison, other studies from northeastern Siberia reported much lower pore water DOC values such as for early to middle Weichselian sediments on the Cape Mamontov Klyk, ranging from 4 to 305 mg L^{-1} (Mitzscherling et al., 2019), or for Samoylov Island, ranging from 57 to 288 mg L^{-1} (Liebner et al., 2008).

The rate and efficiency of hydrolysis from POC to DOC as well as the size and quality of the DOC pool are of utmost importance for GHG production since microbes mainly metabolize DOC size fractions (Battin et al., 2009). Therefore, DOC in pore water is readily bioavailable for microbial degradation upon talik formation and hence a very important OM fraction in GHG production process. Recent studies showed that DOC from thawing permafrost is highly biodegradable with the biolabile fractions composing ∼20 to 53% for Alaskan sites (Drake et al., 2015; Ewing et al., 2015) and 34 to 50% for Siberian sites (Spencer et al., 2015; Vonk et al., 2013b). These studies found that the biolabile DOC fraction was lost mainly in the first 1 to 2 weeks upon thaw. Furthermore, it was shown that ancient DOC originating from Pleistocene permafrost was more susceptible to decomposition than modern DOC (Mann et al., 2015;

Vonk et al., 2013b). The relatively high DOC contents in the Pleistocene Yedoma sediments in the bottom of core YU-L15 in combination with the generally high biolability of Yedoma OM could therefore be a reason for the substantial GHG production observed. The generally higher GHG production per g TOC in contrast to unfrozen or Alas lake sediments (Figure 3.4) supports the relatively high bioavailability of Yedoma OM. Whereas the decomposition of labile DOC seems to contribute to the GHG production upon initial talik formation, GHG production at later stages of talik formation is primarily driven by the breakdown of the POC fraction. Only very few studies focus on the breakdown of POC, and the interaction between POC and DOC decomposition is not well understood. Nevertheless, it was shown that POC turnover is relevant for DOC decomposition (Attermeyer et al., 2018; Richardson et al., 2013).

3.5.1.2 Organic matter preservation and talik formation

The characteristics of the sediments directly below alas lakes are often the result of several subsequent lake generations at a location with sometimes lacustrine and subaerial deposition alternating (Katasonov et al., 1979; Lenz et al., 2016b; Soloviev, 1959). In many thermokarst lake regions, multiple thermokarst lake generations over the past centuries to millennia led to repeated thawing and refreezing of the sediments (**e.g.**; Jones et al., 2012a) and therefore likely also recurring talik formation (Grosse et al., 2013). For the Yukechi Alas, the domination of long-chained alkanes (n-C_{29} and n-C_{31}) throughout both cores, indicating OM from higher terrestrial plants, suggests that the Alas lake sediments are primarily thawed Yedoma sediments. However, dated macrofossils at 290 cm bss yielded a Holocene age (3.75 ± 0.12 cal kyr BP) (Jongejans et al., 2019), suggesting a recent productivity signal in these sediments. The sediments at 518 cm bss had an age of 13.53 ± 0.66 cal kyr BP and all dated sediments below yielded ^{14}C ages >24 cal kyr BP.

In the uppermost sediments of the Yedoma lake core (170 cm bss), the OM is of recent origin (0.14 ± 0.05 cal kyr BP). This could be caused by sediment mixing during surface subsidence (Farquharson et al., 2016). Alternatively, active layer dynamics or cryoturbation could have played a role in the uppermost sediments during various sedimentation stages as well as the input of eroded material from the lakeshore. All other dated samples yielded ^{14}C ages >24 cal kyr BP. Hence, we measured GHG production from samples containing old and recent OM but found no clear pattern between the amount of GHG produced and the age of the OM. Nevertheless, the high and constant ACL over depth in both cores suggests that the OM source was rather similar over time.

With thaw and talik formation at our Alas site, microbial decomposition of OM led to GHG production. Furthermore, the drying of the basins could have favored aerobic conditions and OM cycling as well as potentially permafrost re-aggradation (Lee et al., 2012). This, in combination with the low TOC in the Yukechi Alas, could explain the low DOC values in the Alas core. During phases of intensified lake formation, interactions between pore water and the mineral phase could have led to liberation of DOC and the microbial transformation of the most biolabile fraction into GHG.

The sediments underneath the Yedoma lake have been thawed from the top down only for the last ~70 years for the first time since deposition (Ulrich et al., 2017), explaining the rather shallow talik compared to the Alas lake. The sediments at 778 cm bss of the Yedoma lake core, which was part of the talik, were attributed to the bottom cluster. This suggests that the studied OM characteristics in this sample are still more similar to the frozen sediments underneath than to the talik sediments above.

The frozen sediments in the bottom part have likely not been thawed since permafrost formation in the late Pleistocene. This suggests OM was better preserved in the permafrost sediments of the Yedoma lake compared to the top of the Alas lake sediments (Schuur et al., 2009). This was corroborated by a higher C/N ratio in the Yedoma lake sediments and in the bottom of the Alas lake sediments compared to the top and middle of YU-L7 ($p<0.05$; Figure 3.4). However, we found no significant correlation between the OC loss (Figure B.4) and the C/N ratio. This might be the result of the low TOC content in the Yukechi sediments, consequently TOC and C/N are no reliable predictors of CO_2 production. In the biomarker-based degradation indicators such as the $\mathrm{CPI}_{n-alkanes}$, we did not see the better preservation signal of the OM in the Yedoma lake core compared to the Alas lake core (Figure 3.4). Potentially, not enough time has passed since deposition for maturation (Bray and Evans, 1961). The CPI must hence be a result of the original signal and depositional environment of the OM rather than permafrost thaw history (Jongejans et al., 2020a).

Stapel et al. (2018) showed that the OM from Yedoma deposits on Bol'shoy Lyakhovsky Island had a relatively high aliphatic proportion, which suggests the OM is more easily degradable compared to more aromatic OM. Our pyrolysis experiments showed a clear connection between the TOC content and the aliphatic character, which suggest that these samples might contain more biolabile OM.

3.5.1.3 Presence of methanogenic communities

Archaeol and isoGDGT-0 concentrations were significantly higher in the Alas compared to the Yedoma lake sediments ($p<0.05$ and $p<0.01$, respectively) (Figure 3.4). Archaeol and isoGDGT 0 are breakdown products of intact polar membrane lipids and represent the past archaeal biomass as a degradation product (Bischoff et al., 2013; Stapel et al., 2018). Archaeol, one of the main core membrane lipids of archaea, was used to infer methanogenic abundance specifically before (Bischoff et al., 2013; Pancost et al., 2011). Increased isoGDGT-0 and archaeol concentrations in thawed sediments can indicate a mixture of past and present archaea including methanogens. The higher archaeal marker concentration in the Alas lake core suggests that the methanogenic communities were likely established after talik formation.

In previous studies, a positive correlation was found between CH_4 production in thawing permafrost and the presence of methanogenic archaea (Carnevali et al., 2015; Holm et al., 2020; Knoblauch et al., 2018). In our study, the CH_4 production was higher in the talik sediments of the Yedoma lake core. Lower CH_4 and CO_2 production in YU-L7 compared to YU-L15 suggest that the biolabile fraction of OM was already largely decomposed in a talik in previous thermokarst lake stages. This is corroborated by the lower C/N ratio in the Alas lake sediments. The moderate concentrations in the Yedoma lake core between 1161 and 966 cm bss might result from microbial activity during sedimentation (Bischoff et al., 2013). Holm et al. (2020) showed that microbial communities established prior to freezing could lead to an earlier start and stronger CH_4 production compared to sediments where no prior communities were established. Further research is needed to study the interactions between present and past microbial communities, and the factors controlling GHG production in thawing permafrost.

3.5.2 Greenhouse gas production

The one-year-long incubation experiments showed distinct differences between the first-generation and multiple-generation thermokarst lake sediments. Both CH_4 and CO_2 production were higher in the Yedoma lake sediments compared to the Alas lake sediments (3 and 1.5 times higher mean, respectively). The GHG production did neither correlate with the TOC content, nor with the biomarker concentrations and indices. Previous incubation studies of permafrost sediments found a positive correlation between CO_2 production and TOC (Knoblauch et al., 2013; Lee et al., 2012; Walter Anthony et al., 2016). These studies, however, analyzed sediment samples with higher TOC contents compared to our study (median: 1.2, 5.0 and ~4 wt%, respectively). Furthermore, we compared sediment samples that have undergone different depositional conditions and thaw legacy, which might explain the lack of correlation between TOC content and GHG production.

3.5.2.1 Carbon dioxide production

CO_2 production was highest in the bottom of YU-L15 (Figure 3.4). This is likely because the sediments were thawed for the first time since deposition, and the presence of readily bioavailable DOC after thaw. The latter is corroborated by the positive correlation between the initial DOC values in samples adjacent to the incubation samples and the CO_2 production, supporting the rapid turnover of biolabile DOC fractions (Vonk et al., 2013b). The CO_2 production from the still frozen Yedoma sediments in our core (1713-996 cm bss) is in the same order of magnitude as from Pleistocene sediments in the Lena Delta (0.13 ± 0.06 mg CO_2-C gdw^{-1}) (Knoblauch et al., 2013) and from mineral soils in Alaska and Siberia (0.34 ± 0.13 mg CO_2-C gdw^{-1}) (Lee et al., 2012). When expressed on a bulk carbon basis, however, the CO_2 production in the permafrost sediments of the Yedoma lake (50.6 ± 53.4 mg CO_2-C g^{-1} TOC) is much higher than from other Yedoma sites as reported by Knoblauch et al. (2013) (4.9 ± 2.1 mg CO_2-C g^{-1} TOC) and Lee et al. (2012) (11.3 ± 12.3 mg CO_2-C g^{-1} TOC). This means that despite the low carbon content of these sediments, the overall mineral OM has a high potential for being degraded into CO_2. Nevertheless, the percentage of initial C that was mineralized to CO_2 (2.3 ± 3.1%) was low in comparison with one-year-long incubation studies of organic-rich active layer sediments such as reported by Schädel et al. (2016) (6% loss) and Faucherre et al. (2018) (8% loss).

The median CO_2 rates over time in the bottom unit of the Yedoma lake core was 50 μg CO_2-C g^{-1} TOC day^{-1}. While some anaerobic incubations studies with permafrost samples had much lower CO_2 production rates (median: 1.6-3.6 μg CO_2-C g^{-1} TOC day^{-1}) (Knoblauch et al., 2013; Zona et al., 2012), other studies found rates in the same order of magnitude as our data such as Lupascu et al. (2012) and Santruckova et al. (unpublished data) (median 37.8 and 68.6 μg CO_2-C g^{-1} TOC day^{-1}, respectively). However, of these studies, only Knoblauch et al. (2013) reported CO_2 production in sediments >1 m below the sediment surface (i.e. down to 25 m depth).

The relatively high GHG production at the uppermost sample (290 cm bss) of the Alas lake sediment core might be explained by the input of Holocene OM (see 4.1.2) during a previous thermokarst lake stage where methanogenic communities were established, which might have a priming effect on the older carbon in these sediments (Wild et al., 2014).

3.5.2.2 Methane production

In most of our samples, a significant start of CH_4 production could be recognized only after 200 days (e.g., Figure B.6). Previous incubation studies also observed this lag phase and explained it as the result of the low initial abundance of methanogens in the sediments, which increases with thaw (Knoblauch et al., 2018; Knoblauch et al., 2013; Treat et al., 2014; Waldrop et al., 2010). Interestingly, the frozen sample below the talik boundary in the Yedoma lake core (996 cm bss), showed the highest maximum CH_4 production rate (252.2 μg CH_4-C g^{-1} TOC day^{-1}). As these sediments were frozen continuously since deposition and permafrost incorporation, these findings suggest that methanogenic communities were established here prior or during deposition and survived while being freeze-locked (Holm et al., 2020). In this particular sample, methanogenic taxa were likely present that produce CH_4 using very low substrate TOC concentrations as reported from low-temperature incubations of Arctic soils (Blake et al., 2015), but further detailed microbial analyses are required to substantiate this hypothesis.

CH_4 production was highest in the top of Yedoma lake core (Figure 3.7), which is corroborated by a negative correlation between CH_4 production and the depth bss in this core. This fits well to thaw front migration with talik formation and subsequent gradual population of methanogenic communities. In their study of methanogenesis response to permafrost thaw, Holm et al. (2020) found that CH_4 production was not correlated to C content, but rather to paleoenvironmental conditions. They argued that CH_4 production is more vulnerable to disturbance than anoxic CO_2 production, because methanogenesis is restricted to a very small group of archaea whereas there are many different groups of microorganisms producing CO_2 under anoxic conditions. Their findings show that anaerobic GHG release from thawing permafrost is complex and not yet well understood.

To our knowledge, Heslop et al. (2015) present the only other CH_4 production rates from Yedoma deposits that were thawed in a talik. They measured C release rates as CH_4 along a talik profile below an Alaskan first-generation thermokarst lake. In contrast to our data, Heslop et al. (2015) found highest CH_4 production rates in the recently thawed sediments (59.6 ± 51.5 μg CH_4-C g^{-1} TOC day^{-1}) compared to the transitional permafrost (15.3 ± 9.1 μg CH_4-C g^{-1} TOC day^{-1}) and the thawed Yedoma sediments (17.9 ± 13.6 μg CH_4-C g^{-1} TOC day^{-1}). Our data did not show such a trend: sediments from the recently thawed permafrost (778 cm bss) had a low maximum CH_4 production rate (2.5 μg CH_4-C g^{-1} TOC day^{-1}). However, the rates from the top of YU-L15 (81.8-135.1 μg CH_4-C g^{-1} TOC day^{-1}) were much higher. Nevertheless, the CH_4 production is not necessarily directly linked to CH_4 release, since a part of the produced CH_4 might be oxidized in the sediment column before being released into the atmosphere (Winkel et al., 2019).

The CH_4 production rates in the bottom unit of the Yedoma lake core (median: 0.02 μg CH_4-C g^{-1} TOC day^{-1}) were much lower compared to previously published CH_4 rates in 4 °C permafrost incubation studies (0.12-0.56 μg CH_4-C g^{-1} TOC day^{-1}) (**Santruckova et al.**; **unpublished data**; Knoblauch et al., 2013; Lupascu et al., 2012; Zona et al., 2012).

3.5.3 GHG links with other parameters and outlook

Using the generalized linear regression models, we found that CO_2 production was mainly explained by the ACL and the DOC content: sediments with the lowest ACL and highest DOC content produced the most CO_2 (Figure 3.8). This suggests that these parameters describe the lability of the OM best for our study. While the DOC seems to indicate the abundance of bioavailable OM (see chapter 3.4.1.2), the ACL signal might represent a more labile OM source fraction from the respective surrounding ecosystem.

In some cases, we did find high archaeal markers or a strong aliphatic character corresponding to a higher CH_4 production, but in other samples, this was the exact opposite. We did not find significant correlations between the biomarker distribution and the CH_4 production (Figure B.5). Therefore, we assume that the variation must be explained by a complex interplay of different external factors controlling the GHG production. The varying sedimentation history of the Yukechi sediments might play an important role in this, as different depositional mechanisms could have resulted in OM from different sources (e.g. transported vs. in situ, different types of plants) leading to a mixture of labile and recalcitrant OM. This could have led to an activation of OM in some (sub-)samples but not in others. For the samples with increased bacterial and archaeal markers but low GHG production, the biomarkers might indicate past microbial activity rather than the presence of active methanogenic communities. The reactivation of such paleo-active horizons depends on factors which are not yet fully understood, but intense remineralization in the past as indicated by the high lipid biomarker concentrations might have strongly depleted labile organic compounds from the overall OM pool. Further research into intact polar lipids could help to quantify the interaction between present and past microorganisms (Bischoff et al., 2013; Stapel et al., 2018).

In contrast to our incubation experiment, external factors could influence the oxygen content of the sediments as well as the soil microbial communities under in situ conditions. Differences between the temperature used in our incubations (4 °C) and the actual temperature in talik sediments, which varies seasonally depending on the depth and probably ranges from ~0 to about 4 °C (Heslop et al., 2015), might lead to over- or underestimation of the GHG production. Earlier incubations (**e.g.**; Tanski et al., 2019) and modeling research (**e.g.**; Knoblauch et al., 2013) considered GHG production for 4 months per year, which represents the summer thaw season. GHG production in talik sediments, however, continues year-round, which is why we incubated our samples for one entire year.

Thermokarst lake initiation and expansion in a warming climate will continue to set free OM. Even though initially microbial abundances might be low in permafrost soils, long-term thawing of ice-rich sediments underneath thermokarst lakes will promote anaerobic conditions and activate methanogenic OM degradation, leading to substantial GHG production. Walter Anthony et al. (2016) showed that anaerobic carbon release from thermokarst lakes was directly proportional to the amount of carbon input by thawing of sediments. They calculated that, since the 1950s, 0.2 to 2.5 Gt permafrost carbon was released as GHG in thermokarst expansion zones of pan-Arctic lakes. Converted to annual release, they found a mean CH_4 production of

0.50 ± 0.09 mg CH_4 C g^{-1} TOC y^{-1}, which is much lower than the mean of all our samples after 1 year (3.80 ± 5.66 mg CH_4-C g^{-1} TOC). Our findings underline the vast potential of thermokarst lake formation and subsequent GHG release. Considering the importance of this input for the global climate system, this topic should receive continued attention.

3.6 Conclusion

In this study, we analyzed greenhouse gas production and lipid biomarker distributions in two 17 m long thermokarst lake sediment cores taken in Central Yakutia, Russia. We found that the sediments in both cores were relatively OC poor, which is in agreement with previous research in the Yukechi region. We found substantial differences between the well-preserved sediments below a young Yedoma lake, and the heavily thermokarst affected sediments below an Alas lake. Both CH_4 and CO_2 production were higher in the Yedoma lake deposits compared to Alas lake deposits. The highest CO_2 production was measured in the deepest, in situ still frozen part of the Yedoma lake core, which shows that potential CO_2 production in newly thawed sediments strongly depends on the decomposition of readily available DOC. In contrast to previous research, we found no correlation between the CO_2 production and the TOC content. However, the CO_2 production could mainly be explained by the ACL and DOC content, suggesting that OM source and quality is the main driver for the CO_2 production. The CH_4 production showed a different pattern: most CH_4 was produced in the talik sediments below the Yedoma lake, suggesting that methanogenic communities were established in the thawed sediments but not yet in the frozen sediments in the bottom of the core. We assume that the variable depositional history of the Yukechi region led to the accumulation of OM from a different source and quality in different sediment layers, which explains the variation in GHG production in the sediments. The lower GHG production in the Alas lake core is a result of a degradation legacy that led to OM decomposition during earlier thermokarst lake generations. GHG production from thawed permafrost was substantial even from OC-poor sediments, highlighting the importance of thermokarst formation in general, and thaw of mineral permafrost in particular for the climate system. Therefore, our study presents novel insights that are relevant for mineral-dominated deposits with generally low TOC contents, which are widespread throughout the Arctic.

3.7 Acknowledgements

We thank the drilling team from the private company Stroiizyskaniya from Yakutsk. The expedition team thanks the local community of Chyuyya, a small village near the Yukechi Alas, for their hospitality and hosting us during the fieldwork. We thank the lab staff for helping with the biogeochemical analyses conducted at AWI Potsdam labs (Dyke Scheidemann and Antje Eulenburg), and incubation experiments and lipid biomarker analyses conducted at GFZ labs (Oliver Burckhardt, Charlotte Haugk, Lucas Horstmann, Daria Kapustina, Cornelia Karger, Ferdinand Perssen and Anke Sobotta). The field campaign was supported by Avksentry P. Kondakov. This research was supported by the International Permafrost Association Action Group “The Yedoma Region”.

4

Sobo-Sise cliff

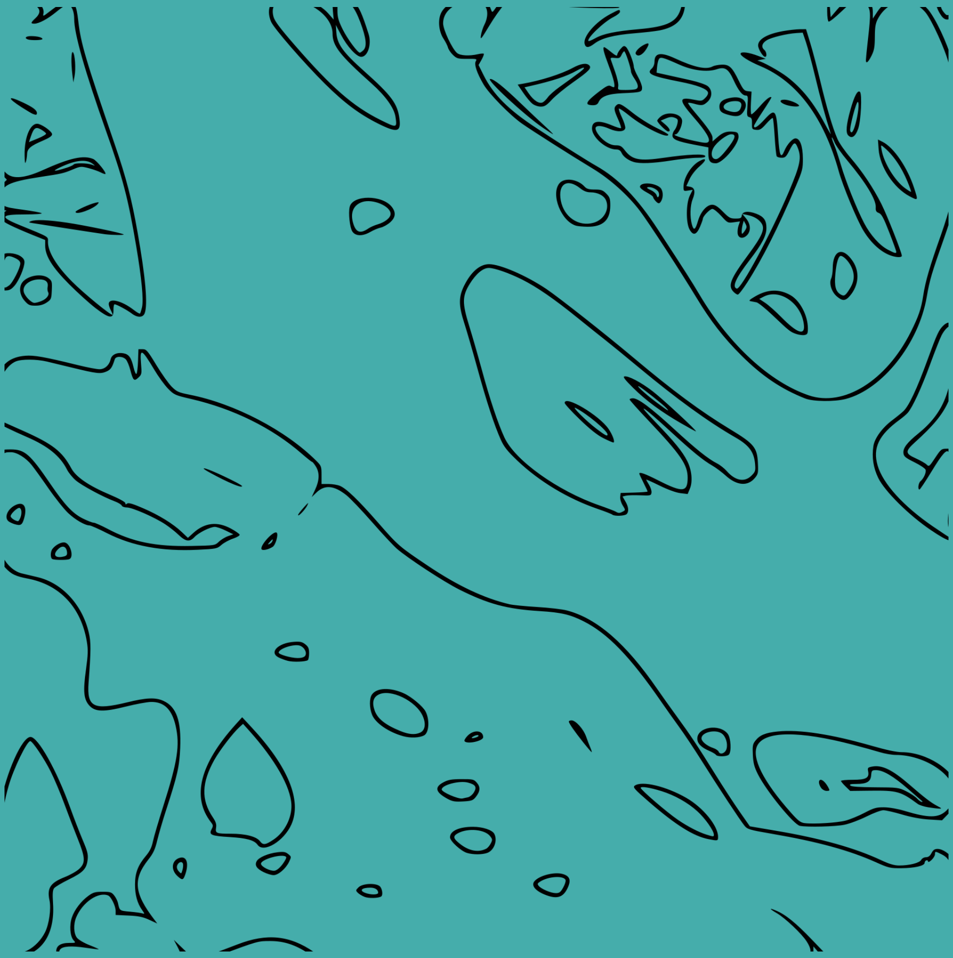

We move further back
Faster than the cliff can sing
Its erosion song

4 Organic matter characteristics of a rapidly eroding permafrost cliff

4.1 Abstract

Organic carbon (OC) stored in Arctic permafrost represents one of Earth's largest and most vulnerable terrestrial carbon pools. Amplified climate warming across the Arctic results in widespread permafrost thaw. Permafrost deposits exposed at river cliffs and coasts are particularly susceptible to thawing processes. Accelerating erosion of terrestrial permafrost along shorelines leads to increased transfer of organic matter (OM) to nearshore waters. However, the amount of terrestrial permafrost carbon and nitrogen as well as the OM quality in these deposits are still poorly quantified. Here, we characterize the sources and the quality of OM supplied to the Lena River at a rapidly eroding permafrost river shoreline cliff in the eastern part of the delta (Sobo-Sise Island). Our multi-proxy approach captures bulk elemental, molecular geochemical and carbon isotopic analyses of late Pleistocene Yedoma permafrost and Holocene cover deposits, discontinuously spanning the last ∼52 ka. We show that the ancient permafrost exposed in the Sobo-Sise cliff has a high organic carbon content (mean of about 5 wt%). We found that the OM quality, which we define as the intrinsic potential to further transformation, decomposition, and mineralization, is also high as inferred by the lipid biomarker inventory. The oldest sediments stem from Marine Isotope Stage (MIS) 3 interstadial deposits (dated to 52 to 28 cal kyr BP) and is overlaid by Last Glacial MIS 2 (dated to 28 to 15 cal ka BP) and Holocene MIS 1 (dated to 7-0 cal ka BP) deposits. The relatively high average chain length (ACL) index of *n*-alkanes along the cliff profile indicates a predominant contribution of vascular plants to the OM composition. The elevated ratio of *iso*- and *anteiso*-branched FAs relative to long chain ($C \geq 20$) *n*-FAs in the interstadial MIS 3 and the interglacial MIS 1 deposits, suggests stronger microbial activity and consequently higher input of bacterial biomass during these climatically warmer periods. The overall high carbon preference index (CPI) and higher plant fatty acid (HPFA) values as well as high C/N ratios point to a good quality of the preserved OM and thus to a high potential of the OM for decomposition upon thaw. A decrease of HPFA values downwards along the profile probably indicates a relatively stronger OM decomposition in the oldest (MIS 3) deposits of the cliff. The characterization of OM from eroding permafrost leads to a better assessment of the greenhouse gas potential of the OC released into river and nearshore waters in future, which is important to understand the consequences of a warming climate in Arctic environments on the global carbon cycle.

4.2 Introduction

The terrestrial Arctic is highly vulnerable to climate warming as large areas are underlain by ice-rich permafrost (**e.g.**; Strauss et al., 2021a). Terrestrial permafrost ecosystems are affected by the ongoing climate warming with consequences for geomorphological, hydrological and biogeochemical processes from a local to regional scale (IPCC, 2019). Almost twice as much carbon is stored in the permafrost region than what is currently contained in the atmosphere (Hugelius et al., 2014; Mishra et al., 2021), making permafrost carbon dynamics a globally relevant issue (Grosse et al., 2011; Schuur et al., 2008; Strauss et al., 2021a; Turetsky et al., 2020). Total estimated soil organic carbon (SOC) storage for the permafrost region is 1100-1600 Gt of which 181 ± 54 Gt are attributed to deep permafrost (below 3 m depth) of the Yedoma region (Hugelius et al., 2014; Strauss et al., 2021b; Strauss et al., 2013). Extensive river networks like the Lena River, especially in their delta zones, carry large nutrient and organic matter (OM) loads to the nearshore zone and onto the Arctic Shelf (Mann et al., 2021; Sanders et al., accepted). The Arctic river discharge increased significantly in recent decades, transporting organic-rich waters to the nearshore area (Holmes et al., 2015; Holmes et al., 2012). Increased river bank erosion of Arctic rivers following warming during the last decades poses an important mechanism of carbon export from land to water (Fuchs et al., 2020; Zhang et al., 2021; Zhang et al., 2017).

Warming throughout the Arctic prolongs the season for permafrost thaw and open ice-free water bodies, resulting in increasing erosion of ice- and carbon-rich permafrost sediments exposed at coasts (Günther et al., 2013; Jones et al., 2020). Very ice-rich permafrost deposits (i.e., 50-90 vol% ice) such as the late Pleistocene Yedoma Ice Complex (Schirrmeister et al., 2013; Strauss et al., 2017) are particularly vulnerable to rapid thermo-denudation and thermo-erosion processes along river shores (Costard et al., 2014; Fuchs et al., 2020; Kanevskiy et al., 2016; Stettner et al., 2018). Vonk et al. (2013b) showed that Yedoma ice-wedge meltwater can increase the decomposition of OM due to co-metabolizing effects. Another potential impact of the decomposition of terrestrial OM and discharge with Arctic river water, is the change in biochemical properties that may increase ocean acidification and anthropogenic carbon dioxide uptake from the atmosphere (Semiletov et al., 2016). Furthermore, Semiletov et al. (2016) estimated that 57% of the terrestrial organic carbon in the East Siberian Shelf originates from ancient Pleistocene age permafrost C, such as Yedoma deposits adjacent to river or coastal zones. These studies stress the need to better understand the interactions between thawing permafrost and river and nearshore waters.

The study of fossil biomolecules and other OM characteristics provides insights into the composition and level of OM decomposition and hence can greatly improve estimates on the greenhouse gas potential of thaw-mobilized OM from permafrost deposits (Andersson & Meyers, 2012; Sánchez-García et al., 2014). A few studies have previously focused on molecular biomarkers in northeastern Siberian permafrost deposits (**e.g.**; Höfle et al., 2013; Jongejans et al., 2020a; Stapel et al., 2016; Strauss et al., 2015; Zech et al., 2010). In general, the abundance and distribution of *n*-alkanes, which are long-chained, single bonded hydrocarbons, are used for OM characterization where the chain length of *n*-alkanes indicates OM sources.

In our study, we estimate molecular biomarkers (*n*-alkanes, *n*-fatty acids) and use established biomarker proxies and indices such as the average chain length of *n*-alkanes (ACL), the carbon preference index (CPI), and the higher plant fatty acid (HPFA) index to test whether they mirror OM degree of decomposition and reflect the OM quality in ancient permafrost deposits. Additionally, analyses of the total organic carbon content (TOC), the stable carbon isotope ratios (δ^{13}C of TOC), the total nitrogen content (TN), and TOC/TN (here referred to as C/N ratios), are applied to our sample set. Hierarchical clustering is used to identify the stratigraphical units along the sample profile based on the major changes in OM composition.

Thus, the OM characteristics of permafrost deposits, rapidly eroding at a cliff site in the eastern Lena Delta, are analyzed for the first time for biomarkers. The set of frozen samples was obtained along a 25 m vertical cliff profile with relatively high sampling density of about 1 m covering all exposed cryostratigraphic units. In this study, we aim (1) to characterize the OM composition of ancient permafrost that accumulated under different climate conditions, (2) to assess the degree of decomposition that the OM already experienced, and (3) to hypothesize, based on the decomposition legacy, the potential of future decomposability and microbial decomposition of the permafrost OM.

4.3 Study area

The Lena River forms the largest delta in the Arctic covering an area of 29,000 km^2 (Schneider et al., 2009) and discharges the second highest freshwater load into the Laptev Sea, with a mean annual discharge of 525 km^3/yr (Holmes et al., 2015). It also transports a lot of summer 'heat' from the south to the north (Yang et al., 2005). The study area on Sobo-Sise Island (Figure 4.1a-b) is located in the continuous permafrost zone. The island stretches between the Sardakhskaya and Bykovskaya main channels in the eastern part of the delta. In addition to the modern floodplain, there are three geomorphic units in the delta (Grigoriev, 1993; Schwamborn et al., 2002). While the first unit consists of Holocene floodplains, the second unit consists of late Pleistocene and Holocene fluvial deposits that are mostly located in the north-western part of the delta and are cut off from the current delta dynamics (Schirrmeister et al., 2011b). The third geomorphological unit consists of erosional remnants of a late Pleistocene accumulation plain with ice-rich Yedoma Ice Complex deposits (Schwamborn et al., 2002; Wetterich et al., 2008). According to a landform classification for Sobo-Sise Island, 43% of the land surface is occupied by Yedoma uplands and Yedoma slopes, 43% are thermokarst basins with the remaining 14% being thermokarst lakes (Fuchs et al., 2018). The terrain is affected by rapid thermokarst processes (Nitze & Grosse, 2016) and surface thaw subsidence (Chen et al., 2018). The distinct surface morphology of Sobo-Sise Island includes Yedoma uplands intersected by thermo-erosional valleys and thermokarst basins. Syngenetic permafrost formation in polygonal tundra landscapes over long periods in the late Pleistocene formed thick deposits with large ice wedges that are exposed at the cliff (Jongejans et al., 2018; Schirrmeister et al., 2020; Schirrmeister et al., 2011b; Strauss et al., 2015). Schirrmeister et al. (2011b) attributed parts of the third geomorphological unit in the Lena Delta in the western and southern parts of the delta to remnants of a Yedoma accumulation plain. This formed during the late Pleistocene when the Lena River had its delta farther north. Radiocarbon ages corroborated that Yedoma deposits on Sobo-Sise Island accumulated during the late Pleistocene between about 52 and 15 cal kyr BP. Substantial hiatuses were found at about 36–29 cal kyr BP and at 20 to 17 cal kyr BP, which may be related to fluvial erosion and/or changed discharge patterns of the Lena River (Wetterich et al., 2020). Middle to late Holocene ages from 6.36 to 2.5 cal kyr BP were found in the uppermost cover deposits of the cliff, which is also in agreement with other cover deposits found on top of Yedoma such as on the nearby Bykovsky Peninsula (Grosse et al., 2007; Schirrmeister et al., 2002b).

The Sobo-Sise Yedoma cliff has an average height of 22 m with a maximum height of 27.7 m above the river water level (m arl) (Fuchs et al., 2020) and is affected by fluvio-thermal erosion. The current average shoreline retreat rate, which was calculated using satellite data, is 15.7 m/yr (2015-2018), which is remarkably high (Fuchs et al., 2020). The Sobo-Sise Yedoma cliff (72°32 N, 128°17 E; Figure 4.1c) extends over 1,660 m in length and is facing north to the Sardakhskaya Channel. Here, the water discharge amounts to ~8000 m^3/s during the summer-low period (Fedorova et al., 2015) and the Lena River is ice-covered for about 8 months per year between October and May. The river ice thickness reaches up to 2 m. Water depth at the beginning of the Sardakhskaya Channel (close to Stolp and Sardakh islands) can reach up to 22 m (Fedorova et al., 2015) and is approximately 11 m in front of the Sobo-Sise Yedoma cliff, allowing for water flow underneath the river ice cover during the winter months (Fuchs et al., 2020).

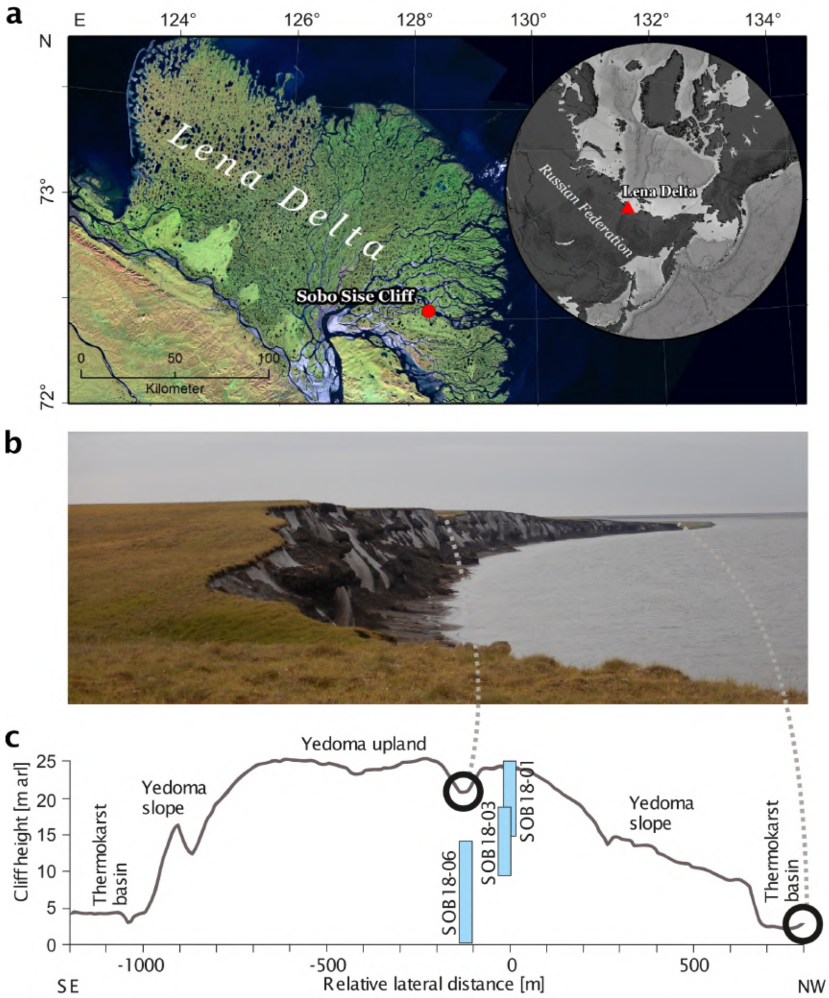

Figure 4.1: Overview of the Sobo-Sise Yedoma cliff. (a) Location of the Sobo-Sise Yedoma cliff in the Lena Delta in north-eastern Siberia; (b) picture of the Sobo-Sise Yedoma cliff from the east to west; (c) cross-section of the cliff profile indicating the three vertical sampled sections: SOB18-01, SOB18-03 & SOB18-06, adapted from Wetterich et al. (2020a).

4.4 Methods

4.4.1 Fieldwork

The Sobo-Sise Yedoma cliff was sampled in three overlapping vertical sediment profiles (Figure 4.1b) covering the entire exposed permafrost section (profile SOB18-01: 24.1 to 15.7 m arl, profile SOB18-03: 18.2 to 10.2 m arl and profile SOB18-06: 13.4 to 0.9 m arl). Each profile was cryolithologically described (Wetterich et al., 2020; Wetterich et al., 2018) and samples were collected at 0.5 m intervals by rappelling down on a rope from the top of the cliff. We used an axe and hammer to extract defined cubes of frozen ground (∼20x10x10 cm) from the cliff wall. Samples were collected after cleaning and scraping off the outermost unfrozen and frozen parts of the cliff wall in order to collect frozen uncontaminated samples. Then, the samples were lifted upward, cleaned and subsampled for biomarker analysis. In total, we collected 61 sediment samples of which 28 were selected for biomarker analysis at about 1 m intervals covering the entire exposed section. The samples were stored frozen in pre-combusted glass jars, apart from 9 samples (SOB18-06-09 to SOB18-06-34) which were initially stored in plastic whirl packs, before being transferred in a frozen state to glass containers after transport to the laboratories.

4.4.2 Sedimentological organic matter parameters

Prior to bulk geochemical analyses all samples were freeze dried (Sublimator, ZIRBUS technology), grinded and homogenized (Fritsch pulverisette 5 planetary mill; 8 min at 360 rotations per minute). Total elemental carbon (TC) and total nitrogen (TN) content of sediment samples in weight percentage (wt%) were measured with a carbon–nitrogen–sulphur analyzer (Vario EL III, Elementar) with a detection limit of 0.1 wt% for carbon and nitrogen. Sample below this detection limit were set to 0.05 wt% (half the detection limit) so that the statistics could be calculated. Total organic carbon (TOC) content in weight percentage (wt%) was measured with a TOC analyzer (Vario Max C, Elementar). The TOC to TN (C/N) ratio has been used as a rough first indicator of the degree of OM decomposition with decreasing values indicating proceeding decomposition (Palmtag et al., 2015). The stable carbon isotope ratio (δ^{13}C) of TOC reflects both the initial contribution from different plant species and plant components, and OM decomposition processes (Gundelwein et al., 2007). Samples for δ^{13}C analyses were treated with hydrochloric acid (20 mL, 1.3 molar), heated on a hotplate (97.7 °C for 3h) to remove carbonates, and subsequently washed with distilled water. All δ^{13}C samples were measured using a Delta V Advantage isotope ratio MS equipped with a Flash 2000 Analyzer (ThermoFisher Scientific), using helium as a carrier gas. The δ^{13}C (^{13}C/^{12}C) value is reported in per mille (‰) compared to the standard ratio Vienna Pee Dee Belemnite (VPDB). In addition, the radiocarbon ages of selected plant remains were determined on a MICADAS system. The radiocarbon dating laboratory procedures are given in Mollenhauer et al. (2021). Original data including a Bayesian age-depth model were adopted from Wetterich et al. (2020).

4.4.3 Lipid biomarkers

Lipid biomarkers provide information on a molecular level about the source of OM, the environmental conditions during deposition, and the degree of decomposition. In this study, we focused on *n*-alkanes in the aliphatic OM fraction and *n*-fatty acids in the polar hetero-compound fraction. Changes in their relative abundance can provide indication on the degree of decomposition (Kim et al., 2005) as outlined below. We analyzed the *n*-alkane distributions of all 28 samples and selected 13 samples for the analysis of *n*-fatty acids. The selection of the *n*-fatty acids was made to cover the entire profile continuously (approximately every 2 m).

4.4.3.1 Extraction and fraction separation

Following freeze-drying and grinding, biomarker subsamples were transferred into glass jars. Extraction and separation was conducted according to Schulte et al. (2000) and Strauss et al. (2015). Samples were processed in two batches, each containing 14 samples. We weighed between 8 and 11 g in extraction cell bodies fit for the accelerated solvent extractor (ASE 200 Dionex). Dichloromethane/methanol (ratio 99:1) was used as a solvent mixture for OM extraction. Each sample was held in a static phase (20 min at 75 °C and 5 MPa, following 5 min of heating). Dissolved compounds were then further concentrated at $\sim$42 °C using a closed-cell concentrator (TurboVap 500 Zymark) and the remaining solvent was evaporated under N_2. Afterwards, internal standards were added: 5α-androstane for the aliphatic fraction, ethylpyrene for the aromatic fraction, 5α-androstan-17-one for the NSO (nitrogen-, sulphur- and/or oxygen) neutral polar fraction and erucic acid for the NSO fatty-acid fraction (80 μL each from respective 100 μg/mL standard solutions). Subsequently, an asphaltene precipitation was performed to remove compounds with higher molecular complexity (asphaltenes) by dissolving the extracts in a small amount of dichloromethane and adding a fortyfold excess of *n*-hexane. Precipitated asphaltenes were removed by filtration through a sodium sulphate filled funnel. Subsequently, the *n*-hexane-soluble portion was separated by medium pressure liquid chromatography (MPLC) (Radke et al., 1980) into three fractions of different polarities: aliphatic hydrocarbons, aromatic hydrocarbons and polar hetero compounds (NSO compounds). Finally, the NSO fractions of 13 samples were split into an acid and neutral polar (alcohol) fraction using a KOH impregnated column. While the *n*-fatty acid potassium salts were attached to the silica gel, the neutral polar compounds were eluted with dichloromethane. After remobilizing the *n*-fatty acids by protonation of their salts with formic acid, the *n*-fatty acid fraction was obtained with dichloromethane.

4.4.3.2 GC-MS measurements and compound quantification

n-Alkanes and *n*-fatty acids were analyzed using gas chromatography coupled with a mass spectrometer (GC-MS; GC - Trace GC Ultra and MS - DSQ, both Thermo Fisher Scientific). Prior to the analyses, *n*-fatty acids were methylated with diazomethane. The GC was equipped with a cold injection system operating in the split-less mode. The injector temperature was programmed from 50 to 300 °C at a rate of 10 °C/s. Helium was used as carrier gas with a constant flow of 1 mL/min. After injection, the compounds of interest were separated on an SGE BPX 5 fused-silica capillary column (50 m length, 0.22 mm ID, 0.25 μm film thickness) using the following temperature conditions: initial temperature of 50 °C (1 min isothermal), heating rate of 3 °C/min to 310 °C, held isothermal for 30 min. The MS operated in the electron impact mode at 70 eV. Full-scan mass spectra were recorded from m/z 50–600 at a scan rate of 2.5 scans/s. Using the software XCalibur (Thermo Fisher Scientific), peaks in the GC-MS run were quantified using the internal standards for *n*-alkanes and *n*-fatty-acids. All biomarker concentrations are expressed in μg per gram of dry sediment (μg/gSed) and per gram of TOC (μg/gTOC).

4.4.4 Biomarker indices

4.4.4.1 Average Chain Length

The *n*-alkane average chain length (ACL) is the weighted average number of carbon atoms used for determining OM sources. Long chain odd-numbered *n*-alkanes ($> C_{25}$) are essential constituents that serve as biomarkers for higher terrestrial plants (Schäfer et al., 2016), whereas shorter chain lengths indicate bryophyte, bacterial or algal origin. A change of the ACL in the long chain range can suggest a change in the terrestrial source biota. We used the equation (Equation 4.1) first described by Poynter (1989) and then applied by Schäfer et al. (2016), but with a chain interval from C_{23} to C_{33} following Strauss et al. (2015) and Jongejans et al. (2018):

$$ACL_{23-33} = \frac{\Sigma\, i\, C_i}{\Sigma\, C_i}\ (C = concentration, i = carbonnumber) \tag{4.1}$$

4.4.4.2 Carbon Preference Index

The CPI (carbon preference index) was originally introduced by Bray and Evans (1961) as the ratio of odd over even numbered *n*-alkanes and indicates the level of OM transformation which decreases with progressing maturation. OM decomposition leading to lower CPI values is a measure of thermal alteration referring to rocks or oils on a geological timescale. However, this ratio, as well as the very similar odd-over-even predominance (OEP) ratio, were previously used in Quaternary permafrost deposits as indicator for OM decomposition (Jongejans et al., 2020a; Strauss et al., 2015; Struck et al., 2019; Zech et al., 2009). Based on these studies, we refer to values over 5 as less degraded OM of high-quality. Equation 4.2 describes the CPI and was modified after Marzi et al. (1993) using C_{23-33} as a chain length interval.

$$CPI_{23-33} = \frac{\Sigma\, odd\, C_{23-31} + odd\, C_{25-33}}{2\, \Sigma\, even\, C_{24-32}} \tag{4.2}$$

4.4.4.3 Higher Plant Fatty Acids

For each sample, the absolute *n*-fatty acid (FA) concentration was measured and the most abundant homologue's chain length was identified. Also, we looked at the share of *iso*- and *anteiso*-branched FAs which are indicators for microbial biomass (Rilfors et al., 1978; Stapel et al., 2016). Furthermore, we calculated the higher plant fatty acids (HPFA) index, which is the relative amount of the long chain n-fatty acids to long chain n-alkanes in the sediments. The HPFA was introduced by Strauss et al. (2015) following the principles of the HPA index of Poynter (1989), only with using fatty acids instead of wax alcohols (Equation 4.3). The HPFA index reflects the degree of preservation of OM due to the higher lability of n-fatty acids in relation to n-alkanes (Canuel & Martens, 1996). The preferential decomposition of fatty acids is due to their functional group leading to a chemical polarization within the molecule forming an attack point for geochemical or microbiological decomposition and/or decarboxylation (Killops & Killops, 2013). Therefore, a decrease in the HPFA index indicates increased OM decomposition. We use this index for internal comparison where higher values (above the mean) indicate a comparatively higher quality OM.

$$HPFA = \frac{\Sigma\, n - fatty\, acids\; C_{24}C_{26}C_{28}}{\Sigma\, n - fatty\, acids\; C_{24}C_{26}C_{28} + n - alkanes\; C_{27}C_{29}C_{31}} \tag{4.3}$$

4.4.5 Data analysis

In order to identify the stratification along the cliff based on the OM characteristics of the permafrost sediments, the data set was clustered using a constrained agglomerative hierarchical clustering of a distance matrix (chclust of the rioja package, in R version 4.0.4) (Juggins, 2020). We applied the non-parametric Kruskal-Wallis (>2 groups) test for statistical analyses of the data to compare all major parameters (TOC, C/N, n-alkanes, ACL, CPI, short and long n-fatty acids, HPFA index and (*iso*+*anteiso*)/long-fatty acids) between the identified clusters. In the results section, we report the p-values; the correlation coefficients are reported in Table C.1. As an additional data set, we added the age-depth modelling by Wetterich et al. (2020), which is based on Bayesian age-depth modelling (Blaauw & Christen, 2011) and ranged for all sampled horizons from 2.500 (at 23.7 m arl) to 51.880 cal kyr BP (at 0.9 m arl).

4.5 Results

The uppermost sediments of the cliff consisted of Holocene age sediments (from 24.1 to 22.5 m arl; upper part of SOB18-01) on top of late Pleistocene Yedoma sediments from 22.2 m arl down to the cliff base at the river water level. A detailed cryostratigraphic description is given in Wetterich et al. (2020). All data presented here will be available upon publication in the data repository PANGAEA.

4.5.1 Sedimentological organic matter parameters

TOC content was highest in the topmost sample and ranged from <0.1 wt% (below detection limit, sample SOB18-01-18 at 15.7 m arl) to 25.51 wt% (SOB10-01-01 at 24.1 m arl). Both the minimum and maximum TOC values were found within profile SOB18-01 (Figure 4.2). The average TOC content was 4.94 wt% (standard deviation (sd): 4.7, n=28) and values decreased from the cliff top downwards with two values higher than 10 wt% at 24.1 m arl (SOB18-01-01; 25.51 wt%) and at 16.2 m arl (SOB18-03-05; 11.31 wt%). TN content had an average of 0.33 wt% (sd: 0.18) and the highest value was also found at 24.1 m arl (SOB18-01-01; 0.83 wt%)

and the lowest at 15.7 m arl (SOB18-01-18; <0.1 wt%). C/N ratios ranged from 7.20 to 30.55 (Figure 4.2) and displayed, except for the uppermost sample, only little variability over the cliff profile with a mean of 13.24 (sd: 4.23). The δ^{13}C values ranged from -25.2 ‰ (SOB18-01-12 at 18.7 m arl) to -29.4 ‰ (SOB18-03-05 at 16.2 m arl) and had an average of -27.17 ‰ (sd: 1.08). There was a significant negative correlation between δ^{13}C and C/N values (R: -0.59 (Pearson correlation), $p<0.01$).

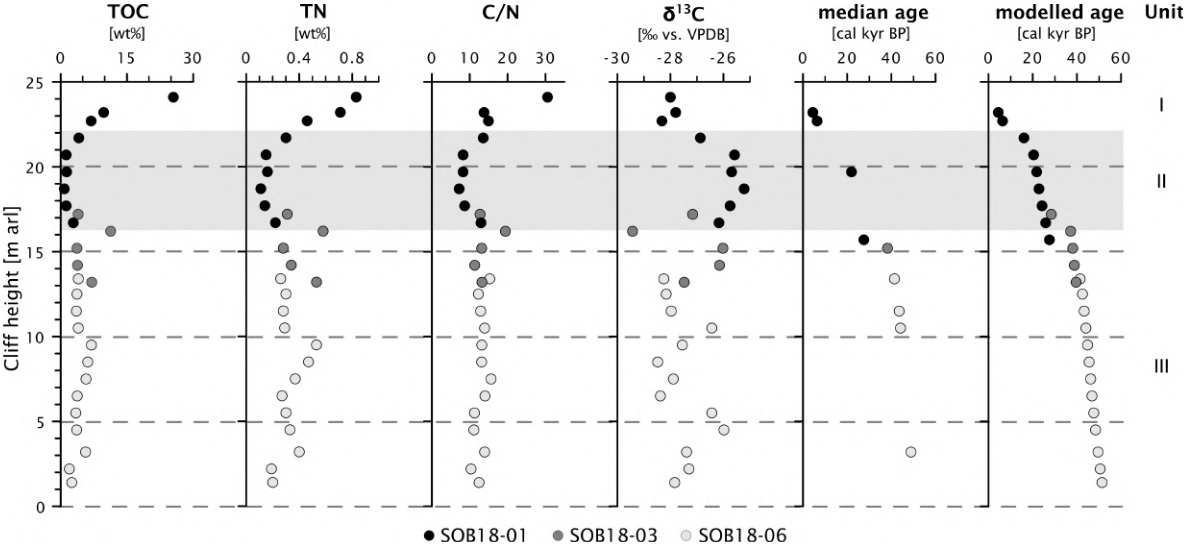

Figure 4.2: Biogeochemical parameters of the Sobo-Sise Yedoma cliff: total organic carbon (TOC) content, total nitrogen (TN) content, carbon over nitrogen (C/N) ratio, bulk stable carbon isotope ratios (δ^{13}C), radiocarbon ages and modelled age in calibrated years before present (cal kyr BP). Data points are displayed over cliff height from cliff top at 25 m above river level (arl) to cliff bottom at 0 m arl. The three sections of SOB18 are plotted separately for each parameter (black, dark grey and light grey circles). Units I, II (grey rectangle) and III correspond to Marine Isotope Stage (MIS) 1 to 3. The radiocarbon ages were published in Wetterich et al., 2020a.

4.5.2 Biomarkers

4.5.2.1 *n*-Alkanes

n-Alkanes were detected in the range between *n*-C_{14} and *n*-C_{35}. Absolute *n*-alkane concentrations ranged from 1 to 172 μg/gTOC (mean: 31, sd: 43) for the short (C_{14} to C_{20}) *n*-alkanes and from 119 to 3192 μg/gTOC (mean: 1050, sd: 897) for the long chain (C_{21} to C_{33}) *n*-alkanes (Figure 4.3). The relative *n*-alkane concentration increased in the lower part of the cliff, closer to the river level. The same is true for the absolute concentration of the short chain (mean: 1 μg/gSed, sd: 1) and long chain *n*-alkanes (mean: 42 μg/gTOC, sd: 32). The main dominating *n*-alkane chain length was *n*-C_{27} in the lower part of the cliff and alternated between *n*-C_{27} and *n*-C_{29} in the upper part (Figure C.1). Four samples were dominated by the *n*-C_{31} *n*-alkane. The *n*-alkane based ACL showed variations between 27.1 (SOB18-06-19 at 4.5 m arl) and 29.0 (SOB18-01-06 at 21.7 m arl) with a mean of 28.0 across the cliff (sd: 0.50; Figure 4.3). The CPI of *n*-alkanes (C_{23} to C_{33}) ranged from 5.76 (SOB18-06-15; 6.5 m arl) to 16.29 (SOB18-06-05; 11.5 m arl) with a mean value of 9.89 (sd: 2.79). Below 7 m arl, the CPI significantly decreased.

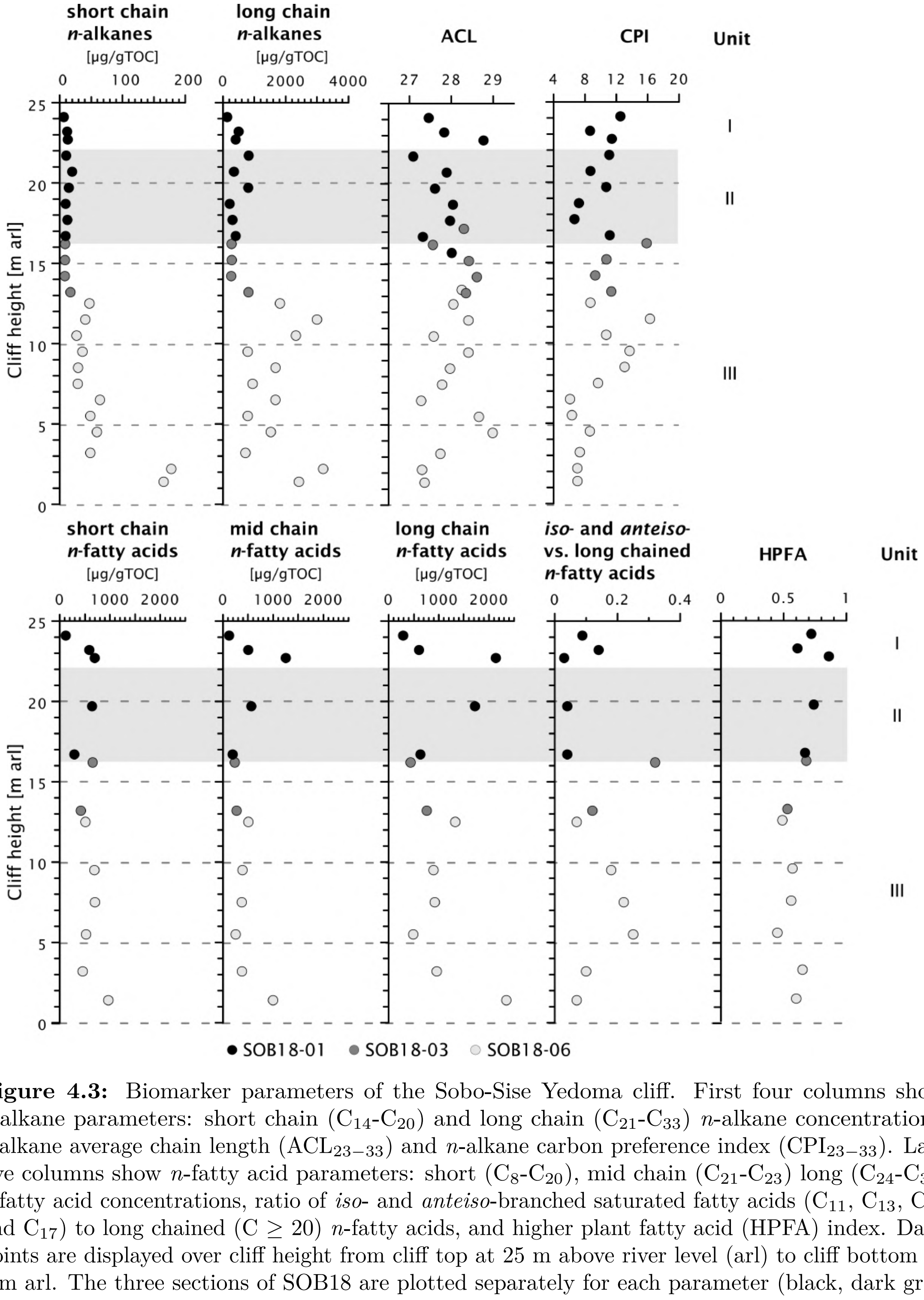

Figure 4.3: Biomarker parameters of the Sobo-Sise Yedoma cliff. First four columns show *n*-alkane parameters: short chain (C_{14}-C_{20}) and long chain (C_{21}-C_{33}) *n*-alkane concentrations, *n*-alkane average chain length (ACL_{23-33}) and *n*-alkane carbon preference index (CPI_{23-33}). Last five columns show *n*-fatty acid parameters: short (C_8-C_{20}), mid chain (C_{21}-C_{23}) long (C_{24}-C_{32}) *n*-fatty acid concentrations, ratio of *iso*- and *anteiso*-branched saturated fatty acids (C_{11}, C_{13}, C_{15} and C_{17}) to long chained ($C \geq 20$) *n*-fatty acids, and higher plant fatty acid (HPFA) index. Data points are displayed over cliff height from cliff top at 25 m above river level (arl) to cliff bottom at 0 m arl. The three sections of SOB18 are plotted separately for each parameter (black, dark grey and light grey circles). Units I, II (grey rectangle) and III correspond to Marine Isotope Stage (MIS) 1 to 3.

4.5.2.2 Fatty acids

We found *n*-FAs with carbon numbers between C_8 and C_{32} and a strong even-over-odd carbon number predominance. Furthermore, hydroxy FAs (C_6 to C_8), *iso*-branched FAs (C_{10} to C_{19}), *anteiso*-branched FAs (C_{11}, C_{12}, C_{13}, C_{15} and C_{17}), monounsaturated FAs (C_{16} to C_{20} and C_{24}), unsaturated *iso*- and *anteiso*-branched FAs (C_{17}), cyclopropyl FAs (C_{17} and C_{19}), di- and triunsaturated FAs (C_{18}) and phytanoic acid were detected (Figure C.2, Table C.2). Concentration of long chain *n*-FAs (C_{24} to- C_{32}) ranged from 290 μg/gTOC at 24.1 m arl to 2346 μg/gTOC at 1.4 m arl (mean: 1041 μg/gTOC, sd: 655). The most abundant long chain *n*-FA was *n*-C_{24} for all samples, except at 16.7 m arl (*n*-C_{26}) (Figure 4.2 and C.2). The mid chain *n*-FA (C_{21} to C_{23}) concentration ranged from 121 to 1250 μg/gTOC (mean: 463 μg/gTOC, sd: 314) and was highest at 22.7 m arl. The short chain *n*-FA concentration (C_8 to C_{20}) ranged from 120 to 968 μg/gTOC (mean: 560 μg/gTOC, sd: 212) and was highest in the bottom sample at 1.4 m arl. Among the short chain FAs, the *n*-C_{16} dominated all samples (Figure C.2). The *iso*- and *anteiso*-branched FAs were more abundant in the bottom section of the cliff and lowest in the middle section and the ratio of *iso*- and *anteiso*-branched saturated fatty acids (C_{11}, C_{13}, C_{15} and C_{17}) to long chained ($C \geq 20$) *n*-FAs range from 0.03 to 0.32 (mean 0.13, sd: 0.09; Figure 4.3 and C.2). The HPFA index had a mean value of 0.63 (sd: 0.11, n=13), a minimum of 0.45 (SOB18-06-17 at 5.5 m arl) and a maximum of 0.86 (SOB18-01-04 at 22.7 m arl) close to the cliff top. Overall, HPFA values below 16 m arl were slightly lower than in the upper section.

4.5.3 Clustering

We identified three main sub-groups using agglomerative hierarchical clustering (Figure 4.4a): unit I from 24.1 to 22.7 m arl (n=3), unit II from 21.7 to 16.7 m arl (n=7) and unit III from 16.2 to 1.4 m arl (n=18). Our clustering matched the three cryostratigraphic units as defined by Wetterich et al. (2020) which further corresponded to MIS 1, MIS 2 and MIS 3 from the top to the bottom. The TOC content (Figure 4.4b) and C/N ratio were significantly highest in unit I and lowest in unit II ($p<0.01$ and $p<0.05$, respectively; Figure 4.2 and Table C.1). The short and long chain *n*-alkane concentration, expressed in μg/gTOC, was higher in unit III, but the differences were only significant for the short chain *n*-alkanes ($p<0.01$) (Figure 4.4c). The short, mid and long-chain *n*-fatty acid concentrations expressed in μg/gTOC did not differ significantly between the units. The ACL and CPI values were similar for each unit (Figure 4.3). The HPFA index was significantly different between the units ($p<0.05$) with highest values in unit I and lowest values in unit II (Figure 4.4d). The share of *iso*- and *anteiso*-branched FAs compared to long *n*-FAs was highest in unit III and lowest in unit II (Figure 4.4e), but the differences were not significant.

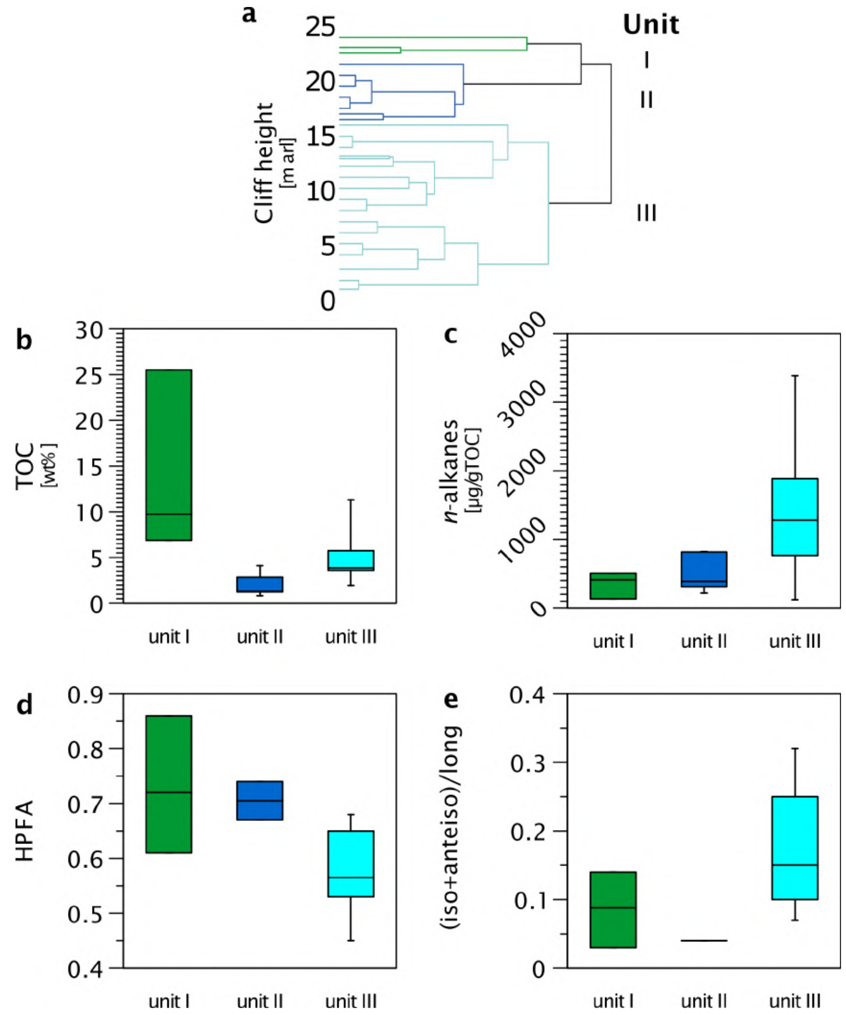

Figure 4.4: Statistical separation of the Sobo-Sise Yedoma cliff profile and selected parameters of the separated cliff units; (a) Clustering of samples with y-axis representing cliff height from cliff top at 25 m above river level (arl) to cliff bottom at 0 m arl. Unit I corresponds to Marine Isotope Stage (MIS) 1, unit II to MIS 2 and unit III to MIS 3. Resulting box plots allow better visualization of OM distribution along the Sobo-Sise Yedoma cliff profile from 25 to 0 m arl, (b) total organic carbon (TOC) content in wt%, (c) n-alkane concentration in μg/gTOC, (d) higher plant fatty acid (HPFA) index and e) ratio of *iso*- and *anteiso*-branched saturated fatty acids (C_{11}, C_{13}, C_{15} and C_{17}) to long chained ($C \geq 20$) n-fatty acids.

4.6 Discussion

4.6.1 Terrestrial depositional environment

4.6.1.1 Organic matter source

We found that the n-alkane distributions were dominated by the long chain n-alkanes ($\geq C_{21}$) and that short chain n-alkanes only play a marginal role (Figure C.1). The most abundant n-alkane homologues in the entire dataset were n-C_{27}, n-C_{29} and n-C_{31}, which indicates that the OM stemmed from higher land plants (Eglinton & Hamilton, 1967). This is confirmed by the dominance of long chain n-FAs (C_{24}-C_{32}) with a strong even over odd carbon number predominance (Figure C.2). The ACL_{23-33} varied around a mean of 28 across the cliff and there were no significant differences between the three units. The relatively high ACL across the cliff (Figure 4.3) further indicates a predominant contribution of vascular plants, which corroborates the pollen record presented by Wetterich et al. (2021). Their results indicated the presence of tundra-steppe vegetation during MIS 3-2, while MIS 1 pollen spectra of the uppermost three samples indicated a shift from tundra-steppe to shrub-tundra vegetation. Occasional warmer-than-today summers were recorded during early MIS 3 as well as the presence of low-center polygons with favorable (stable) aquatic conditions during the MIS 3. Cooler and drier summer conditions as well as unstable (draining and rewetting phases) aquatic conditions were reconstructed for the MIS 2 Wetterich et al. (2021). In our study, the elevated ratio of *iso* and *anteiso*-branched FAs relative to longer chain ($C \geq 20$) *n*-FAs in unit I (MIS 1) and III (MIS 3) compared to unit II (MIS 2; Figure 4.4e and C.2) suggests stronger microbial activity during the warmer MIS 3 and MIS 1 periods (Rilfors et al., 1978; Stapel et al., 2016) and points to a higher input of bacterial biomass during that time. Additionally, we found a significant abundance of short chain FAs especially n-C_{16} in all samples (Figure C.2). However, these FAs are not only common in bacterial but also in eukaryotic microorganisms (Gunstone & Harwood, 2007), and thus represent a mixing signal. Therefore, we focused here on *iso*- and *anteiso* FAs as they are more specific biomarkers for bacterial biomass (Kaneda, 1991).

The source and nature of the OM preserved in permafrost influences both its quantity and quality (Jongejans et al., 2018). TOC, TN, C/N and $\delta^{13}C$ variations result from changes in biomass productivity and/or decomposition, from different OM sources, from changes in depositional conditions influencing OM preservation and from different characteristics of cryosol formation. Generally, enriched $\delta^{13}C$ and low TOC and C/N values, as we found in unit II and III (Figure 4.2), are typical for Yedoma deposits that formed during cold stages (Schirrmeister, 2012). However, climate variations during the last ice age differentiated into warmer interstadials (e.g. MIS 3) and colder stadial periods (e.g. MIS 2) which climatically triggered changes in vegetation and cryosol formation. At the Sobo-Sise Yedoma cliff, the TOC values were higher during MIS 1 and 3 compared to the last Glacial (MIS 2) deposits, suggesting higher OM accumulation, which was presumably triggered by higher biomass production. The TOC values from the MIS 3 and MIS 2 sediments of the Sobo-Sise Yedoma cliff (<0.10-11.31 wt%, mean: 4.01 wt%) were significantly higher ($p<0.01$) than those of other Siberian Yedoma sites (<0.1-27 wt%, mean: 3.0 wt%; 17 study sites, 719 samples) but very similar to data from Kurungnakh Island (mean: 3.8 wt%) which is located about 70 km west-south-west from the Sobo-Sise Island in the central Lena River Delta (Strauss et al., 2020; Strauss et al., 2012a). Likely, the high TOC values in the Sobo-Sise record are a result of past wetter conditions leading to the formation of peat layers. Comparable to the Kurungnakh Island Yedoma record, the Sobo-Sise Yedoma cliff is characterized by silty sediments with multiple layers enriched in peat pointing to paleosol formation during permafrost aggradation. The MIS 3 deposits contained rather less decomposed twigs and grass remains as well as single peaty lenses (15-20 cm in diameter) and peat layers (10-20 cm up to 130 cm thick). A similar occurrence of single twig remains (2-4 mm in diameter), dark brown spots, finely dispersed organic remains, and peaty lenses (5-25 cm in diameter) were found in MIS 2 deposits, while MIS 1 deposits contained much more peaty components, i.e. numerous peaty lenses (2-25 cm in diameter), which was reflected in higher TOC values compared to MIS 3 and MIS 2 deposits (Wetterich et al., 2020).

At 16.2 m arl, we found a peak in TOC (11.31 wt%, SOB18-03-05) and a simultaneously depleted δ^{13}C value (-29.43 ‰). High TOC and low δ^{13}C values have been found to be indicative for peat accumulation and low decomposition under wetter conditions in a more anaerobic regime (Schirrmeister et al., 2011a; Strauss et al., 2012a; Wetterich et al., 2009). These peat layers can form by moss accumulation which is hardly decomposed and/or incorporated soon upon accumulation. From a biomarker perspective, this sample was not much different regarding the biomolecular composition, indicating a similar organic biomass (Figure C.2). The higher relative abundance of long chain *n*-FAs compared to the short chain FAs which might, with all uncertainties, rather represent microbial biomass, may point to less microbial decomposition and better preservation of OM at the time of deposition. Considering paleoenvironmental studies from Kurungnakh Island in the central Lena Delta, paleosol formation was intensified by relatively warm and wet summers during the climate optimum of the interstadial MIS 3 between 40 and 32 kyr BP (Wetterich et al., 2008; Wetterich et al., 2014). Therefore, it is very likely that this layer is a buried paleosol layer containing peaty material.

4.6.1.2 Organic matter quality

OM from different vegetation types was incorporated from the active layer into the permafrost during and after different phases of decomposition. The biogeochemical and biomarker proxies outlined in the previous chapter mainly describe the sources and composition of permafrost OM. In addition, biomarker ratios provide information on the decomposition level of the OM and with that, the potential 'decomposability' (quality) of the respective permafrost OM upon thaw. The OM assessment of this study via agglomerative clustering found overall high OM quality of the Sobo-Sise Yedoma deposits with high CPI values (mean: 9.89) and higher C/N ratios (mean: 13.24) compared to the other Yedoma deposits such as those on the Buor Khaya Peninsula (Central Laptev Sea) with mean C/N values of about 10 Strauss et al. (2015). The elevated C/N value in the top sample of the Sobo-Sise record likely results from the influence of modern plants rooted in the active layer. For the rest of the profile, the C/N ratios were rather uniform. The high CPI in our study is comparable to other Yedoma sites as reported by Strauss et al. (2015) for the Buor Khaya Peninsula (mean 11.6) and Jongejans et al. (2018) for the Baldwin Peninsula (western Alaska; 12.2). At the Sobo-Sise Yedoma cliff, the CPI values scattered around a mean of 9.89 and decreased in the lowermost 7 m of the cliff profile. This could probably indicate a higher level of OM decomposition for the lower cliff part, but can also be influenced by the vegetation type and species prevailing during early MIS 3 with stagnant water and partly warmer-than-today summer climate conditions Wetterich et al. (2020). The HPFA values (0.45-0.86, median: 0.61) are a bit higher compared to Yedoma deposits investigated by Strauss et al. (2015) on Buor Khaya Peninsula (0.15-0.69, median: 0.54). Overall, the HPFA significantly decreased downwards (Figure 4.3; $p<0.05$), which suggests that the OM is further decomposed downwards. This fits to the assumption that there was more time for OM decomposition for the lower, older cliff parts of the paleo active layer. A higher decomposition for the lower cliff part is also supported by the highest ratio of the *iso*- and *anteiso*-branched FAs vs long chain FAs in the MIS 3 deposits and indicating a higher relative amount of microbial biomass and suggesting a higher microbial activity during this warmer interval (Figure 4.4). As outlined above, three stages of permafrost aggradation on Sobo-Sise Island linked to climatic variability were identified according to Strauss et al. (2015). OM preservation during these stages is strongly impacted by the duration of freezing and thawing periods, the associated presence and absence of oxygen in the soil, the related level of microbial activity, and/or physical protection of the OM by the inorganic matrices (e.g., Fe complexation) (**e.g.**; Freeman et al., 2001; Hedges & Keil, 1995; Lützow et al., 2006). As these factors are all closely interlinked, it is almost impossible to decipher the control of these processes on the finally preserved OM biomarker signatures.

4.6.2 Implications and outlook

(Nitzbon et al., 2020) found that terrestrial permafrost-locked OC will be significantly thaw-affected by 2100, and it could be even up to three-fold (twelve-fold) more under warming scenario RCP4.5 (RCP8.5) compared to previous estimates if including thermokarst-inducing processes. Deep OM as characterized in our study can be released by deep disturbance processes such as thermokarst, thermal-erosion or riverbank erosion. Our findings show that freshly thawed and high quality OM is mobilized with annual erosion rates of 15.7 m/yr (2015-18, on the long-term 9 m/yr) (Fuchs et al., 2020). Furthermore, we suggest that the very ice-rich cliff wall sections are not exposed to aerobic conditions for very long time periods before being eroded into the Lena River. Thus, aerobic microbial decomposition of the OM at the cliff front is presumably playing only a minor role. Additionally, cliff erosion is mainly driven by thermo-erosion and niche formation at the base of the ice-rich Yedoma cliff resulting in block-failure instead of slow gradual cliff retreat (Fuchs et al., 2020). Accordingly, some of the OM in the cliff may not even become exposed to the air and thaw at all before being eroded into the river. Fuchs et al. (2020) showed an average loss of 5.2 x 10^6 kg OC and 0.4 x 10^6 kg N per year (2015-2018). For the OC flux sourced from permafrost and peat deposits (and in particular from erosive locations like our study site on Sobo-Sise Island), Wild et al. (2019) estimated 0.9 x 10^8 kg C/yr.

By using a biomarker approach (e.g. *n*-alcohols, *n*-fatty acids, *n*-alkanes) on sub-aquatic sediments, van Dongen et al. (2008) found a greater degree of decomposition of the old terrestrial OM released by the eastern great Arctic rivers, including the Lena River. Thus, they predicted greater remineralization rates and release of carbon dioxide and methane. Our biomarker findings of terrestrial permafrost fit well into this scenario. Winterfeld et al. (2015) studied the lignin phenol composition of the Lena River, Lena Delta and Laptev Sea nearshore zones, and proposed that OM decomposition is considerable after permafrost thawing on land and during transport and sedimentation in the water. The present study on the OM origin and the annual OC erosion rates at the Sobo-Sise Yedoma cliff complements ongoing research on mobilization of permafrost-locked carbon from late Pleistocene Yedoma deposits, while thermal erosion is a widespread and climate-sensitive phenomenon in the Yedoma domain, covering nearly 500,000 km^2 in Siberia and Alaska (Strauss et al., 2021b). This indicates the high potential of thermal erosion for mobilization and release upon thaw of not only large amounts of carbon but also well-preserved OM into the aquatic system of the Lena Delta and nearshore Laptev Sea and Arctic Ocean areas, which will affect local but likely also regional biogeochemical cycles in the marine realm Grotheer et al. (2020), Mann et al. (2021), and Tanski et al. (2021) and the shelf seas. Once mobilized and transported into inland waters, permafrost-derived OC can be rapidly used by aquatic microorganisms, increasing OM decomposition in riverine and coastal Arctic waters (Drake et al., 2015; Mann et al., 2015; Vonk et al., 2013a). In contrast, Bröder et al. (2019) showed that more than half of the carbon transported and deposited on the shelf sea floor likely resists decomposition on a centennial scale, while the rest decays faster, but relatively slowly. In addition, Karlsson et al. (2011) hypothesized that Yedoma OC, associated with mineral-rich matter from coastal erosion, is ballasted and thus quickly settles to the bottom.Nevertheless, the input of suspended sediments and OM might cause reduced light conditions (Klein et al., 2021; Polimene et al., 2022) leading to a reduced photosynthetic uptake of CO_2 (Retamal et al., 2007). The higher CO_2 production in the aquatic systems will lead to higher CO_2 emission, and might further reduce the aragonite saturation of the water (Anderson et al., 2011; Tank et al., 2012). How the different biochemical processes in near-shore waters will interact with ongoing climate change is still largely unknown and will be the subject of intense scientific research in future.

4.7 Conclusion

Sedimentological and biogeochemical analyses showed that the sediments exposed at the Sobo-Sise Yedoma cliff contain a high TOC content (mean 5 wt%) and well-preserved OM (C/N mean 13, mean CPI: 10) in comparison to other Yedoma permafrost sites. Our study corroborated the paleoenvironmental data from the Sobo-Sise Yedoma cliff from previous research which suggested that Yedoma formation during the interstadial MIS 3 and the accumulation of the topmost Holocene deposits (MIS 1) were associated with more microbial activity than during the stadial MIS 2. In addition, our findings suggest that mainly high-quality OM has been freeze-locked perennially into permafrost during the late Pleistocene to Holocene. Biomarker parameters indicate a higher level of OM decomposition for the bottom 7 m of the cliff profile of MIS 3 age and less OM accumulation during MIS 2 in contrast to the warmer MIS 3 and 1 sequences is assumed. At the Sobo-Sise Yedoma cliff, representing an example of rapidly eroding permafrost shorelines in the Lena Delta, OM with a high decomposition potential is being mobilized from almost all sections of the cliff profile. This material is suggested to rapidly enter the fluvial and probably also the offshore aquatic ecosystem. Thus, OM mobilization at the Sobo-Sise Yedoma cliff and similarly eroding permafrost sites bear the potential to impact the carbon dynamics, the biogeochemistry and the riverine and near-shore marine ecosystems.

4.8 Acknowledgements

This study was carried out within the CACOON project and the joint Russian-German expeditions Lena 2018 and Sobo-Sise 2018 supported by the Samoylov Research Station. We thank Michael Fritz (AWI Potsdam) and Aleksey Aksenov (Arctic and Antarctic Research Institute St. Petersburg) for supporting the permafrost sampling on Sobo-Sise in August 2018. We thank Justin Lindemann (AWI Potsdam) and Anke Sobotta (German Research Centre for Geoscience) as well as Hanno Meyer and Mikaela Weiner (AWI-ISOLAB Facility) for support with laboratory analysis.

5

Batagay thaw slump

Between the tusks rise
Tall ice wedges like giants
I stand before them

5 Assessing organic matter characteristics in ancient permafrost: A biogeochemical study at the Batagay megaslump, East Siberia

5.1 Abstract

A recently recognized permafrost thaw feature in NE Siberia - the Batagay megaslump - provides access to ancient permafrost up to about 650 ka old. The headwall of the slump, a vertical cliff up to 55 m high, exposes six stratigraphic units. We sampled material from five of the six units and applied lipid biomarker analysis to obtain insights into the permafrost-locked organic matter (OM) quality and quantities and to deduce paleoenvironmental information on glacial-interglacial time scales. The largest part (45 from 55 m) of the exposed sequences comprises the Lower Ice Complex (Marine Isotope Stage (MIS) 16 or earlier), the Lower Sand Unit (some time between MIS 16-4) and the Upper Ice Complex (MIS 4-2), representing glacial periods. The biomarker data revealed similar biogeochemical signatures for these units, the OM has a terrestrial character, and microbial activity was likely limited. In contrast, the *n*-alkane and fatty acid distributions differed for the Woody Layer (MIS 5), separating the Lower Sand and the Upper Ice Complex, as well as the Holocene Cover (MIS 1), on top of the Upper Ice Complex. The Woody Layer, marking an interglacial permafrost degradation disconformity, contained markers of terrestrial origin (sterols) and high microbial decomposition (*iso*- and *anteiso*-fatty acids). In the Holocene Cover sediments, we identified abundant branched and cyclic alkanes, which are likely of microbial or bacterial origin. This, and the aquatic OM parameter P_{aq} suggest relatively wet depositional conditions. Furthermore, the biomarker data suggest higher OM decomposition for the interglacial periods and a variable but overall better OM quality for the glacial periods. As climate warming will continue permafrost degradation in the Batagay megaslump and in other areas, large amounts of deeply buried, ancient OM with a variable composition and degradability are mobilized, likely significantly enhancing greenhouse gas emissions from permafrost regions.

5.2 Introduction

Rapid warming of the terrestrial Arctic leads to widespread permafrost thaw. This can mobilize organic matter (OM) and results in greenhouse gas (GHG) release, which contributes to the permafrost-carbon climate feedback (Schuur et al., 2015). The global permafrost region contains roughly half of the world's soil carbon (3350 Gt) (Strauss et al., 2021a). The deep permafrost carbon pool (> 3 m) is often not accounted for and its amount is uncertain ($\sim$500 Gt) (Strauss et al., 2021a). While it was estimated that gradual permafrost thaw might contribute up to 208 Gt carbon into the atmosphere until 2300 (McGuire et al., 2018), abrupt permafrost thaw processes, such as the formation of retrogressive thaw slumps and thermokarst development, could contribute an additional 80 ± 19 Gt of carbon to be released into the atmosphere (Turetsky et al., 2020). Abrupt thaw processes occur on local to regional scales and are difficult to capture, which is why they are not yet implemented in climate models.

Retrogressive thaw slumps are a result of slope failure following the thaw of ice-rich permafrost. They develop rapidly and can displace large amounts of ice/water, sediments and OM (Lantuit & Pollard, 2005; Lewkowicz, 1987; Tanski et al., 2017). Thaw slumps typically consist of a nearly vertical headwall, a slump floor and a lobe, and are often situated along rivers or coasts. Triggers for the formation include lateral or thermal erosion by water (Kokelj et al., 2013), active layer detachment following heavy rainfall (Lacelle et al., 2010) and human activity such as road construction, mining or deforestation. Once initiated, thaw slumps can develop very rapidly due to the constant removal of thawed material by meltwater streams, changes in the vegetation and snow cover, and the albedo leading to further intense permafrost degradation.

The Batagay megaslump in East Siberia is the largest known retrogressive thaw slump on Earth (roughly 1.8 km long and 0.9 km wide in 2019) that developed over the last ~5 decades (Kunitsky et al., 2013). The megaslump provides access to ancient permafrost deposits, with stratigraphical discordances, including the second oldest directly dated permafrost in the Northern Hemisphere (Murton et al., 2021). This makes the large slump headwall an ideal target for paleoenvironmental studies, including cryostratigraphy, sedimentology and chronology (Ashastina et al., 2017; Murton et al., 2017; Murton et al., 2021), ground ice stable isotopes (Opel et al., 2019; Vasil'chuk et al., 2020), pollen and plant macro remains (Ashastina et al., 2018) and ancient DNA (Courtin et al., 2022).

The study of lipid biomarkers to characterize permafrost OM has proven useful in previous work (Jongejans et al., 2020a; Jongejans et al., 2018; Stapel et al., 2016; Strauss et al., 2015; Zech et al., 2009). With the present study we aim (1) to explore the source and preservation of biomarkers in permafrost on geologic time scales during several glacial and interglacial periods, and (2) to deduce the past floral and microbial sources of the still preserved OM in order to characterize paleoenvironments of OM deposition. To our knowledge, we present the first OM signatures, i.e. biomarkers preserved in ancient permafrost since about 650 ka.

5.3 Study site

The Batagay megaslump (67.58°N, 134.77°E) close to the village of Batagay is located in the Yana Uplands, part of Yana-Oymyakon mountain region (interior Yakutia; Figure 5.1a). This region is characterized by the most continental climatic conditions of the Northern Hemisphere, manifesting in an extreme climate with a mean winter (December to February) temperature of -40.0 °C, a mean summer (July to August) temperature of 13.7 °C and a mean annual temperature of -12.4 °C (period 1988-2017) (Murton et al., accepted). For the same time period, mean annual precipitation was 203 mm, with mean summer precipitation of 106 mm. Since the mid-20th century, both temperature and precipitation have significantly increased. The permafrost in this region is continuous and ~200 to 500 m thick with mean annual ground temperatures of -8.0 to -5.5 °C (Murton et al., accepted). The seasonally thawed uppermost (active) layer is between 0.2 and 1.2 m thick, depending on vegetation type (Murton et al., accepted). The modern vegetation is dominated by open larch forest (*Larix gmelinii*), and Siberian dwarf pines (*Pinus pumila*) and birch trees (*Betula exilis*, *B. divaricata* and sparse

B. pendula) are common. The ground is covered by a thick layer of lichens and mosses, and almost no grasses and herbs occur (Ashastina et al., 2018; Murton et al., accepted).

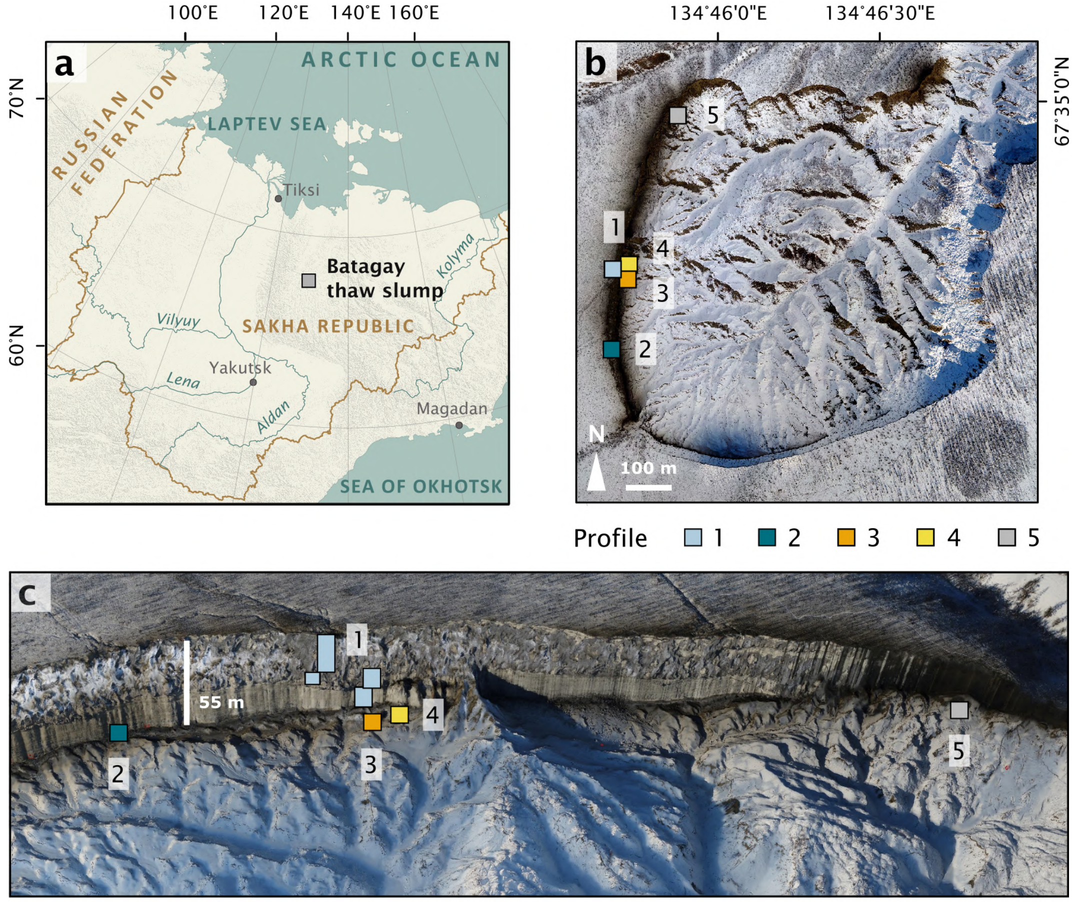

Figure 5.1: Location of the Batagay thaw slump. (a) Overview of Yakutia (Republic Sakha) and location of the Batagay thaw slump (gray square), (b) aerial view of slump with sampling locations profile 1 to 5, and (c) front view of the east-facing headwall. Photos (b, c) from Spring Expedition to Batagay in 2019.

The Batagay megaslump is located on an east-facing hillslope and has developed after anthropogenic disturbance of the protective vegetation cover in the middle of the 20th century (Kunitsky et al., 2013; Murton et al., accepted). A gully formed in the 1960s that grew progressively wider and deeper, and developed into a retrogressive thaw slump. In spring 2019, the slump diameter, which was determined using a UAV survey (Jongejans et al., 2021g), was about 890 m. Grow rates are fast with spatially and temporally varying headwall retreat rates of 7 up to 30 m y^{-1} (Günther et al., 2015; Kunitsky et al., 2013; Vadakkedath et al., 2020). The ~55 m high headwall and the slopes of the slump provide access to stratigraphically discontinuous ancient permafrost deposits since the Middle Pleistocene (Murton et al., 2021). The headwall consists of six stratigraphical units from the bottom to the top: the Lower Ice Complex (Marine Isotope Stage (MIS) 16 or earlier), the Lower Sand Unit (some time between MIS 16 and 4), the Woody Layer (MIS 5) which was present as lenses up to 3 m thick, the Upper Ice Complex (MIS 4-2) also called Yedoma, the Upper Sand Unit (MIS 3-2) and the Holocene Cover on top (MIS 1) (Ashastina et al., 2017; Murton et al., 2021). It should be noted that there are large hiatuses (marked by erosional surfaces below and above the Lower Sand) and dating uncertainties in the chronostratigraphy (Murton et al., 2021). While the ancient permafrost buried deep in the ground has survived multiple interglacials, the region has been subject to repeated permafrost thaw and sediment removal by thermo-erosional processes, amplified in recent decades.

5.4 Methods

5.4.1 Sample collection

The slump headwall was sampled during the Spring Expedition to Batagay in March and April 2019 (Figure 5.1b and c) (Jongejans et al., 2021g). The samples were taken by rappelling with a rope from the top of the slump headwall to each sample location and then using a hole saw (diameter: 57 mm, 40 mm deep) mounted on a hand-held power drill to sample small horizontal cores of frozen sediments exposed in the headwall. Sample depth is given in meters below the surface (m bs) (Figure D.1). At each sampled depth, three cores were taken next to each other for biomarker, sedimentological and ancient DNA analyses. Sampling resolution was 0.5 m in the top 10 m and 1 m below. Due to the presence of large ice wedges, profile 1 consisted of 4 sub-profiles (Figure 5.1c). Using a hammer, axe and a chainsaw, more profiles were sampled at the lower part of the headwall from the slump bottom (profile 2), as well as at two large permafrost blocks at the slump bottom that have fallen from the headwall (profile 3 and 4), and at a baidzherakh (thermokarst mound) in the north of the slump (profile 5) (Figure 5.1b and c). All samples were stored in sterilized glass jars and kept frozen until laboratory analyses at AWI Potsdam. 30 samples (19 from profile 1, five from profile 2, and two each from profile 3, 4 and 5) were selected for biomarker analysis. With these profiles, we covered five of the six stratigraphical units (all but the Upper Sand Unit which is not exposed in the central headwall). As we have no detailed sample depth information from the blocks and the baidzherakh, we report the results according to the respective stratigraphic units.

5.4.2 Laboratory analyses

The samples were freeze-dried and after homogenization of the samples, the total carbon (TC) and total organic carbon (TOC) content, as well as the total nitrogen (TN) content were measured (Elementar Vario EL III and Elementar Vario Max C) and expressed in wt%.

Samples were treated for biomarker analysis as described by Jongejans et al. (2021f): after extraction of the OM (Dionex ASE 350) and removal of asphaltenes, four internal standards were added and the extracts were separated by medium pressure liquid chromatography into an aliphatic, aromatic and polar NSO (nitrogen, sulfur and oxygen-containing) fraction. We selected 10 samples for further separation of the NSO fraction into an acid and neutral polar fraction using a KOH-impregnated silica gel column (Schulte et al., 2000). This sample selection was based on the biogeochemical and alkane parameters, as well as to cover the entire profile.

We measured alkanes, fatty acids and alcohols using a TRACE 1310 Gas Chromatograph coupled to a TSQ 9000 Mass Spectrometer (Thermo Scientific), following the same method and settings as Jongejans et al. (2021f). Prior to the measurements, the fatty acid fraction was methylated using diazomethane and the alcohol fraction was silylated using N-methyl-N-(trimethylsilyl)trifluoroacetamide (MSTFA). We quantified the compounds relative to the internal standards from full scan mass spectra (m/z 50-600 Da, 2.5 scans s^{-1}) using the software XCalibur.

We calculated indices from the *n*-alkane and *n*-fatty acid concentrations (Table 5.1) to obtain insights into OM origin and preservation: the average chain length (ACL), the proxy for aquatic OM (P_{aq}), the carbon preference index (CPI), the ratio of *iso*- and *anteiso*-branched to long FAs (IA) and the higher-plants fatty acid (HPFA) index. The ACL can be used as an indicator of OM source, where long-chain *n*-alkanes (>25) are mostly produced by terrestrial higher plants (Ficken et al., 1998; Poynter & Eglinton, 1990; Zech et al., 2009). The P_{aq} shows the share of OM derived from aquatic plants, which are thought to contain relatively more C_{23} and C_{25} *n*-alkanes - compared to terrestrial plants which generally have longer chains (Ficken et al., 2000). The CPI expresses the ratio of the odd over even *n*-alkane chains and decreases with OM decomposition (Marzi et al., 1993). We calculated the IA using the *iso*- and *anteiso*-branched FAs C_{15} and C_{17}. These FAs are of microbial origin and are thought to reflect changes in the depositional regime, where a higher ratio may correspond to microbial membrane adaptation with respect to warmer environmental conditions (Rilfors et al., 1978; Stapel et al., 2016). Finally, the HPFA index was used to indicate the level of OM degradation: due to the presence of the polar carboxyl group, FAs are more vulnerable to biological and chemical degradation (Killops & Killops, 2013) compared to respective *n*-alkanes, leading to decreased HPFA values with decomposition.

Acronym	**Proxy**	**Equation**
ACL	Average chain length of *n*-alkanes	$ACL_{23-33} = \frac{\Sigma\, i\, C_i}{\Sigma\, C_i}$
P_{aq}	Aquatic organic matter proxy of *n*-alkanes	$P_{aq} = \frac{C_{23}+C_{25}}{C_{23}+C_{25}+C_{29}+C_{31}}$
CPI	Carbon preference index of *n*-alkanes	$CPI_{23-33} = \frac{\Sigma\, odd\, C_{23-31} + odd\, C_{25-33}}{2\, \Sigma\, even\, C_{24-32}}$
IA	*Iso*- and *anteiso*-C_{15} and C_{17} FAs vs. long *n*-FAs	$IA = \frac{iso+anteiso}{long\, n-FAs}$
HPFA	Higher-plant fatty-acid: even *n*-FAs and odd *n*-alkanes	$HPFA = \frac{\Sigma\, n-FA\, C_{24-28}}{\Sigma\, n-FA\, C_{24-28} + n-alkane\, C_{27-31}}$

Table 5.1: Overview of the main biomarker proxies. Acronyms and equations of calculated indices from *n*-alkane concentrations

5.5 Results

5.5.1 Detected biomolecules

We measured hydrocarbons in 30 samples. These compounds comprised short ($< C_{20}$) and long chain *n*-alkanes (C_{20} to C_{33}), alkylcyclohexanes (C_{17} to C_{25}), alkylcyclopentanes (even carbon numbered from C_{18} to C_{24}), methylalkanes (C_{19} to C_{25}), as well as diethylalkanes and ethyl-methylalkanes (C_{19} to C_{25}) (Figure D.2). The concentrations of the branched (methylalkanes, diethylalkanes and ethyl-methylalkanes) and cyclic (alkylcyclohexanes and alkylcyclopentanes) alkanes strongly correlate with each other (R: 0.97 to 0.99, $p<0.01$).

Additionally, we measured FA concentrations of 10 samples. However, the acid fraction of the uppermost sample (0.2 m) contained a plastic contamination and coelutions with FAs prevented the quantification of FAs in this sample. Overall, normal fatty acids (*n*-C_{12} to C_{34}), *iso*-branched FAs (*iso*-C_{14} to C_{17}), *anteiso*-branched FAs (*ai*-C_{15} to C_{17}), saturated branched FAs (10-Me16, 10-Me17, 10-Me18, 12-Me18), monounsaturated FAs (16:17, 16:15, 18:19, 18:17, 19:1, 20:19), a polyunsaturated FA (18:26-9), FAs with a cyclopropyl ring (cycl-17:0, cycl-19:0), hydroxyl FAs (22-OH, 24-OH) and phytanoic acid were found. In the neutral polar fraction, a homologous series of *n*-alcohols as well as sterols and triterpenoids were detected.

5.5.2 Lower Ice Complex

This lowermost exposed sediment sequence consisted mostly of sandy silt to silty sand. The Lower Ice Complex (profile 2: 53.1-52.0 m bs) contained partly truncated ice wedges and composite wedges. A reddish erosional layer containing gravel marked the top of the Lower Ice Complex. In places, a similar layer cuts through the Lower Ice Complex at an angle. We found pool ice and wooden remains. The TOC (0.69-0.83 wt%) and the TN (0.10-0.11 wt%) were very low in this unit (Figure 5.2 and D.1) and the C/N ratio ranged from 6.4 to 7.5. The concentrations of short *n*-alkanes (47-75 μg g^{-1} TOC), long *n*-alkanes (213-405 μg g^{-1} TOC) and branched and cyclic alkanes (46-161 μg g^{-1} TOC) were also quite low in this unit. The ACL ranged between 28.5 and 29.2, and the P_{aq} from 0.14 to 0.23. The CPI varied between 6.4 and 7.6. The main fatty acids were the *n*-fatty acids (*n*-FAs). The short and long chain *n*-FA concentrations were 163 and 610 μg g^{-1} TOC in this unit, respectively (Figure 5.3 and D.2). The IA index was very low (0.03) and the HPFA index was comparably high (0.67).

5.5.3 Lower Sand Unit

The Lower Sand Unit (profile 2: 51.5-51.0 m bs; profile 1: 49.4-38.4 m bs; one sample of profile 4) was characterized by narrow chimney-like composite ice-sand wedges. The TOC was higher (0.65 to 1.36 wt%) compared to the Lower Ice Complex, and the TN was comparably low (<0.10-0.13 wt%). The C/N ratio ranged from 7.6 to 10.8; it could only be calculated for the samples with a TOC and TN content above the detection limit. The alkane concentrations ranged between 13 and 145 μg g^{-1} TOC for the short *n*-alkanes, 140 to 1329 μg g^{-1} TOC for the long *n*-alkanes and between 41 and 553 μg g^{-1} TOC for the branched and cyclic alkanes. The ACL and P_{aq} ranged from 28.6 to 29.2 and 0.11 to 0.20, respectively. The CPI ranged between 7.2 and 11.5. The concentrations of short chain *n*-FAs spanned a large range from 130 to 432 μg g^{-1} TOC and the long *n*-FAs ranged from 214 to 447 μg g^{-1} TOC. The IA was on the low end (0.04 to 0.08) and the HPFA index was between 0.18 and 0.58.

5.5.4 Woody Layer

The Woody Layer (profile 1: 33.5-31.7 m bs; one sample each of profiles 3 and 4) was present in lenses up to 3 m thick. This debris layer was abundant in organic remains, peat lenses, roots, and wood. The TOC (1.47 to 4.93 wt%) and TN (0.12 to 0.40 wt%), as well as the C/N ratio (12.4 to 16.7) were highest in this unit. Here, the short *n*-alkanes, branched and cyclic alkanes were scarce (13-71 and 16-132 μg g^{-1} TOC, respectively; Figure D.2), but the

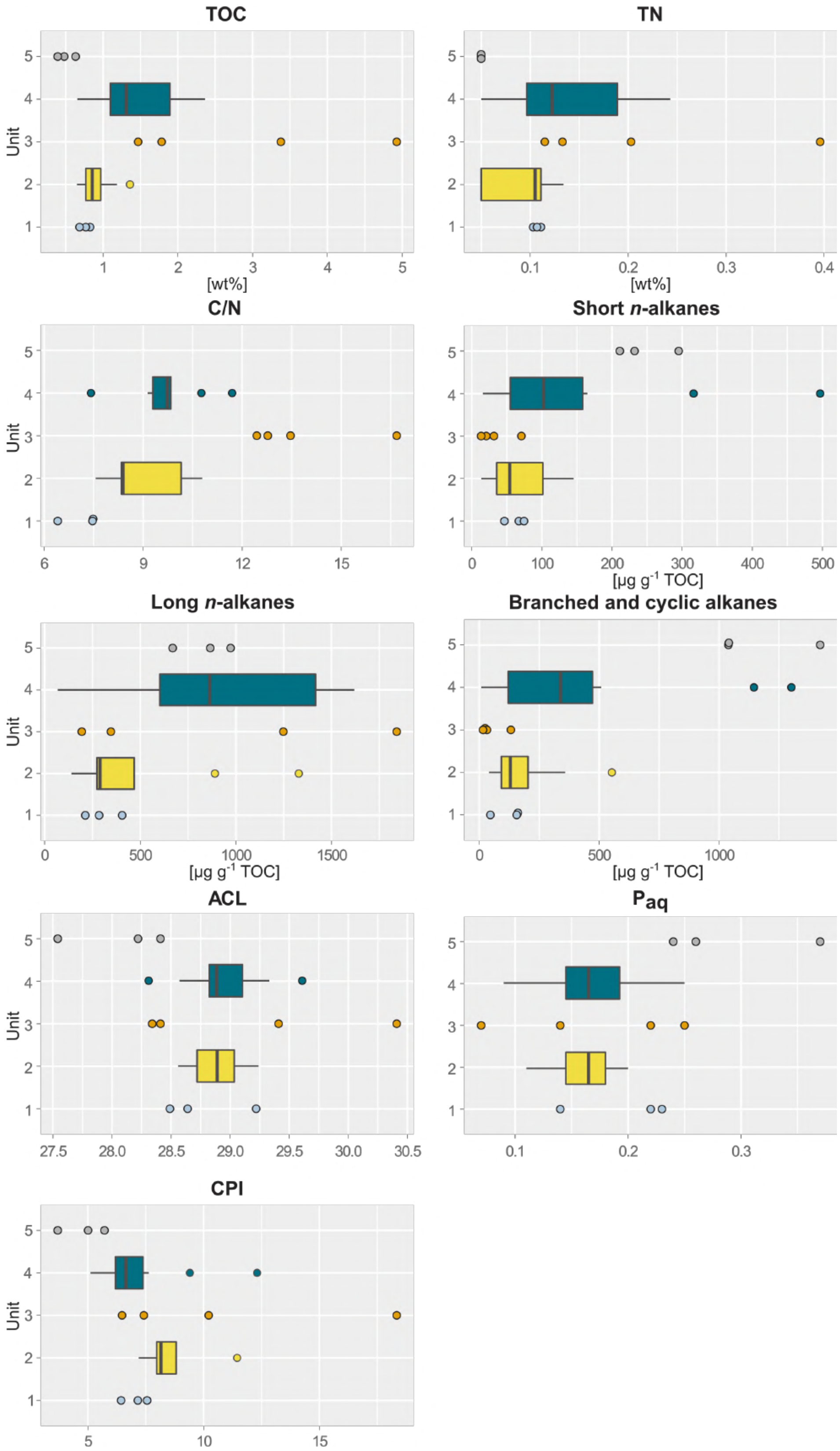

Figure 5.2: Boxplots of biogeochemical and alkane parameters of sediment samples taken from five different profile units of the main headwall of the Batagay megaslump. From left to right and top to bottom: total organic carbon content (TOC), total nitrogen content (TN), carbon to nitrogen ratio (C/N), short chain *n*-alkane concentration, long chain *n*-alkane concentration, concentration of branched and cyclic alkanes combined, average chain length of *n*-alkanes (ACL), aquatic organic matter proxy P_{aq}, and carbon preference index (CPI). 1. Lower Ice Complex (n=3), 2. Lower Sand Unit (n=12), 3. Woody Layer (n=4), 4. Upper Ice Complex (n=8), 5. Holocene Cover (n=3). For units with <5 samples, beeswarm plots are shown instead of boxplots.

Figure 5.3: Beeswarm plots of fatty acid concentrations of sediment samples of the main headwall of the Batagay megaslump. From left to right and top to bottom: short *n*-fatty acid (FA) concentration, long *n*-fatty acid concentration, ratio of *iso*- and *anteiso*-FA C_{15} and C_{17} vs. long FAs (IA index) and higher-plants fatty acid (HPFA) index. Units: 1. Lower Ice Complex (n=1), 2. Lower Sand Unit (n=3), 3. Woody Layer (n=1), 4. Upper Ice Complex (n=4).

long chain *n*-alkanes covered a large range (194-1841 μg g^{-1} TOC). The ACL (28.3-30.4) had its maximum in this unit and the P_{aq} (0.07-0.25) its minimum (both at 31.7 m bs in profile 1). The CPI was moderate to high (6.5 to 18.3). In this unit, we analyzed the neutral fraction of one sample: the sample at 31.7 m bs from profile 1. In this sample, the *iso*- and *anteiso*-FAs (as well as the unsaturated FAs) were most abundant (Figure D.3) and therefore, the IA value was the highest (0.41). The FA concentrations were 328 μg g^{-1} TOC for the short and 313 μg g^{-1} TOC for the long chain *n*-FAs. The HPFA index was very low (0.09). Furthermore, we found many different sterols and triterpenoids in this sample (Table 5.2). The gas chromatogram and molecular structures can be found in the supplements (Figures D.4 and D.5). In the samples from the other units (n=9), we found only the sterols campesterol and β-sitosterol.

5.5.5 Upper Ice Complex - Yedoma

Above, the Upper Ice Complex (profile 1: 30.7-4.2 m bs; one sample of profile 3; profile 5) contained large (up to a few meters wide) syngenetic ice wedges. The TOC (0.66-2.36 wt%) and TN (<0.10-0.24 wt%) contents were medium high compared to the other units. The C/N values (7.4-11.7) were very similar to those of the Lower Sand Unit. Alkane concentrations spanned a wide range in the Upper Ice Complex: 16-497 μg g^{-1} TOC for the short chain *n*-alkanes, 68-1620 μg g^{-1} TOC for the long *n*-alkanes and 8-1302 μg g^{-1} TOC for the branched and cyclic alkanes. The ACL and P_{aq} spanned quite a wide range (28.6 to 29.2 and 0.11 to 0.20, respectively). The CPI was low to moderate in this unit (5.11 to 12.3). The *n*-FA concentrations were also quite variable with the short chain *n*-FAs ranging between 144 and 262 μg g^{-1} TOC and the long chain *n*-FAs between 294 and 666 μg g^{-1} TOC. The IA index was very low (0.03 to 0.05) and the HPFA index low to medium (0.13 to 0.36).

5.5.6 Holocene Cover

The Holocene Cover Unit (profile 1: 2.0-0.2 m bs) seemed quite organic-rich and contained a variety of cryostructures (e.g., massive, porphyric, basal, belt-like and layered). Nevertheless, the TOC (0.39 to 0.63 wt%) and TN (< 0.10 wt%) values were very low. Due to the TN values below the detection limit, we could not calculate the C/N values of this unit. Especially the branched and cyclic alkanes were very abundant (1039-1422 μg g^{-1} TOC), whereas the short (211-295 μg g^{-1} TOC) and long chain *n*-alkanes (669-972 μg g^{-1} TOC) were medium high. The ACL (27.5-28.4) was lowest in this unit and the P_{aq} the highest (0.24-0.37) in all profiles. The CPI was also lowest and ranged from 3.7 to 5.7.

No.	Trivial name	Full name	Ret. time [min]	Class
1	Cholesterol	Cholest-5-en-3β-ol	89.55	1
2	Cholestanol	5α(H)-Cholestan-3β-ol	89.87	2
3	Brassicasterol	24-Methylcholesta-5,22-dien-3β-ol	90.50	1
4	Campesterol	24-Methylcholest-5-en-3β-ol	92.15	1
5	Stigmasterol	24-Ethylcholesta-5,22-dien-3β-ol	92.71	1
6	β-Sitosterol	24-Ethylcholest-5-en-3β-ol	94.60	1
7	Stigmastanol	24-Ethylcholestan-3β-ol	94.96	2
8	β-Amyrin	Olean-12-en-3β-ol	95.77	3
9	Stigmastenol	24-Ethylcholest-7-en-3β-ol	96.55	1
10	α-Amyrin	Urs-12-en-3β-ol	97.29	3
11	Oleanenone	Olean-12-en-3-one	97.77	3
12	Stigmadienone	24-Ethylcholesta-3,5-dien-7-one	98.41	1
13	Stigmastenone	24-Ethylcholest-4-en-3-one	99.73	1
14	Lupeol	Lup-20(29)-en-3β-ol	100.37	3

Table 5.2: Identified sterols and triterpenoids in sediments in the Woody Layer at 31.7 m bs (profile 1) of the Batagay megaslump. The chemical structures are shown in Figure D.5. Classes: 1. stenol, 2. stanol, 3. triterpenoid.

5.6 Discussion

Variations in the TOC contents and fossil biomolecule concentrations along a depositional succession provide insights into quantitative differences of the OM deposited in sedimentary layers deposited over time. These differences are mainly caused by changes in the depositional regime (e.g., water availability, temperature, accumulation rates), the associated bioproductivity (autochthonous signal) and transport processes of the OM (allochthonous signal). Additionally, qualitative variations of the fossil biomolecules can give insight into different OM sources. Indicative biomarkers are a useful tool in these old sediments, as they are generally very well preserved in sediments, even on geological timescales, compared to for example proteins and DNA.

5.6.1 Biogeochemical legacy of glacial periods

In the Batagay dataset, we found generally only minor variations in the biogeochemical and biomarker parameters for the Lower Ice Complex, Lower Sand Unit and Upper Ice Complex. This suggests that the OM signal representing permafrost deposits since about 650 ka is qualitatively and to some extent also quantitatively similar, suggesting that vegetation patterns might have been similar over time in glacial periods. These observations fit well with the paleo-vegetation records of Ashastina et al. (2018). They found that meadow-steppe vegetation persisted throughout most of the reconstructed period (i.e., Lower Sand Unit and Upper Ice Complex) and argued that fossil plant macro-remains mirror mostly changes in the relative abundance of plant communities rather than complete changes in plant species compositions over time (Ashastina et al., 2018). Such relative quantitative variations in the vegetation might be responsible for the observed variability in individual biomolecule markers (e.g., *n*-alkanes and FAs).

The general high ACL and low P_{aq} in these units indicate a less aquatic and more terrestrial character of the OM in these deposits. This corroborates the strong continentality and dry conditions, especially during the cold stages, as found by isotopic and paleoecological analyses (Ashastina et al., 2018; Opel et al., 2019). The relatively low IA index presumably points to lower microbial activity during the glacial periods.

Cryostratigraphic observations and isotopic findings suggest that the Lower Ice Complex sediments might have been deposited under relatively wet conditions providing enough snowmelt water to form huge ice wedges (Opel et al., 2019). These findings suggest that these sediments were formed during a glacial period. In contrast, shotgun DNA analyses from samples taken in 2017 close to the erosional surface above the Lower Ice Complex point to an interglacial origin of the deposited OM (Courtin et al., 2022). Furthermore, they found signs for strong microbial activity related to soil decomposition. Pollen findings (A. Andreev, unpublished data) of the same samples from the Lower Ice Complex at its transition into the above-lying erosional surface point to woodland and steppe vegetation, characteristic of an interglacial period that might have induced thermo-erosion and permafrost thaw that partly degraded the Lower Ice Complex from above. In contrast to this transition layer, the samples of the underlying Lower Ice Complex taken in 2019 cover the entire exposed sequence and our biochemical and biomarker results do not differ for the Lower Ice Complex, the Lower Sand and the Upper Ice Complex. Therefore, we assume that all three sequences formed during glacial periods. Moreover, we found relatively low values for the IA index in the Lower Ice Complex deposits, suggesting low microbial activity. Possibly the samples from the Lower Ice Complex (2017 and 2019) represent a transition from a glacial into an interglacial period of which the latter is represented in the erosional surface topping the Lower Ice Complex. In any case, the complicated permafrost formation and degradation history might also explain the mixed signal in the OM: the C/N ratio and HPFA index show opposite results for the Lower Ice Complex. The high HPFA index might be influenced by the high long *n*-FA concentration. The low C/N could point to the deposition of older transported OM. The CPI was strongly correlated with the ACL (R: 0.74, $p<0.01$) and P_{aq} (R: -0.70, $p<0.01$) across all units. This suggests that the CPI is highly influenced by the OM source and therefore, its use as an OM quality indicator might be restricted. However, general CPI values above 5 might indicate that the

OM is still of relatively good quality. A deeper insight on the quality might be provided by the FA concentrations as they are indicators for more labile biomolecules. The FA data show quite variable values within the individual glacial periods (Figure 5.2). In addition to a mixed OM source, this might also indicate a heterogenous level of OM decomposition, which is supported also by variable HPFA values. Thus, the data point to an overall variable OM quality in the glacial deposits.

The occurrence of narrow composite sand-ice wedges in the Lower Sand Unit compared to the large ice-wedges in both Ice Complex units suggests very high accumulation rates in the Lower Sand Unit. Furthermore, there was likely more snowmelt water available during the Ice Complex formation that allowed the formation of huge ice wedges as present in the Lower and the Upper Ice Complex units. Nevertheless, these changes in available winter moisture are not reflected in the biomarker record of the e.g. ACL and P_{aq} values.

5.6.2 Biogeochemical legacy of interglacial periods

In contrast, the Woody Layer and the Holocene Cover differ in biogeochemical and biomarker parameters from the other stratigraphic units. Compared to the glacial units, we found distinct differences in the *n*-alkane and FA distribution for the Holocene Cover and the Woody Layer, but also some specific biomarkers in these sediments such as branched and cyclic alkanes, stenols, stanols and pentacyclic triterpenoids. We discuss the characteristics of the OM in these sediments, and the sources and implications of these compounds in the Woody Layer and the Holocene Cover below.

The Woody Layer samples show a wide variability among all determined biogeochemical and biomolecular parameters indicating a layer of high inhomogeneity. Variable but overall higher TOC contents point to a high OM accumulation in this layer, and compared to the other units, higher C/N and ACL_{23-33} suggest a strong terrestrial character of the deposited OM. However, a variable input of aquatic organic biomass is indicated by the P_{aq} index. The stronger OM accumulation could result from higher productivity as typical for warmer conditions during interglacial periods. However, the fact that the Woody Layer marks a disconformity related to massive permafrost degradation and erosion suggests that the OM can also stem from remobilization of older material, redistribution, and accumulation in erosional forms.

The sediments of the Woody Layer had a distinctly different *n*-alkane and FA distribution compared to the other studied sediment units. The Woody Layer almost completely lacked the short *n*-alkanes, and branched and cyclic alkanes, and the high ACL and low P_{aq} suggest drier conditions (Ficken et al., 1998; Ficken et al., 2000). Apart from the distinct *n*-alkane and fatty acid distribution, the sediments from the Woody Layer (sample at 31.7 m in profile 1) also contained specific stenols, stanols and pentacyclic triterpenoids. While it is thought that C_{27} and C_{28} sterols dominate in algae and zooplankton, C_{29} sterols are generally abundant in vascular plants (Volkman, 1986). Furthermore, many of the compounds identified in the Batagay sediments were found to be typical for higher land plants: campesterol, stigmasterol, β-sitosterol, stigmastanol, β-amyrin, α-amyrin, oleanenone and lupeol (Brassell et al., 1983; Killops & Killops, 2013; Peters et al., 2005). The presence of these markers point to a strong terrestrial signal of OM, which is corroborated by the high ACL and lower P_{aq} values in the Woody Layer sediments.

The Woody Layer accumulated in an erosional gully, which is indicated by the presence of organic-rich lenses and abundant trash-wood in the headwall. Similar “forest beds” that were associated with the Last Interglacial were found in non-glaciated Yukon and Alaska (Hamilton & Brigham-Grette, 1991; Reyes et al., 2010). In the Woody Layer, a mixture of different autochthonous and allochthonous organic biomass was transported and accumulated. Thermo-erosional processes such as the formation of gullies (the combined mechanical and thermal action of moving water) (Van Everdingen, 2005), is associated with running or standing water that can transport sediments and organic remains. However, aquatic markers are only present in minor abundance but might be represented by short chain FAs and sterols such as brassicasterol (Killops & Killops, 2013). In addition, Ashastina et al. (2018) reconstructed dry conditions during the Last Interglacial with a herb-rich light coniferous taiga and a pronounced plant litter cover. Furthermore, they found that plant and insect species composition pointed to frequent fire disturbances in the Last Interglacial. The high abundance of *iso*- and *anteiso*-FAs (IA index) as well as high amounts of branched and unsaturated short chain FAs (Figure D.3) suggests increased microbial activity for this interval (Stapel et al., 2016). Together with the low HPFA index, this indicates an increased level of microbial transformation of the OM, and thus a lower quality of the OM in the Woody Layer.

In the Holocene Cover sediments, the relatively low ACL and high P_{aq} values suggest an increasing amount of the growth of aquatic plants formed under wet conditions (Ficken et al., 1998; Ficken et al., 2000). In the sediments of the Holocene Cover and some samples from the Upper Ice Complex, the short *n*-alkanes were abundant. Especially, in these sediments, we found the presence of branched and cyclic alkanes. The branched alkanes, among which are the diethylalkanes and the ethyl-methylalkanes, have one or two quaternary carbon atoms (branched aliphatic alkanes with a quaternary substituted carbon atom: BAQCs). Kenig et al. (2005) argued that the BAQCs are widespread in sediments and sedimentary rocks due to their low biodegradability, but were not identified often or misidentified before. The source of these, as well as of the cyclic alkanes (alkylcyclohexanes and alkylcyclopentanes) and methylalkanes, has been a topic of debate (**e.g.**; Greenwood et al., 2004; Kenig et al., 2005; Shiea et al., 1990). The strong positive correlation ($R>0.97$) between the concentrations of the BAQCs and cyclic alkanes suggests similar sources for these compounds. Previous studies also found the co-occurrence of these compounds (**e.g.**; Kenig et al., 2005; Ogihara & Ishiwatari, 1998). Several studies proposed a microbial or bacterial origin, such as cyanobacteria (Shiea et al., 1990), non-photosynthetic sulfidic oxidizing bacteria (Kenig et al., 2003), thermophilic acidophilic bacteria (Ogihara & Ishiwatari, 1998) or microbes exploiting redox gradients or that are involved in either the sulfur or nitrogen cycle (Greenwood et al., 2004). Zhang et al. (2014) stated that the long-chain cyclic alkanes are produced by the reduction of FAs. Cyanobacteria could have been present in polygonal ponds, running water or even in liquid pore water. However, we did not find a correlation with concentrations of certain FAs that are major components produced by cyanobacteria such as 16:0, $16{:}1\omega7$ and $18{:}1\omega9$ (Piorreck et al., 1984). Nevertheless, these FAs are not very specific and thus can be a signal of different sources preventing a direct correlation to the alkylated and cyclic alkanes. A plastic contamination was also proposed as the source of BAQCs by Brocks et al. (2008), but we would expect that previous studies where sediment samples were prepared in a similar way would have found these compounds as well (**e.g.**; Jongejans et al., 2021f; Jongejans et al., 2020a; Jongejans et al., 2018; Strauss et al., 2015). Further, a petroleum contamination can be ruled out as we did not find corresponding oil-related geothermally transformed compounds such as hopanes and steranes. Further research is needed to be able to reduce the amount of possible sources. Generally, we assume a microbial or bacterial origin for the branched and cyclic alkanes. This is corroborated by the strong positive correlation between the branched and cyclic alkanes, and the short *n*-alkanes (R: 0.90, $p<0.01$). Also, even though the correlation was not significant when looking at the complete sample set, higher concentrations of branched and cyclic alkanes did match lower ACL and higher P_{aq} values. These findings suggest that these alkanes are also produced under relatively warmer and wetter conditions which fits the Holocene origin of these samples very well. The low TOC contents and lowest CPI values suggest a higher degradation level and thus lower quality for the Holocene OM.

Altogether, it would be expected that there is a distinct difference between the Upper Ice Complex and the Holocene Cover. Still, it is likely that the uppermost part of the Upper Ice Complex was degraded during the Holocene. This might have led to a rather gradual transition of the biogeochemical and biomarker parameters within the Holocene Cover sediments and into the Upper Ice Complex.

5.6.3 Modern organic matter mobilization in the Batagay megaslump

Using satellite imagery, Vadakkedath et al. (2020) analyzed the expansion of the thaw slump for the past three decades (1991-2018) and found increasing expansion rates over time with a mean of 2.6 ha y^{-1}. This means that an enormous amount of sediments and OM is mobilized every year. Following the thaw of the ice-rich sediments (especially of the Lower and Upper Ice Complex units), the mobilized material can be transported by the meltwater rapidly downslope through a gully network into the Batagay River and further into the Yana River. The OM in these sediments can be decomposed by microbes upon thaw, leading to greenhouse gas emission from the sediments directly (Vonk et al., 2013b) or from the river.

Intense permafrost thaw occurred during interglacials and we found stratigraphic discordances above the Lower Ice Complex, the Lower Sand Unit and the Lower Ice Complex. Nevertheless, the presence of large ice wedges in the Lower Ice Complex and the Upper Ice Complex and composite wedges in the Lower Sand Unit, suggests that the sediments that are still exposed in the Batagay megaslump were affected only in their upper parts and remained largely undisturbed. Hence, OM decomposition was presumably limited. Previous studies showed the high lability of OM in permafrost and especially in the MIS 4-2 Yedoma Ice Complex sediments (Jongejans et al., 2021f; Vonk et al., 2013b). Although the biomarkers indicate variable OM quality for the different sedimentary intervals, we expect that still a large amount of biodegradable OM is mobilized from the Batagay thaw slump every thawing season. The increased formation of retrogressive thaw slumps that has been observed over the past decades in many arctic regions (**e.g.**; Lacelle et al., 2010), is likely to continue with ongoing climate warming, and the mobilization of large amounts of previously frozen sediments and OM likely will lead to higher GHG release from thawing permafrost (Mann et al., 2021).

5.7 Conclusion

Biogeochemical analyses provide valuable information on past environments. Here, for the first time ancient permafrost that formed since about 650 ka ago in NE Siberia was studied for carbon and nitrogen contents, and lipid biomarker characteristics. Our findings show that there was no substantial vegetation change of prevailing meadow steppe over large glacial periods during MIS 16, some time between MIS 16 and MIS 4, and MIS 4-2, which are represented in the exposed strata of the Batagay megaslump by the Lower Ice Complex, Lower Sand Unit and the Upper Ice Complex, respectively. The interglacial Woody Layer (MIS 5), a layer of eroded and accumulated material, showed a highly terrestrial character and strong microbial decomposition. In the Holocene Cover, we found relatively wet depositional conditions. For the interglacial periods, the biomolecule inventory indicates a higher microbial OM transformation and thus a decreased OM quality. In contrast, in the glacial periods a variable but overall higher OM quality is suggested by the biomolecules compared to the interglacial periods. Thus, microbial decomposition was likely limited during the glacial periods. Therefore, a substantial amount of less decomposed OM is mobilized in the Batagay thaw slump every year, in particular since the thaw slump process allows access to deeply buried OM.

5.8 Acknowledgements

We would like to thank Dmitry Ukhin for his support in sample collection, and Ilya Kozhenikov and Stepan Vasiliev for their logistical support during the field work. We thank Justin Lindemann, Angélique Opitz, Jonas Sernau (AWI), and Anke Sobotta (GFZ) for their assistance in the laboratory. We thank AWI logistics for their help in the field work logistics.

6

Synthesis

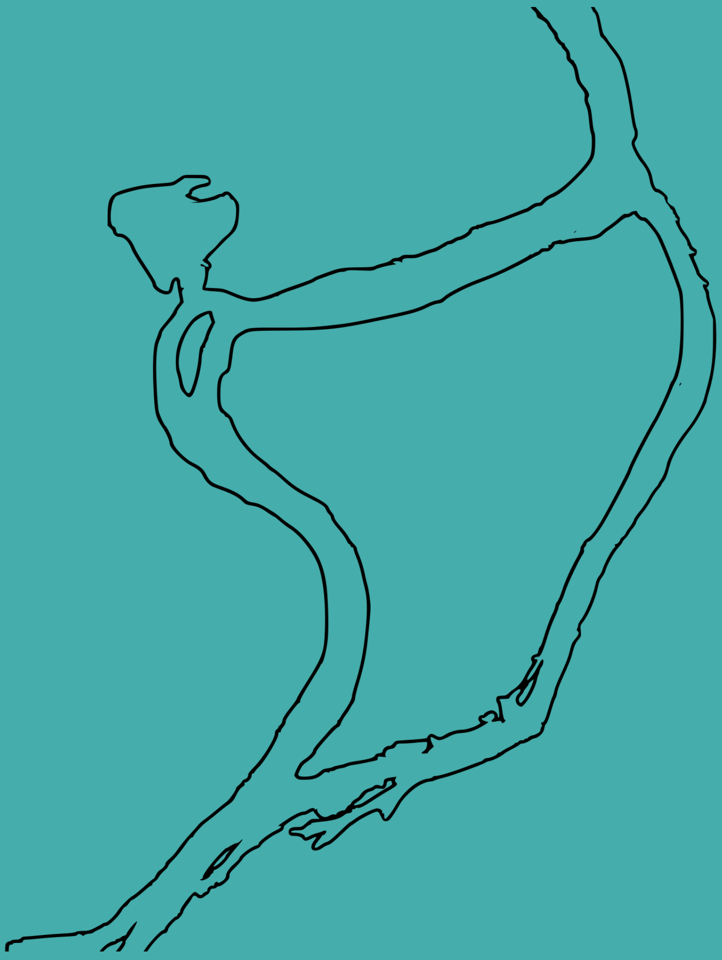

A heron waiting
The circles keep on growing
Everything is one

6 Synthesis

Permafrost thaw will continue with ongoing climate change. While continuous permafrost might transition to discontinuous permafrost, shallow or discontinuous permafrost might disappear completely in the next decades to centuries. Even though ongoing permafrost degradation will lead to widespread reduction of thermokarst lake area (Nitze et al., 2017) and wetland area (Avis et al., 2011), the formation of new lakes and taliks, especially in the continuous permafrost zone, will continue to contribute to GHG emissions. Furthermore, talik formation will increase even below shallow lakes, as the thinning of lake ice leads to the shift of bedfast-ice lakes to floating-ice regimes (Arp et al., 2012). Yedoma permafrost is widespread (Strauss et al., 2021b) and has been shown to be very vulnerable in ongoing climate change, and contains a large OM storage. Even though carbon storage estimates have been improved in the last decades (Hugelius et al., 2014; Mishra et al., 2021), large uncertainties still remain on the share of deep OM that will be mobilized upon thaw. This brings me to my main research question: how does permafrost thaw affect its OM storage? I studied frozen Yedoma sediments and Yedoma sediments that were thawed below a lake, and presented the first molecular biomarker distributions and OC turnover data in thawed Yedoma sediments. My research represents the vanguard for many more studies focusing on these questions in other regions to gather a larger data set.

In my research, I studied several snapshots of permafrost sediments in the Arctic. A snapshot because the Arctic is a dynamic region and permafrost regions are constantly changing; now even faster. A great example of such a snapshot is the sediments I studied from the Sobo-Sise Cliff (Chapter 4) and the Batagay thaw slump (Chapter 5): as sediments in such places erode rapidly every thawing season from the steep headwall, I have explored sediments that are not there anymore today. Furthermore, I studied ancient permafrost sediments exposed in the Batagay thaw slump that have survived multiple interglacials. Only very few studies analyzed this particular thaw slump and its biogeochemistry before.

Moreover, the depth of the sediments I studied (max. 55 m) is unique. Only few studies carried out lipid biomarker analyses and incubation experiments of permafrost sediments below 10 m, and these did not include thawed Yedoma permafrost sediments. My results highlight the importance of OM studies of deep permafrost sediments.

Based on my research (Chapter 2 to 5), I place my findings in a broader perspective and provide an outlook on how lipid biomarkers can be used in the characterization of permafrost organic matter (Chapter 6.1), how OM is mobilized and how much GHG can be produced in thawed permafrost (Chapter 6.2), and what the quality of frozen and thawed OM is (in both chapters). I conclude with listing recommendations for future research (Chapter 6.4).

6.1 Lipid biomarkers to characterize permafrost organic matter

6.1.1 Organic matter source

In all four publications, I analyzed lipid biomarkers in sediments. Originally, lipid or molecular biomarkers were analyzed by geologists in crude oils and extracts of petroleum (Peters et al., 2005), because they can give insights into many aspects such as the source rock, thermal maturity and the degree of decomposition. Yet, more and more studies measured biomarkers in sediments and tried to link them to biological productivity and preservation of OM. Biomarkers can provide information on the source of the OM. In my research, I found that the *n*-alkane proxies ACL and P_{aq} (Chapter 1.4) were useful in the reconstruction of the OM source and more specifically, the distinction between OM derived from terrestrial higher plants (higher ACL and lower P_{aq}) or aquatic plants (lower ACL and higher P_{aq}). These proxies could be useful to reconstruct for example stages of ice-wedge degradation (wet conditions in low-centered polygons vs. drier conditions in high-centered polygons) and thermokarst lake dynamics (wetland stage, drainage history). Furthermore, I identified when increased microbial activity corresponded to periods with a warmer climate than today. This could help to deduce information on permafrost degradation history during warmer times.

Zech et al. (2009) developed an end-member model with two end-members: deciduous trees and shrubs, and grasses and herbs. This model is based on the ratios of odd long-chain *n*-alkanes, where *n*-C_{27} and *n*-C_{29} are likely derived from deciduous trees and shrubs, while *n*-C_{31} and *n*-C_{33} dominate in grasslands (e.g. grasses and herbs). The change in the OEP (Chapter 1.4) has been used as indicator of OM decomposition where higher values indicate better-preserved OM. Therefore, they defined “degradation lines” of OM for the two end-members. In Figure 6.1a, I plotted the data from my four sites in this end-member model, as well as other Yedoma sites in Siberia and Alaska (Jongejans et al., 2018; Strauss et al., 2015; Strauss et al., 2012b). In Chapter 2, I concluded that for my data from the Goltsovoye Lake sediment core, the model showed a mixed signal for the OM. This is also the case for the other study sites. The values don’t fall on the “degradation line” or show a certain trend. Specifically, the sediments with the lowest *n*-alkane ratio (Sobo-Sise cliff, Goltsovoye Lake) fall close to the “degradation line” for deciduous trees and shrubs, even though no trees were growing in these places during the Late Pleistocene nor are they now. This suggests that this end-member model might not be suitable for OM from Arctic sediments.

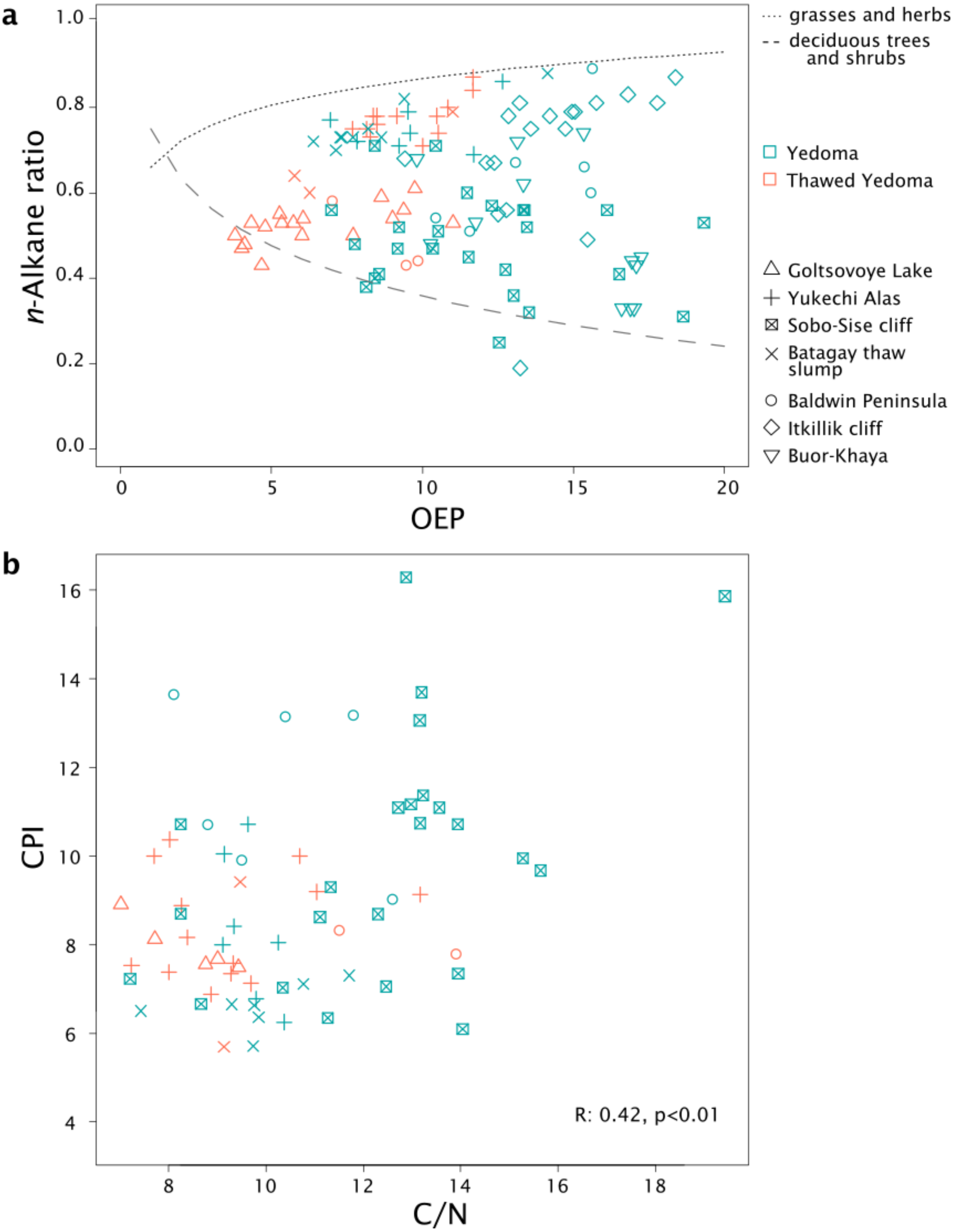

Figure 6.1: Biomarker proxies of Siberian and Alaskan Yedoma sites. (a) Odd-over-even predominance (OEP) vs. *n*-alkane ratio with "degradation lines" for grasses and herbs (dotted) and for deciduous trees and shrubs (dashed), (b) carbon to nitrogen (C/N) ratio vs. carbon preference index (CPI). Yedoma sediments in turquois and thawed Yedoma deposits in orange. Study sites (indicated with different symbols): Goltsovoye Lake, Yukechi Alas, Sobo-Sise cliff, Batagay thaw slump, Baldwin Peninsula (Jongejans et al., 2018), Itkillik cliff (Strauss et al., 2012b), Buor-Khaya (Strauss et al., 2015).

6.1.2 Organic matter quality

However, regarding the preservation of OM, as decomposition of crude oils happens on geological time scales, these are not directly translatable to sediment OM. Previous studies used the carbon to nitrogen (C/N) ratio (Gundelwein et al., 2007; Kuhry & Vitt, 1996), as well as the CPI (Chapter 1.4) (Bray & Evans, 1961; Marzi et al., 1993) which both decrease with ongoing decomposition. However, both ratios are also dependent on the input signal of the OM. I found a moderate positive correlation (R: 0.42, $p<0.01$) between the C/N ratio and CPI (Figure 6.1b), which suggests that these parameters do show a decomposition signal. Furthermore, the thawed Yedoma sediments have a significantly lower C/N ratio, CPI and OEP than the undisturbed Yedoma sediments ($p<0.01$). This indicates that OM exposed to microbes in the thawed Yedoma was further decomposed compared to the undisturbed Yedoma deposits. These findings show that the *n*-alkane proxies are helpful in the assessment of the quality of OM.

6.2 Mobilization of organic matter in thawing permafrost

In Chapter 3, I showed that, regardless of the low TOC content, GHG production in thawing permafrost sediments was significant. I showed that the GHG production was higher in the sediments below the Yedoma lake, which recently thawed for the first time since deposition, compared to the Alas lake sediments, which thawed in previous thermokarst lake cycles and therefore microbial decomposition happened already. Especially, I showed that the still-frozen Yedoma sediments contained labile OM, as indicated by the highest CO_2 production. One of the main discriminators for the CO_2 production was the dissolved organic carbon (DOC) content. This corroborates the high biolability of DOC in thawing permafrost found in previous studies (Abbott et al., 2014; Drake et al., 2015; Ewing et al., 2015; Spencer et al., 2015). Specifically, DOC from Pleistocene permafrost was shown to be more susceptible to decomposition than modern DOC (Abbott et al., 2014; Spencer et al., 2015; Vonk et al., 2013b). Mann et al. (2021) found that increasing discharge and permafrost thaw contributions will increase the bioreactivity of nearshore organic carbon, meaning the organic carbon will be utilized by microbes faster.

With the CH_4 measurements, I showed that microbial communities were established in the thawed sediments below the Yedoma lake but not yet in the deeper still-frozen Yedoma sediments. I did not find significant correlations between the biomarker distribution and CH_4 production, and I found no drivers for the CH_4 production within our dataset. Generally, the water-saturated sediments below thermokarst lakes pose favorable environmental conditions for CH_4 production. However, it seems that CH_4 production is more complex and more vulnerable to disturbance than CO_2 production. Likely drivers for CH_4 production are the initial presence of methanogenic archaea (Holm et al., 2020; Knoblauch et al., 2018), the modern oxygen conditions in the soil, as well as the paleoenvironmental conditions during deposition (Holm et al., 2020). Regarding the latter, exposure of the sediments to oxygen during drilling or subsampling of the sediment cores (even when frozen) could have disturbed the communities. Furthermore, the sediments below the Alas lake might have been exposed to oxic conditions during lake drainage in previous thermokarst lake cycles, thereby causing unfavorable conditions for the methanogens (Holm et al., 2020; Van Huissteden et al., 2011). In a study of 40 thermokarst lakes along a latitudinal transect in Alaska, Sepulveda-Jauregui et al. (2015) found that all lakes were net sources of atmospheric CH_4 and CO_2. They showed that CH_4 release, even though it was lower than the CO_2 release, had a stronger impact on the climate in this region due to the stronger global warming potential of CH_4 compared to CO_2. Especially, CH_4 release from permafrost was shown to be highest along thermokarst lake margins (Walter et al., 2006) and in early stages of the formation of thermokarst lakes and thaw depressions (Desyatkin et al., 2009; Kessler et al., 2012). Sepulveda-Jauregui et al. (2015) stated that methanogenesis in near-surface sediments is mainly fueled by primary production and the supply of allochthonous OM from eroding lake margins, which is common for Yedoma lakes. For deeper sediments, such as the case for Yedoma taliks, old OM poses an important substrate for methanogenesis.

In permafrost regions close to the coast, permafrost or thermokarst lakes can be affected by salt diffusion, marine inundation or the transition to thermokarst lagoons. The input of salt plays a major role for permafrost, as higher solute concentrations decrease the freezing temperature of the water (Overduin et al., 2008). This means that sediments can be unfrozen even though the temperature is below 0 °C and thus, more liquid water is present in the sediments and more microbial activity can take place. In their study of microbial communities in subsea permafrost, Mitzscherling et al. (2017) found changes in the bacterial community structure, abundance, and diversity between subsea and terrestrial permafrost, but that the communities themselves remained terrestrial. Further research into the response of microbes and its impact on the GHG emissions following the marine influence of terrestrial permafrost is needed.

6.2.1 Methane production vs. emission

A challenge with upscaling the CH_4 production in the thawed sediments, is that the produced amount does not equal the emission, because part of the produced CH_4 can still be oxidized. Aerobic CH_4 oxidation can occur in the water column (Martinez-Cruz et al., 2015), in and under the winter ice cover (Elder et al., 2019; Greene et al., 2014), as well as in near surface sediments (He et al., 2012; Martinez-Cruz et al., 2017). Furthermore, CH_4 oxidation was also shown to be significant under anoxic conditions. For example, Thalasso et al. (2020) showed that all CH_4 produced in the sediments below a stratified Siberian lake was removed in the anoxic part of the water column, resulting in no exchange with the oxic part of the water column or the atmosphere. Also, it was shown that AOM even takes place at near-zero temperature: Winkel et al. (2019) found that 41-83% of the produced CH_4 was oxidized anaerobically in deeper (3-5 m) thawed sediments below an Alaskan lake. Mean bottom water temperatures of thermokarst lakes, though, are generally higher (between 2.7 to 4.0 °C) (Boike et al., 2015), meaning the AOM might even be further increased (Fan et al., 2021). Still, research on AOM in permafrost and taliks is limited and the process is not well understood. Furthermore, it is largely unknown how the four major CH_4 emission pathways (direct ebullition, diffusion, storage flux, and ice-bubble storage flux) (Greene et al., 2014; Sepulveda-Jauregui et al., 2015) will be affected with ongoing climate change. For instance, several studies showed that anaerobic CH_4 oxidation under ice will be decreased with ongoing warming and hence shorter ice-covered periods of thermokarst lakes, leading to higher CH_4 emissions (Elder et al., 2019; Greene et al., 2014).

6.2.2 Using the data in models

The next step in the GHG production estimation of thawing permafrost is using and upscaling the numbers in models. This is challenging for multiple reasons. For example, CO_2 production generally happens fast upon thawing (days to months), whereas CH_4 production can be delayed months to years. This lag time of CH_4 production is likely caused by the vulnerability of methanogenic communities and a low initial abundance of methanogens (Knoblauch et al., 2018; Knoblauch et al., 2013; Treat et al., 2014; Waldrop et al., 2010). Nevertheless, as opposed to the closed system of the laboratory experiment, the exchange of nutrients and organisms throughout the soil profile (Knoblauch et al., 2018), and higher substrate availability under field conditions might lead to an earlier or stronger onset of CH_4 production. Another point is that the GHG production rates are not linear: they slow down over time because on the one hand, the OM pool is reduced with further decomposition, and on the other hand, relatively more recalcitrant OM remains. Simple models nowadays often take into account two or three OM pools (labile, intermediate and recalcitrant), with corresponding GHG production rates. Furthermore, I only measured anaerobic GHG production. Even though this might be a fitting scenario for water-saturated sediments in taliks below lakes, this likely is not the case for taliks developing underneath land, for example when the active layer deepens and does not refreeze again. With a modeling study, it was shown that land taliks will take the overhand on the long-term (decennia to centuries) over lake taliks (M. Langer, personal communication, 2021). This stresses the need to better understand OM decomposition dynamics under different conditions.

6.2.3 Transport of OM into aquatic systems

Permafrost thaw also leads to the transport of sediments, organic matter, nutrients, major ions and contaminants into aquatic systems. The formation of retrogressive thaw slumps has increased since the 1950s (Lacelle et al., 2010; Lantuit & Pollard, 2008; Ramage et al., 2018) leading to increased transport of sediments, OM and nutrients into aquatic systems and higher GHG release from thawing permafrost (Couture, 2010; Mann et al., 2021; Ramage et al., 2018; Tanski et al., 2016). Many studies tried to estimate the transport of OC into aquatic systems. Arctic rivers are thought to transport large amounts of DOC (34-38 x 10^3 Gt) into the pan-Arctic watershed on an annual basis (Holmes et al., 2012; Manizza et al., 2009; Raymond et al., 2007). Coastal erosion might contribute 4.9-14.0 x 10^3 Gt of OC into the Arctic Ocean every year (Wegner et al., 2015). Nevertheless, it is thought that only half of inland aquatic OC reaches the ocean due to respiration to the atmosphere or burial in lake and river sediments (Battin et al., 2009). Vonk et al. (2013b) argued that with press disturbances, such as active layer deepening, mainly soluble materials (e.g. OC, nutrients and base cations) are transported but that pulse disturbances, such as thermo-erosional processes, likely favor the delivery of particulate materials.

The impact of the large amount of sediments, OM and nutrients that are transported into aquatic systems is still largely unknown. Possible consequences are a reduced photosynthetic uptake of CO_2 following reduced light conditions and changes in plankton community dynamics in the water column (Polimene et al., 2022; Retamal et al., 2007), higher CO_2 release into the atmosphere and acidification of the water (Anderson et al., 2011; Tank et al., 2012). These processes will have a major impact on the trophic structure and food web processes of rivers and near-shore regions. Meredith et al. (2019) argued that exactly this – the fact that there are so many competing mechanisms that influence carbon export – is what complicates our understanding of the influence of permafrost thaw on aquatic systems. These mechanisms should be the focus of future research.

6.3 Recommendations for future research

Most biomarker proxies that I used were useful in assessing the source of OM. To further improve permafrost OM source assessment, further studies could implement isotopic analyses of different biomarker classes. It would be beneficial if more studies explore proxies to assess the OM quality. Such studies could be pure methodology studies including samples from different stratigraphic units (e.g., Yedoma, talik, lacustrine, Holocene sediments) so that new possible proxies can be developed. From this, OM decomposition end-member models could be developed. Furthermore, a useful study would be to compare specific biomarker classes before and after incubation experiments. This would improve the estimates of labile and recalcitrant fractions and thereby the understanding of permafrost OM decomposition upon thaw.

More long-term in situ measurements and incubation experiments should be carried out to get a better understanding of the lag times of CH_4 production. Also, it would be good if incubation experiments could capture field conditions better to improve GHG production estimates. Another aspect that should be studied in more detail is the microbial community structure in permafrost and thawed permafrost sediments. It would be very useful to combine these results with the incubation results so that the drivers of the GHG production can be better assessed. In order to improve upscaling of GHG emissions, future research should further develop GHG measuring (e.g., eddy covariance techniques) and detection techniques (e.g., high resolution imagery from UAV flights and satellites).

More research should also focus on how permafrost landscapes might be changing in the near future. Biomarker and incubation studies should be carried out in for example marine-affected terrestrial permafrost, drained thermokarst lakes and wetlands, landscapes affected by forest and tundra fires, as well as vegetation changes.

Personal note

During my research, I have made an effort to make my science available to students, school kids and the public at large. Science communication is becoming more important than ever before, thus it is crucial that researchers make their research tangible and comprehensible. It is rewarding to explain your science to an excited audience. More and more projects include outreach activities, but also actively involve those interested or influenced in the form of citizen science and participatory research. However, this is only the beginning of the transformation of science. It is often assumed that natural science is objective because we observe, measure and quantify. In a time when alternative facts and fake news are becoming more obvious (they surely were there before, but less magnified), it is especially important that we are critical of how we carry out science. What if the tools we use don't apply to all situations and all environments? And what happens after we share our knowledge? What if we report, for example, what the consequences of climate change will be on a certain landscape or on a native community living in the Arctic? This knowledge alone won't help to mitigate, adapt and make the world a better place. We need to put our heads together and work together and include all parties. We need to carry out more transdisciplinary research, which aims to integrate knowledge across academic disciplines and involve non-academic stakeholders during all phases of research. In order to do that, scientists need to be better informed about the applications of transdisciplinary research, and the academic structures and cultures (i.e. discipline-based organizational structures and reputational system) need to be adapted so that they can integrate better with this form of research (Zscheischler et al., 2017).

References

Aalstad, K., Westermann, S., Schuler, T. V., Boike, J., & Bertino, L. (2018). Ensemble-based assimilation of fractional snow-covered area satellite retrievals to estimate the snow distribution at Arctic sites. *The Cryosphere*, *12*(1), 247–270. https://doi.org/10.5194/tc-12-247-2018

Abbott, B. W., Larouche, J. R., Jones Jr., J. B., Bowden, W. B., & Balser, A. W. (2014). Elevated dissolved organic carbon biodegradability from thawing and collapsing permafrost. *Journal of Geophysical Research: Biogeosciences*, *119*(10), 2049–2063. https://doi.org/10.1002/2014JG002678

Abbott, G. D., Swain, E. Y., Muhammad, A. B., Allton, K., Belyea, L. R., Laing, C. G., & Cowie, G. L. (2013). Effect of water-table fluctuations on the degradation of Sphagnum phenols in surficial peats. *Geochimica et Cosmochimica Acta*, *106*, 177–191. https://doi.org/10.1016/j.gca.2012.12.013

Anderson, L., Björk, G., Jutterström, S., Pipko, I., Shakhova, N., Semiletov, I., & Wåhlström, I. (2011). East Siberian Sea, an Arctic region of very high biogeochemical activity. *Biogeosciences*, *8*(6), 1745–1754. https://doi.org/10.5194/bg-8-1745-2011

Andersson, R. A., Kuhry, P., Meyers, P., Zebühr, Y., Crill, P., & Mörth, M. (2011). Impacts of paleohydrological changes on *n*-alkane biomarker compositions of a Holocene peat sequence in the eastern European Russian Arctic. *Organic Geochemistry*, *42*(9), 1065–1075. https://doi.org/10.1016/j.orggeochem.2011.06.020

Andersson, R. A., & Meyers, P. A. (2012). Effect of climate change on delivery and degradation of lipid biomarkers in a Holocene peat sequence in the Eastern European Russian Arctic. *Organic Geochemistry*, *53*, 63–72. https://doi.org/10.1016/j.orggeochem.2012.05.002

Andersson, R. A., Meyers, P., Hornibrook, E., Kuhry, P., & Mörth, C.-M. (2012). Elemental and isotopic carbon and nitrogen records of organic matter accumulation in a Holocene permafrost peat sequence in the East European Russian Arctic. *Journal of Quaternary Science*, *27*(6), 545–552. https://doi.org/10.1002/jqs.2541

Angelopoulos, M., Overduin, P. P., Westermann, S., Tronicke, J., Strauss, J., Schirrmeister, L., Biskaborn, B. K., Liebner, S., Maksimov, G., Grigoriev, M. N., & Grosse, G. (2020). Thermokarst Lake to Lagoon Transitions in Eastern Siberia: Do Submerged Taliks Refreeze? *Journal of Geophysical Research: Earth Surface*, *125*(10), e2019JF005424. https://doi.org/10.1029/2019JF005424

Arp, C. D., Jones, B. M., Lu, Z., & Whitman, M. S. (2012). Shifting balance of thermokarst lake ice regimes across the Arctic Coastal Plain of northern Alaska. *Geophysical Research Letters*, *39*(16). https://doi.org/10.1029/2012GL052518

Ashastina, K., Kuzmina, S., Rudaya, N., Troeva, E., Schoch, W. H., Römermann, C., Reinecke, J., Otte, V., Savvinov, G., Wesche, K., & Kienast, F. (2018). Woodlands and steppes: Pleistocene vegetation in Yakutia's most continental part recorded in the Batagay permafrost sequence. *Quaternary Science Reviews*, *196*, 38–61. https://doi.org/10.1016/j.quascirev.2018.07.032

Ashastina, K., Schirrmeister, L., Fuchs, M., & Kienast, F. (2017). Palaeoclimate characteristics in interior Siberia of MIS 6–2: first insights from the Batagay permafrost mega-thaw slump in the Yana Highlands. *Climate of the Past*, *13*, 795–818. https://doi.org/10.5194/cp-13-795-2017

Attermeyer, K., Catalán, N., Einarsdóttir, K., Freixa, A., Groeneveld, M., Hawkes, J., Bergquist, J., & Tranvik, L. (2018). Organic Carbon Processing During Transport Through Boreal Inland Waters: Particles as Important Sites. *Journal of Geophysical Research: Biogeosciences*, *123*. https://doi.org/10.1029/2018JG004500

Avis, C. A., Weaver, A. J., & Meissner, K. J. (2011). Reduction in areal extent of high-latitude wetlands in response to permafrost thaw. *Nature Geoscience*, *4*(7), 444–448. https://doi.org/10.1038/ngeo1160

Battin, T. J., Kaplan, L. A., Findlay, S., Hopkinson, C. S., Marti, E., Packman, A. I., Newbold, J. D., & Sabater, F. (2009). Erratum: Biophysical controls on organic carbon fluxes in fluvial networks. *Nature Geoscience*, *2*(8), 595–595. https://doi.org/10.1038/ngeo602

Bhatt, U. S., Walker, D. A., Raynolds, M. K., Bieniek, P. A., Epstein, H. E., Comiso, J. C., Pinzon, J. E., Tucker, C. J., Steele, M., Ermold, W., & Zhang, J. (2017). Changing seasonality of panarctic tundra vegetation in relationship to climatic variables. *Environmental Research Letters*, *12*(5), 055003. https://doi.org/10.1088/1748-9326/aa6b0b

Bingham, E. M., McClymont, E. L., Väliranta, M., Mauquoy, D., Roberts, Z., Chambers, F. M., Pancost, R. D., & Evershed, R. P. (2010). Conservative composition of *n*-alkane biomarkers in Sphagnum species: Implications for palaeoclimate reconstruction in ombrotrophic peat bogs. *Organic Geochemistry*, *41*(2), 214–220. https://doi.org/10.1016/j.orggeochem.2009.06.010

Bintanja, R. (2018). The impact of Arctic warming on increased rainfall. *Scientific Reports*, *8*(1), 16001. https://doi.org/10.1038/s41598-018-34450-3

Bischoff, J., Mangelsdorf, K., Gattinger, A., Schloter, M., Kurchatova, A. N., Herzschuh, U., & Wagner, D. (2013). Response of methanogenic archaea to Late Pleistocene and Holocene climate changes in the Siberian Arctic: Methanogenic Response to Climate Changes. *Global Biogeochemical Cycles*, *27*(2), 305–317. https://doi.org/10.1029/2011GB004238

Biskaborn, B. K., Herzschuh, U., Bolshiyanov, D., Savelieva, L., Zibulski, R., & Diekmann, B. (2013a). Late Holocene thermokarst variability inferred from diatoms in a lake sediment record from the Lena Delta, Siberian Arctic. *Journal of Paleolimnology*, *49*(2), 155–170. https://doi.org/10.1007/s10933-012-9650-1

Biskaborn, B. K., Herzschuh, U., Bolshiyanov, D. Y., Schwamborn, G., & Diekmann, B. (2013b). Thermokarst processes and depositional events in a tundra lake, northeastern Siberia. *Permafrost and Periglacial Processes*, *24*(3), 160–174. https://doi.org/10.1002/ppp.1769

Biskaborn, B. K., & Sens, M. (2020). Biogeochemical and radiocarbon data of sediment core PG2420 (Lake Goltsovoye, Bykovsky Peninsula, Arctic Siberia) [Type: data set]. *PANGAEA*, https://doi.pangaea.de/10.1594/PANGAEA.918729.

Biskaborn, B. K., Smith, S. L., Noetzli, J., Matthes, H., Vieira, G., Streletskiy, D. A., Schoeneich, P., Romanovsky, V. E., Lewkowicz, A. G., Abramov, A., Allard, M., Boike, J., Cable, W. L., Christiansen, H. H., Delaloye, R., Diekmann, B., Drozdov, D., Etzelmüller, B., Grosse, G., … Lantuit, H. (2019). Permafrost is warming at a global scale. *Nature Communications*, *10*(1), 264. https://doi.org/10.1038/s41467-018-08240-4

Blaauw, M., & Christen, J. A. (2011). Flexible paleoclimate age-depth models using an autoregressive gamma process. *Bayesian Analysis*, *6*(3), 457–474. https://doi.org/10.1214/11-BA618

Blake, L. I., Tveit, A., Øvreås, L., Head, I. M., & Gray, N. D. (2015). Response of Methanogens in Arctic Sediments to Temperature and Methanogenic Substrate Availability (J. H. Badger, Ed.). *PLOS ONE*, *10*(6), e0129733. https://doi.org/10.1371/journal.pone.0129733

Boike, J., Georgi, C., Kirilin, G., Muster, S., Abramova, K., Fedorova, I., Chetverova, A., Grigoriev, M., Bornemann, N., & Langer, M. (2015). Thermal processes of thermokarst lakes in the continuous permafrost zone of northern Siberia–observations and modeling (Lena River Delta, Siberia). *Biogeosciences*, *12*(20), 5941–5965. https://doi.org/10.5194/bg-12-5941-2015

Brassell, S. C., Eglinton, G., & Maxwell, J. R. (1983). The geochemistry of terpenoids and steroids. *Biochemical Society Transactions*, *11*. https://doi.org/10.1042/bst0110575

Bray, E. E., & Evans, E. D. (1961). Distribution of n-paraffins as a clue to recognition of source beds. *Geochimica et Cosmochimica Acta*, *22*(1), 2–15. https://doi.org/10.1016/0016-7037(61)90069-2

Brocks, J. J., Grosjean, E., & Logan, G. A. (2008). Assessing biomarker syngeneity using branched alkanes with quaternary carbon (BAQCs) and other plastic contaminants [Publisher: Elsevier]. *Geochimica et Cosmochimica Acta*, *72*(3), 871–888. https://doi.org/10.1016/j.gca.2007.11.028

Bröder, L., Andersson, A., Tesi, T., Semiletov, I., & Gustafsson, Ö. (2019). Quantifying degradative loss of terrigenous organic carbon in surface sediments across the Laptev and East Siberian Sea. *Global biogeochemical cycles*, *33*(1), 85–99. https://doi.org/10.1029/2018GB005967

Bush, R. T., & McInerney, F. A. (2013). Leaf wax *n*-alkane distributions in and across modern plants: Implications for paleoecology and chemotaxonomy. *Geochimica et Cosmochimica Acta*, *117*, 161–179. https://doi.org/10.1016/j.gca.2013.04.016

Canuel, E. A., & Martens, C. S. (1996). Reactivity of recently deposited organic matter: Degradation of lipid compounds near the sediment-water interface. *Geochimica et Cosmochimica Acta*, *60*(10), 1793–1806. https://doi.org/10.1016/0016-7037(96)00045-2

Čapek, P., Diáková, K., Dickopp, J.-E., Bárta, J., Wild, B., Schnecker, J., Alves, R. J. E., Aiglsdorfer, S., Guggenberger, G., Gentsch, N., Hugelius, G., Lashchinsky, N., Gittel, A., Schleper, C., Mikutta, R., Palmtag, J., Shibistova, O., Urich, T., Richter, A., & Šantrůčková, H. (2015). The effect of warming on the vulnerability of subducted organic carbon in arctic soils. *Soil Biology and Biochemistry*, *90*, 19–29. https://doi.org/10.1016/j.soilbio.2015.07.013

Carnevali, P. B. M., Rohrssen, M., Williams, M. R., Michaud, A. B., Adams, H., Berisford, D., Love, G. D., Priscu, J. C., Rassuchine, O., Hand, K. P., & Murray, A. E. (2015). Methane sources in arctic thermokarst lake sediments on the North Slope of Alaska. *Geobiology*, *13*(2), 181–197. https://doi.org/10.1111/gbi.12124

Chen, L., Liu, L., Mao, C., Qin, S., Wang, J., Liu, F., Blagodatsky, S., Yang, G., Zhang, Q., Zhang, D., et al. (2018). Nitrogen availability regulates topsoil carbon dynamics after permafrost thaw by altering microbial metabolic efficiency. *Nature communications*, *9*(1), 1–11. https://doi.org/10.1038/s41467-018-06232-y

Climate-data.org. (2020). Climate data for cities worldwide.

Costard, F., Gautier, E., Fedorov, A., Konstantinov, P., & Dupeyrat, L. (2014). An Assessment of the Erosion Potential of the Fluvial Thermal Process during Ice Breakups of the Lena River (Siberia). *Permafrost and Periglacial Processes*, *25*(3), 162–171. https://doi.org/10.1002/ppp.1812

Courtin, J., Perfumo, A., Andreev, A. A., Opel, T., Stoof-Leichsenring, K. R., Edwards, M., Murton, J. B., & Herzschuh, U. (2022). Pleistocene glacial and interglacial ecosystems inferred from ancient DNA analyses of permafrost sediments from Batagay megaslump, east Siberia. *Molecular Ecology*, *00*, 1–19. https://doi.org/10.1002/edn3.336

Couture, N. (2010). *Fluxes of Soil Organic Carbon from Eroding Permafrost Coasts, Canadian Beaufort Sea* (PhD Dissertation). Department of Geography, McGill University. Montreal.

Crate, S., Ulrich, M., Habeck, J. O., Desyatkin, A. R., Desyatkin, R. V., Fedorov, A. N., Hiyama, T., Iijima, Y., Ksenofontov, S., Mészáros, C., & Takakura, H. (2017). Permafrost livelihoods: A transdisciplinary review and analysis of thermokarst-based systems of indigenous land use. *Anthropocene*, *18*, 89–104. https://doi.org/10.1016/j.ancene.2017.06.001

Creighton, A. L.-T., Parsekian, A. D., Angelopoulos, M., Jones, B. M., Bondurant, A. C., Engram, M., Lenz, J., Overduin, P., Grosse, G., Babcock, E. L., & Arp, C. D. (2018). Transient Electromagnetic Surveys for the Determination of Talik Depth and Geometry Beneath Thermokarst Lakes. *Journal of Geophysical Research-Solid Earth*, *123*(11), 9310–9323. https://doi.org/10.1029/2018JB016121

Daley, K., Castleden, H., Jamieson, R., Furgal, C., & Ell, L. (2015). Water systems, sanitation, and public health risks in remote communities: Inuit resident perspectives from the Canadian Arctic. *Social Science & Medicine*, *135*, 124–132. https://doi.org/10.1016/j.socscimed.2015.04.017

Dean, J. F., Middelburg, J. J., Röckmann, T., Aerts, R., Blauw, L. G., Egger, M., Jetten, M. S. M., Jong, A. E. E. d., Meisel, O. H., Rasigraf, O., Slomp, C. P., Zandt, M. H. i., & Dolman, A. J. (2018). Methane Feedbacks to the Global Climate System in a Warmer World. *Reviews of Geophysics*, *56*(1), 207–250. https://doi.org/10.1002/2017RG000559

Desyatkin, A. R., Takakai, F., Fedorov, P. P., Nikolaeva, M. C., Desyatkin, R. V., & Hatano, R. (2009). CH_4 emission from different stages of thermokarst formation in Central Yakutia, East Siberia. *Soil Science and Plant Nutrition*, *55*(4), 558–570. https://doi.org/10.1111/j.1747-0765.2009.00389.x

Diáková, K., Čapek, P., Kohoutová, I., Mpamah, P. A., Bárta, J., Biasi, C., Martikainen, P. J., & Šantrůčková, H. (2016). Heterogeneity of carbon loss and its temperature sensitivity in East-European subarctic tundra soils. *FEMS Microbiology Ecology*, *92*(9). https://doi.org/10.1093/femsec/fiw140

Drake, T. W., Wickland, K. P., Spencer, R. G. M., McKnight, D. M., & Striegl, R. G. (2015). Ancient low–molecular-weight organic acids in permafrost fuel rapid carbon dioxide production upon thaw. *Proceedings of the National Academy of Sciences*, *112*(45), 13946–13951. https://doi.org/10.1073/pnas.1511705112

Dutta, K., Schuur, E. A. G., Neff, J. C., & Zimov, S. A. (2006). Potential carbon release from permafrost soils of Northeastern Siberia [00238]. *Global Change Biology*, *12*(12), 2336–2351. https://doi.org/10.1111/j.1365-2486.2006.01259.x

Eglinton, G., & Hamilton, R. J. (1967). Leaf Epicuticular Waxes. *Science*, *156*(3780), 1322–1335. https://doi.org/10.1126/science.156.3780.1322

Elberling, B., Michelsen, A., Schädel, C., Schuur, E. A. G., Christiansen, H. H., Berg, L., Tamstorf, M. P., & Sigsgaard, C. (2013). Long-term CO_2 production following permafrost thaw. *Nature Climate Change*, *3*(10), 890–894. https://doi.org/10.1038/nclimate1955

Elder, C. D., Schweiger, M., Lam, B., Crook, E. D., Xu, X., Walker, J., Walter Anthony, K. M., & Czimczik, C. I. (2019). Seasonal Sources of Whole-Lake CH_4 and CO_2 Emissions From Interior Alaskan Thermokarst Lakes. *Journal of Geophysical Research: Biogeosciences*, *124*(5), 1209–1229. https://doi.org/10.1029/2018JG004735

Estop-Aragonés, C., & Blodau, C. (2012). Effects of experimental drying intensity and duration on respiration and methane production recovery in fen peat incubations. *Soil Biology and Biochemistry*, *47*, 1–9. https://doi.org/10.1016/j.soilbio.2011.12.008

Ewing, S. A., O'Donnell, J. A., Aiken, G. R., Butler, K., Butman, D., Windham-Myers, L., & Kanevskiy, M. Z. (2015). Long-term anoxia and release of ancient, labile carbon upon thaw of Pleistocene permafrost. *Geophysical Research Letters*, *42*(24). https://doi.org/10.1002/2015GL066296

Fan, L., Dippold, M. A., Thiel, V., Ge, T., Wu, J., Kuzyakov, Y., & Dorodnikov, M. (2021). Temperature sensitivity of anaerobic methane oxidation versus methanogenesis in paddy soil: Implications for the CH_4 balance under global warming. *Global Change Biology*, *n/a*(n/a). https://doi.org/10.1111/gcb.15935

Farquharson, L., Anthony, K. W., Bigelow, N., Edwards, M., & Grosse, G. (2016). Facies analysis of yedoma thermokarst lakes on the northern Seward Peninsula, Alaska. *Sedimentary Geology*, *340*, 25–37. https://doi.org/10.1016/j.sedgeo.2016.01.002

Faucherre, S., Jørgensen, C. J., Blok, D., Weiss, N., Siewert, M. B., Bang-Andreasen, T., Hugelius, G., Kuhry, P., & Elberling, B. (2018). Short and Long-Term Controls on Active Layer and Permafrost Carbon Turnover Across the Arctic. *Journal of Geophysical Research: Biogeosciences*, *123*(2), 372–390. https://doi.org/10.1002/2017JG004069

Fedorov, A. N., Gavriliev, P. P., Konstantinov, P. Y., Hiyama, T., Iijima, Y., & Iwahana, G. (2014). Estimating the water balance of a thermokarst lake in the middle of the Lena

River basin, eastern Siberia. *Ecohydrology*, *7*(2), 188–196. https://doi.org/10.1002/eco.1378

Fedorov, A. N., & Konstantinov, P. (2003). Observations of surface dynamics with thermokarst initiation, Yukechi site, Central Yakutia. *Proceedings of the 8th International Conference on Permafrost, 21-25 July 2003, Zurich, Switzerland*, 239–243.

Fedorova, I., Chetverova, A., Bolshiyanov, D., Makarov, A., Boike, J., Heim, B., Morgenstern, A., Overduin, P. P., Wegner, C., Kashina, V., et al. (2015). Lena Delta hydrology and geochemistry: long-term hydrological data and recent field observations. *Biogeosciences*, *12*(2), 345–363. https://doi.org/10.5194/bg-12-345-2015,2015

Ficken, K. J., Barber, K. E., & Eglinton, G. (1998). Lipid biomarker, δ^{13}C and plant macrofossil stratigraphy of a Scottish montane peat bog over the last two millennia. *Organic Geochemistry*, *28*(3), 217–237. https://doi.org/10.1016/S0146-6380(97)00126-5

Ficken, K., Li, B., Swain, D., & Eglinton, G. (2000). An *n*-alkane proxy for the sedimentary input of submerged/floating freshwater aquatic macrophytes. *Organic Geochemistry*, *31*, 745–749. https://doi.org/10.1016/S0146-6380(00)00081-4

Freeman, C., Evans, C. D., Monteith, D. T., Reynolds, B., & Fenner, N. (2001). Export of organic carbon from peat soils. *Nature*, *412*(6849), 785–785. https://doi.org/10.1038/35090628

French, H. M. (1999). Past and present permafrost as an indicator of climate change. *Polar Research*, *18*(2), 269–274. https://doi.org/10.3402/polar.v18i2.6584

Fuchs, M., Grosse, G., Strauss, J., Günther, F., Grigoriev, M., Maximov, G. M., & Hugelius, G. (2018). Carbon and nitrogen pools in thermokarst-affected permafrost landscapes in Arctic Siberia. *Biogeosciences*, *15*(3), 953–971. https://doi.org/10.5194/bg-15-953-2018

Fuchs, M., Nitze, I., Strauss, J., Günther, F., Wetterich, S., Kizyakov, A., Fritz, M., Opel, T., Grigoriev, M. N., Maksimov, G. T., & Grosse, G. (2020). Rapid Fluvio-Thermal Erosion of a Yedoma Permafrost Cliff in the Lena River Delta. *Frontiers in Earth Science*, *8*, 336. https://doi.org/10.3389/feart.2020.00336

Gaglioti, B. V., Mann, D. H., Jones, B. M., Pohlman, J. W., Kunz, M. L., & Wooller, M. J. (2014). Radiocarbon age-offsets in an arctic lake reveal the long-term response of permafrost carbon to climate change. *Journal of Geophysical Research: Biogeosciences*, *119*(8), 1630–1651. https://doi.org/10.1002/2014JG002688

Goldhar, C., Bell, T., & Wolf, J. (2013). Rethinking existing approaches to water security in remote communities: an analysis of two drinking water systems in Nunatsiavut, Labrador, Canada. *Water Alternatives*, *6*(3), 462.

Goldhar, C., Bell, T., & Wolf, J. (2014). Vulnerability to freshwater changes in the Inuit settlement region of Nunatsiavut, Labrador: A case study from Rigolet. *Arctic*, 71–83. https://doi.org/10.14430/arctic4365

Grebenets, V., Streletskiy, D., & Shiklomanov, N. (2012). Geotechnical safety issues in the cities of Polar Regions. *Geography, Environment, Sustainability*, *5*(3), 104–119. https://doi.org/10.24057/2071-9388-2012-5-3-104-119

Greene, S., Walter Anthony, K. M., Archer, D., Sepulveda-Jauregui, A., & Martinez-Cruz, K. (2014). Modeling the impediment of methane ebullition bubbles by seasonal lake ice. *Biogeosciences*, *11*(23), 6791–6811. https://doi.org/10.5194/bg-11-6791-2014

Greenwood, P. F., Arouri, K. R., Logan, G. A., & Summons, R. E. (2004). Abundance and geochemical significance of C2n dialkylalkanes and highly branched C3n alkanes in diverse Meso-and Neoproterozoic sediments. [Publisher: Elsevier]. *Organic Geochemistry*, *35*(3), 331–346. https://doi.org/10.1016/j.orggeochem.2003.10.013

Grigoriev, M. (1993). Cryomorphogenesis of the Lena River mouth area, Siberian Branch. *USSR Academy of Sciences*, *176*, In Russian.

Grigoriev, N. (1960). The temperature of permafrost in the Lena delta basin–deposit conditions and properties of the permafrost in Yakutia. *Yakutsk*, *2*, 97–101. In Russian.

Groemping, U. (2006). Relative Importance for Linear Regression in R: The Package relaimpo. *Journal of Statistical Software, Articles*, *17*(1), 1–27. https://doi.org/10.18637/jss.v017.i01

Grosse, G., Harden, J., Turetsky, M., McGuire, A. D., Camill, P., Tarnocai, C., Frolking, S., Schuur, E. A. G., Jorgenson, T., Marchenko, S., Romanovsky, V., Wickland, K. P., French, N., Waldrop, M., Bourgeau-Chavez, L., & Striegl, R. G. (2011). Vulnerability of high-latitude soil organic carbon in North America to disturbance. *Journal of Geophysical Research: Biogeosciences*, *116*(G4). https://doi.org/10.1029/2010JG001507

Grosse, G., Jones, B., & Arp, C. (2013). 8.21 Thermokarst Lakes, Drainage, and Drained Basins. In J. F. (i. C. Shroder, R. Giardino, & J. Harbor (Eds.), *Treatise on Geomorphology* (pp. 325–353). Academic Press. https://doi.org/10.1016/B978-0-12-374739-6.00216-5

Grosse, G., Schirrmeister, L., Kunitsky, V., Rachold, V., Grigoriev, M. N., & Hubberten, H.-W. (2005). Volumetric balance of Ice Complex deposits at Bykovsky Peninsula (NE Siberia), using field data, remote sensing and digital elevation models. *EUCOP II, 2nd European Conference on Permafrost, Potsdam, Germany, June 2005.*, *12*.

Grosse, G., Schirrmeister, L., Siegert, C., Kunitsky, V. V., Slagoda, E. A., Andreev, A. A., & Dereviagyn, A. Y. (2007). Geological and geomorphological evolution of a sedimentary periglacial landscape in Northeast Siberia during the Late Quaternary. *Geomorphology*, *86*(1), 25–51. https://doi.org/10.1016/j.geomorph.2006.08.005

Grotheer, H., Meyer, V., Riedel, T., Pfalz, G., Mathieu, L., Hefter, J., Gentz, T., Lantuit, H., Mollenhauer, G., & Fritz, M. (2020). Burial and origin of permafrost-derived carbon in the nearshore zone of the southern Canadian Beaufort Sea. *Geophysical Research Letters*, *47*(3), e2019GL085897. https://doi.org/10.1029/2019GL085897

Gundelwein, A., Müller-Lupp, T., Sommerkorn, M., Haupt, E. T. K., Pfeiffer, E.-M., & Wiechmann, H. (2007). Carbon in tundra soils in the Lake Labaz region of arctic Siberia. *European Journal of Soil Science*, *58*(5), 1164–1174. https://doi.org/10.1111/j.1365-2389.2007.00908.x

Gunstone, F., & Harwood, J. (2007). *Occurrence and characterisation of oils and fats*. CRC press.

Günther, F., Grosse, G., Wetterich, S., Jones, B. M., Kunitsky, V. V., Kienast, F., & Schirrmeister, L. (2015). The Batagay mega thaw slump, Yana Uplands, Yakutia, Russia: permafrost thaw dynamics on decadal time scale. *PAST Gateways - Palaeo-Arctic Spatial and Temporal Gateways - Third International Conference and Workshop*, 3.

Günther, F., Overduin, P. P., Baranskaya, A., Opel, T., & Grigoriev, M. N. (2013). Observing Muostakh Island disappear: erosion of a ground-ice-rich coast in response to summer warming and sea ice reduction on the East Siberian shelf. *The Cryosphere Discussions*, *7*(4), 4101–4176. https://doi.org/10.5194/tcd-7-4101-2013

Hamilton, T. D., & Brigham-Grette, J. (1991). The last interglaciation in Alaska: Stratigraphy and paleoecology of potential sites. *Quaternary International*, *10-12*, 49–71. https://doi.org/10.1016/1040-6182(91)90040-U

Hansen, J., Ruedy, R., Sato, M., & Lo, K. (2010). Global surface temperature change. *Reviews of Geophysics*, *48*(4). https://doi.org/10.1029/2010RG000345

Haugk, C., Jongejans, L. L., Mangelsdorf, K., Fuchs, M., Ogneva, O., Palmtag, J., Mollenhauer, G., Mann, P. J., Overduin, P. P., Grosse, G., Sanders, T., Tuerena, R., Schirrmeister, L., Wetterich, S., Kizyakov, A., & Strauss, J. (2022). Organic matter characteristics of a rapidly eroding permafrost cliff in NE Siberia (Lena Delta, Laptev Sea region). *Biogeosciences*, *19*, 2079–2094. https://doi.org/10.5194/bg-19-2079-2022

He, R., Wooller, M. J., Pohlman, J. W., Quensen, J., Tiedje, J. M., & Leigh, M. B. (2012). Diversity of active aerobic methanotrophs along depth profiles of arctic and subarctic lake water column and sediments. *The ISME Journal*, *6*(10), 1937–1948. https://doi.org/10.1038/ismej.2012.34

Hedges, J. I., & Keil, R. G. (1995). Sedimentary organic matter preservation: an assessment and speculative synthesis [01705]. *Marine chemistry*, *49*(2-3), 81–115. https://doi.org/10.1016/0304-4203(95)00008-F

Heslop, J. K., Anthony, K. M. W., Grosse, G., Liebner, S., & Winkel, M. (2019). Century-scale time since permafrost thaw affects temperature sensitivity of net methane production in thermokarst-lake and talik sediments. *Science of The Total Environment*, *691*, 124–134. https://doi.org/10.1016/j.scitotenv.2019.06.402

Heslop, J. K., Walter Anthony, K. M., Sepulveda-Jauregui, A., Martinez-Cruz, K., Bondurant, A., Grosse, G., & Jones, M. C. (2015). Thermokarst lake methanogenesis along a complete talik profile. *Biogeosciences*, *12*(14), 4317–4331. https://doi.org/10.5194/bg-12-4317-2015

Hjort, J., Karjalainen, O., Aalto, J., Westermann, S., Romanovsky, V. E., Nelson, F. E., Etzelmüller, B., & Luoto, M. (2018). Degrading permafrost puts Arctic infrastructure at risk by mid-century. *Nature Communications*, *9*(1), 5147. https://doi.org/10.1038/s41467-018-07557-4

Höfle, S., Rethemeyer, J., Mueller, C. W., & John, S. (2013). Organic matter composition and stabilization in a polygonal tundra soil of the Lena Delta. *Biogeosciences*, *10*(5), 3145–3158. https://doi.org/10.5194/bg-10-3145-2013

Holm, S., Walz, J., Horn, F., Yang, S., Grigoriev, M. N., Wagner, D., Knoblauch, C., & Liebner, S. (2020). Methanogenic response to long-term permafrost thaw is determined by paleoenvironment. *FEMS Microbiology Ecology*, *96*(3), fiaa021. https://doi.org/10.1093/femsec/fiaa021

Holmes, R., Shiklomanov, A., Suslova, A., Tretiakov, M., McClelland, J. W., Spencer, R., & et al. (2015). River Discharge. *Arctic report card*.

Holmes, R. M., McClelland, J. W., Peterson, B. J., Tank, S. E., Bulygina, E., Eglinton, T. I., Gordeev, V. V., Gurtovaya, T. Y., Raymond, P. A., Repeta, D. J., et al. (2012). Seasonal and annual fluxes of nutrients and organic matter from large rivers to the Arctic Ocean and surrounding seas. *Estuaries and Coasts*, *35*(2), 369–382. https://doi.org/10.1007/s12237-011-9386-6

Horsfield, B., Disko, U., & Leistner, F. (1989). The micro-scale simulation of maturation: outline of a new technique and its potential applications. *Geologische Rundschau*, *78*. https://doi.org/10.1007/BF01988370

Hugelius, G., Strauss, J., Zubrzycki, S., Harden, J. W., Schuur, E. A. G., Ping, C.-L., Schirrmeister, L., Grosse, G., Michaelson, G. J., Koven, C. D., O'Donnell, J. A., Elberling, B., Mishra, U., Camill, P., Yu, Z., Palmtag, J., & Kuhry, P. (2014). Estimated stocks of circumpolar permafrost carbon with quantified uncertainty ranges and identified data gaps. *Biogeosciences*, *11*(23), 6573–6593. https://doi.org/10.5194/bg-11-6573-2014

Hutchings, J., Bianchi, T., Kaufman, D., Kholodov, A., Vaughn, D., & Schuur, E. (2019). Millennial-scale carbon accumulation and molecular transformation in a permafrost core from Interior Alaska. *Geochimica et Cosmochimica Acta*, *253*, 231–248. https://doi.org/10.1016/j.gca.2019.03.028

Inuit Circumpolar Council-Alaska. (2015). *Alaskan Inuit Food Security Conceptual Framework: How to Assess the Arctic from An Inuit Perspective: Summary and Recommendations Report*. Anchorage, AK.

IPCC. (2019). Climate change and land: an IPCC special report on climate change, desertification, land degradation, sustainable land management, food security, and greenhouse gas fluxes in terrestrial ecosystems. *Report, Intergovernmental Panel on Climate Change, Switzerland.*

Jenrich, M., Angelopoulos, M., Grosse, G., Overduin, P. P., Schirrmeister, L., Nitze, I., Biskaborn, B. K., Liebner, S., Grigoriev, M., Murray, A., Jongejans, L. L., & Strauss, J. (2021). Thermokarst Lagoons: A Core-Based Assessment of Depositional Characteristics and an Estimate of Carbon Pools on the Bykovsky Peninsula. *Frontiers in Earth Science*, *9*, 518. https://doi.org/10.3389/feart.2021.637899

Jones, B. M., Irrgang, A. M., Farquharson, L. M., Lantuit, H., Whalen, D., Ogorodov, S., Grigoriev, M., Tweedie, C., Gibbs, A. E., Strzelecki, M. C., et al. (2020). Coastal Permafrost Erosion. *Arctic report card*, *15*. https://doi.org/10.25923/e47w-dw52

Jones, M. C., Grosse, G., Jones, B. M., & Walter Anthony, K. (2012a). Peat accumulation in drained thermokarst lake basins in continuous, ice-rich permafrost, northern Seward Peninsula, Alaska. *Journal of Geophysical Research: Biogeosciences*, *117*(G2). https://doi.org/10.1029/2011JG001766

Jones, P., Lister, D., Osborn, T., Harpham, C., Salmon, M., & Morice, C. (2012b). Hemispheric and large-scale land-surface air temperature variations: An extensive revision and an update to 2010. *Journal of Geophysical Research: Atmospheres*, *117*(D5). https://doi.org/10.1029/2011JD017139

Jongejans, L. L., Grosse, G., Ulrich, M., Fedorov, A. N., Konstantinov, P., & Strauss, J. (2019). Radiocarbon ages of talik sediments of an alas lake and a yedoma lake in the Yukechi Alas, Siberia [Type: data set]. *PANGAEA*. https://doi.org/10.1594/PANGAEA.904738

Jongejans, L. L., Liebner, S., Knoblauch, C., Mangelsdorf, K., & Strauss, J. (2021a). Biogeochemical parameters of thawed sediments underneath a Yedoma and Alas thermokarst lake in Eastern Siberia [Type: data set]. *PANGAEA*. https://doi.org/10.1594/PANGAEA.928132

Jongejans, L. L., Liebner, S., Knoblauch, C., Mangelsdorf, K., & Strauss, J. (2021b). Branched glyerol diakyl glyerol tetraether (brGDGT) concentration in thawed sediments underneath a Yedoma and Alas thermokarst lake in Eastern Siberia [Type: data set]. *PANGAEA*. https://doi.org/10.1594/PANGAEA.928135

Jongejans, L. L., Liebner, S., Knoblauch, C., Mangelsdorf, K., & Strauss, J. (2021c). Cumulative greenhouse gas production in thawed sediments underneath a Yedoma and Alas thermokarst lake in Eastern Siberia [Type: data set]. *PANGAEA*. https://doi.org/10.1594/PANGAEA.928140

Jongejans, L. L., Liebner, S., Knoblauch, C., Mangelsdorf, K., & Strauss, J. (2021d). Dissolved organic carbon content in thawed sediments underneath a Yedoma and Alas thermokarst lake in Eastern Siberia [Type: data set]. *PANGAEA*. https://doi.org/10.1594/PANGAEA.928136

Jongejans, L. L., Liebner, S., Knoblauch, C., Mangelsdorf, K., & Strauss, J. (2021e). *n*-Alkane concentration in thawed sediments underneath a Yedoma and Alas thermokarst lake in Eastern Siberia [Type: data set]. *PANGAEA*. https://doi.org/10.1594/PANGAEA.928134

Jongejans, L. L., Liebner, S., Knoblauch, C., Mangelsdorf, K., Ulrich, M., Grosse, G., Tanski, G., Fedorov, A. N., Konstantinov, P. Y., Windirsch, T., et al. (2021f). Greenhouse gas production and lipid biomarker distribution in Yedoma and Alas thermokarst lake sediments in Eastern Siberia. *Global Change Biology*. https://doi.org/10.1111/gcb.15566

Jongejans, L. L., Mangelsdorf, K., Karger, C., Opel, T., Courtin, J., Meyer, H., Wetterich, S., Kizyakov, A., Grosse, G., Shepelev, A., Syromyatnikov, I. I., Fedorov, A., & Strauss, J. (2022). Molecular biomarkers in Batagay megaslump permafrost deposits reveal clear differences in organic matter preservation between glacial and interglacial periods. *The Cryosphere*, *16*, 3601–3617. https://doi.org/10.5194/tc-16-3601-2022

Jongejans, L. L., Mangelsdorf, K., Schirrmeister, L., Grigoriev, M. N., Maksimov, G. M., Biskaborn, B. K., Grosse, G., & Strauss, J. (2020a). *n*-Alkane Characteristics of Thawed Permafrost Deposits Below a Thermokarst Lake on Bykovsky Peninsula, Northeastern Siberia. *Frontiers in Environmental Science*, *8*, 118. https://doi.org/10.3389/fenvs.2020.00118

Jongejans, L. L., Mangelsdorf, K., & Strauss, J. (2020b). *n*-Alkanes, total organic carbon content, radiocarbon ages, grain size distribution, biogeochemical and hydrochemical parameters of sediment core beneath thermokarst lake Goltsovoye Lake on the Bykovsky Pensinula, northeastern Siberia [Type: data set]. https://doi.org/10.1594/PANGAEA.919811

Jongejans, L. L., Opel, T., Courtin, J., Meyer, H., Kizyakov, A. I., Syromyatnikov, I., Shepelev, A., & Wetterich, S. (2021g). Batagay Spring 2019 [Publication Title: Berichte zur Polar- und Meeresforschung = Reports on polar and marine research]. *Russian-German Cooperation: Expeditions to Siberia in 2019*. Alfred Wegener Institute for Polar; Marine Research. https://doi.org/10.48433/BzPM_0749_2021

Jongejans, L. L., Strauss, J., Lenz, J., Peterse, F., Mangelsdorf, K., Fuchs, M., & Grosse, G. (2018). Organic matter characteristics in yedoma and thermokarst deposits on Baldwin Peninsula, west Alaska. *Biogeosciences*, *15*(20), 6033–6048. https://doi.org/10.5194/bg-15-6033-2018

Jorgenson, M. T., & Brown, J. (2005). Classification of the Alaskan Beaufort Sea Coast and estimation of carbon and sediment inputs from coastal erosion. *Geo-Marine Letters*, *25*(2), 69–80. https://doi.org/10.1007/s00367-004-0188-8

Ju, J., & Masek, J. G. (2016). The vegetation greenness trend in Canada and US Alaska from 1984–2012 Landsat data. *Remote Sensing of Environment*, *176*, 1–16. https://doi.org/10.1016/j.rse.2016.01.001

Juggins, S. (2020). *rioja: Analysis of Quaternary Science Data*.

Kaiser, C., Meyer, H., Biasi, C., Rusalimova, O., Barsukov, P., & Richter, A. (2007). Conservation of soil organic matter through cryoturbation in arctic soils in Siberia. *Journal of Geophysical Research: Biogeosciences*, *112*(G2). https://doi.org/10.1029/2006JG000258

Kaneda, T. (1991). Iso-and anteiso-fatty acids in bacteria: biosynthesis, function, and taxonomic significance. *Microbiological reviews*, *55*(2), 288–302. https://doi.org/10.1128/mr.55.2.288-302.1991

Kanevskiy, M., Shur, Y., Fortier, D., Jorgenson, M. T., & Stephani, E. (2011). Cryostratigraphy of late Pleistocene syngenetic permafrost (yedoma) in northern Alaska, Itkillik River exposure. *Quaternary Research*, *75*(3), 584–596. https://doi.org/10.1016/j.yqres.2010.12.003

Kanevskiy, M., Shur, Y., Strauss, J., Jorgenson, T., Fortier, D., Stephani, E., & Vasiliev, A. (2016). Patterns and rates of riverbank erosion involving ice-rich permafrost (yedoma) in northern Alaska. *Geomorphology*, *253*, 370–384. https://doi.org/10.1016/j.geomorph.2015.10.023

Karlsson, E. S., Charkin, A., Dudarev, O., Semiletov, I., Vonk, J. E., Sánchez-García, L., Andersson, A., & Gustafsson, Ö. (2011). Carbon isotopes and lipid biomarker investigation of sources, transport and degradation of terrestrial organic matter in the Buor-Khaya Bay, SE Laptev Sea. *Biogeosciences*, *8*(7), 1865–1879. https://doi.org/10.5194/bg-8-1865-2011

Katasonov, E., Ivanov, M., Pudov, G., et al. (1979). Structure and absolute geochronology of alas deposits in Central Yakutia. *Novosibirsk: Science*, 95.

Kenig, F., Simons, D.-J. H., Crich, D., Cowen, J. P., Ventura, G. T., Rehbein-Khalily, T., Brown, T. C., & Anderson, K. B. (2003). Branched aliphatic alkanes with quaternary substituted carbon atoms in modern and ancient geologic samples. *Proceedings of the National Academy of Sciences*, *100*(22), 12554–12558. https://doi.org/10.1073/pnas.1735581100

Kenig, F., Simons, D.-J. H., Crich, D., Cowen, J. P., Ventura, G. T., & Rehbein-Khalily, T. (2005). Structure and distribution of branched aliphatic alkanes with quaternary carbon atoms in Cenomanian and Turonian black shales of Pasquia Hills (Saskatchewan, Canada). *Organic Geochemistry*, *36*(1), 117–138. https://doi.org/10.1016/j.orggeochem.2004.06.014

Kessler, M. A., Plug, L. J., & Walter Anthony, K. M. (2012). Simulating the decadal- to millennial-scale dynamics of morphology and sequestered carbon mobilization of two thermokarst lakes in NW Alaska. *Journal of Geophysical Research: Biogeosciences*, *117*(G2). https://doi.org/10.1029/2011JG001796

Killops, S. D., & Killops, V. J. (2013). *Introduction to organic geochemistry.* John Wiley & Sons.

Kim, S., Stanford, L. A., Rodgers, R. P., Marshall, A. G., Walters, C. C., Qian, K., Wenger, L. M., & Mankiewicz, P. (2005). Microbial alteration of the acidic and neutral polar NSO compounds revealed by Fourier transform ion cyclotron resonance mass spectrometry. *Organic Geochemistry*, *36*(8), 1117–1134. https://doi.org/10.1016/j.orggeochem.2005.03.010

Klein, K. P., Lantuit, H., Heim, B., Doxaran, D., Juhls, B., Nitze, I., Walch, D., Poste, A., & Søreide, J. E. (2021). The Arctic Nearshore Turbidity Algorithm (ANTA)-A multi sensor turbidity algorithm for Arctic nearshore environments. *Science of Remote Sensing*, 100036. https://doi.org/10.1016/j.srs.2021.100036

Knoblauch, C., Beer, C., Liebner, S., Grigoriev, M. N., & Pfeiffer, E.-M. (2018). Methane production as key to the greenhouse gas budget of thawing permafrost. *Nature Climate Change*, *8*(4), 309–312. https://doi.org/10.1038/s41558-018-0095-z

Knoblauch, C., Beer, C., Sosnin, A., Wagner, D., & Pfeiffer, E.-M. (2013). Predicting long-term carbon mineralization and trace gas production from thawing permafrost of Northeast Siberia. *Global Change Biology*, *19*(4), 1160–1172. https://doi.org/10.1111/gcb.12116

Kokelj, S. V., Lacelle, D., Lantz, T. C., Tunnicliffe, J., Malone, L., Clark, I. D., & Chin, K. S. (2013). Thawing of massive ground ice in mega slumps drives increases in stream sediment and solute flux across a range of watershed scales [00060]. *Journal of Geophysical Research: Earth Surface*, *118*(2), 681–692. https://doi.org/10.1002/jgrf.20063

Kuhry, P., Bárta, J., Blok, D., Elberling, B., Faucherre, S., Hugelius, G., Jørgensen, C. J., Richter, A., Šantrůčková, H., & Weiss, N. (2020). Lability classification of soil organic matter in the northern permafrost region. *Biogeosciences*, *17*(2), 361–379. https://doi.org/10.5194/bg-17-361-2020

Kuhry, P., & Vitt, D. H. (1996). Fossil Carbon/Nitrogen Ratios as a Measure of Peat Decomposition. *Ecology*, *77*(1), 271–275. https://doi.org/10.2307/2265676

Kunitsky, V. V. (1989). Kriolitologiya nizo'ev Leny (Cryolithology ofthe Lower Lena). *Permafrost Institute Press, Yakutsk*, In Russian.

Kunitsky, V. V., Syromyatnikov, I., Schirrmeister, L., Skachov, Y. B., Grosse, G., Wetterich, S., & Grigoriev, M. N. (2013). Ice-rich Permafrost and thermal denudation in the Batagay area (Yana Upland, East Siberia). *Earth Cryosphere (Kriosfera Zemli)*, *17*(1), 56–58.

Kutzbach, L., Wagner, D., & Pfeiffer, E.-M. (2004). Effect of microrelief and vegetation on methane emission from wet polygonal tundra, Lena Delta, Northern Siberia. *Biogeochemistry*, *69*(3), 341–362. https://doi.org/10.1023/B:BIOG.0000031053.81520.db

Lacelle, D., Bjornson, J., & Lauriol, B. (2010). Climatic and geomorphic factors affecting contemporary (1950–2004) activity of retrogressive thaw slumps on the Aklavik Plateau, Richardson Mountains, NWT, Canada. *Permafrost and Periglacial Processes*, *21*(1), 1–15. https://doi.org/10.1002/ppp.666

Lacelle, D., Fontaine, M., Pellerin, A., Kokelj, S. V., & Clark, I. D. (2019). Legacy of Holocene Landscape Changes on Soil Biogeochemistry: A Perspective From Paleo-Active Layers in Northwestern Canada. *Journal of Geophysical Research: Biogeosciences*, *124*(9), 2662–2679. https://doi.org/10.1029/2018JG004916

Lantuit, H., & Pollard, W. H. (2005). Temporal stereophotogrammetric analysis of retrogressive thaw slumps on Herschel Island, Yukon Territory. *Natural Hazards and Earth System Sciences*, *5*(3), 413–423. https://doi.org/10.5194/nhess-5-413-2005

Lantuit, H., & Pollard, W. H. (2008). Fifty years of coastal erosion and retrogressive thaw slump activity on Herschel Island, Southern Beaufort Sea, Yukon Territory, Canada. *Geomorphology*, *95*(1), 84–102. https://doi.org/10.1016/j.geomorph.2006.07.040

Lawrimore, J. H., Menne, M. J., Gleason, B. E., Williams, C. N., Wuertz, D. B., Vose, R. S., & Rennie, J. (2011). An overview of the Global Historical Climatology Network monthly mean temperature data set, version 3. *Journal of Geophysical Research: Atmospheres*, *116*(D19). https://doi.org/10.1029/2011JD016187

Lee, H., Schuur, E. A. G., Inglett, K. S., Lavoie, M., & Chanton, J. P. (2012). The rate of permafrost carbon release under aerobic and anaerobic conditions and its potential effects on climate. *Global Change Biology*, *18*(2), 515–527. https://doi.org/10.1111/j.1365-2486.2011.02519.x

Lenz, J., Jones, B. M., Wetterich, S., Tjallingii, R., Fritz, M., Arp, C. D., Rudaya, N., & Grosse, G. (2016a). Impacts of shore expansion and catchment characteristics on lacustrine thermokarst records in permafrost lowlands, Alaska Arctic Coastal Plain. *arktos*, *2*(1), 25. https://doi.org/10.1007/s41063-016-0025-0

Lenz, J., Wetterich, S., Jones, B. M., Meyer, H., Bobrov, A., & Grosse, G. (2016b). Evidence of multiple thermokarst lake generations from an 11 800-year-old permafrost core on the northern Seward Peninsula, Alaska. *Boreas*, *45*(4), 584–603. https://doi.org/10.1111/bor.12186

Lewkowicz, A. G. (1987). Headwall retreat of ground-ice slumps, Banks Island, Northwest Territories. *Canadian Journal of Earth Sciences*, *24*(6), 1077–1085. https://doi.org/10.1139/e87-105

Liebner, S., Harder, J., & Wagner, D. (2008). Bacterial diversity and community structure in polygonal tundra soils from Samoylov Island, Lena Delta, Siberia. *International Microbiology*, *11*, 195–202. https://doi.org/10.2436/20.1501.01.60

Liljedahl, A. K., Boike, J., Daanen, R. P., Fedorov, A. N., Frost, G. V., Grosse, G., Hinzman, L. D., Iijma, Y., Jorgenson, J. C., Matveyeva, N., Necsoiu, M., Raynolds, M. K., Romanovsky, V. E., Schulla, J., Tape, K. D., Walker, D. A., Wilson, C. J., Yabuki, H., & Zona, D. (2016). Pan-Arctic ice-wedge degradation in warming permafrost and its influence on tundra hydrology. *Nature Geoscience*, *9*(4), 312–318. https://doi.org/10.1038/ngeo2674

Ling, F., & Zhang, T. (2003). Numerical simulation of permafrost thermal regime and talik development under shallow thaw lakes on the Alaskan Arctic Coastal Plain. *Journal of Geophysical Research: Atmospheres*, *108*(D16). https://doi.org/10.1029/2002JD003014

Lupascu, M., Wadham, J. L., Hornibrook, E. R. C., & Pancost, R. D. (2012). Temperature Sensitivity of Methane Production in the Permafrost Active Layer at Stordalen, Sweden: A Comparison with Non-permafrost Northern Wetlands. *Arctic, Antarctic, and Alpine Research*, *44*(4), 469–482. https://doi.org/10.1657/1938-4246-44.4.469

Lützow, M. v., Kögel-Knabner, I., Ekschmitt, K., Matzner, E., Guggenberger, G., Marschner, B., & Flessa, H. (2006). Stabilization of organic matter in temperate soils: mechanisms and their relevance under different soil conditions – a review. *European Journal of Soil Science*, *57*(4), 426–445. https://doi.org/10.1111/j.1365-2389.2006.00809.x

Mackelprang, R., Burkert, A., Haw, M., Mahendrarajah, T., Conaway, C. H., Douglas, T. A., & Waldrop, M. P. (2017). Microbial survival strategies in ancient permafrost: insights from metagenomics. *The ISME Journal*, *11*(10), 2305–2318. https://doi.org/10.1038/ismej.2017.93

Mackelprang, R., Waldrop, M. P., DeAngelis, K. M., David, M. M., Chavarria, K. L., Blazewicz, S. J., Rubin, E. M., & Jansson, J. K. (2011). Metagenomic analysis of a permafrost microbial community reveals a rapid response to thaw. *Nature*, *480*(7377), 368–371. https://doi.org/10.1038/nature10576

Manizza, M., Follows, M. J., Dutkiewicz, S., McClelland, J. W., Menemenlis, D., Hill, C. N., Townsend-Small, A., & Peterson, B. J. (2009). Modeling transport and fate of riverine dissolved organic carbon in the Arctic Ocean. *Global Biogeochemical Cycles*, *23*(4). https://doi.org/10.1029/2008GB003396

Mann, P. J., Eglinton, T. I., McIntyre, C. P., Zimov, N., Davydova, A., Vonk, J. E., Holmes, R. M., & Spencer, R. G. M. (2015). Utilization of ancient permafrost carbon in headwaters of Arctic fluvial networks. *Nature Communications*, *6*, 7856. https://doi.org/10.1038/ncomms8856

Mann, P. J., Strauss, J., Palmtag, J., Dowdy, K., Ogneva, O., Fuchs, M., Bedington, M., Torres, R., Polimene, L., Overduin, P., Mollenhauer, G., Grosse, G., Rachold, V., Sobczak, W. V., Spencer, R. G. M., & Juhls, B. (2021). Degrading permafrost river catchments and their impact on Arctic Ocean nearshore processes. *Ambio*. https://doi.org/10.1007/s13280-021-01666-z

Manson, G. K., & Solomon, S. M. (2007). Past and future forcing of Beaufort Sea coastal change. *Atmosphere-Ocean*, *45*(2), 107–122. https://doi.org/10.3137/ao.450204

Martinez-Cruz, K., Sepulveda-Jauregui, A., Walter Anthony, K., & Thalasso, F. (2015). Geographic and seasonal variation of dissolved methane and aerobic methane oxidation in Alaskan lakes. *Biogeosciences*, *12*(15), 4595–4606. https://doi.org/10.5194/bg-12-4595-2015

Martinez-Cruz, K., Leewis, M.-C., Herriott, I. C., Sepulveda-Jauregui, A., Anthony, K. W., Thalasso, F., & Leigh, M. B. (2017). Anaerobic oxidation of methane by aerobic methanotrophs in sub-Arctic lake sediments. *Science of The Total Environment*, *607-608*, 23–31. https://doi.org/10.1016/j.scitotenv.2017.06.187

Marzi, R., Torkelson, B. E., & Olson, R. K. (1993). A revised carbon preference index. *Organic Geochemistry*, *20*(8), 1303–1306. https://doi.org/10.1016/0146-6380(93)90016-5

McGuire, A. D., Lawrence, D. M., Koven, C., Clein, J. S., Burke, E., Chen, G., Jafarov, E., MacDougall, A. H., Marchenko, S., Nicolsky, D., et al. (2018). Dependence of the evolution of carbon dynamics in the northern permafrost region on the trajectory of climate change. *Proceedings of the National Academy of Sciences*, *115*(15), 3882–3887. https://doi.org/10.1073/pnas.1719903115

Meredith, M., Sommerkorn, M., Cassotta, S., Derksen, C., Ekaykin, A., Hollowed, A., Kofinas, G., Mackintosh, A., Melbourne-Thomas, J., Muelbert, M., Ottersen, G., Pritchard, H., & Schuur, E. (2019). Polar Regions. In H.-O. Pörtner, D. Roberts, V. Masson-Delmotte, P. Zhai, M. Tignor, E. Poloczanska, K. Mintenbeck, A. Alegría, M. Nicolai, A. Okern, J. Petzold, B. Rama, & N. Weyer (Eds.), *IPCC Special Report on the Ocean and Cryosphere in a Changing Climate*.

Meyers, P. A. (1994). Preservation of elemental and isotopic source identification of sedimentary organic matter. *Chemical geology*, *114*(3-4), 289–302. https://doi.org/10.1016/0009-2541(94)90059-0

Miller, P. A., & Smith, B. (2012). Modelling Tundra Vegetation Response to Recent Arctic Warming. *AMBIO*, *41*(3), 281–291. https://doi.org/10.1007/s13280-012-0306-1

Mishra, U., Hugelius, G., Shelef, E., Yang, Y., Strauss, J., Lupachev, A., Harden, J. W., Jastrow, J. D., Ping, C.-L., Riley, W. J., et al. (2021). Spatial heterogeneity and environmental predictors of permafrost region soil organic carbon stocks. *Science advances*, *7*(9), eaaz5236. https://doi.org/10.1126/sciadv.aaz5236

Mitzscherling, J., Horn, F., Winterfeld, M., Mahler, L., Kallmeyer, J., Overduin, P. P., Schirrmeister, L., Winkel, M., Grigoriev, M. N., Wagner, D., & Liebner, S. (2019). Microbial community composition and abundance after millennia of submarine permafrost warming. *Biogeosciences*, *16*(19), 3941–3958. https://doi.org/10.5194/bg-16-3941-2019

Mitzscherling, J., Winkel, M., Winterfeld, M., Horn, F., Yang, S., Grigoriev, M. N., Wagner, D., Overduin, P. P., & Liebner, S. (2017). The development of permafrost bacterial communities under submarine conditions. *Journal of Geophysical Research: Biogeosciences*, *122*(7), 1689–1704. https://doi.org/10.1002/2017JG003859

Mollenhauer, G., Grotheer, H., Gentz, T., Bonk, E., & Hefter, J. H. (2021). Standard operation procedures and performance of the MICADAS radiocarbon laboratory at Alfred Wegener Institute (AWI), Germany. *Nuclear Instruments and Methods in Physics Research Section B: Beam Interactions with Materials and Atoms*, *496*, 45–51. https://doi.org/10.1016/j.nimb.2021.03.016

Morgenstern, A., Grosse, G., Günther, F., Fedorova, I., & Schirrmeister, L. (2011). Spatial analyses of thermokarst lakes and basins in Yedoma landscapes of the Lena Delta. *The Cryosphere*, *5*(4), 849–867. https://doi.org/10.5194/tc-5-849-2011

Mueller, C. W., Rethemeyer, J., Kao-Kniffin, J., Löppmann, S., Hinkel, K. M., & G Bockheim, J. (2015). Large amounts of labile organic carbon in permafrost soils of northern Alaska. *Global change biology*, *21*(7), 2804–2817. https://doi.org/10.1111/gcb.12876

Murton, J. B., Edwards, M. E., Lozhkin, A. V., Anderson, P. M., Savvinov, G. N., Bakulina, N., Bondarenko, O. V., Cherepanova, M. V., Danilov, P. P., Boeskorov, V., Goslar, T., Grigoriev, S., Gubin, S. V., Korzun, J. A., Lupachev, A. V., Tikhonov, A., Tsygankova, V. I., Vasilieva, G. V., & Zanina, O. G. (2017). Preliminary paleoenvironmental analysis of permafrost deposits at Batagaika megaslump, Yana Uplands, northeast Siberia [Edition: 2017/02/16 Publisher: Cambridge University Press]. *Quaternary Research*, *87*(2), 314–330. https://doi.org/10.1017/qua.2016.15

Murton, J. B., Opel, T., Toms, P., Blinov, A., Fuchs, M., Wood, J., Gärtner, A., Merchel, S., Rugel, G., Savvinov, G., & Wetterich, S. (2021). A multimethod dating study of ancient permafrost, Batagay megaslump, east Siberia. *Quaternary Research*, 1–22. https://doi.org/10.1017/qua.2021.27

Murton, J. B., Savvinov, G., & Opel, T. (accepted). Batagay Megaslump. In A. Panin & F. Romanenko (Eds.).

Myhre, G., Shindell, D., Bréon, F.-M., Collins, W., Fuglestvedt, J., Huang, J., Koch, D., Lamarque, J.-F., Lee, D., Mendoza, B., Nakajima, T., Robock, A., Stephens, G., Takemura, T., & Zhang, H. (2013). Anthropogenic and Natural Radiative Forcing. In T. Stocker, D. Qin, G.-K. Plattner, M. Tignor, S. Allen, J. Boschung, A. Nauels, Y. Xia, V. Bex, & P. Midgley (Eds.), *Climate Change 2013: The Physical Science Basis. Contribution of Working Group I to the Fifth Assessment Report of the Intergovernmental Panel on Climate Change* (pp. 659–740). Cambridge University Press.

Neubauer, D. (2016). Characterization of organic matter stored in Yedoma and thermokarst permafrost. *Unpublished MSc Thesis, Freie Universität Berlin.*

Nitzbon, J., Westermann, S., Langer, M., Martin, L. C., Strauss, J., Laboor, S., & Boike, J. (2020). Fast response of cold ice-rich permafrost in northeast Siberia to a warming climate. *Nature communications*, *11*(1), 1–11. https://doi.org/10.1038/s41467-020-15725-8

Nitze, I., & Grosse, G. (2016). Detection of landscape dynamics in the Arctic Lena Delta with temporally dense Landsat time-series stacks. *Remote Sensing of Environment*, *181*, 27–41. https://doi.org/10.1016/j.rse.2016.03.038

Nitze, I., Grosse, G., Jones, B. M., Arp, C. D., Ulrich, M., Fedorov, A., & Veremeeva, A. (2017). Landsat-Based Trend Analysis of Lake Dynamics across Northern Permafrost Regions. *Remote Sensing*, *9*(7, 640), 1–28. https://doi.org/10.3390/rs9070640

Obu, J., Westermann, S., Bartsch, A., Berdnikov, N., Christiansen, H. H., Dashtseren, A., Delaloye, R., Elberling, B., Etzelmüller, B., Kholodov, A., Khomutov, A., Kääb, A., Leibman, M. O., Lewkowicz, A. G., Panda, S. K., Romanovsky, V., Way, R. G., Westergaard-Nielsen, A., Wu, T., … Zou, D. (2019). Northern Hemisphere permafrost map based on TTOP modelling for 2000–2016 at 1 km^2 scale. *Earth-Science Reviews*, *193*, 299–316. https://doi.org/10.1016/j.earscirev.2019.04.023

Ogihara, S., & Ishiwatari, R. (1998). Unusual distribution of hydrocarbons in a hydrothermally altered phosphorite nodule from Kusu Basin, northern Kyushu, Japan. *Organic Geochemistry*, *29*(1-3), 155–161. https://doi.org/10.1016/S0146-6380(98)00052-7

Opel, T., Murton, J. B., Wetterich, S., Meyer, H., Ashastina, K., Günther, F., Grotheer, H., Mollenhauer, G., Danilov, P. P., Boeskorov, V., Savvinov, G. N., & Schirrmeister, L. (2019). Past climate and continentality inferred from ice wedges at Batagay megaslump in the Northern Hemisphere's most continental region, Yana Highlands, interior Yakutia. *Climate of the Past*, *15*(4), 1443–1461. https://doi.org/10.5194/cp-15-1443-2019

Overduin, P. P., Rachold, V., & Grigoriev, M. N. (2008). The State of Subsea Permafrost in the Western Laptev Nearshore Zone. *Proceedings of the Ninth International Conference on Permafrost, Faribanks, Alaska*, *2008*, 1345–1350.

Palmtag, J., Hugelius, G., Lashchinskiy, N., Tamstorf, M. P., Richter, A., Elberling, B., & Kuhry, P. (2015). Storage, landscape distribution, and burial history of soil organic matter in contrasting areas of continuous permafrost. *Arctic, Antarctic, and Alpine Research*, *47*(1), 71–88. https://doi.org/10.1657/AAAR0014-027

Pancost, R. D., McClymont, E. L., Bingham, E. M., Roberts, Z., Charman, D. J., Hornibrook, E. R., Blundell, A., Chambers, F. M., Lim, K. L., & Evershed, R. P. (2011). Archaeol as a methanogen biomarker in ombrotrophic bogs. *Organic Geochemistry*, *42*(10), 1279–1287. https://doi.org/10.1016/j.orggeochem.2011.07.003

Peters, K. E., Walters, C. C., & Moldowan, J. M. (2005). *The biomarker guide, 1, Biomarkers and isotopes in the environment and human history* (Second). Cambridge University Press.

Phoenix, G. K., & Bjerke, J. W. (2016). Arctic browning: extreme events and trends reversing arctic greening. *Global Change Biology*, *22*(9), 2960–2962. https://doi.org/10.1111/gcb.13261

Piorreck, M., Baasch, K.-H., & Pohl, P. (1984). Biomass production, total protein, chlorophylls, lipids and fatty acids of freshwater green and blue-green algae under different nitrogen regimes. *Phytochemistry*, *23*(2), 207–216. https://doi.org/10.1016/S0031-9422(00)80304-0

Polimene, L., Torres, R., Powley, H. R., Bedington, M., Juhls, B., Palmtag, J., Strauss, J., & Mann, P. J. (2022). Biological lability of terrigenous DOC increases CO_2 outgassing across Arctic shelves. *Biogeochemistry Letters*. https://doi.org/10.1007/s10533-022-00961-5

Poynter, J. (1989). Molecular stratigraphy: The recognition of palaeoclimatic signals in organic geochemical data. *PhD, School of Chemistry, University of Bristol, Bristol.*

Poynter, J., & Eglinton, G. (1990). 14. Molecular composition of three sediments from hole 717c: The Bengal fan. *Proceedings of the Ocean Drilling Program: Scientific results*, *116*, 155–161.

Radke, M., Willsch, H., & Welte, D. H. (1980). Preparative hydrocarbon group type determination by automated medium pressure liquid chromatography. *Analytical Chemistry*, *52*(3), 406–411. https://doi.org/10.1021/ac50053a009

Rajendran, S., Sadooni, F. N., Al-Kuwari, H. A.-S., Oleg, A., Govil, H., Nasir, S., & Vethamony, P. (2021). Monitoring oil spill in Norilsk, Russia using satellite data. *Scientific Reports*, *11*(1), 3817. https://doi.org/10.1038/s41598-021-83260-7

Ramage, J. L., Irrgang, A. M., Morgenstern, A., & Lantuit, H. (2018). Increasing coastal slump activity impacts the release of sediment and organic carbon into the Arctic Ocean. *Biogeosciences*, *15*(5), 1483–1495. https://doi.org/10.5194/bg-15-1483-2018

Raymond, P. A., McClelland, J., Holmes, R., Zhulidov, A., Mull, K., Peterson, B., Striegl, R. G., Aiken, G., & Gurtovaya, T. (2007). Flux and age of dissolved organic carbon exported to the Arctic Ocean: A carbon isotopic study of the five largest arctic rivers. *Global Biogeochemical Cycles*, *21*(4). https://doi.org/10.1029/2007GB002934

Retamal, L., Bonilla, S., & Vincent, W. F. (2007). Optical gradients and phytoplankton production in the Mackenzie River and the coastal Beaufort Sea. *Polar Biology*, *31*(3), 363–379. https://doi.org/10.1007/s00300-007-0365-0

Reyes, A. V., Froese, D. G., & Jensen, B. J. L. (2010). Permafrost response to last interglacial warming: field evidence from non-glaciated Yukon and Alaska. *Quaternary Science Reviews*, *29*(23), 3256–3274. https://doi.org/10.1016/j.quascirev.2010.07.013

Richardson, D. C., Newbold, J. D., Aufdenkampe, A. K., Taylor, P. G., & Kaplan, L. A. (2013). Measuring heterotrophic respiration rates of suspended particulate organic carbon from stream ecosystems. *Limnology and Oceanography: Methods*, *11*(5), 247–261. https://doi.org/10.4319/lom.2013.11.247

Richter-Menge, J., Overland, J., Mathis, J., & Osborne, E. (Eds.). (2017). *Arctic Report Card 2017*.

Rilfors, L., Wieslander, Å., & Ståhl, S. (1978). Lipid and protein composition of membranes of Bacillus megaterium variants in the temperature range 5 to 70 degrees C. *Journal of Bacteriology*, *135*(3), 1043–1052.

Rohde, R., Muller, R., Jacobsen, R., Muller, E., Perlmutter, S., Rosenfeld, A., Wurtele, J., Groom, D., & Wickham, C. (2013). A New Estimate of the Average Earth Surface Land Temperature Spanning 1753 to 2011, Geoinfor Geostat: An Overview 1: 1. *of*, *7*, 2. https://doi.org/10.4172/2327-4581.1000101

Romankevich, E. A., Vetrov, A. A., Belyaev, N. A., Sergienko, V. I., Semiletov, I. P., Sukhoverkhov, S. V., Bratskaya, S. Y., Prokuda, N. A., & Ulyantsev, A. S. (2017). Alkanes in Quaternary deposits of the Laptev Sea. *Doklady Earth Sciences*, *472*(1), 36–39. https://doi.org/10.1134/S1028334X17010093

Romanovskii, N. (1993). *Fundamentals of cryogenesis of lithosphere.* Moscow University Press, Moscow. In Russian.

Sánchez-García, L., Vonk, J. E., Charkin, A. N., Kosmach, D., Dudarev, O. V., Semiletov, I. P., & Gustafsson, Ö. (2014). Characterisation of Three Regimes of Collapsing Arctic Ice Complex Deposits on the SE Laptev Sea Coast using Biomarkers and Dual Carbon Isotopes. *Permafrost and Periglacial Processes*, *25*(3), 172–183. https://doi.org/10.1002/ppp.1815

Sanders, T., Fiencke, C., Fuchs, M., Haugk, C., Juhls, B., Mollenhauer, G., Ogneva, O., Overduin, P. P., Palmtag, J., Povazhniy, V., Strauss, J., Tuerena, R., Zell, N., &

Dähnke, K. (accepted). Seasonal nitrogen fluxes of the Lena River Delta. *Ambio*. https://doi.org/10.1007/s13280-021-01665-0

Savvinov, G., Danilov, P., Petrov, A., Makarov, V., Boeskorov, V., & Grigoriev, S. (2018). Environmental problems of the Verkhoyansky Region. *Vestnik of North-Eastern Federal University. Series "Earth Sciences*, (6), 68.

Schädel, C., Bader, M. K.-F., Schuur, E. A. G., Biasi, C., Bracho, R., Čapek, P., De Baets, S., Diáková, K., Ernakovich, J., Estop-Aragones, C., Graham, D. E., Hartley, I. P., Iversen, C. M., Kane, E., Knoblauch, C., Lupascu, M., Martikainen, P. J., Natali, S. M., Norby, R. J., … Wickland, K. P. (2016). Potential carbon emissions dominated by carbon dioxide from thawed permafrost soils. *Nature Climate Change*, *6*, 950–954. https://doi.org/10.1038/nclimate3054

Schädel, C., Schuur, E. A. G., Bracho, R., Elberling, B., Knoblauch, C., Lee, H., Luo, Y., Shaver, G. R., & Turetsky, M. R. (2014). Circumpolar assessment of permafrost C quality and its vulnerability over time using long-term incubation data. *Global Change Biology*, *20*(2), 641–652. https://doi.org/10.1111/gcb.12417

Schäfer, I. K., Lanny, V., Franke, J., Eglinton, T. I., Zech, M., Vysloužilová, B., & Zech, R. (2016). Leaf waxes in litter and topsoils along a European transect. *Soil*, *2*(4), 551–564. https://doi.org/10.5194/soil-2-551-2016

Schellekens, J., Bindler, R., Martínez-Cortizas, A., McClymont, E. L., Abbott, G. D., Biester, H., Pontevedra-Pombal, X., & Buurman, P. (2015). Preferential degradation of polyphenols from Sphagnum – 4-Isopropenylphenol as a proxy for past hydrological conditions in Sphagnum-dominated peat. *Geochimica et Cosmochimica Acta*, *150*, 74–89. https://doi.org/10.1016/j.gca.2014.12.003

Schirrmeister, L. (2012). Late Glacial to Holocene landscape dynamics of Arctic coastal lowlands in NE Siberia. *Quaternary International*, (279-280), 434. https://doi.org/10.1016/j.quaint.2012.08.1413

Schirrmeister, L., Bobrov, A., Raschke, E., Herzschuh, U., Strauss, J., Pestryakova, L. A., & Wetterich, S. (2018). Late Holocene ice-wedge polygon dynamics in northeastern Siberian coastal lowlands. *Arctic, Antarctic, and Alpine Research*, *50*(1), e1462595. https://doi.org/10.1080/15230430.2018.1462595

Schirrmeister, L., Dietze, E., Matthes, H., Grosse, G., Strauss, J., Laboor, S., Ulrich, M., Kienast, F., & Wetterich, S. (2020). The genesis of Yedoma Ice Complex permafrost – grain-size endmember modeling analysis from Siberia and Alaska. *E&G Quaternary Science Journal*, *69*(1), 33–53. https://doi.org/10.5194/egqsj-69-33-2020

Schirrmeister, L., Froese, D., Tumskoy, V., Grosse, G., & Wetterich, S. (2013). Yedoma: Late Pleistocene ice-rich syngenetic permafrost of Beringia. *Encyclopedia of Quaternary Science. 2nd edition* (pp. 542–552). Elsevier. https://doi.org/10.1016/b978-0-444-53643-3.00106-0

Schirrmeister, L., Grosse, G., Kunitsky, V., Magens, D., Meyer, H., Dereviagin, A., Kuznetsova, T., Andreev, A., Babiy, O., Kienast, F., Grigoriev, M., Overduin, P. P., & Preusser, F. (2008a). Periglacial landscape evolution and environmental changes of Arctic lowland areas for the last 60 000 years (western Laptev Sea coast, Cape Mamontov Klyk). *Polar Research*, *27*(2), 249–272. https://doi.org/10.1111/j.1751-8369.2008.00067.x

Schirrmeister, L., Grosse, G., Schwamborn, G., Andreev, A., Meyer, H., Kunitsky, V. V., Kuznetsova, T., Dorozhkina, M. V., Pavlova, E. Y., Bobrov, A., & Oezen, D. (2003). Late Quaternary history of the accumulation plain north of the Chekanovsky Ridge (Lena Delta, Russia) - a multidisciplinary approach. *Polar Geography*, *27*(4), 277–319. https://doi.org/10.1080/789610225

Schirrmeister, L., Grosse, G., Wetterich, S., Overduin, P. P., Strauss, J., Schuur, E. A. G., & Hubberten, H.-W. (2011a). Fossil organic matter characteristics in permafrost deposits of the northeast Siberian Arctic. *Journal of Geophysical Research: Biogeosciences*, *116*(G2), 1–16. https://doi.org/10.1029/2011JG001647

Schirrmeister, L., Kunitsky, V., Grosse, G., Wetterich, S., Meyer, H., Schwamborn, G., Babiy, O., Derevyagin, A., & Siegert, C. (2011b). Sedimentary characteristics and origin of the Late Pleistocene Ice Complex on north-east Siberian Arctic coastal lowlands and islands - A review. *Quaternary international*, *241*(1-2), 3–25. https://doi.org/10.1016/j.quaint.2010.04.004

Schirrmeister, L., Kunitsky, V. V., Grosse, G., Kuznetsova, T. V., Derevyagin, A. Y., Wetterich, S., & Siegert, C. (2008b). The Yedoma Suite of the Northeastern Siberian Shelf Region characteristics and concept of formation. *Proceedings of the Ninth International Conference on Permafrost.*

Schirrmeister, L., Schwamborn, G., Overduin, P. P., Strauss, J., Fuchs, M. C., Grigoriev, M., Yakshina, I., Rethemeyer, J., Dietze, E., & Wetterich, S. (2017). Yedoma Ice Complex of the Buor Khaya Peninsula (southern Laptev Sea). *Biogeosciences*, *14*(5), 1261–1283. https://doi.org/10.5194/bg-14-1261-2017

Schirrmeister, L., Siegert, C., Kunitzky, V. V., Grootes, P. M., & Erlenkeuser, H. (2002a). Late Quaternary ice-rich permafrost sequences as a paleoenvironmental archive for the Laptev Sea Region in northern Siberia. *International journal of earth sciences*, *91*(1), 154–167. https://doi.org/10.1007/s005310100205

Schirrmeister, L., Siegert, C., Kuznetsova, T., Kuzmina, S., Andreev, A., Kienast, F., Meyer, H., & Bobrov, A. (2002b). Paleoenvironmental and paleoclimatic records from permafrost deposits in the Arctic region of Northern Siberia. *Quaternary International*, *89*(1), 97–118. https://doi.org/10.1016/S1040-6182(01)00083-0

Schleusner, P., Biskaborn, B. K., Kienast, F., Wolter, J., Subetto, D., & Diekmann, B. (2015). Basin evolution and palaeoenvironmental variability of the thermokarst lake E l'gene-K yuele, Arctic Siberia. *Boreas*, *44*(1), 216–229. https://doi.org/10.1111/bor.12084

Schneider, J., Grosse, G., & Wagner, D. (2009). Land cover classification of tundra environments in the Arctic Lena Delta based on Landsat 7 ETM+ data and its application for upscaling of methane emissions. *Remote Sensing of Environment*, *113*(2), 380–391. https://doi.org/10.1016/j.rse.2008.10.013

Schulte, S., Mangelsdorf, K., & Rullkötter, J. (2000). Organic matter preservation on the Pakistan continental margin as revealed by biomarker geochemistry. *Organic Geochemistry*, *31*(10), 1005–1022. https://doi.org/10.1016/S0146-6380(00)00108-X

Schuur, E. A. G., & Abbott, B. (2011). High risk of permafrost thaw. *Nature*, *480*(7375), 32–33. https://doi.org/10.1038/480032a

Schuur, E. A. G., Bockheim, J., Canadell, J. G., Euskirchen, E., Field, C. B., Goryachkin, S. V., Hagemann, S., Kuhry, P., Lafleur, P. M., Lee, H., Mazhitova, G., Nelson, F. E., Rinke, A., Romanovsky, V. E., Shiklomanov, N., Tarnocai, C., Venevsky, S., Vogel, J. G., & Zimov, S. A. (2008). Vulnerability of Permafrost Carbon to Climate Change: Implications for the Global Carbon Cycle. *BioScience*, *58*(8), 701–714. https://doi.org/10.1641/B580807

Schuur, E. A. G., McGuire, A. D., Schädel, C., Grosse, G., Harden, J. W., Hayes, D. J., Hugelius, G., Koven, C. D., Kuhry, P., Lawrence, D. M., Natali, S. M., Olefeldt, D., Romanovsky, V. E., Schaefer, K., Turetsky, M. R., Treat, C. C., & Vonk, J. E. (2015). Climate change and the permafrost carbon feedback. *Nature*, *520*, 171–179. https://doi.org/10.1038/nature14338

Schuur, E. A. G., Vogel, J. G., Crummer, K. G., Lee, H., Sickman, J. O., & Osterkamp, T. (2009). The effect of permafrost thaw on old carbon release and net carbon exchange from tundra. *Nature*, *459*(7246), 556–559. https://doi.org/10.1038/nature08031

Schwamborn, G., Rachold, V., & Grigoriev, M. N. (2002). Late Quaternary sedimentation history of the Lena Delta. *Quaternary International*, *89*(1), 119–134. https://doi.org/10.1016/S1040-6182(01)00084-2

Semiletov, I., Pipko, I., Gustafsson, Ö., Anderson, L. G., Sergienko, V., Pugach, S., Dudarev, O., Charkin, A., Gukov, A., Bröder, L., Andersson, A., Spivak, E., & Shakhova, N. (2016). Acidification of East Siberian Arctic Shelf waters through addition of freshwater and terrestrial carbon. *Nature Geoscience*, *9*(5), 361–365. https://doi.org/10.1038/ngeo2695

Sepulveda-Jauregui, A., Walter Anthony, K. M., Martinez-Cruz, K., Greene, S., & Thalasso, F. (2015). Methane and carbon dioxide emissions from 40 lakes along a north–south latitudinal transect in Alaska. *Biogeosciences*, *12*(11), 3197–3223. https://doi.org/10.5194/bg-12-3197-2015

Serreze, M. C., & Barry, R. G. (2011). Processes and impacts of Arctic amplification: A research synthesis. *Global and Planetary Change*, *77*(1–2), 85–96. https://doi.org/10.1016/j.gloplacha.2011.03.004

Shiea, J., Brassell, S. C., & Ward, D. M. (1990). Mid-chain branched mono- and dimethyl alkanes in hot spring cyanobacterial mats: A direct biogenic source for branched alkanes in ancient sediments? *Organic Geochemistry*, *15*(3), 223–231. https://doi.org/10.1016/0146-6380(90)90001-G

Shiklomanov, N. I., Streletskiy, D. A., Grebenets, V. I., & Suter, L. (2017a). Conquering the permafrost: urban infrastructure development in Norilsk, Russia. *Polar Geography*, *40*(4), 273–290. https://doi.org/10.1080/1088937X.2017.1329237

Shiklomanov, N. I., Streletskiy, D. A., Swales, T. B., & Kokorev, V. A. (2017b). Climate Change and Stability of Urban Infrastructure in Russian Permafrost Regions: Prognostic Assessment based on GCM Climate Projections. *Geographical Review*, *107*(1), 125–142. https://doi.org/10.1111/gere.12214

Siegert, C., Schirrmeister, L., & Babiy, O. (2002). The sedimentological, mineralogical and geochemical composition of late Pleistocene deposits from the ice complex on the Bykovsky peninsula, northern Siberia. *Polarforschung, 70*, *2000*, 3–11.

Slagoda, E. A. (1993). Genesis i mikrostroenie kriolitogennykh otlozhenii Bykovskogo polyostrova i ostrova Muoastakh [Genesis and microstructure of cryolithogenic deposits at the Bykovsky Peninsula and the Muostakh Island], Ph.D. Thesis. Russian Academy of Science, Siberian Branch, Permafrost Institute Yakutsk. In Russian.

Slagoda, E. A. (2004). Kriogennye otlozheniya Primorskoi ravninymorya Laptebykh: litologiya i mikromorfologiya [CryolithogenicDeposits of the Laptev Sea Coastal Plain: Lithology andMicromorphology]. *Publishing and Printing Centre "Express", Tyumen*, In Russian.

Slagoda, E. A. (2005). Cryogenic structure and genesis of Late Cenozoicwatershed formations at the Primorsky mountain range adjacent tothe Bykovsky Peninsula, Laptev Sea, Russia, 23–24. In Russian.

Smith, L. C. (2005). Disappearing Arctic Lakes. *Science*, *308*(5727), 1429–1429. https://doi.org/10.1126/science.1108142

Soloviev, P. A. (1959). Cryolithic Zone of the Northern Part of Lena-Amga Interfluve. *Izdatel'stvo Akademii SSSR*, *Moscow, p. 142*, In Russian.

Soloviev, P. A. (1973). Thermokarst phenomena and land-forms due to frost heaving in Central Yakutia. *Biuletyn Peryglacialny*, *23*, 135–155.

Spencer, R. G. M., Mann, P. J., Dittmar, T., Eglinton, T. I., McIntyre, C., Holmes, R. M., Zimov, N., & Stubbins, A. (2015). Detecting the signature of permafrost thaw in Arctic rivers. *Geophysical Research Letters*, *42*(8), 2830–2835. https://doi.org/10.1002/2015GL063498

Stapel, J. G., Schirrmeister, L., Overduin, P. P., Wetterich, S., Strauss, J., Horsfield, B., & Mangelsdorf, K. (2016). Microbial lipid signatures and substrate potential of organic matter in permafrost deposits: Implications for future greenhouse gas production. *Journal of Geophysical Research: Biogeosciences*, *121*(10), 2652–2666. https://doi.org/10.1002/2016JG003483

Stapel, J. G., Schwamborn, G., Schirrmeister, L., Horsfield, B., & Mangelsdorf, K. (2018). Substrate potential of last interglacial to Holocene permafrost organic matter for future microbial greenhouse gas production. *Biogeosciences*, *15*(7), 1969–1985. https://doi.org/10.5194/bg-15-1969-2018

Stettner, S., Beamish, A. L., Bartsch, A., Heim, B., Grosse, G., Roth, A., & Lantuit, H. (2018). Monitoring Inter- and Intra-Seasonal Dynamics of Rapidly Degrading Ice-Rich Permafrost Riverbanks in the Lena Delta with TerraSAR-X Time Series. *Remote Sensing*, *10*(1). https://doi.org/10.3390/rs10010051

Strauss, J., Abbott, B. W., Hugelius, G., Schuur, E. A., Treat, C. C., Fuchs, M., Schädel, C., Ulrich, M., Turetsky, M., Keuschnig, M., Biasi, C., Yang, Y., & Grosse, G. (2021a). Permafrost. *Recarbonizing global soils: A technical manual of recommended management practices. Volume 2: Hot spots and bright spots of soil organic carbon.*

Strauss, J., Boike, J., Bolshiyanov, D. Y., Grigoriev, M. N., El-Hajj, H., Morgenstern, A., Overduin, P. P., & Udke, A. (2018). *Russian-German Cooperation: Expeditions to Siberia in 2017* (Vol. 725). Alfred Wegener Institute for Polar; Marine Research. https://doi.org/10.2312/BzPM_0725_2018

Strauss, J., Laboor, S., Schirrmeister, L., Fedorov, A. N., Fortier, D., Froese, D., Fuchs, M., Günther, F., Grigoriev, M., Harden, J., Hugelius, G., Jongejans, L. L., Kanevskiy, M., Kholodov, A., Kunitsky, V., Kraev, G., Lozhkin, A., Rivkina, E., Shur, Y., … Grosse, G. (2021b). Circum-Arctic Map of the Yedoma Permafrost Domain. *Frontiers in Earth Science*, *9*, 1001. https://doi.org/10.3389/feart.2021.758360

Strauss, J., Laboor, S., Schirrmeister, L., Grosse, G., Fortier, D., Hugelius, G., Knoblauch, C., Romanovsky, V. E., Schädel, C., Schneider von Deimling, T., Schuur, E. A. G., Shmelev, D., Ulrich, M., & Veremeeva, A. (2020). Yedoma and Thermokarst site characteristics from sample analysis, 1998-2016, Alaska (US), Northern Siberia (RU) [Type: data set]. *PANGAEA*. https://doi.org/10.1594/PANGAEA.919064

Strauss, J., Schirrmeister, L., Grosse, G., Fortier, D., Hugelius, G., Knoblauch, C., Romanovsky, V., Schädel, C., Deimling, T. S. v., Schuur, E. A. G., Shmelev, D., Ulrich, M., & Veremeeva, A. (2017). Deep Yedoma permafrost: A synthesis of depositional characteristics and carbon vulnerability. *Earth-Science Reviews*, *172*, 75–86. https://doi.org/10.1016/j.earscirev.2017.07.007

Strauss, J., Schirrmeister, L., Grosse, G., Wetterich, S., Ulrich, M., Herzschuh, U., & Hubberten, H.-W. (2013). The deep permafrost carbon pool of the Yedoma region in Siberia and Alaska. *Geophysical Research Letters*, *40*(23), 6165–6170. https://doi.org/10.1002/2013GL058088

Strauss, J., Schirrmeister, L., Mangelsdorf, K., Eichhorn, L., Wetterich, S., & Herzschuh, U. (2015). Organic-matter quality of deep permafrost carbon - a study from Arctic Siberia. *Biogeosciences*, *12*, 2227–2245. https://doi.org/10.5194/bg-12-2227-2015

Strauss, J., Schirrmeister, L., Wetterich, S., Borchers, A., & Davydov, S. P. (2012a). Grain-size properties and organic-carbon stock of Yedoma Ice Complex permafrost from the Kolyma lowland, northeastern Siberia. *Global Biogeochemical Cycles*, *26*(3). https://doi.org/10.1029/2011GB004104

Strauss, J., Ulrich, M., & Buchhorn, M. (2012b). Expeditions to permafrost 2012 : "Alaskan North Slope/Itkillik", "Thermokarst in Central Yakutia", "EyeSight-NAAT-Alaska". https://doi.org/10.2312/BzPM_0655_2012

Streletskiy, D. A., Shiklomanov, N. I., & Nelson, F. E. (2012). Permafrost, Infrastructure, and Climate Change: A GIS-Based Landscape Approach to Geotechnical Modeling. *Arctic, Antarctic, and Alpine Research*, *44*(3), 368–380. https://doi.org/10.1657/1938-4246-44.3.368

Stroeve, J., & Notz, D. (2018). Changing state of Arctic sea ice across all seasons. *Environmental Research Letters*, *13*(10), 103001. https://doi.org/10.1088/1748-9326/aade56

Struck, J., Bliedtner, M., Strobel, P., Schumacher, J., Bazarradnaa, E., & Zech, R. (2019). Leaf wax *n*-alkane pattern and compound-specific δ^{13}C of plants and topsoils from semi-arid Mongolia. *Biogeosciences Discussions*, *2019*, 1–23. https://doi.org/10.5194/bg-2019-251

Struck, J., Roettig, C. B., Faust, D., & Zech, R. (2018). Leaf waxes from aeolianite–paleosol sequences on Fuerteventura and their potential for paleoenvironmental and climate reconstructions in the arid subtropics. *E&G quaternary science journal*, *66*(2), 109–114. https://doi.org/10.5194/egqsj-66-109-2018

Stuecker, M. F., Bitz, C. M., Armour, K. C., Proistosescu, C., Kang, S. M., Xie, S.-P., Kim, D., McGregor, S., Zhang, W., Zhao, S., Cai, W., Dong, Y., & Jin, F.-F. (2018). Polar amplification dominated by local forcing and feedbacks. *Nature Climate Change*, *8*(12), 1076–1081. https://doi.org/10.1038/s41558-018-0339-y

Stuiver, M., Reimer, P. J., & Reimer, R. W. (2017). CALIB ^{14}C Calibration Program.

Tank, S. E., Raymond, P. A., Striegl, R. G., McClelland, J. W., Holmes, R. M., Fiske, G. J., & Peterson, B. J. (2012). A land-to-ocean perspective on the magnitude, source and implication of DIC flux from major Arctic rivers to the Arctic Ocean. *Global Biogeochemical Cycles*, *26*(4). https://doi.org/10.1029/2011GB004192

Tanski, G., Wagner, D., Knoblauch, C., Fritz, M., Sachs, T., & Lantuit, H. (2019). Rapid CO_2 Release from Eroding Permafrost in Seawater. *Geophysical Research Letters*, *46*(20), 11244–11252. https://doi.org/10.1029/2019GL084303

Tanski, G., Bröder, L., Wagner, D., Knoblauch, C., Lantuit, H., Beer, C., Sachs, T., Fritz, M., Tesi, T., Koch, B. P., et al. (2021). Permafrost carbon and CO_2 pathways differ at contrasting coastal erosion sites in the Canadian Arctic. *Frontiers in Earth Science*, *9*, 207. https://doi.org/10.3389/feart.2021.630493

Tanski, G., Couture, N., Lantuit, H., Eulenburg, A., & Fritz, M. (2016). Eroding permafrost coasts release low amounts of dissolved organic carbon (DOC) from ground ice into the nearshore zone of the Arctic Ocean. *Global Biogeochemical Cycles*, *30*(7), 1054–1068. https://doi.org/10.1002/2015GB005337

Tanski, G., Lantuit, H., Ruttor, S., Knoblauch, C., Radosavljevic, B., Strauss, J., Wolter, J., Irrgang, A. M., Ramage, J., & Fritz, M. (2017). Transformation of terrestrial organic matter along thermokarst-affected permafrost coasts in the Arctic. *Science of The Total Environment*, *581–582*, 434–447. https://doi.org/10.1016/j.scitotenv.2016.12.152

Thalasso, F., Sepulveda-Jauregui, A., Gandois, L., Martinez-Cruz, K., Gerardo-Nieto, O., Astorga-España, M. S., Teisserenc, R., Lavergne, C., Tananaev, N., Barret, M., & Cabrol, L. (2020). Sub-oxycline methane oxidation can fully uptake CH_4 produced in sediments: case study of a lake in Siberia. *Scientific Reports*, *10*(1), 3423. https://doi.org/10.1038/s41598-020-60394-8

Timmermans, M.-L., & Labe, Z. (2020). Sea Surface Temperature. *Arctic Report Card*.

Treat, C. C., Natali, S. M., Ernakovich, J., Iversen, C. M., Lupascu, M., McGuire, A. D., Norby, R. J., Roy Chowdhury, T., Richter, A., Šantrůčková, H., Schädel, C., Schuur, E. A. G., Sloan, V. L., Turetsky, M. R., & Waldrop, M. P. (2015). A pan-Arctic synthesis of CH_4 and CO_2 production from anoxic soil incubations. *Global Change Biology*, *21*(7), 2787–2803. https://doi.org/10.1111/gcb.12875

Treat, C. C., Wollheim, W. M., Varner, R. K., Grandy, A. S., Talbot, J., & Frolking, S. (2014). Temperature and peat type control CO_2 and CH_4 production in Alaskan permafrost peats. *Global Change Biology*, *20*(8), 2674–2686. https://doi.org/10.1111/gcb.12572

Treshnikov, A. (1985). Atlas Arktiki [Atlas of the Arctic]. *Moskow: Glavnoe upravlenie geodezii i kartographii pri sovete ministerstvo SSSR*, In Russian.

Turetsky, M. R., Abbott, B. W., Jones, M. C., Anthony, K. W., Olefeldt, D., Schuur, E. A. G., Grosse, G., Kuhry, P., Hugelius, G., Koven, C., Lawrence, D. M., Gibson, C., Sannel, A. B. K., & McGuire, A. D. (2020). Carbon release through abrupt permafrost thaw. *Nature Geoscience*, *13*(2), 138–143. https://doi.org/10.1038/s41561-019-0526-0

Ulrich, M., Jongejans, L. L., Grosse, G., Schneider, B., Opel, T., Wetterich, S., Fedorov, A. N., Schirrmeister, L., Windirsch, T., Wiedmann, J., & Strauss, J. (2021). Geochemistry and Weathering Indices of Yedoma and Alas Deposits beneath Thermokarst Lakes in Central Yakutia. *Frontiers in Earth Science*, *9*, 701. https://doi.org/10.3389/feart.2021.704141

Ulrich, M., Matthes, H., Schirrmeister, L., Schütze, J., Park, H., Iijima, Y., & Fedorov, A. N. (2017). Differences in behavior and distribution of permafrost-related lakes in Central Yakutia and their response to climatic drivers. *Water Resources Research*, *53*(2), 1167–1188. https://doi.org/10.1002/2016WR019267

Ulrich, M., Matthes, H., Schmidt, J., Fedorov, A. N., Schirrmeister, L., Siegert, C., Schneider, B., Strauss, J., & Zielhofer, C. (2019). Holocene thermokarst dynamics in Central Yakutia – A multi-core and robust grain-size endmember modeling approach. *Quaternary Science Reviews*, *218*, 10–33. https://doi.org/10.1016/j.quascirev.2019.06.010

Ulyantsev, A. S., Romankevich, E. A., Bratskaya, S. Y., Prokuda, N. A., Sukhoverkhov, S. V., Semiletov, I. P., & Sergienko, V. I. (2017). Characteristic of quaternary sedimentation on a shelf of the Laptev Sea according to the molecular composition of *n*-alkanes. *Doklady Earth Sciences*, *473*(2), 449–453. https://doi.org/10.1134/S1028334X17040158

Vadakkedath, V., Zawadzki, J., & Przeździecki, K. (2020). Multisensory satellite observations of the expansion of the Batagaika crater and succession of vegetation in its interior from 1991 to 2018. *Environmental Earth Sciences*, *79*(6), 150. https://doi.org/10.1007/s12665-020-8895-7

Van Everdingen, R. O. (1998). *Multi-Language Glossary of Permafrost and Related Ground-Ice Terms in Chinese, English, French, German, Icelandic, Italian, Norwegian, Polish, Romanian, Russian, Spanish, and Swedish.* International Permafrost Association, Terminology Working Group.

Van Everdingen, R. O. (2005). Multi-language glossary of permafrost and related ground-ice terms in Chinese, English, French, German, Icelandic, Italian, Norwegian, polish, Romanian, Russian, Spanish, and Swedish.

Van Huissteden, J., Berrittella, C., Parmentier, F., Mi, Y., Maximov, T., & Dolman, A. (2011). Methane emissions from permafrost thaw lakes limited by lake drainage. *Nature Climate Change*, *1*(2), 119–123. https://doi.org/10.1038/nclimate1101

van Dongen, B. E., Semiletov, I., Weijers, J. W. H., & Gustafsson, Ö. (2008). Contrasting lipid biomarker composition of terrestrial organic matter exported from across the Eurasian Arctic by the five great Russian Arctic rivers. *Global Biogeochemical Cycles*, *22*(1). https://doi.org/10.1029/2007GB002974

Vasil'chuk, Y. K., Vasil'chuk, J. Y., Budantseva, N., & Vasil'chuk, A. (2020). New AMS Dates of Organic Microinclusions in Ice Wedges from the Lower Part of Batagay Yedoma, Yakutia. *Doklady Earth Sciences*, *490*(2), 100–103.

Vasilchuk, Y., Vasilchuk, D. Y., & Budantseva, N. (2017). Isotope-geochemical characteristics of the Batagai Yedoma (Preliminary results). *1*, 69–96.

Venables, W. N., & Ripley, B. D. (2002). *Modern Applied Statistics with S* (Fourth). Springer.

Vickers, H., Høgda, K. A., Solbø, S., Karlsen, S. R., Tømmervik, H., Aanes, R., & Hansen, B. B. (2016). Changes in greening in the high Arctic: insights from a 30 year AVHRR max NDVI dataset for Svalbard. *Environmental Research Letters*, *11*(10), 105004. https://doi.org/10.1088/1748-9326/11/10/105004

Vihma, T., Screen, J., Tjernström, M., Newton, B., Zhang, X., Popova, V., Deser, C., Holland, M., & Prowse, T. (2016). The atmospheric role in the Arctic water cycle: A review on processes, past and future changes, and their impacts. *Journal of Geophysical Research: Biogeosciences*, *121*(3), 586–620. https://doi.org/10.1002/2015JG003132

Vincent, W. F., Lemay, M., & Allard, M. (2017). Arctic permafrost landscapes in transition: towards an integrated Earth system approach. *Arctic Science*, *3*(2), 39–64. https://doi.org/10.1139/as-2016-0027

Volkman, J. K. (1986). A review of sterol markers for marine and terrigenous organic matter. *Organic geochemistry*, *9*(2), 83–99.

Vonk, J., Mann, P. J., Dowdy, K., Davydova, A., Davydov, S. P., Zimov, N., Spencer, R. G., Bulygina, E. B., Eglinton, T. I., & Holmes, R. M. (2013a). Dissolved organic carbon loss from Yedoma permafrost amplified by ice wedge thaw. *Environmental Research Letters*, *8*(3), 035023. https://doi.org/10.1088/1748-9326/8/3/035023

Vonk, J. E., Mann, P. J., Davydov, S., Davydova, A., Spencer, R. G. M., Schade, J., Sobczak, W. V., Zimov, N., Zimov, S., Bulygina, E., Eglinton, T. I., & Holmes, R. M. (2013b). High biolability of ancient permafrost carbon upon thaw. *Geophysical Research Letters*, *40*(11), 2689–2693. https://doi.org/10.1002/grl.50348

Waldrop, M. P., Wickland, K. P., White III, R., Berhe, A. A., Harden, J. W., & Romanovsky, V. E. (2010). Molecular investigations into a globally important carbon pool: permafrost-protected carbon in Alaskan soils. *Global Change Biology*, *16*(9), 2543–2554. https://doi.org/10.1111/j.1365-2486.2009.02141.x

Walter, K. M., Edwards, M. E., Grosse, G., Zimov, S. A., & Chapin, F. S. (2007). Thermokarst Lakes as a Source of Atmospheric CH_4 During the Last Deglaciation. *Science*, *318*(5850), 633–636. https://doi.org/10.1126/science.1142924

Walter, K. M., Zimov, S. A., Chanton, J. P., Verbyla, D., & Chapin, F. S. (2006). Methane bubbling from Siberian thaw lakes as a positive feedback to climate warming. *Nature*, *443*(7107), 71–75. https://doi.org/10.1038/nature05040

Walter Anthony, K. M., Zimov, S. A., Grosse, G., Jones, M. C., Anthony, P. M., III, F. S. C., Finlay, J. C., Mack, M. C., Davydov, S., Frenzel, P., & Frolking, S. (2014). A shift of thermokarst lakes from carbon sources to sinks during the Holocene epoch. *Nature*, *511*, 452–456. https://doi.org/10.1038/nature13560

Walter Anthony, K., Daanen, R., Anthony, P., Schneider von Deimling, T., Ping, C.-L., Chanton, J. P., & Grosse, G. (2016). Methane emissions proportional to permafrost carbon thawed in Arctic lakes since the 1950s. *Nature Geoscience*, *9*(9), 679–682. https://doi.org/10.1038/ngeo2795

Walter Anthony, K., Schneider von Deimling, T., Nitze, I., Frolking, S., Emond, A., Daanen, R., Anthony, P., Lindgren, P., Jones, B., & Grosse, G. (2018). 21st-century modeled permafrost carbon emissions accelerated by abrupt thaw beneath lakes. *Nature Communications*, *9*(1), 3262. https://doi.org/10.1038/s41467-018-05738-9

Walz, J., Knoblauch, C., Tigges, R., Opel, T., Schirrmeister, L., & Pfeiffer, E.-M. (2018). Greenhouse gas production in degrading ice-rich permafrost deposits in northeastern Siberia. *Biogeosciences*, *15*(17), 5423–5436. https://doi.org/10.5194/bg-15-5423-2018

Wegner, C., Bennett, K. E., de Vernal, A., Forwick, M., Fritz, M., Heikkilä, M., Łącka, M., Lantuit, H., Laska, M., Moskalik, M., O'Regan, M., Pawłowska, J., Promińska, A., Rachold, V., Vonk, J. E., & Werner, K. (2015). Variability in transport of terrigenous material on the shelves and the deep Arctic Ocean during the Holocene. *Polar Research*, *34*(1), 24964. https://doi.org/10.3402/polar.v34.24964

Weijers, J. W. H., Schouten, S., Spaargaren, O. C., & Damsté, J. S. [(2006). Occurrence and distribution of tetraether membrane lipids in soils: Implications for the use of the TEX86 proxy and the BIT index. *Organic Geochemistry*, *37*(12), 1680–1693. https://doi.org/10.1016/j.orggeochem.2006.07.018

West, J. J., & Plug, L. J. (2008). Time-dependent morphology of thaw lakes and taliks in deep and shallow ground ice. *Journal of Geophysical Research: Earth Surface*, *113*(F1). https://doi.org/10.1029/2006JF000696

Wetterich, S., Kizyakov, A., Fritz, M., Wolter, J., Mollenhauer, G., Meyer, H., Fuchs, M., Aksenov, A., Matthes, H., Schirrmeister, L., & Opel, T. (2020). The cryostratigraphy of the Yedoma cliff of Sobo-Sise Island (Lena delta) reveals permafrost dynamics in the central Laptev Sea coastal region during the last 52 kyr. *The Cryosphere*, *14*(12), 4525–4551. https://doi.org/10.5194/tc-14-4525-2020

Wetterich, S., Rudaya, N., Nazarova, L., Syrykh, L., Pavlova, M., Palagushkina, O., Kizyakov, A., Wolter, J., Kuznetsova, T., Aksenov, A., Stoof-Leichsenring, K. R., Schirrmeister, L., & Fritz, M. (2021). Paleo-Ecology of the Yedoma Ice Complex on Sobo-Sise Island (EasternLena Delta, Siberian Arctic). *Frontiers in Earth Science*, *9*, 489. https://doi.org/10.3389/feart.2021.681511

Wetterich, S., Kizyakov, A., Fritz, M., Aksenov, A., Schirrmeister, L., & Opel, T. (2018). Expedition Report: Permafrost research on Sobo-Sise Island (Lena Delta) [Place: Bremerhaven Publication Title: Berichte zur Polar- und Meeresforschung = Reports on polar and marine research Volume: 734]. In S. Kruse, D. Bolshiyanov, M. N. Grigoriev, A. Morgenstern, L. Pestryakova, L. Tsibizov, & A. Udke (Eds.), *Russian-German Cooperation: Expeditions to Siberia in 2018* (p. 257). Alfred Wegener Institute for Polar; Marine Research. https://doi.org/10.2312/BzPM_0734_2019

Wetterich, S., Kuzmina, S., Andreev, A. A., Kienast, F., Meyer, H., Schirrmeister, L., Kuznetsova, T., & Sierralta, M. (2008). Palaeoenvironmental dynamics inferred from late Quaternary permafrost deposits on Kurungnakh Island, Lena Delta, Northeast Siberia, Russia. *Quaternary Science Reviews*, *27*(15), 1523–1540. https://doi.org/10.1016/j.quascirev.2008.04.007

Wetterich, S., Schirrmeister, L., Andreev, A., Pudenz, M., Plessen, B., Meyer, H., & Kunitsky, V. V. (2009). Eemian and Late Glacial/Holocene palaeoenvironmental records from permafrost sequences at the Dmitry Laptev Strait (NE Siberia, Russia). *Palaeogeography, Palaeoclimatology, Palaeoecology*, *279*(1), 73–95. https://doi.org/10.1016/j.palaeo.2009.05.002

Wetterich, S., Tumskoy, V., Rudaya, N., Andreev, A. A., Opel, T., Meyer, H., Schirrmeister, L., & Hüls, M. (2014). Ice Complex formation in arctic East Siberia during the MIS3 Interstadial. *Quaternary Science Reviews*, *84*, 39–55. https://doi.org/10.1016/j.quascirev.2013.11.009

Wild, B., Andersson, A., Bröder, L., Vonk, J., Hugelius, G., McClelland, J. W., Song, W., Raymond, P. A., & Gustafsson, Ö. (2019). Rivers across the Siberian Arctic unearth the patterns of carbon release from thawing permafrost. *Proceedings of the National Academy of Sciences*, *116*(21), 10280–10285. https://doi.org/10.1073/pnas.1811797116

Wild, B., Schnecker, J., Alves, R. J. E., Barsukov, P., Bárta, J., Čapek, P., Gentsch, N., Gittel, A., Guggenberger, G., Lashchinskiy, N., Mikutta, R., Rusalimova, O., Šantrůčková, H., Shibistova, O., Urich, T., Watzka, M., Zrazhevskaya, G., & Richter, A. (2014). Input of easily available organic C and N stimulates microbial decomposition of soil organic matter in arctic permafrost soil. *Soil Biology and Biochemistry*, *75*, 143–151. https://doi.org/10.1016/j.soilbio.2014.04.014

Windirsch, T., Grosse, G., Ulrich, M., Schirrmeister, L., Fedorov, A. N., Konstantinov, P. Y., Fuchs, M., Jongejans, L. L., Wolter, J., Opel, T., & Strauss, J. (2020). Organic carbon characteristics in ice-rich permafrost in alas and Yedoma deposits, central Yakutia, Siberia. *Biogeosciences*, *17*(14), 3797–3814. https://doi.org/10.5194/bg-17-3797-2020

Winkel, M., Sepulveda-Jauregui, A., Martinez-Cruz, K., Heslop, J. K., Rijkers, R., Horn, F., Liebner, S., & Walter Anthony, K. M. (2019). First evidence for cold-adapted anaerobic oxidation of methane in deep sediments of thermokarst lakes. *Environmental Research Communications*, *1*(2). https://doi.org/10.1088/2515-7620/ab1042

Winterfeld, M., Goñi, M. A., Just, J., Hefter, J., & Mollenhauer, G. (2015). Characterization of particulate organic matter in the Lena River delta and adjacent nearshore zone, NE Siberia – Part 2: Lignin-derived phenol compositions. *Biogeosciences*, *12*(7), 2261–2283. https://doi.org/10.5194/bg-12-2261-2015

Xu, L., Myneni, R. B., Chapin III, F. S., Callaghan, T. V., Pinzon, J. E., Tucker, C. J., Zhu, Z., Bi, J., Ciais, P., Tømmervik, H., Euskirchen, E. S., Forbes, B. C., Piao, S. L., Anderson, B. T., Ganguly, S., Nemani, R. R., Goetz, S. J., Beck, P. S. A., Bunn, A. G., . . . Stroeve, J. C. (2013). Temperature and vegetation seasonality diminishment over northern lands. *Nature Climate Change*, *3*(6), 581–586. https://doi.org/10.1038/nclimate1836

Yang, D., Liu, B., & Ye, B. (2005). Stream temperature changes over Lena River basin in Siberia. *Geophysical Research Letters*, *32*(5). https://doi.org/10.1029/2004GL021568

Yoshikawa, K., Bolton, W. R., Romanovsky, V. E., Fukuda, M., & Hinzman, L. D. (2002). Impacts of wildfire on the permafrost in the boreal forests of Interior Alaska. *Journal of Geophysical Research*, *108*(D1), 8148. https://doi.org/10.1029/2001JD000438

Zech, M., Andreev, A., Zech, R., Müller, S., Hambach, U., Frechen, M., & Zech, W. (2010). Quaternary vegetation changes derived from a loess-like permafrost palaeosol sequence in northeast Siberia using alkane biomarker and pollen analyses. *Boreas 39(3)*, 540–550. https://doi.org/10.1111/j.1502-3885.2009.00132.x

Zech, M., Buggle, B., Leiber, K., Marković, S., Glaser, B., Hambach, U., Huwe, B., Stevens, T., Sümegi, P., Wiesenberg, G., & Zöller, L. (2009). Reconstructing Quaternary vegetation history in the Carpathian Basin, SE-Europe, using n-alkane biomarkers as molecular fossils: Problems and possible solutions, potential and limitations. *E&G Quaternary Science Journal*, *58*(2), 148–155. https://doi.org/10.3285/eg.58.2.03

Zech, M., Krause, T., Meszner, S., & Faust, D. (2013). Incorrect when uncorrected: Reconstructing vegetation history using *n*-alkane biomarkers in loess-paleosol sequences – A case study from the Saxonian loess region, Germany. *Quaternary International*, *296*, 108–116. https://doi.org/10.1016/j.quaint.2012.01.023

Zhang, W., Miller, P. A., Smith, B., Wania, R., Koenigk, T., & Döscher, R. (2013). Tundra shrubification and tree-line advance amplify arctic climate warming: results from an individual-based dynamic vegetation model. *Environmental Research Letters*, *8*(3), 034023. https://doi.org/10.1088/1748-9326/8/3/034023

Zhang, X., Bianchi, T. S., Hanna, A. J. M., Shields, M. R., Izon, G., Hutchings, J. A., Ping, C.-L., Kanevskiy, M., Haghipour, N., & Eglinton, T. I. (2021). Recent Warming Fuels Increased Organic Carbon Export From Arctic Permafrost. *AGU Advances*, *2*(2), e2021AV000396. https://doi.org/10.1029/2021AV000396

Zhang, Y., Zheng, M., Meyers, P., & Huang, X. (2017). Impact of early diagenesis on distributions of Sphagnum *n*-alkanes in peatlands of the monsoon region of China. *Organic Geochemistry*, *105*, 13–19. https://doi.org/10.1016/j.orggeochem.2016.12.007

Zhang, Y., Su, Y., Liu, Z., Chen, X., Yu, J., Di, X., & Jin, M. (2014). Long-chain branched/cyclic alkanes in recent sediment of Lake Fuxian and their environmental implications. *Chinese science bulletin*, *59*(11), 1139–1150. https://doi.org/10.1007/s11434-014-0159-z

Zheng, Y., Zhou, W., Meyers, P. A., & Xie, S. (2007). Lipid biomarkers in the Zoigê-Hongyuan peat deposit: Indicators of Holocene climate changes in West China. *Organic Geochemistry*, *38*(11), 1927–1940. https://doi.org/10.1016/j.orggeochem.2007.06.012

Zimov, S. A., Davydov, S. P., Zimova, G. M., Davydova, A. I., Schuur, E. A. G., Dutta, K., & Chapin, F. S. (2006). Permafrost carbon: Stock and decomposability of a globally significant carbon pool. *Geophysical Research Letters*, *33*(20). https://doi.org/10.1029/2006GL027484

Zimov, S. A., Voropaev, Y. V., Semiletov, I. P., Davidov, S. P., Prosiannikov, S. F., Chapin, F. S., Chapin, M. C., Trumbore, S., & Tyler, S. (1997). North Siberian Lakes: A Methane Source Fueled by Pleistocene Carbon. *Science*, *277*(5327), 800–802. https://doi.org/10.1126/science.277.5327.800

Zona, D., Lipson, D. A., Paw U, K. T., Oberbauer, S. F., Olivas, P., Gioli, B., & Oechel, W. C. (2012). Increased CO_2 loss from vegetated drained lake tundra ecosystems due to flooding: Increased tundra CO_2 loss due to flooding. *Global Biogeochemical Cycles*, *26*(2). https://doi.org/10.1029/2011GB004037

Zscheischler, J., Rogga, S., & Busse, M. (2017). The Adoption and Implementation of Transdisciplinary Research in the Field of Land-Use Science—A Comparative Case Study. *Sustainability*, *9*, 1926. https://doi.org/10.3390/su9111926

A

Supporting information for Chapter 2

Parameter	**Min**	**Median**	**Max**	**Mean**	**Standard deviation**
Biogeochemical parameters					
Total organic carbon [wt%]	<0.1	1.1	17.8	2.6	4.3
Stable carbon isotopes [‰ vs. VPDB]	-28.6	-24.9	-23.8	-25.2	1.1
Hydrochemical parameters					
Water content [wt%]	10.5	17.1	65.4	21.0	12.9
pH	6.3	8.2	8.7	8.0	0.5
EC [μS^{-1}]	202	778	1301	729	261
n-Alkane parameters					
Concentration [μg g^{-1} sed.]	0.57	1.80	20.82	4.76	6.18
Concentration [μg g^{-1} TOC]	50.1	367.5	581.4	347.7	153.1
Average Chain Length	26.5	27.5	28.4	27.5	0.5
Carbon Preference Index	2.3	4.8	8.9	5.4	2.0
Odd-over-even predominance	2.2	5.7	11.0	6.2	2.6
brGDGT parameters					
Concentration [μg g^{-1} sed.]	0.0	0.3	1.1	0.4	0.8
Concentration [μg g^{-1} TOC]	3.4	10.7	26.8	12.4	18.1

Table A.1: General statistics from bulk sediment pore water and lipid biomarker parameters: minimum, median, maximum, mean, standard deviation.

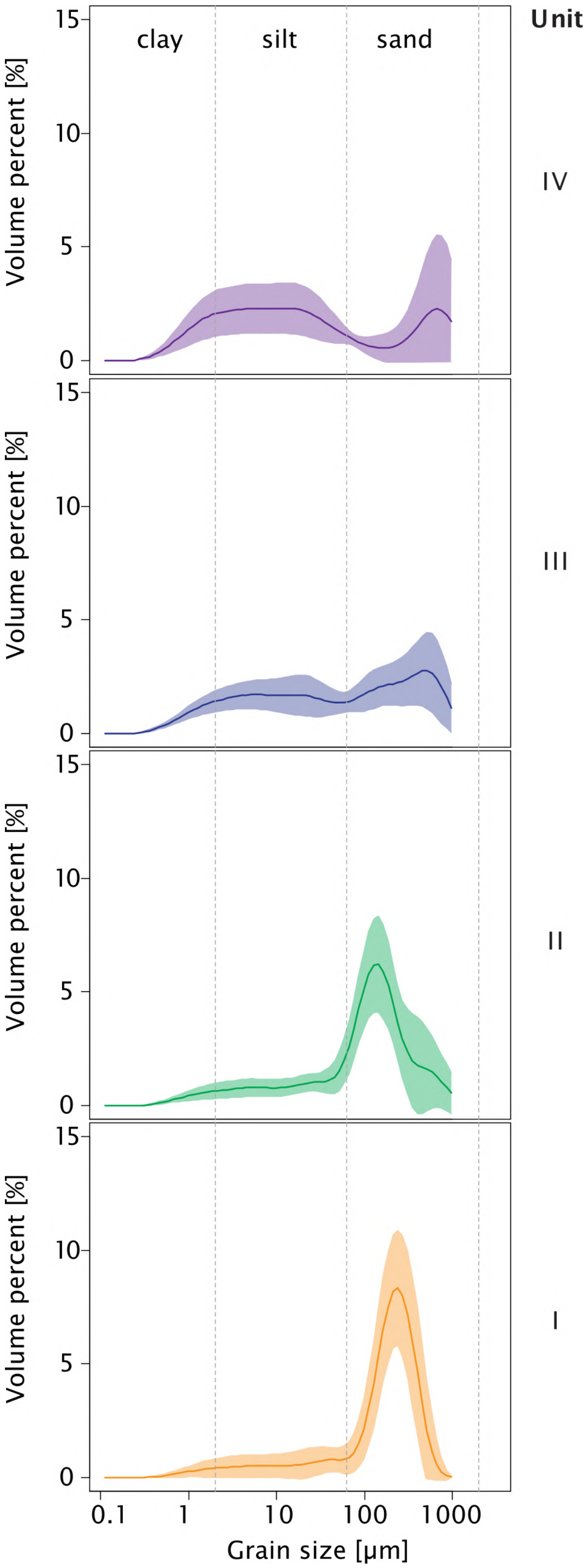

Figure A.1: Grain size distribution of PG2412. Mean and standard deviation plotted per unit. Units indicated on the right.

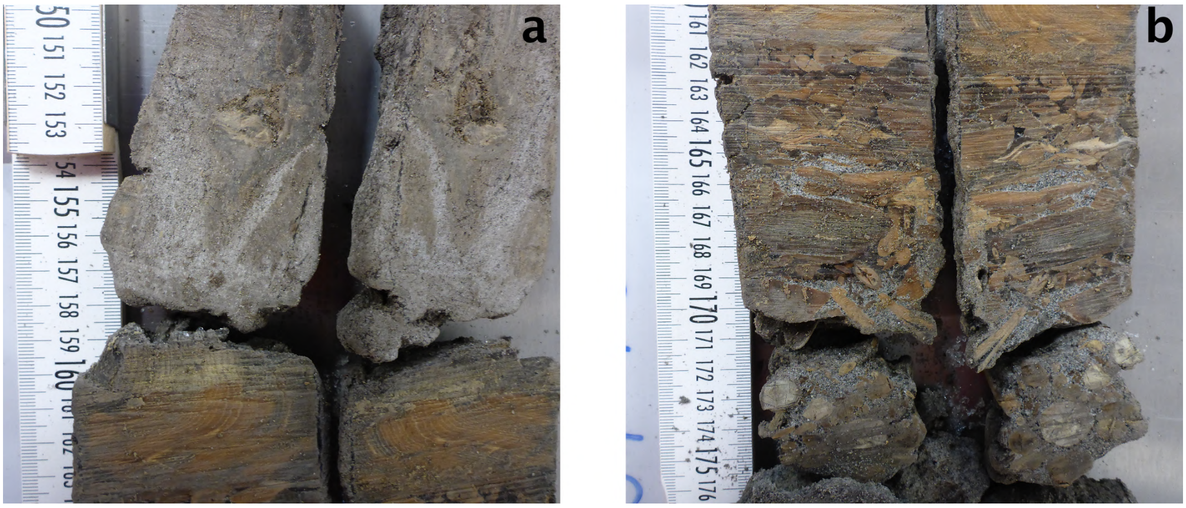

Figure A.2: Pictures of Goltsovoye Lake sediment core PG2412. (a) Cryoturbation of organic material at 3558-3555 cm deep, (b) inclusion of large organic remains up to 4 cm long at 3570 cm deep.

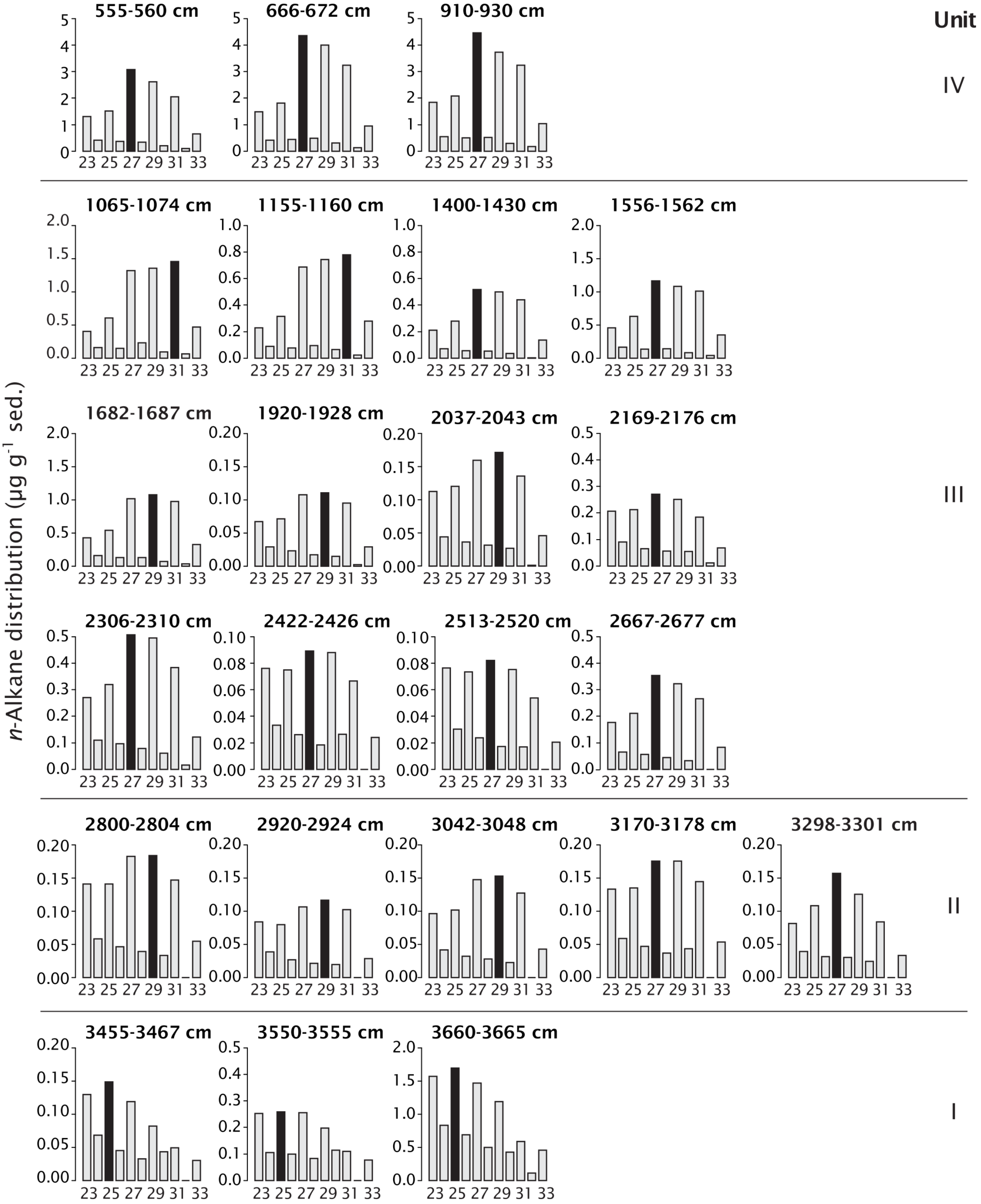

Figure A.3: *n*-Alkane distribution in Goltsovoye Lake sediment core PG2412. Depth in below ice surface indicated above graphs. Maximum abundance marked in black. Note: y-axes are scaled differently. Units indicated on the right.

B

Supporting information for Chapter 3

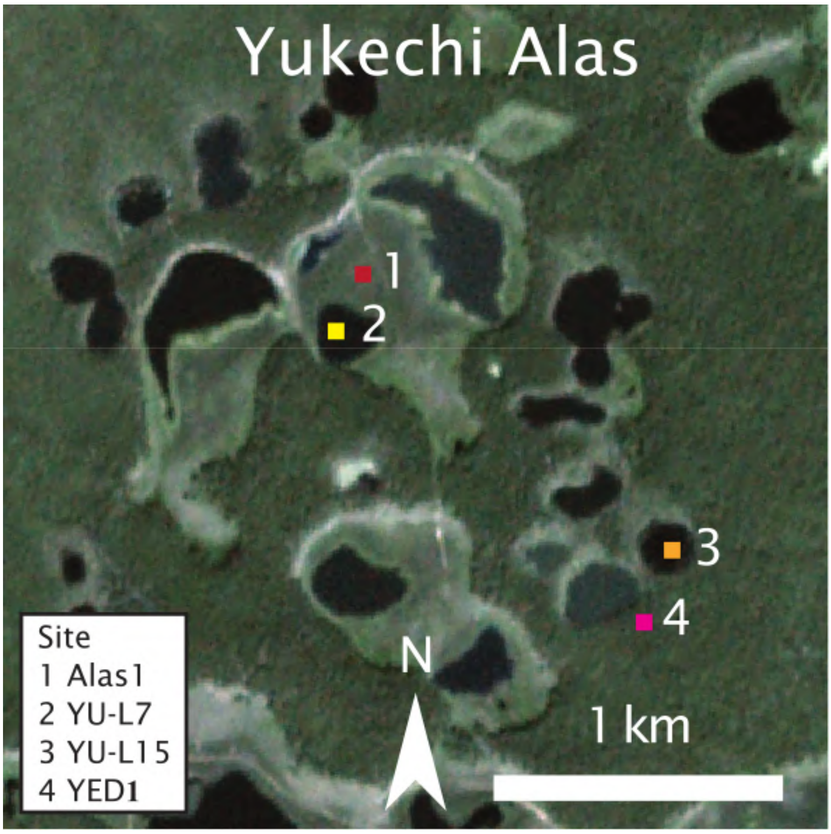

Figure B.1: Overview of deep coring sites in the Yukechi Alas. Site 2 and 3 are included in this study (YU-L7 and YU-L15), sites 1 and 4 are reported by Windirsch et al. (2020) (Alas1 and YED1).

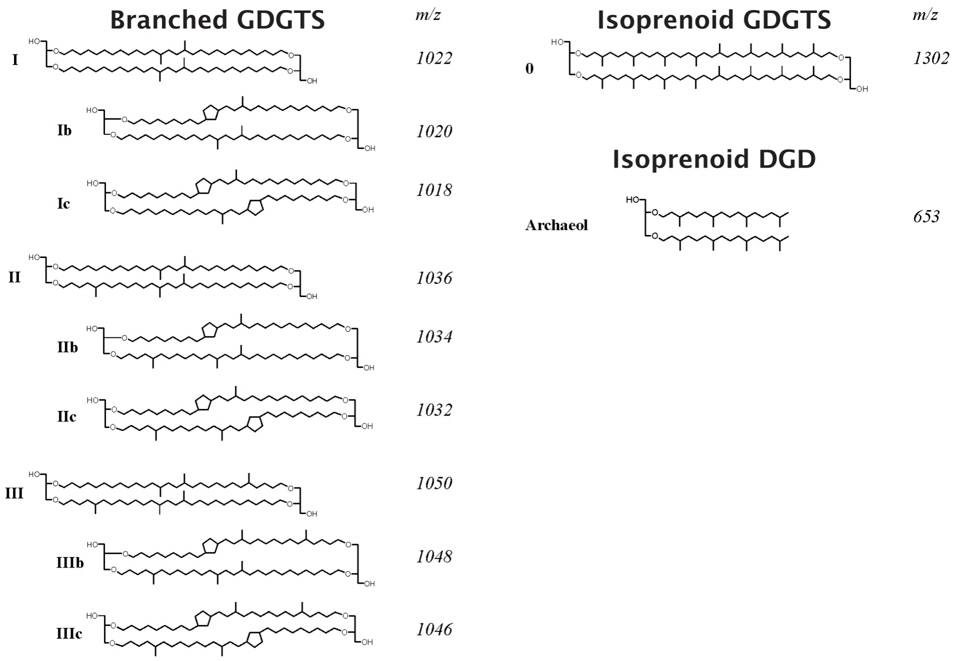

Figure B.2: Chemical structures of the branched and isoprenoid GDGTs and the DGD archaeol. Modified after Weijers et al., (2009).

Greenhouse gas production and DIC

From the measured CO_2 and CH_4 concentrations, we calculated the GHG production. Using the ideal gas law, the amount of gas in the headspace was calculated (Equation B.1) and the amount of CH_4 and CO_2 produced per g dry sediment (Equation B.2).

$$n = \frac{p\,V}{R\,T} \tag{B.1}$$

where n is the amount of gas in the headspace in mol, p the pressure in Pa, V the volume in m^3, R the gas constant in Pa m^3 K^{-1} mol^{-1} and T the temperature in K. The values we used in this calculation and the following are shown in Table B.1.

$$n_X = \frac{n\,X}{m} \tag{B.2}$$

where n_X is the amount of CH_4 or CO_2 in the headspace in µmol, n the amount of gas in the headspace in mol, X is the measured concentration in parts per million (ppm) and m the sediment mass in g. Furthermore, the amount of CH_4 and CO_2 dissolved in the water was calculated according to Equation B.3 and B.4, respectively. The n_{DIC} is the sum of dissolved CO_2, $HCO_3{}^-$ and $CO_3{}^{2-}$.

$$n_{aq} = \frac{S_1\,p\,X\,WC}{m} \tag{B.3}$$

where n$_aq$ is the amount of CH$_4$ dissolved in water in μmol, S$_1$ the solubility of CH$_4$ in water in mole m^{-3} Pa^{-1}, p the pressure in Pa, X the concentration in ppm, WC the water content in m^3 and m the sediment mass in g.

$$n_{DIC} = \frac{S_2\, p\, X\, W\, (1 + \frac{K_1}{10^{-pH}} + \frac{K_1 + K_2}{(10^{-pH})^2})}{m} \tag{B.4}$$

where n$_{DIC}$ is the amount of CO$_2$ dissolved in water in µmole, S$_2$ is the solubility of CO$_2$ in water in mole m^{-3} Pa^{-1}, p the pressure in Pa, X the concentration in ppm, WC the water content in m^3, K$_1$ the first dissociation constant, K$_2$ the second dissociation constant and m the sediment mass in g. For all samples, the sediment pH was assessed by adding 6.12 mL of 0.01 M CaCl$_2$ to ~2.5 g dried sediment and measuring with a Multilab 540 (WTW) at 20°C.

The amount of CH$_4$ and CO$_2$ was converted to mass units and to carbon equivalents CH$_4$-C and CO$_2$-C according to Equation B.5.

$$\begin{aligned} m_{CH_4-C} &= n_{CH_4}\, m_C \\ m_{CO_2-C} &= n_{CO_2}\, m_C \end{aligned} \tag{B.5}$$

Parameter	**Unit**	**Value**
p	Pa	103700
V	m^3	1.03e-4
R	Pa m^3 K^{-1} mol^{-1}	8.314
T	K	277.15
m	g	10
S$_1$	mol m^{-1} Pa^{-1}	2.19e-5
WC	m^3	10e4
S$_2$	mol m^{-1} Pa^{-1}	2.19e-5
K$_1$	-	3e-7
K$_2$	-	2.7e-11

Table B.1: Values used in greenhouse gas calculations: pressure (p), volume (V), gas constant (R), temperature (T), sediment mass (m), solubility of CH$_4$ in water (S$_1$), water content (WC), solubility of CO$_2$ in water (S$_2$), the first dissociation constant (K$_1$) and second dissociation constant (K$_2$).

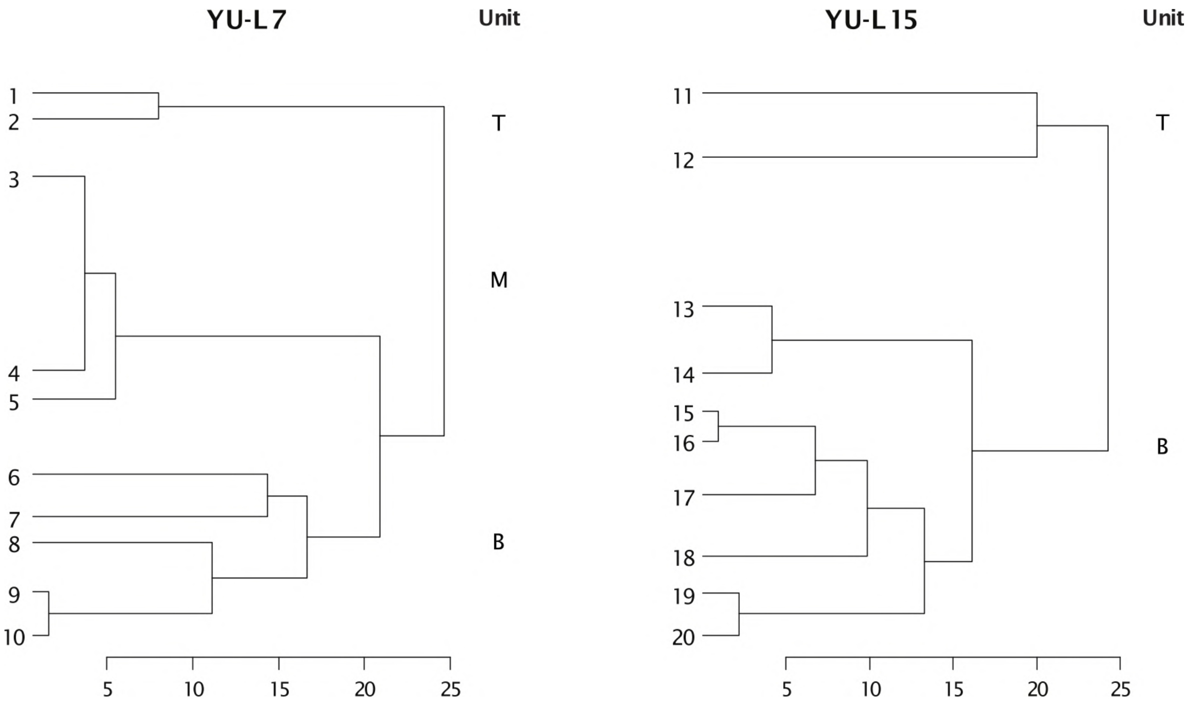

Figure B.3: Clustering of Alas lake sediment core YU-L7 (left) and Yedoma lake sediment core (YU-L15). Clustering was done using the “chclust” function in R v. 3.6.1 in package “rioja” with method “coniss”. Units are indicated on the right: top (T), middle (M) and bottom (B).

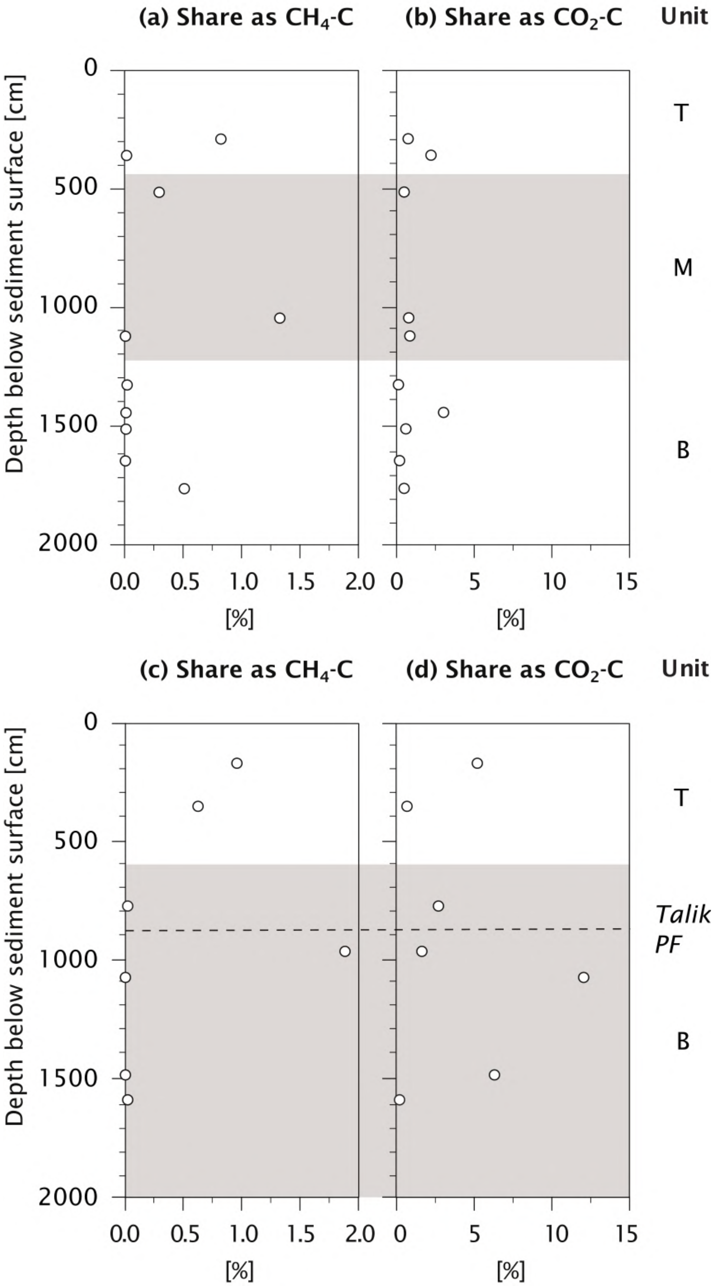

Figure B.4: Percentage of initial carbon mineralized for Alas lake sediment core YU-L7 as (a) CH_4 and (b) CO_2, and for Yedoma lake sediment core YU-L15 as (c) CH_4 and (d) CO_2. Units indicated on right: top (T), middle (M) and bottom (B), boundary talik to permafrost (PF) indicated with grey dashed line.

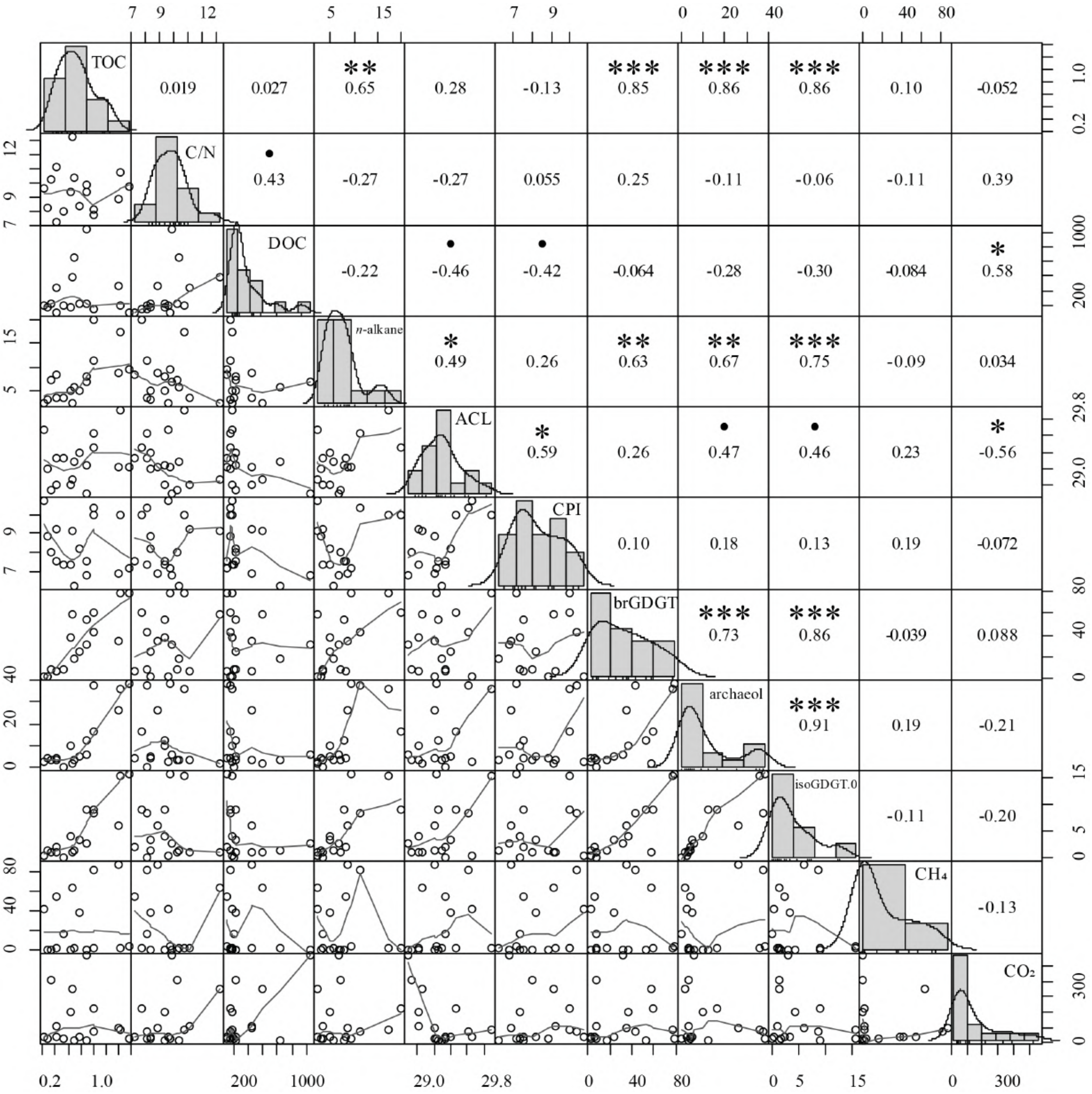

Figure B.5: Correlation matrix. Top: value of correlation (Pearson) and significance level indicated by *** ($p < 0.001$), ** ($p < 0.01$), * ($p < 0.05$) or a dot ($p < 0.1$). Bottom: bivariate scatterplots with fitted line. Diagonal: histograms. From left to right: total organic carbon (TOC) content, carbon to nitrogen (C/N) ratio, dissolved organic carbon (DOC) content, *n*-alkane concentration, average chain length (ACL), carbon preference index (CPI), branched glycerol dialkyl glycerol tetraether (brGDGT) concentration, archaeol concentration, isoprenoid GDGT (isoGDGT-0) concentration, methane (CH_4) production and carbon dioxide (CO_2) production.

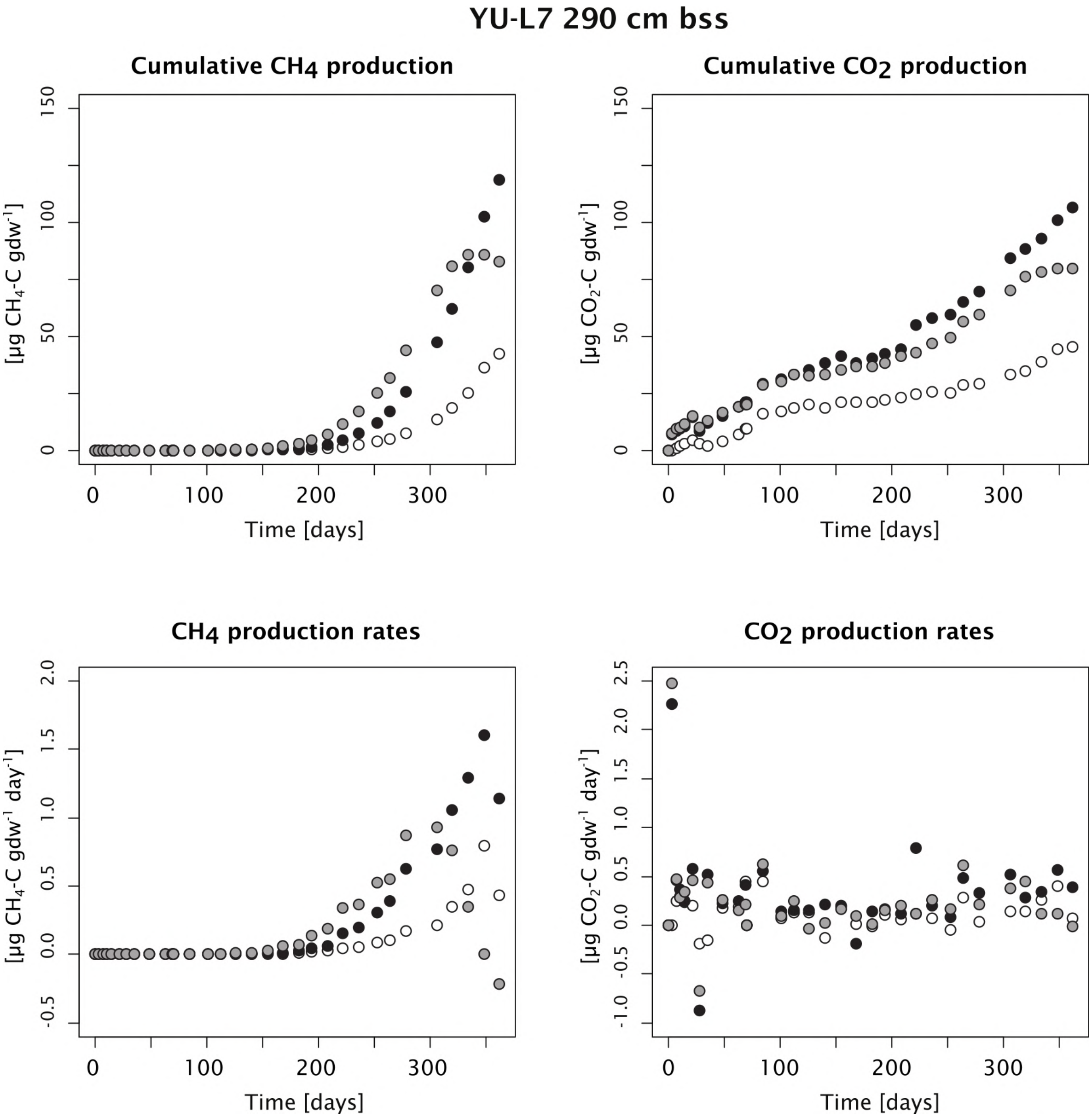

Figure B.6: Greenhouse gas production in Alas lake sediment core YU-L7 at 290 cm below the sediment surface (bss). a. Cumulative CH_4 production over time, b. cumulative CO_2 production over time, c. CH_4 production rates over time, d. CO_2 production over time. White, grey and black circles show three replicates.

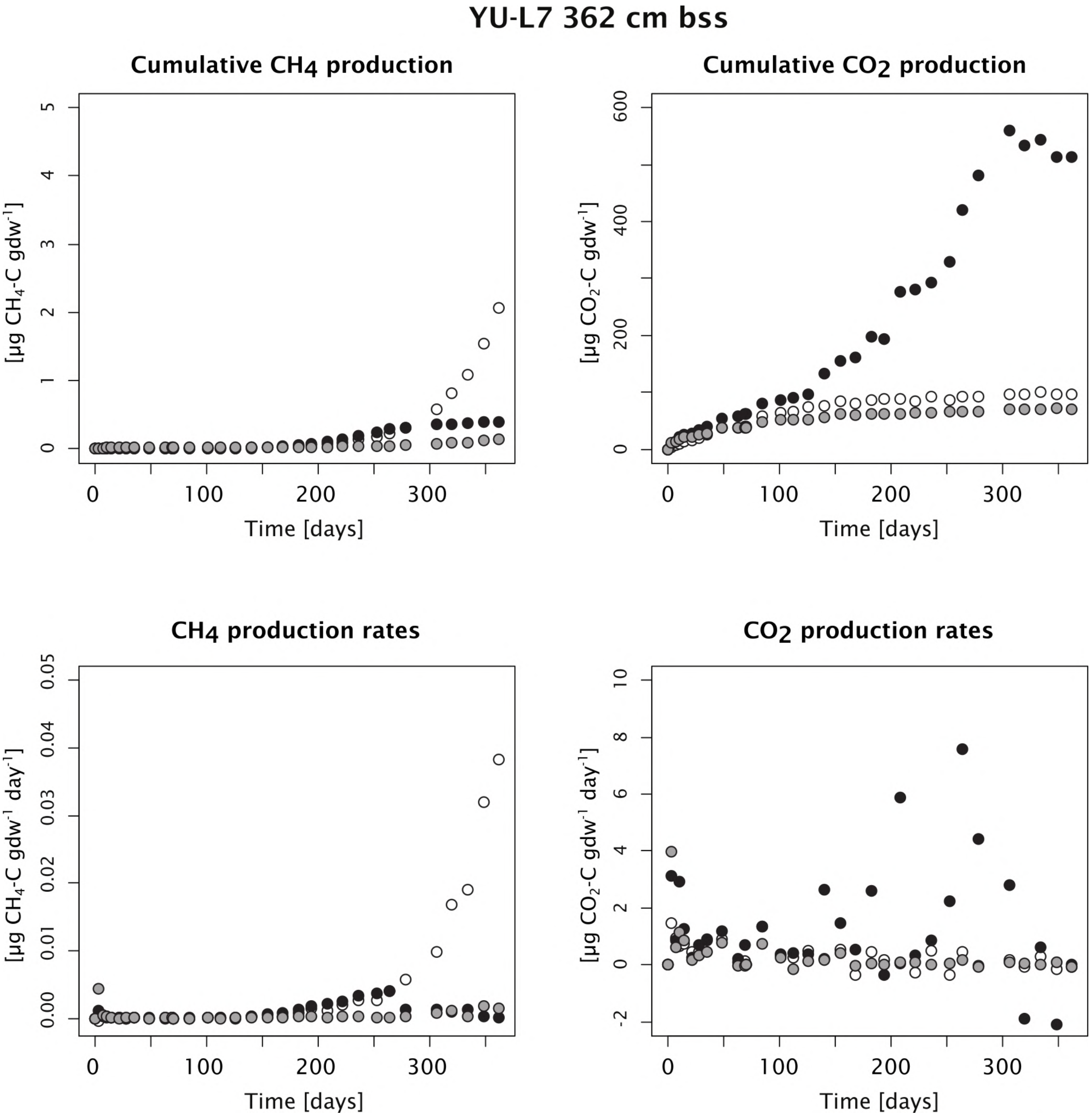

Figure B.7: Greenhouse gas production in Alas lake sediment core YU-L7 at 362 cm below the sediment surface (bss). a. Cumulative CH_4 production over time, b. cumulative CO_2 production over time, c. CH_4 production rates over time, d. CO_2 production over time. White, grey and black circles show three replicates.

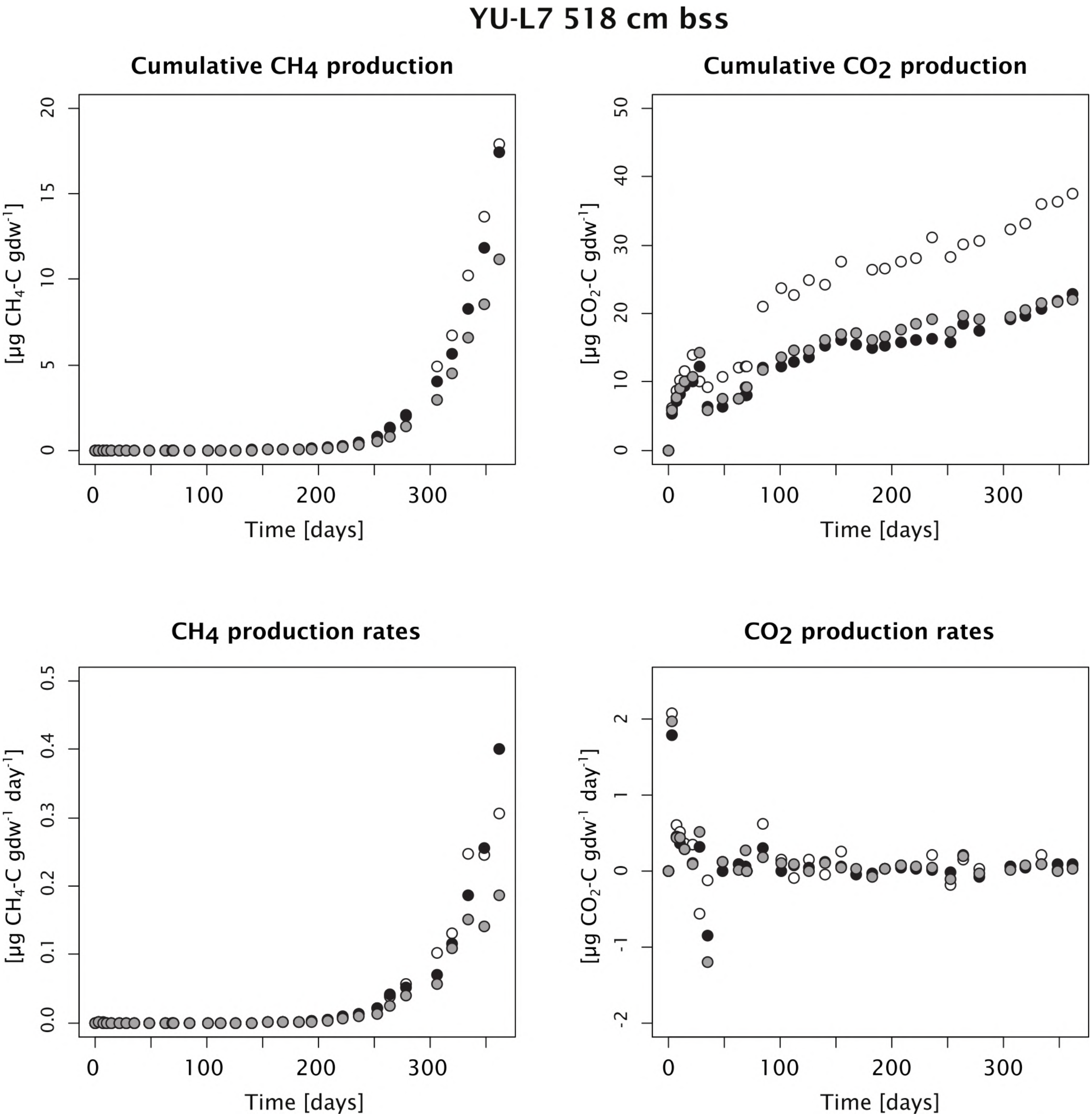

Figure B.8: Greenhouse gas production in Alas lake sediment core YU-L7 at 518 cm below the sediment surface (bss). a. Cumulative CH_4 production over time, b. cumulative CO_2 production over time, c. CH_4 production rates over time, d. CO_2 production over time. White, grey and black circles show three replicates.

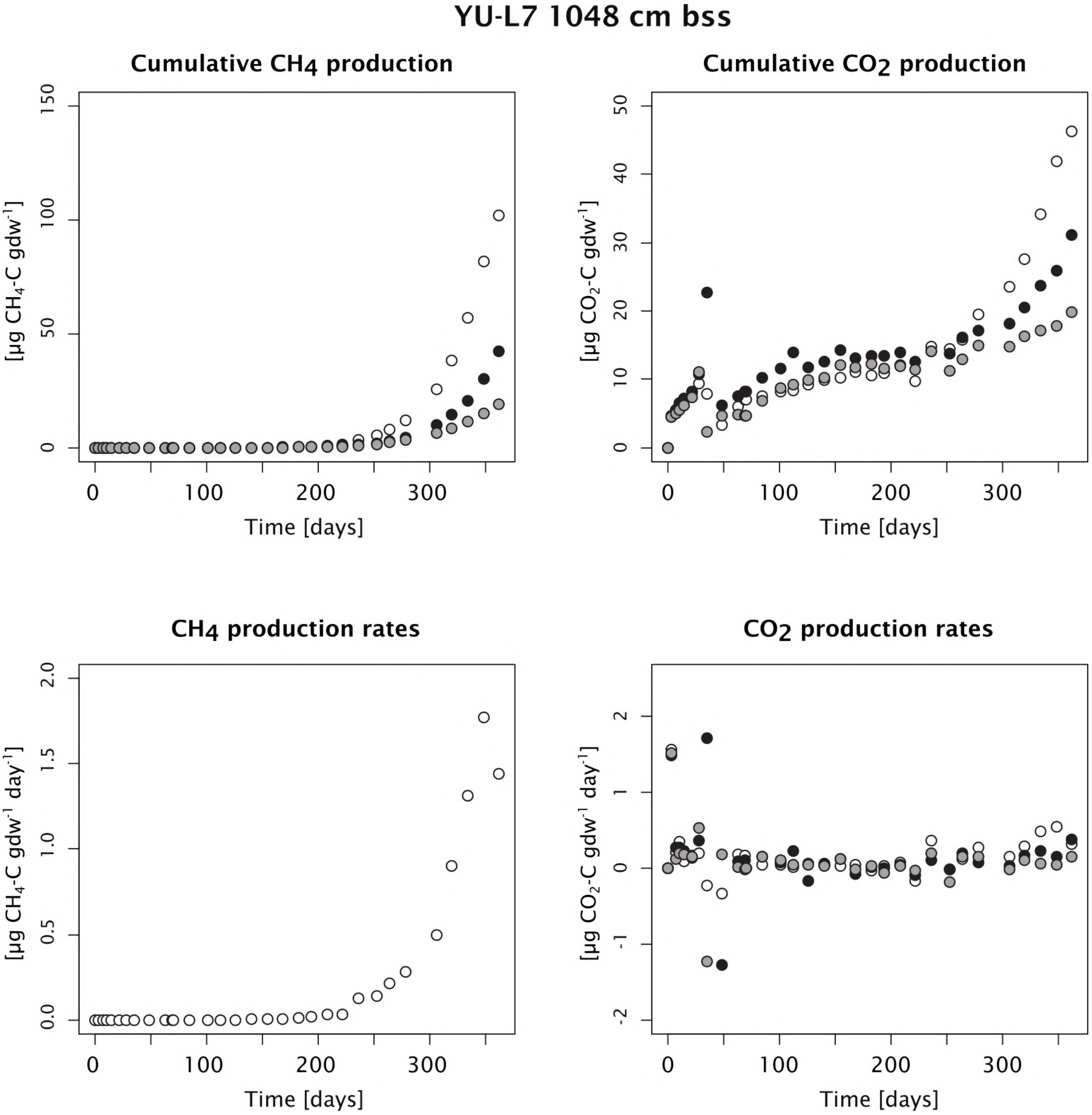

Figure B.9: Greenhouse gas production in Alas lake sediment core YU-L7 at 1048 cm below the sediment surface (bss). a. Cumulative CH_4 production over time, b. cumulative CO_2 production over time, c. CH_4 production rates over time, d. CO_2 production over time. White, grey and black circles show three replicates.

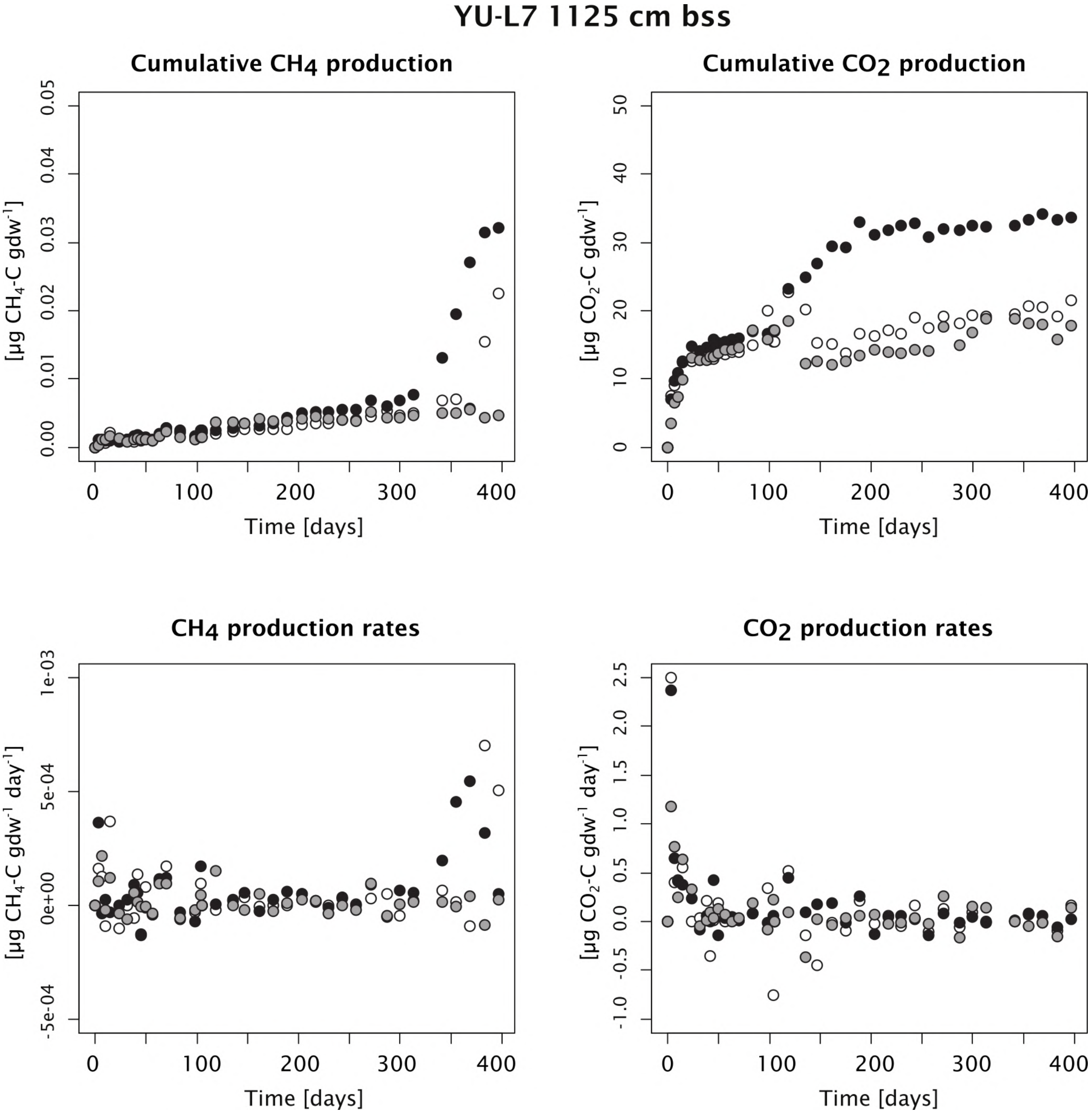

Figure B.10: Greenhouse gas production in Alas lake sediment core YU-L7 at 1125 cm below the sediment surface (bss). a. Cumulative CH_4 production over time, b. cumulative CO_2 production over time, c. CH_4 production rates over time, d. CO_2 production over time. White, grey and black circles show three replicates.

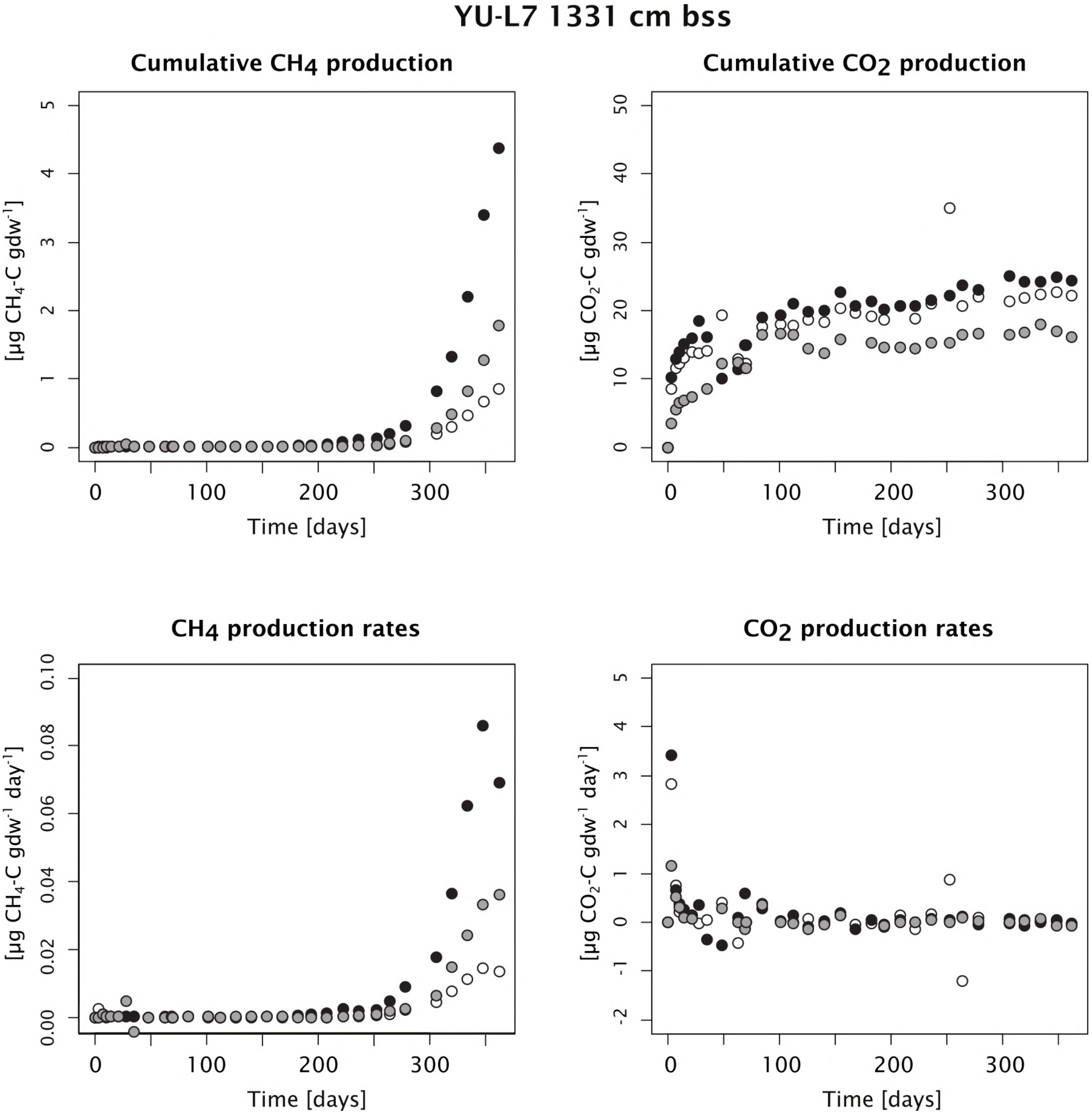

Figure B.11: Greenhouse gas production in Alas lake sediment core YU-L7 at 1331 cm below the sediment surface (bss). a. Cumulative CH_4 production over time, b. cumulative CO_2 production over time, c. CH_4 production rates over time, d. CO_2 production over time. White, grey and black circles show three replicates.

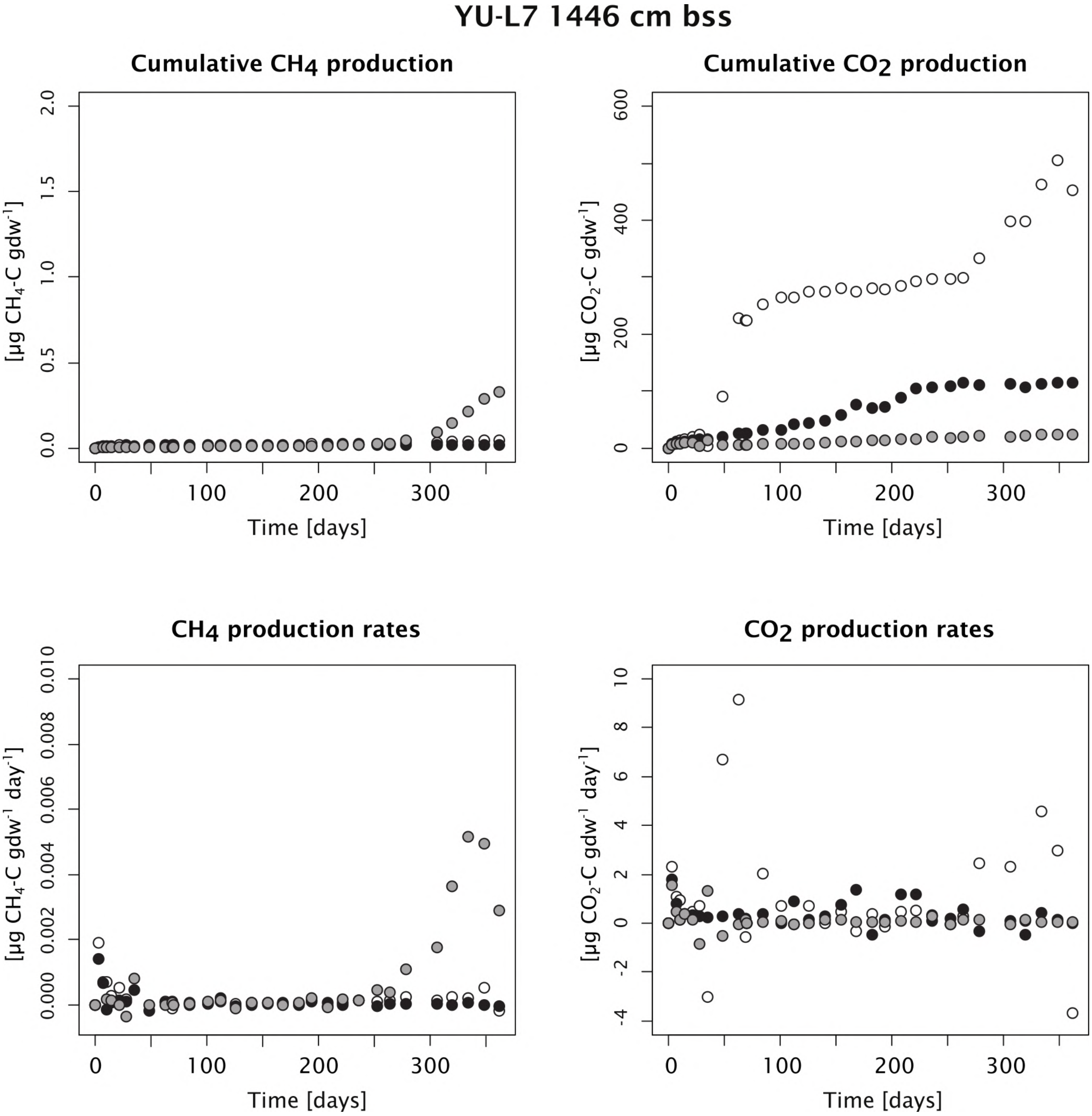

Figure B.12: Greenhouse gas production in Alas lake sediment core YU-L7 at 1446 cm below the sediment surface (bss). a. Cumulative CH_4 production over time, b. cumulative CO_2 production over time, c. CH_4 production rates over time, d. CO_2 production over time. White, grey and black circles show three replicates.

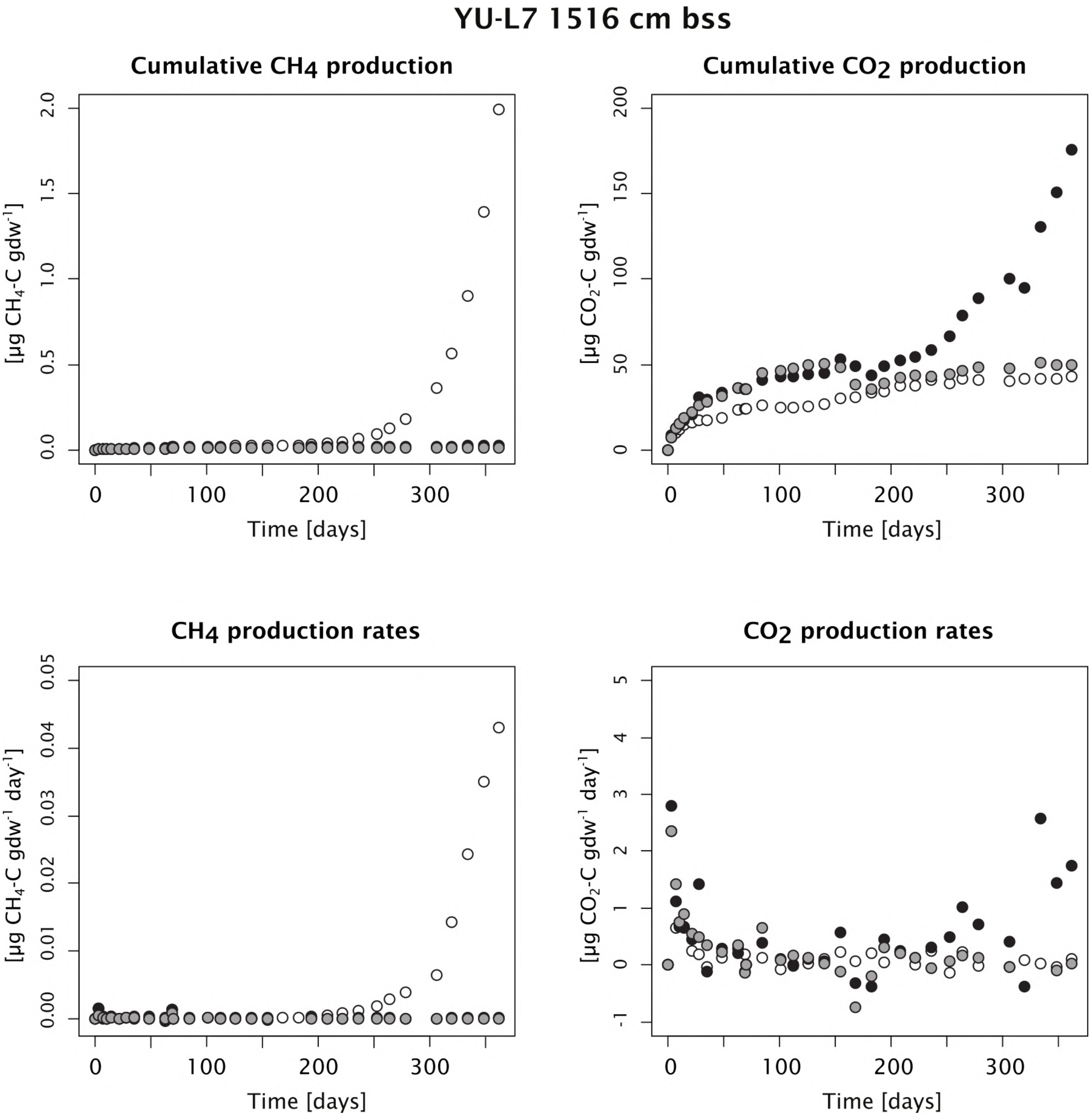

Figure B.13: Greenhouse gas production in Alas lake sediment core YU-L7 at 1516 cm below the sediment surface (bss). a. Cumulative CH_4 production over time, b. cumulative CO_2 production over time, c. CH_4 production rates over time, d. CO_2 production over time. White, grey and black circles show three replicates.

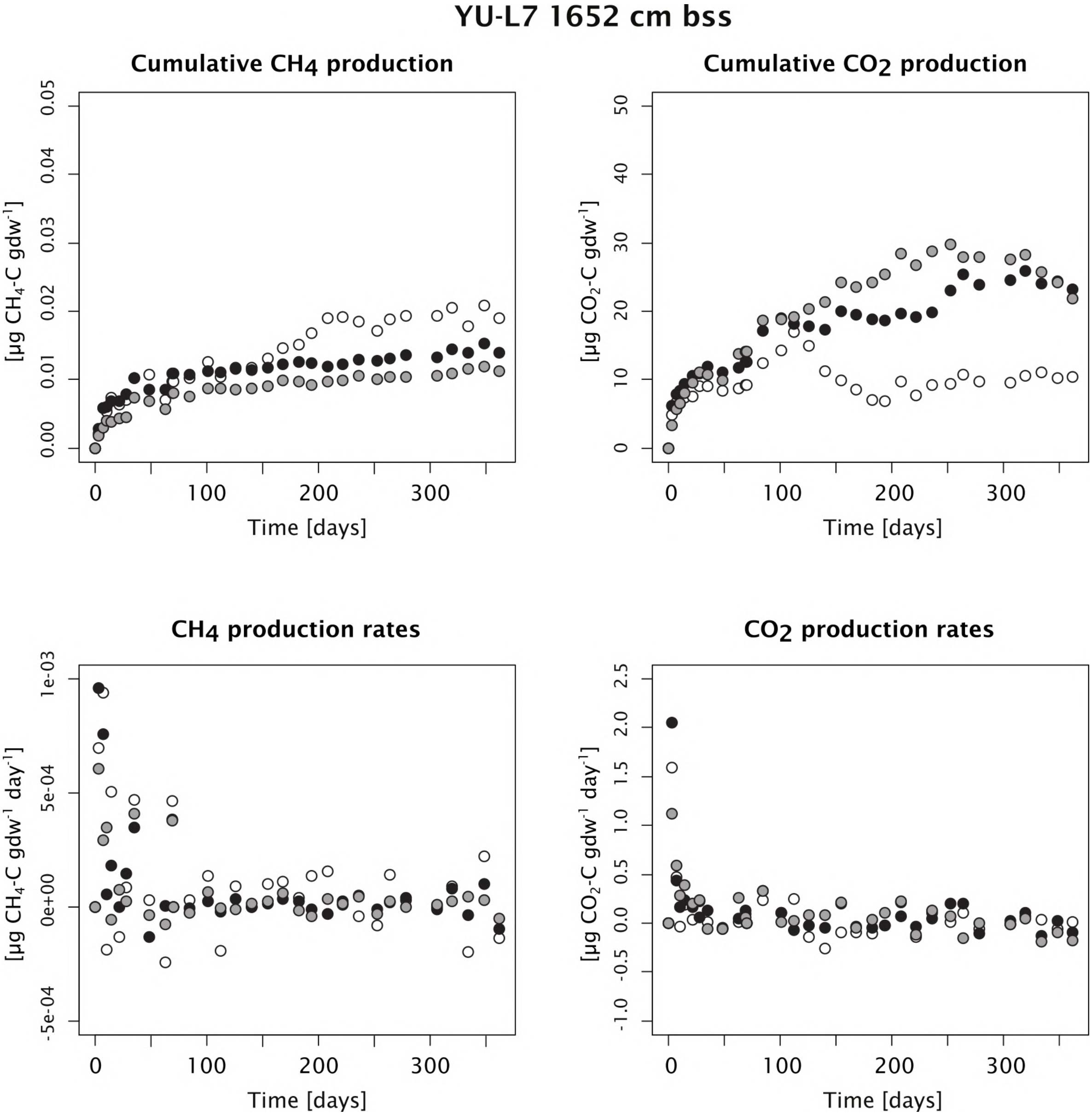

Figure B.14: Greenhouse gas production in Alas lake sediment core YU-L7 at 1652 cm below the sediment surface (bss). a. Cumulative CH_4 production over time, b. cumulative CO_2 production over time, c. CH_4 production rates over time, d. CO_2 production over time. White, grey and black circles show three replicates.

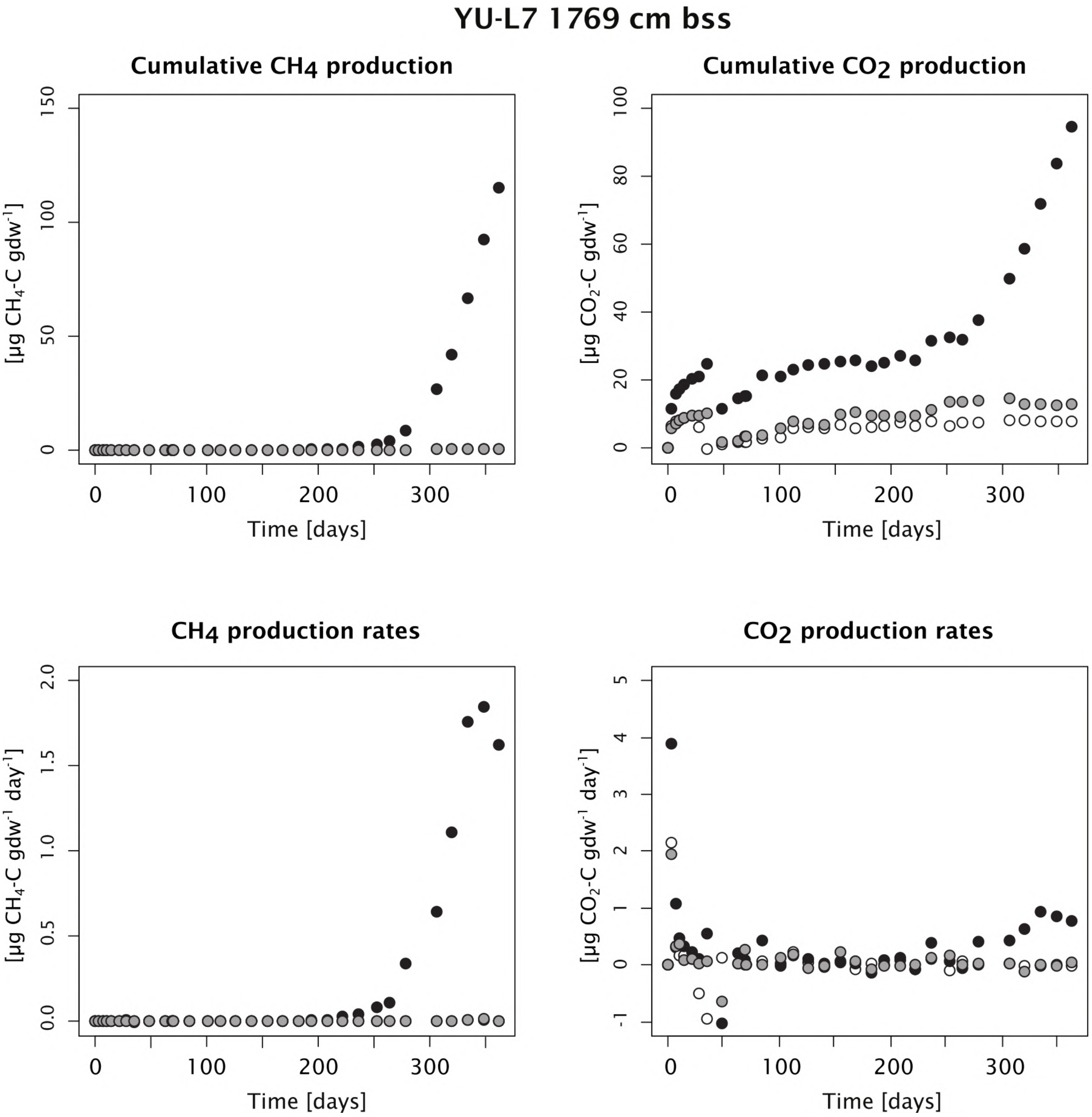

Figure B.15: Greenhouse gas production in Alas lake sediment core YU-L7 at 1769 cm below the sediment surface (bss). a. Cumulative CH_4 production over time, b. cumulative CO_2 production over time, c. CH_4 production rates over time, d. CO_2 production over time. White, grey and black circles show three replicates.

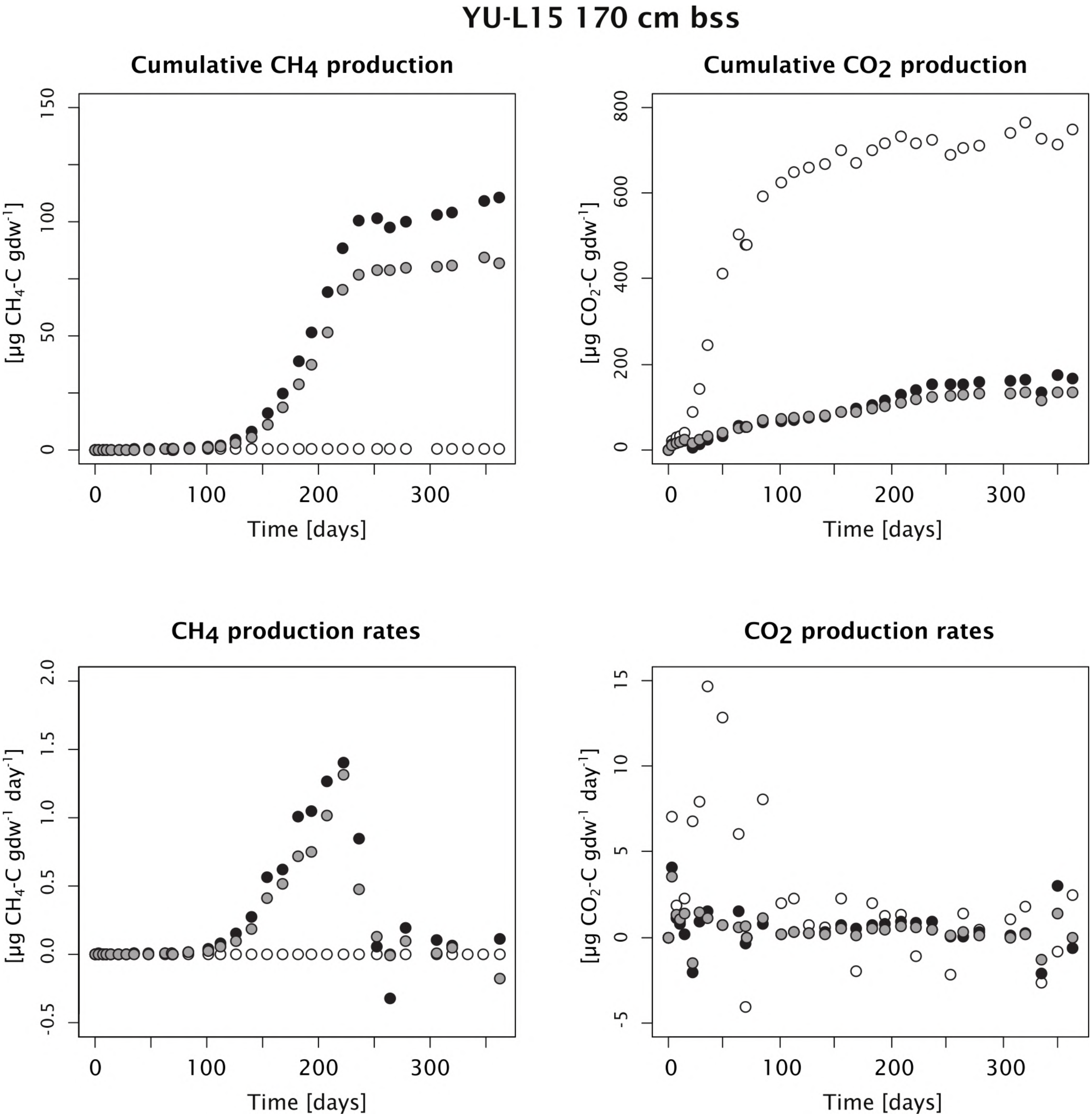

Figure B.16: Greenhouse gas production in Yedoma lake sediment core YU-L15 at 170 cm below the sediment surface (bss). a. Cumulative CH_4 production over time, b. cumulative CO_2 production over time, c. CH_4 production rates over time, d. CO_2 production over time. White, grey and black circles show three replicates.

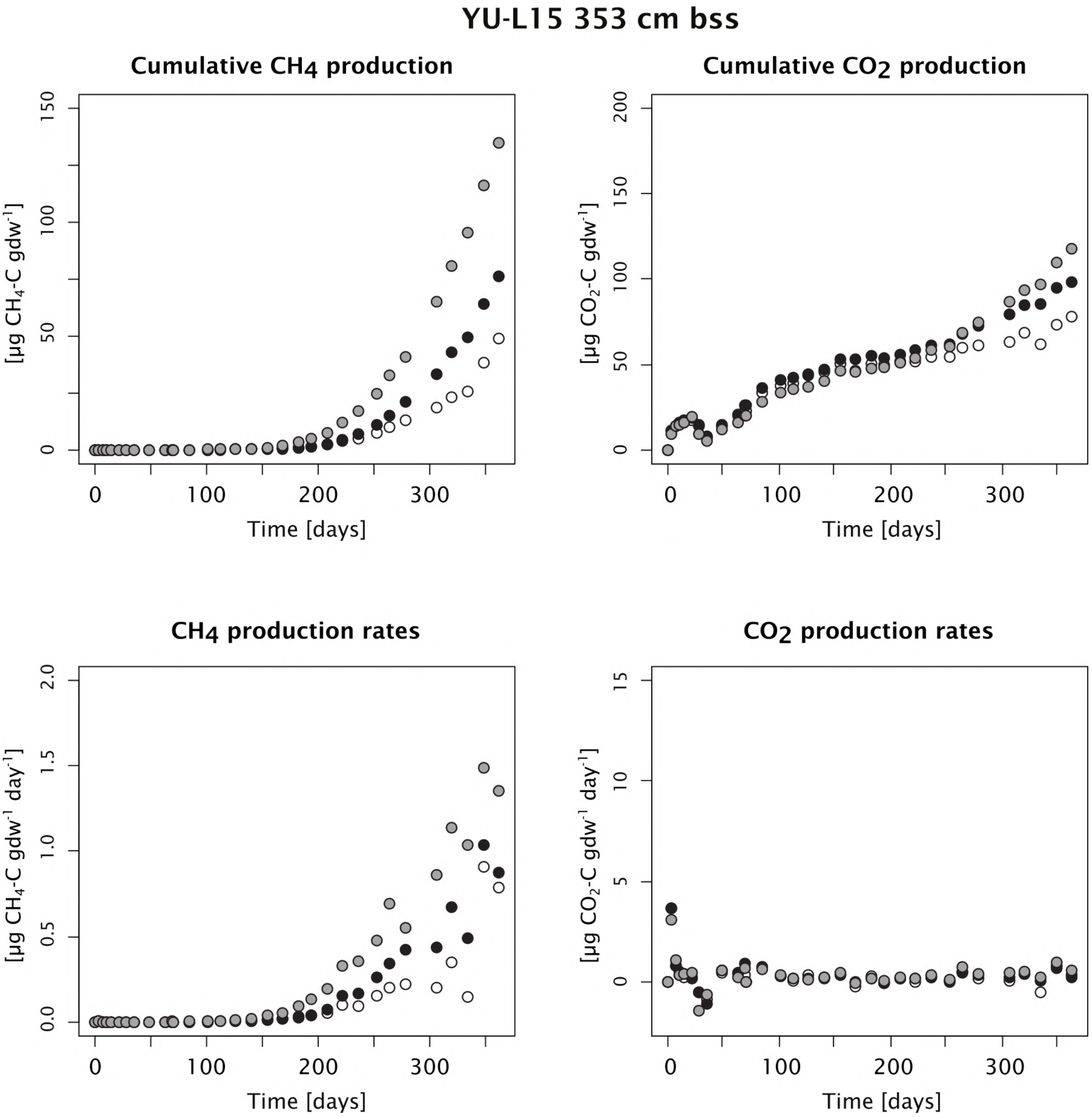

Figure B.17: Greenhouse gas production in Yedoma lake sediment core YU-L15 at 353 cm below the sediment surface (bss). a. Cumulative CH_4 production over time, b. cumulative CO_2 production over time, c. CH_4 production rates over time, d. CO_2 production over time. White, grey and black circles show three replicates.

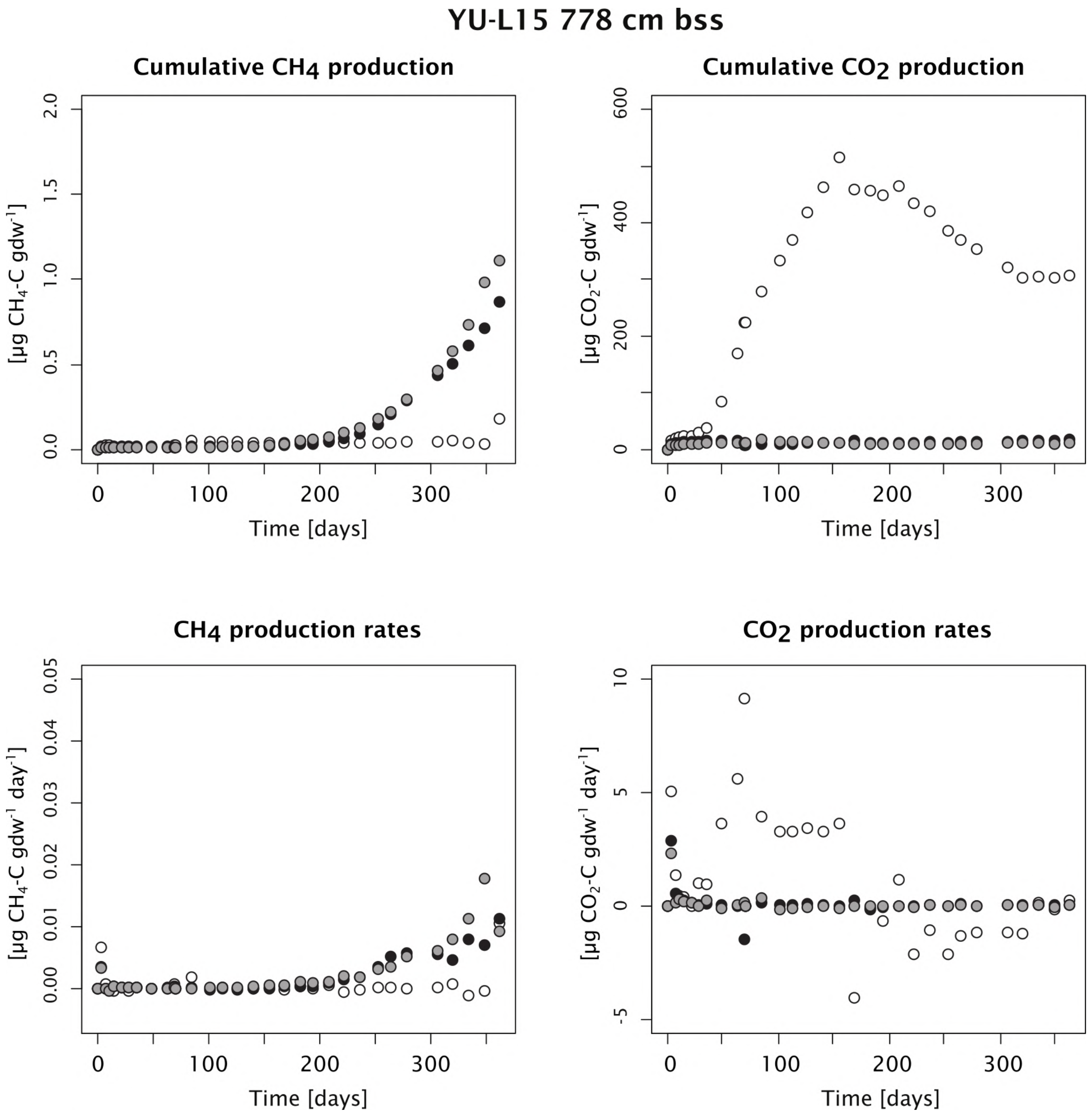

Figure B.18: Greenhouse gas production in Yedoma lake sediment core YU-L15 at 778 cm below the sediment surface (bss). a. Cumulative CH_4 production over time, b. cumulative CO_2 production over time, c. CH_4 production rates over time, d. CO_2 production over time. White, grey and black circles show three replicates.

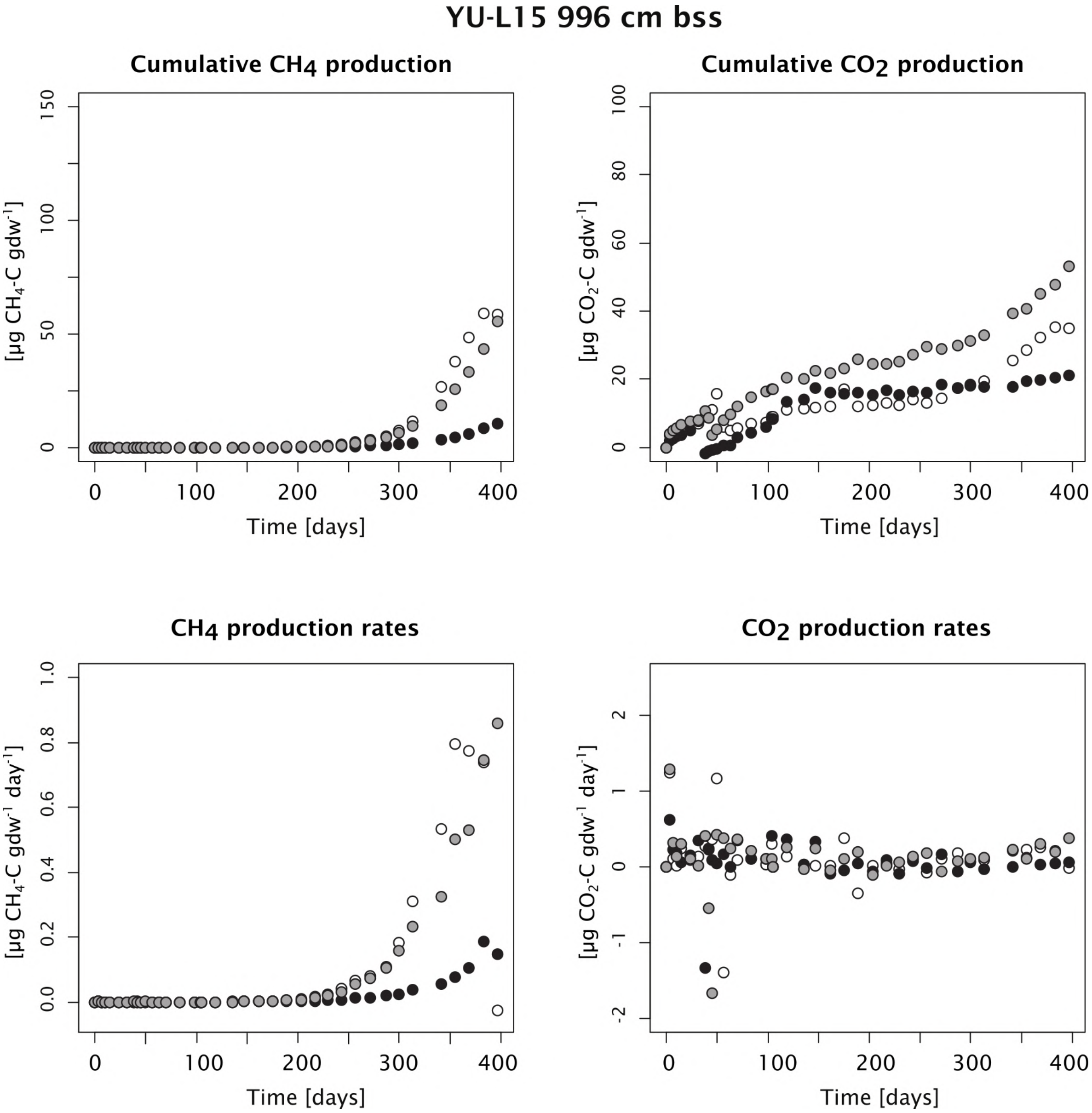

Figure B.19: Greenhouse gas production in Yedoma lake sediment core YU-L15 at 996 cm below the sediment surface (bss). a. Cumulative CH_4 production over time, b. cumulative CO_2 production over time, c. CH_4 production rates over time, d. CO_2 production over time. White, grey and black circles show three replicates.

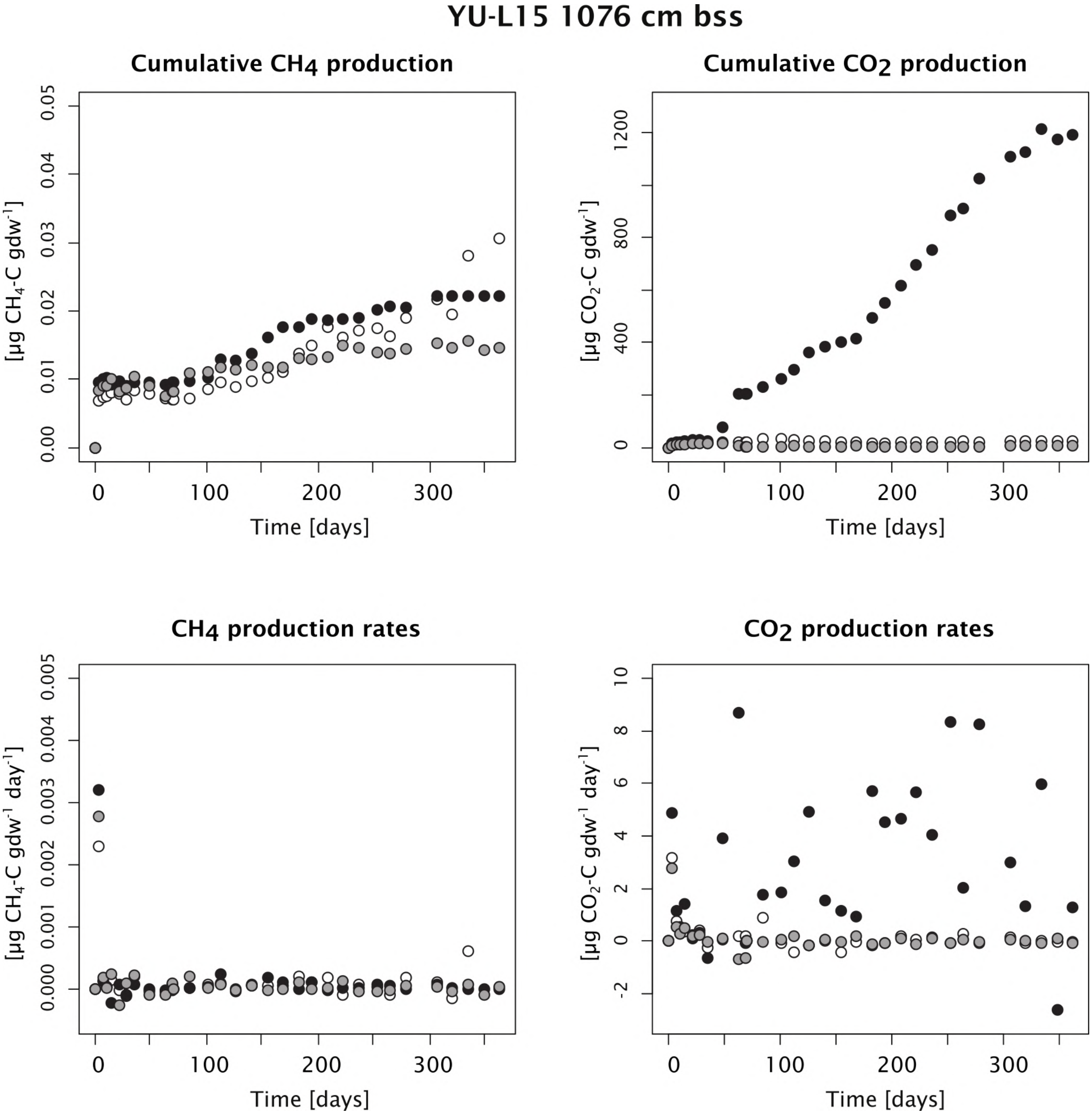

Figure B.20: Greenhouse gas production in Yedoma lake sediment core YU-L15 at 1076 cm below the sediment surface (bss). a. Cumulative CH_4 production over time, b. cumulative CO_2 production over time, c. CH_4 production rates over time, d. CO_2 production over time. White, grey and black circles show three replicates.

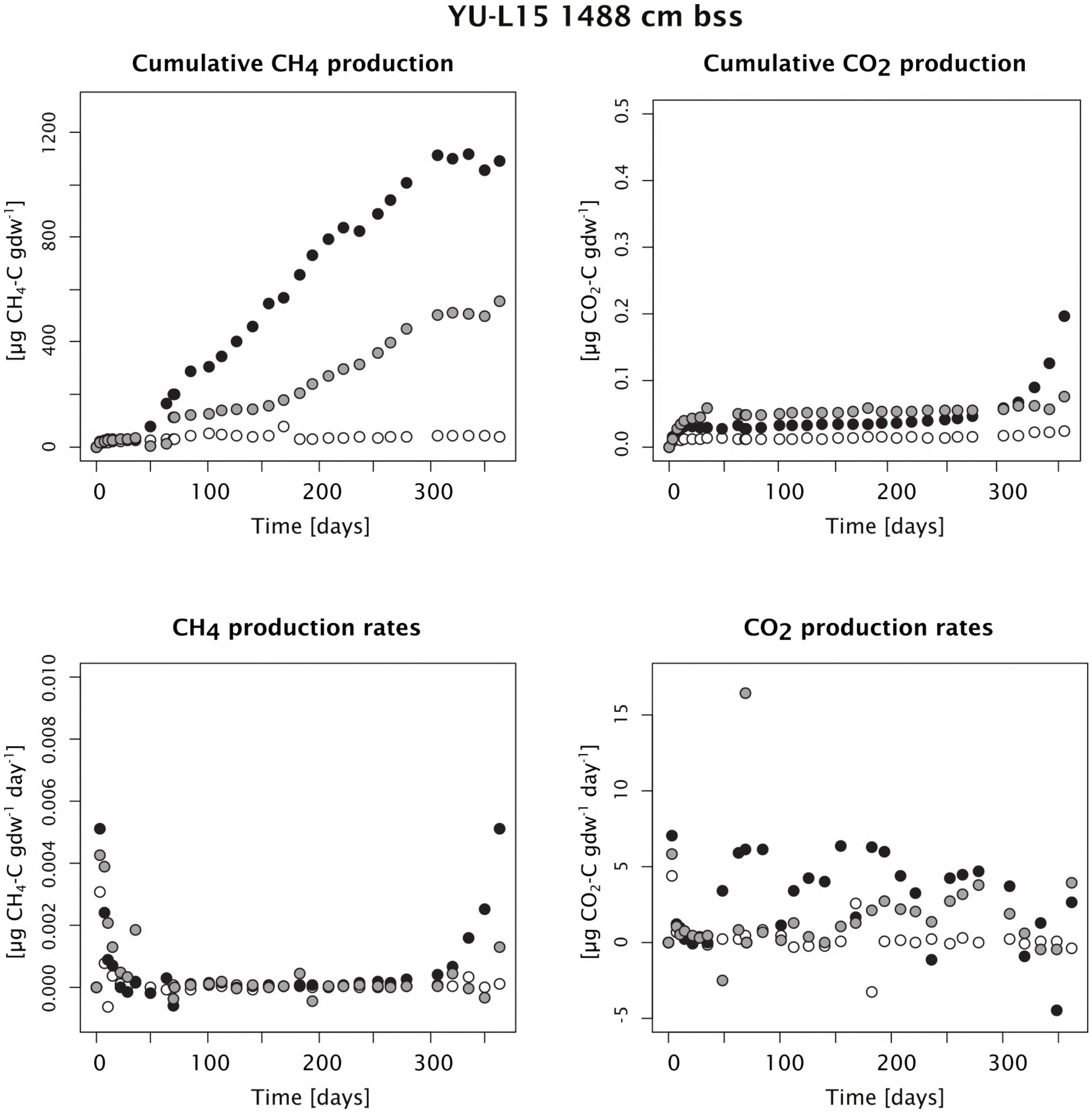

Figure B.21: Greenhouse gas production in Yedoma lake sediment core YU-L15 at 1488 cm below the sediment surface (bss). a. Cumulative CH_4 production over time, b. cumulative CO_2 production over time, c. CH_4 production rates over time, d. CO_2 production over time. White, grey and black circles show three replicates.

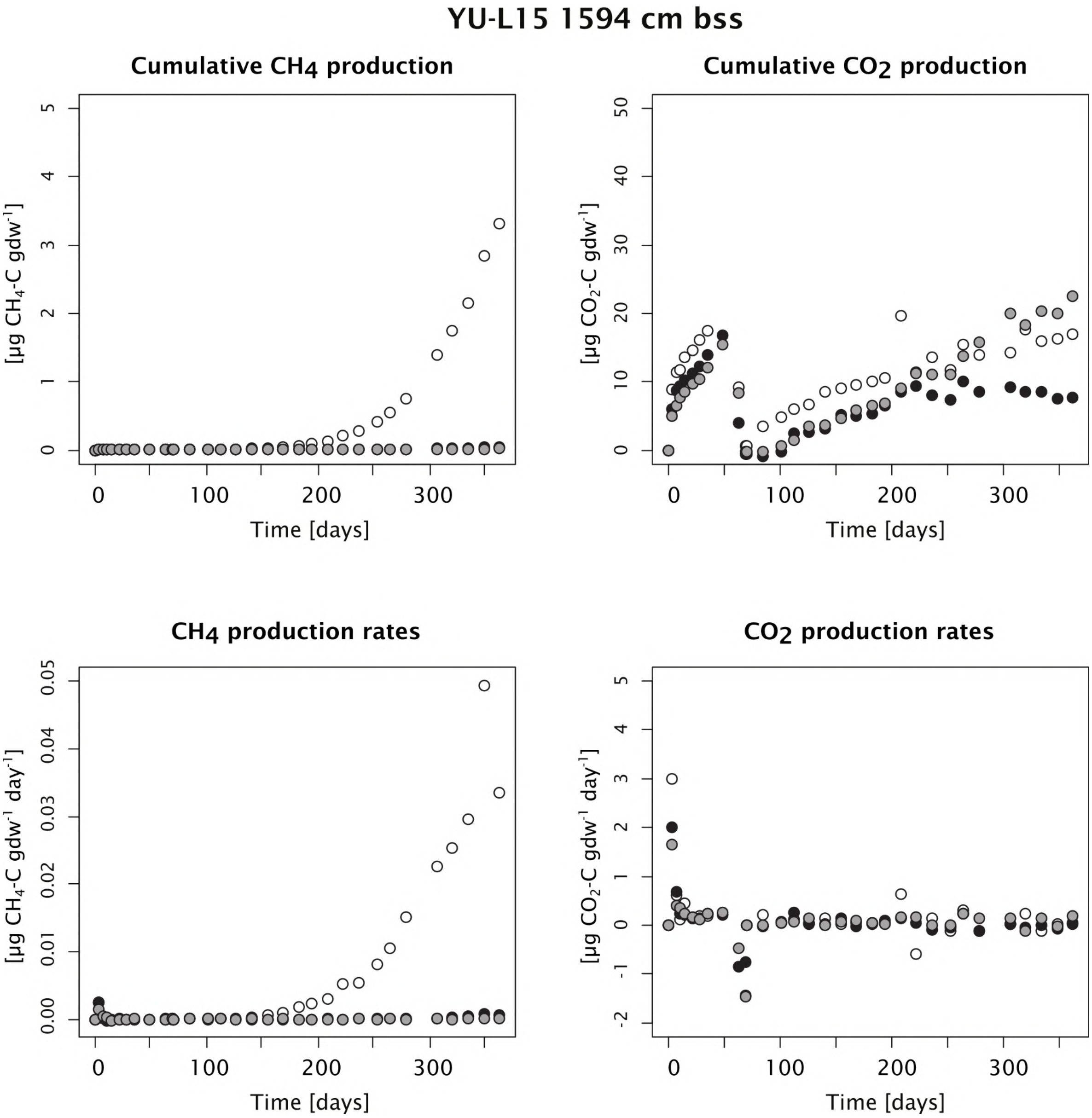

Figure B.22: Greenhouse gas production in Yedoma lake sediment core YU-L15 at 1594 cm below the sediment surface (bss). a. Cumulative CH_4 production over time, b. cumulative CO_2 production over time, c. CH_4 production rates over time, d. CO_2 production over time. White, grey and black circles show three replicates.

C

Supporting information for Chapter 4

Kruskal-Wallis rank sum test	**Unit**	**H-value**	***p*-value**	**df**	**Significance**
TOC	wt%	13.565	0.001133	2	yes
C/N		8.9772	0.01124	2	yes
[short chain *n*-alkanes]	µg/gTOC	6.2937	0.04299	2	yes
[long *n*-alkanes]	µg/gTOC	5.3474	0.06899	2	no
ACL		2.0851	0.3525	2	no
CPI		1.8262	0.4013	2	no
[short chain *n*-fatty acids]	µg/gTOC	0.91209	0.6338	2	no
[mid chain *n*-fatty acids]	µg/gTOC	0.12912	0.9375	2	no
[long chain *n*-fatty acids]	µg/gTOC	0.51648	0.7724	2	no
HPFA		6.1951	0.04516	2	yes
(*iso*+*anteiso*)/long *n*-FAs		4.8619	0.08795	2	no

Table C.1: Results of Kruskal-Wallis rank sum test for the Sobo-Sise Yedoma cliff: H-value, *p*-value, degrees of freedom (df) and indication of significance ($p<0.05$).

Name	**Abbr.**	**FA Class**
3 Hydroxy-hexanoic acid	3OH-6:0	hydroxy-FA
Octanoic acid	8:0	*n*-FA
3-Hydroxy-heptanoic acid	3OH-7:0	hydroxy-FA
Nonanoic acid	9:0	*n*-FA
3 Hydroxy-octanoic acid	3OH-8:0	hydroxy-FA
8 Methyl-nonanoic acid	iso10:0	iso sat. FA
Decanoic acid	10:0	*n*-FA
9 Methyl-decanoic acid	iso11:0	iso sat. FA
8 Methyl-decanoic acid	ai11:0	anteiso sat. FA
Undecanoic acid	11:0	*n*-FA
10 Methyl-undecanoic acid	iso12:0	iso sat. FA
Dodecanoic acid	12:0	*n*-FA
11 Methyl-dodecanoic acid	iso13:0	iso sat. FA
10 Methyl-dodecanoic acid	ai13:0	anteiso sat. FA
Tridecanoic acid	13:0	*n*-FA
12 Methyl-tridecanoic acid	iso14:0	iso sat. FA
Tetradecanoic acid	14:0	*n*-FA
10 Methyl-tetradecanoic acid	10Me-14:0	Me-branched FA
13 Methyl-tetradecanoic acid	iso15:0	iso sat. FA
12 Methyl-tetradecanoic acid	ai15:0	anteiso sat. FA
Pentadecanoic acid	15:0	*n*-FA
14 Methylpentadecanoic acid	iso16:0	iso sat. FA
Hexadec-9(Z)-enoic acid	16:1ω7c	monounsat. FA
Hexadec-9(E)-enoic acid	16:1ω7t	monounsat. FA
Hexadec-11-enoic acid	16:1ω5	monounsat. FA
Hexadecanoic acid	16:0	*n*-FA
15 Methyl-hexadec-9-enoic acid	iso17:1ω7	iso unsat. FA
10 Methyl-hexadecanoic acid	10Me-16:0	Me-branched FA
12 Methyl-hexadecanoic acid	12Me-16:0	Me-branched FA
14 Methyl-hexadec-9-enoic acid	ai17:1ω7	anteiso unsat. FA
Methyl-hexadecanoic acid	Me-16:0	Me-branched FA
15 Methyl-hexadecanoic acid	iso17:0	iso sat. FA
14 Methyl-hexadecanoic acid	ai17:0	anteiso sat.FA
Heptadecenoic acid	17:1	monounsat. FA

Table C.2: List of identified fatty acids (FAs) and their compound classes as used in Figure C-2: hydroxy FA, *n*-FAs, iso saturated (sat.) FA, anteiso sat., methyl (Me)-branched FA, monounsat. FA, isoprenoid FA, di/tri unsat. FA and cyclopropyl FA.

Name	**Abbr.**	**FA Class**
9,10-Methylene-hexadecanoic acid	cyclo-C17	cyclopropyl FA
Heptadecanoic acid	17:0	*n*-FA
10 Methyl-heptadecanoic acid	10Me-17:0	Me-branched FA
Methyl-heptadecanoic acid	Me-17:0	Me-branched FA
3,7,11,15-tetramethyl-hexadecanoic acid	phytanoic acid	isoprenoid FA
16 Methyl-heptadecanoic acid	iso18:0	iso sat. FA
Octadec-9,12-dienoic acid	18:2ω6,9	di/tri unsat. FA
Octadec-9(Z)-enoic acid	18:1ω9c	monounsat. FA
Octadec-9,12,15-trienoic acid	18:3ω3,6,9	di/tri unsat. FA
Octadec-11(Z)-enoic acid	18:1ω7c	monounsat. FA
Octadec-11(E)-enoic acid	18:1ω7t	monounsat. FA
Octadecanoic acid	18:0	*n*-FA
10 Methyl-octadecanoic acid	10Me-18:0	Me-branched FA
12 Methyl-octadecanoic acid	12Me-18:0	Me-branched FA
17 Methyl-octadecanoic acid	iso19:0	iso sat. FA
9,10-Methylene-octadecanoic acid	cyclo-19	cyclopropyl FA
Nonadecenoic acid	19:1	monounsat. FA
Nonadecanoic acid	19:0	*n*-FA
Eicosenoic acid	20:1	monounsat. FA
Eicosanoic acid	20:0	*n*-FA
Uneicosanoic acid	21:0	*n*-FA
Heneicosanoic acid	22:0	*n*-FA
Tricosanoic acid	23:0	*n*-FA
Tetracosenoic acid	24:1	monounsat. FA
Tetracosanoic acid	24:0	*n*-FA
Pentacosanoic acid	25:0	*n*-FA
Uneicosanoic acid	21:0	*n*-FA
Heneicosanoic acid	22:0	*n*-FA
Tricosanoic acid	23:0	*n*-FA
Tetracosenoic acid	24:1	monounsat. FA
Tetracosanoic acid	24:0	*n*-FA
Pentacosanoic acid	25:0	*n*-FA
Hexacosanoic acid	26:0	*n*-FA
Heptacosanoic acid	27:0	*n*-FA
Octacosanoic acid	28:0	*n*-FA
Nonacosanoic acid	29:0	*n*-FA
Triacontanoic acid	30:0	*n*-FA
Dotriacontanoic acid	32:0	*n*-FA
Nonacosanoic acid	29:0	*n*-FA
Triacontanoic acid	30:0	*n*-FA
Dotriacontanoic acid	32:0	*n*-FA

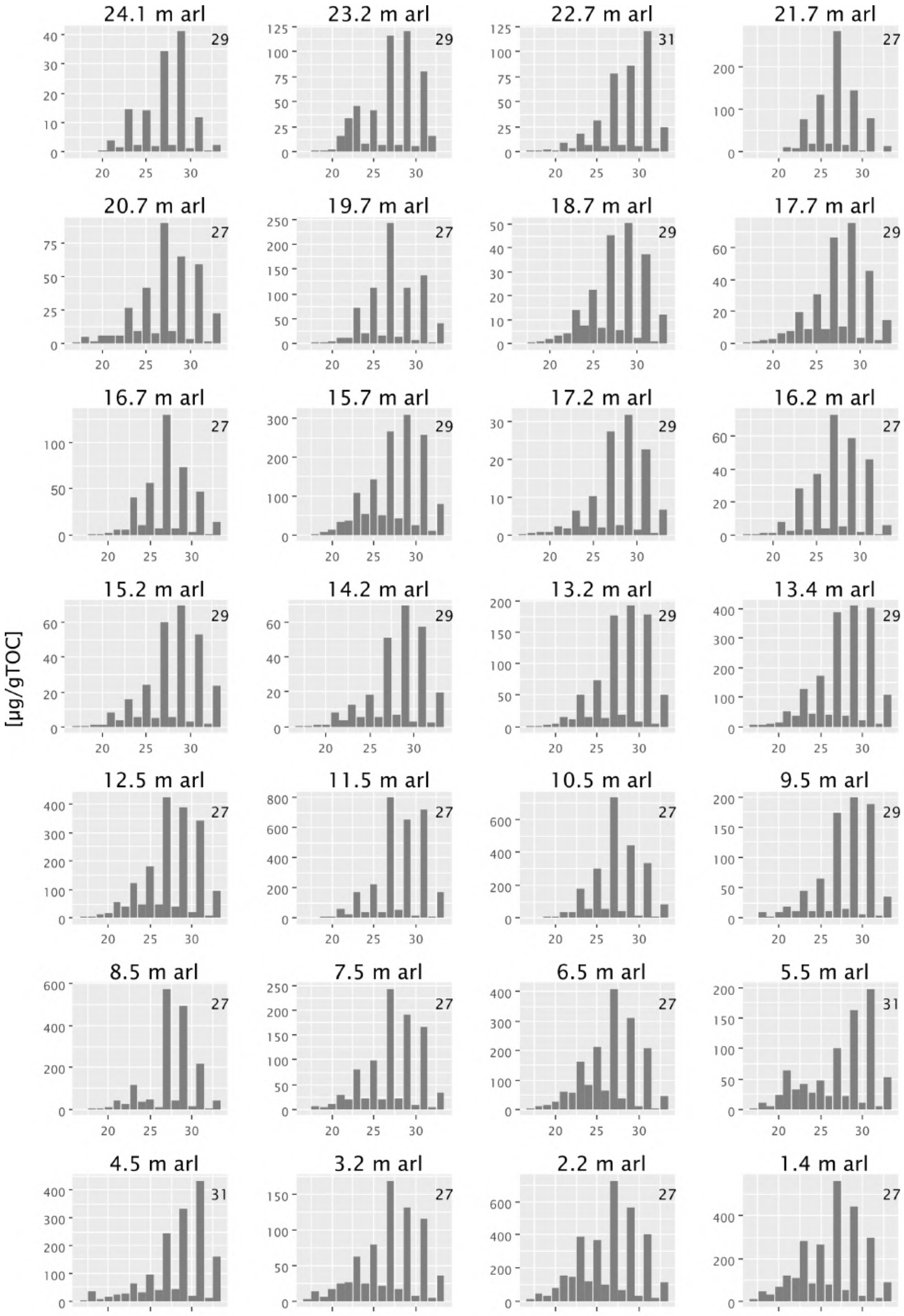

Figure C.1: *n*-Alkane (C_{14}-C_{33}) distribution of the Sobo-Sise Yedoma cliff. Depths are indicated above graphs in meters above river level (arl). The dominant *n*-alkane chain length is indicated in the upper right corner. Concentrations are expressed in µg/gTOC.

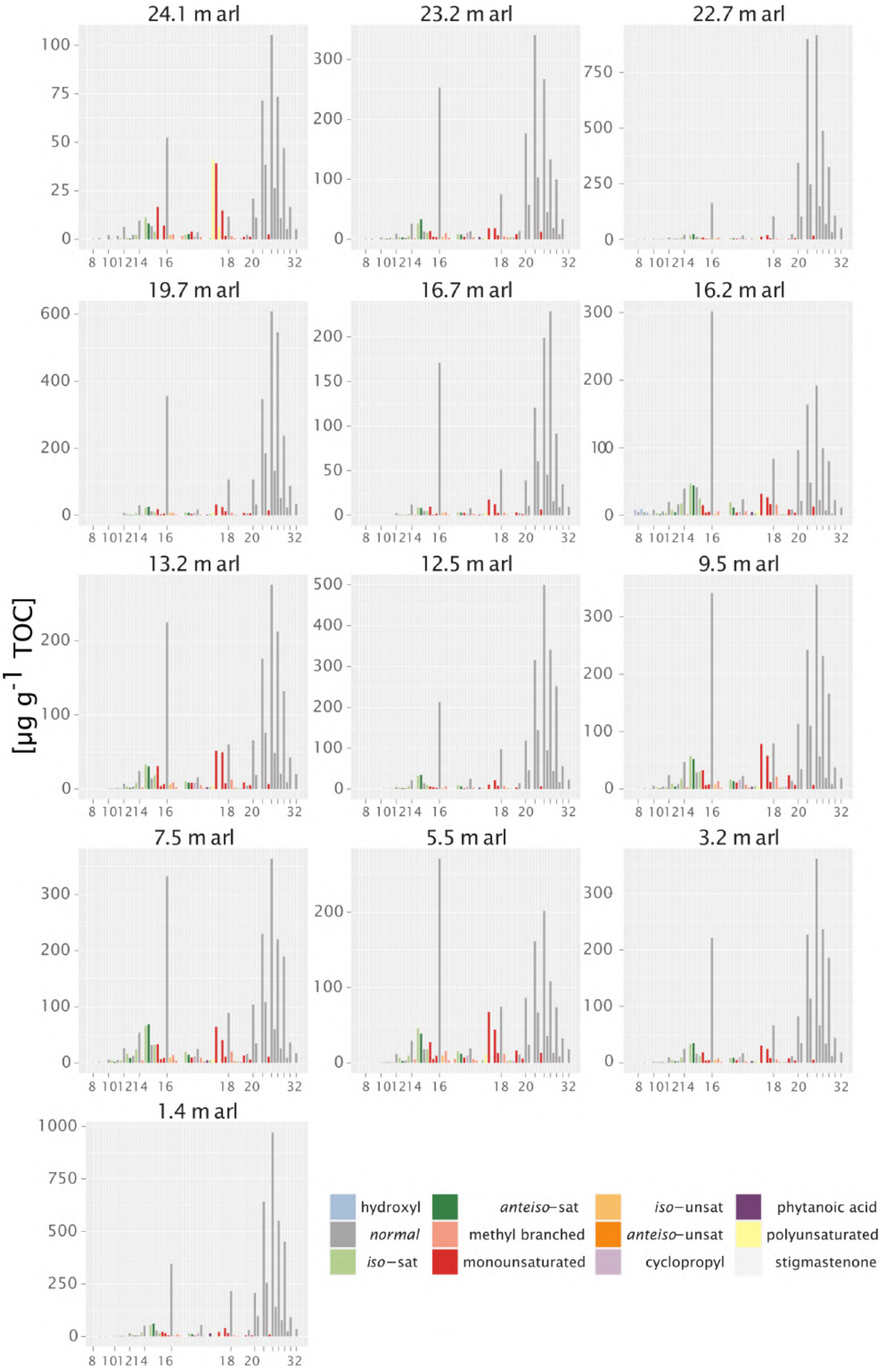

Figure C.2: Fatty acid (C_8-C_{32}) distribution of the Sobo-Sise Yedoma cliff. Depths are indicated above graphs in meters above river level (arl). Concentrations are expressed in µg/gTOC. See Table C.2 for a list of identified FAs and their compound classes.

D

Supporting information for Chapter 5

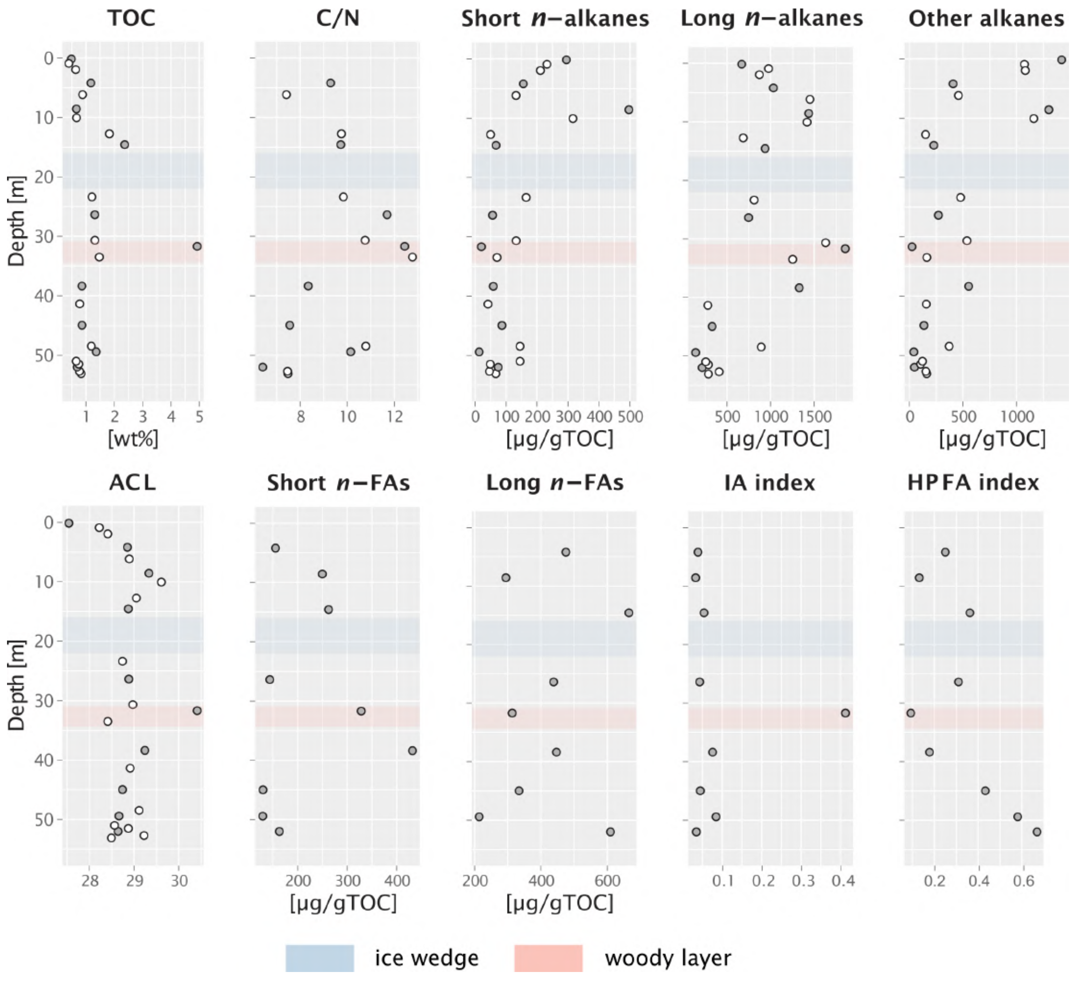

Figure D.1: Biochemical parameters along main headwall (profile 1 and 2). Depth in meters from top headwall. Upper row: total organic carbon (TOC) content, carbon to nitrogen ratio (C/N), concentration of short n-alkanes ($C<20$), long n-alkanes, and other alkanes (branched and cyclic alkanes). Bottom row: n-alkane proxy average chain length (ACL), concentration of short n-fatty acids (n-FAs) ($C<20$), and long n-FAs, ratio of iso/anteiso-branched FA C_{15} and C_{17} vs long n-FAs (IA index) and higher-plant fatty-acid index (HPFA). Grey dots: selected samples for NSO separation.

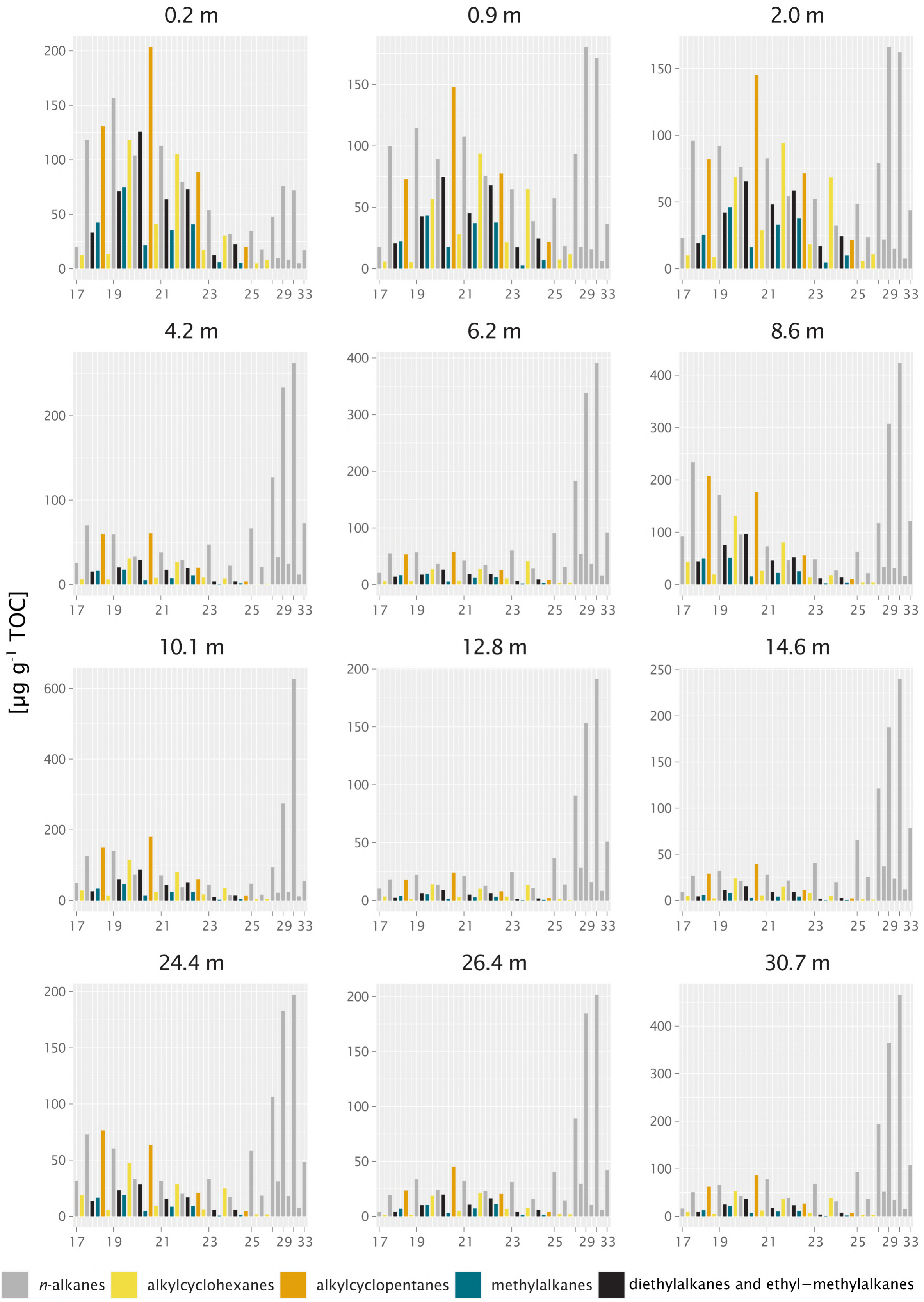

Figure D.2: Alkane distribution of sediment samples of main headwall (profile 1 and 2). Depth in meters from top headwall indicated above graphs, corresponding to stratigraphical units: 1. Lower Ice Complex (53.1-52.0 m), 2. Lower Sand Unit (51.5-33.5 m), 3. Woody Layer (31.7 m), 4. Upper Ice Complex (30.7-4.2 m) and 5. Holocene Cover (2.0-0.2 m). Odd *n*-alkanes indicated with ticks on x-axis. Concentrations on y-axis expressed in µg g^{-1} TOC. Continuation of figure on next page.

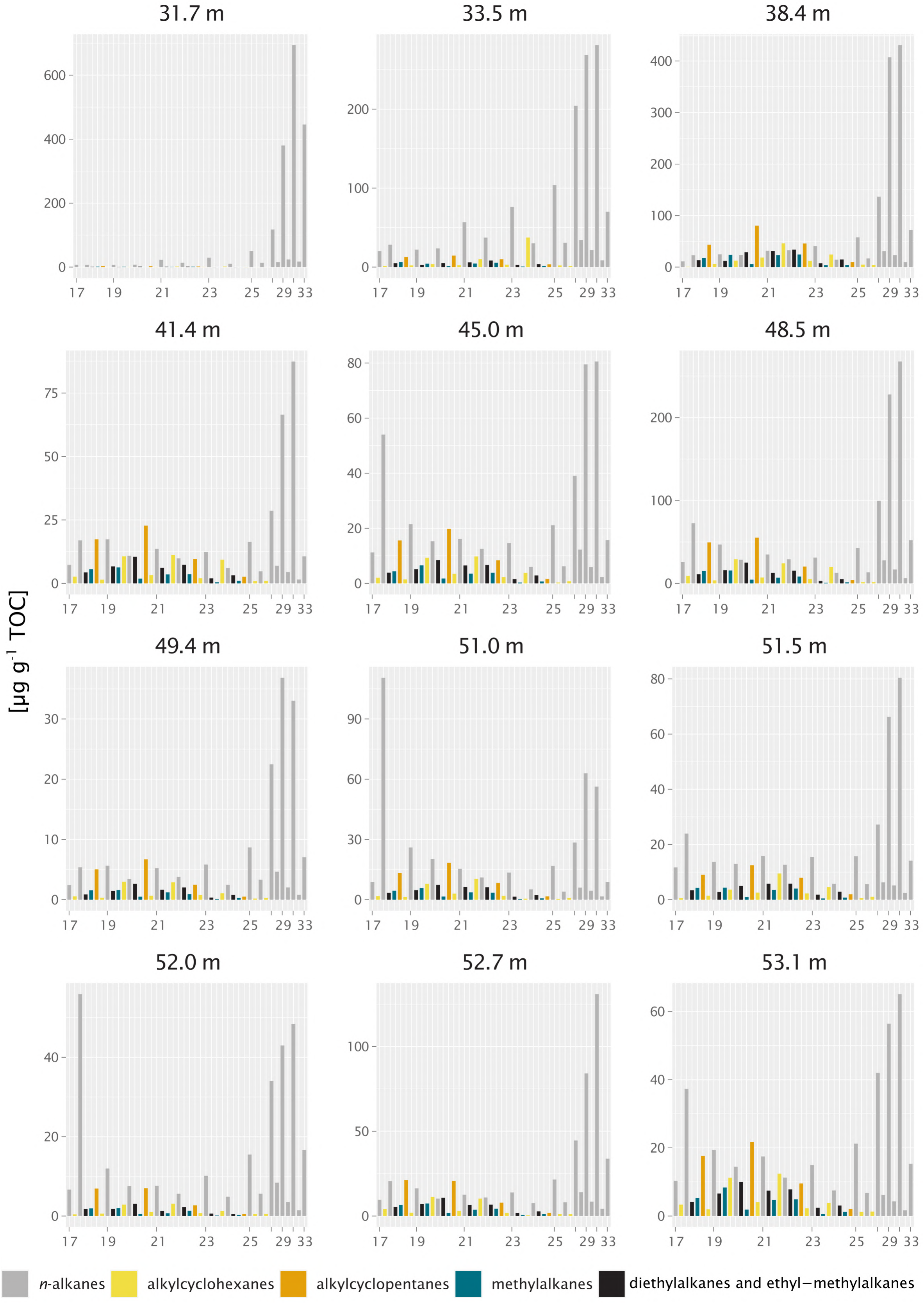
[µg g^{-1} TOC]
31.7 m
0
200
400
600
33.5 m
0
100
200
38.4 m
0
100
200
300
400
41.4 m
0
25
50
75
45.0 m
0
20
40
60
80
48.5 m
0
100
200
49.4 m
0
10
20
30
51.0 m
0
30
60
90
51.5 m
0
20
40
60
80
52.0 m
0
20
40
52.7 m
0
50
100
53.1 m
0
20
40
60
17
19
21
23
25
29
33
n-alkanes
alkylcyclohexanes
alkylcyclopentanes
methylalkanes
diethylalkanes and ethyl−methylalkanes

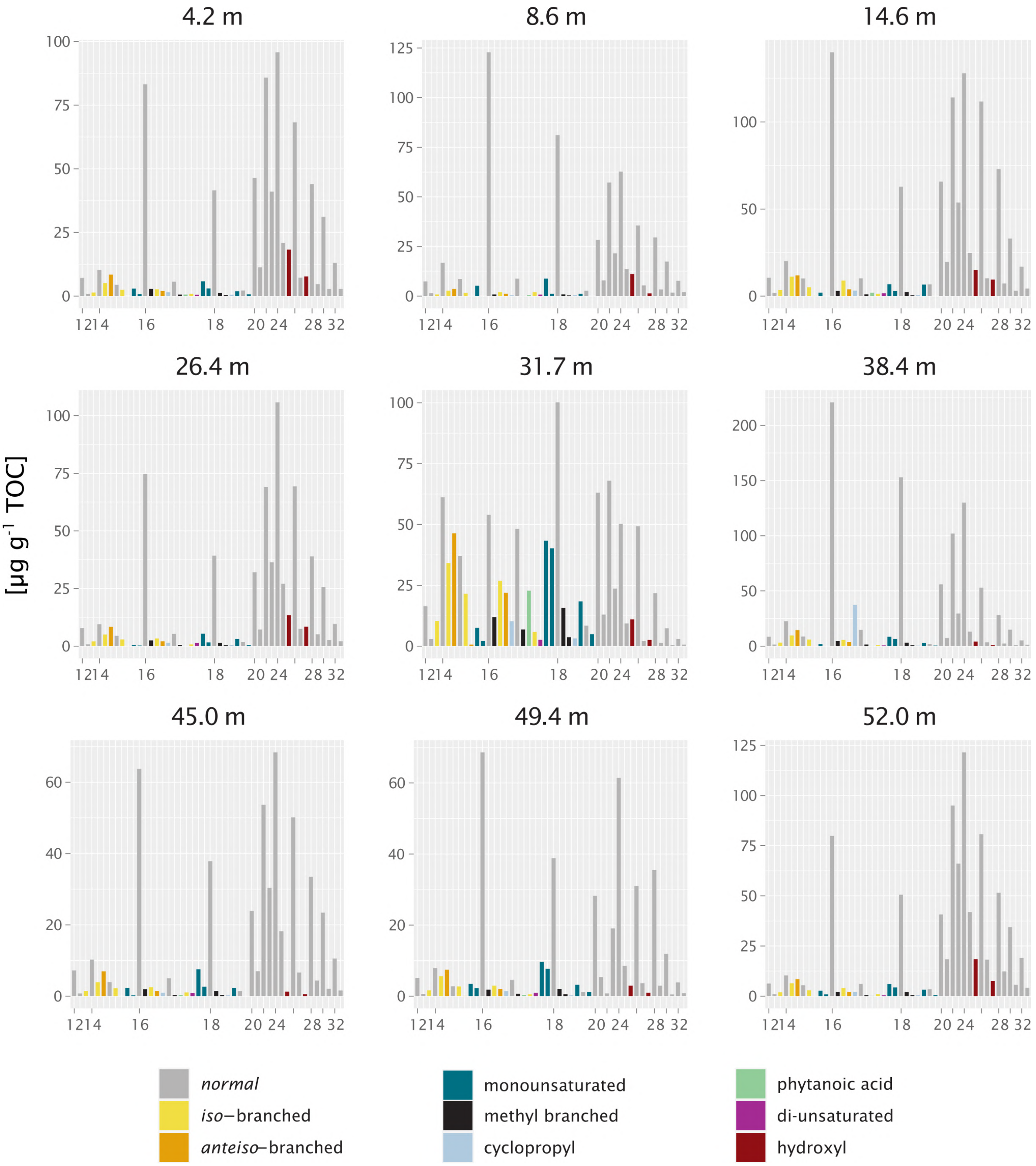

Figure D.3: Fatty acid distribution of selected sediment samples of main headwall (profile 1 and 2). Depth in meters from top headwall indicated above graphs, corresponding to stratigraphical units (see Figure D.1). Even *n*-fatty acids indicated with ticks on x-axis. Concentrations on y-axis expressed in µg g^{-1} TOC.

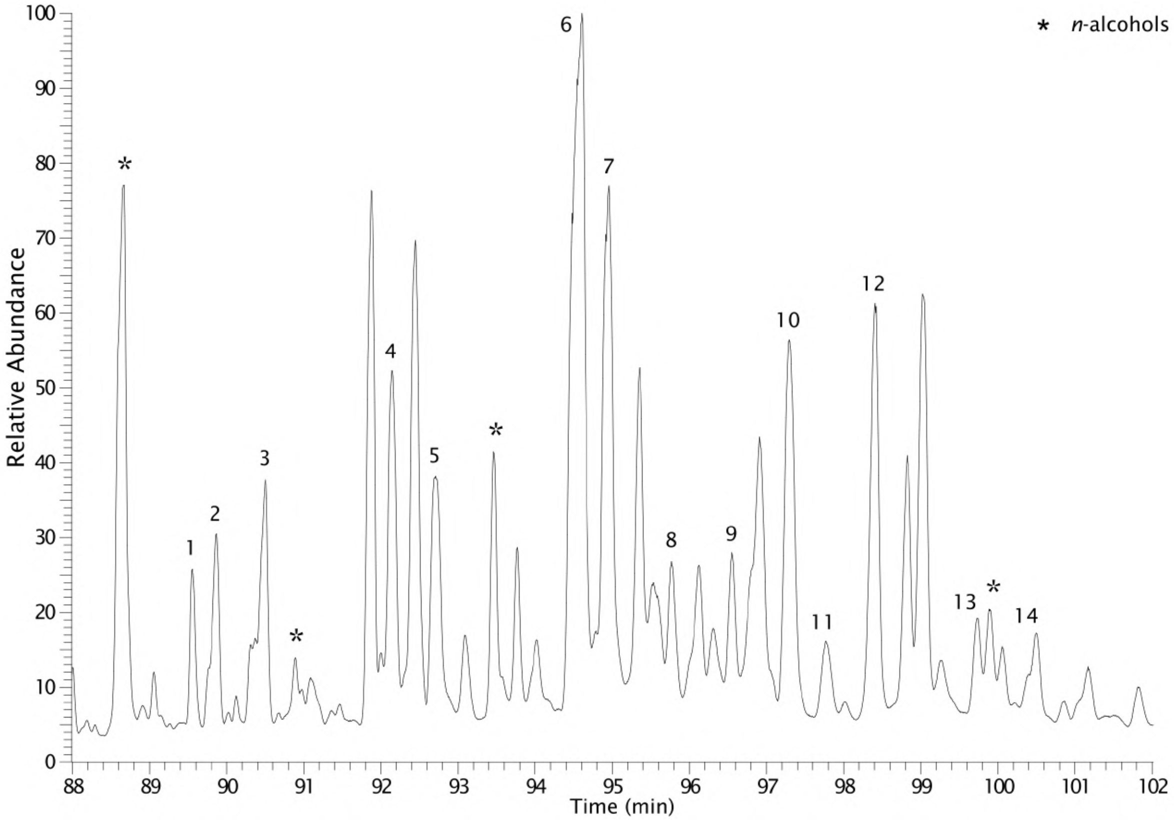

Figure D.4: Total ion current of the sterols and triterpenoids found in the sediments at 31.7 m bs (profile 1). * indicates *n*-alcohols (C_{28}-C_{30} and C_{32}). Numbered peaks are identified in Table 5.1.

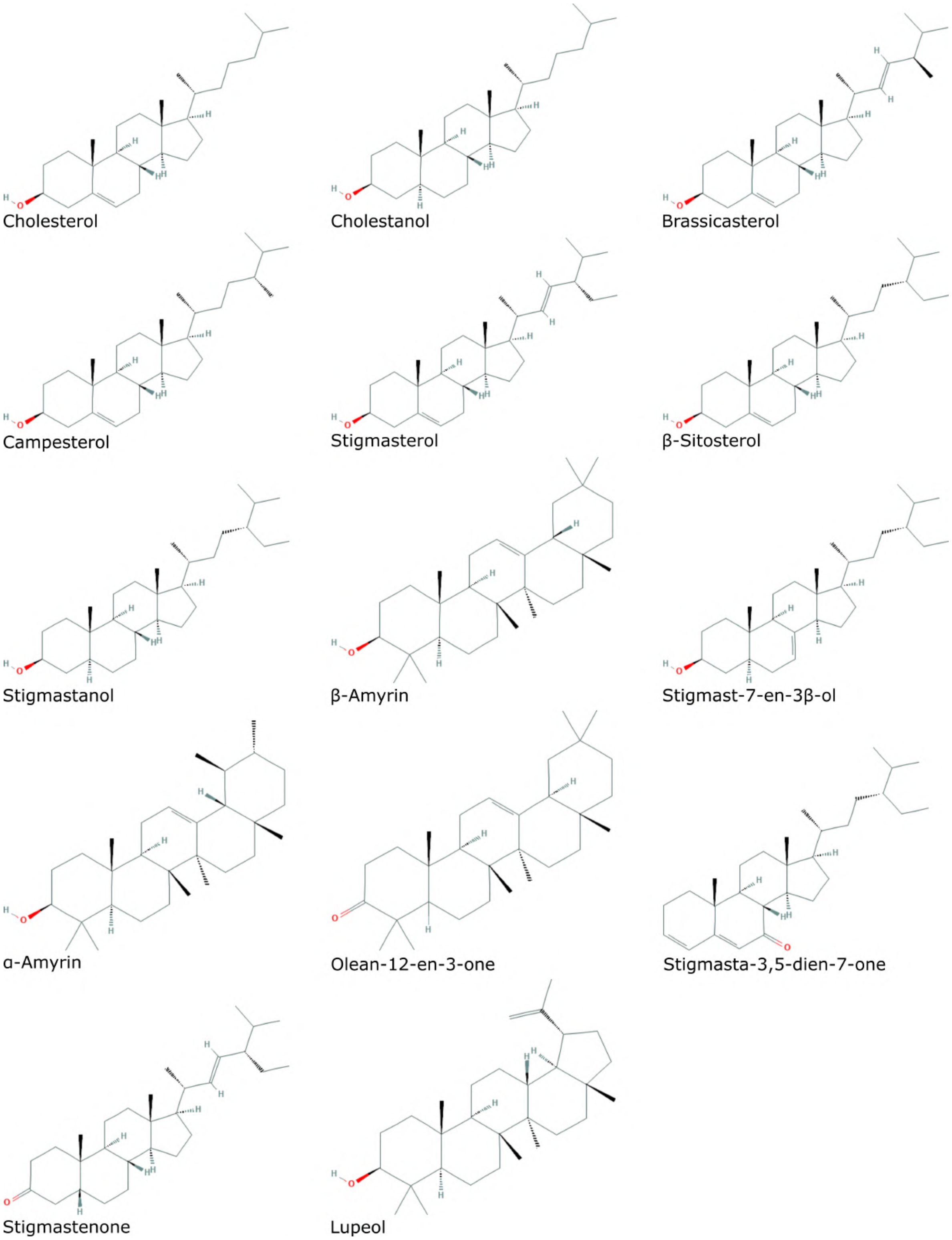

Cholesterol

Cholestanol

Brassicasterol

Campesterol

Stigmasterol

β-Sitosterol

Stigmastanol

β-Amyrin

Stigmast-7-en-3β-ol

α-Amyrin

Olean-12-en-3-one

Stigmasta-3,5-dien-7-one

Stigmastenone

Lupeol

Figure D.5: Chemical structures of sterols and triterpenoids found in the sediments at 31.7 m bs (profile 1).